POLITECNICO DI MILANO
School of Industrial and Information Engineering

MSc in Mechanical Engineering

Combustor non-uniformities convection in a HP Turbine operating in design and off-design conditions

Supervisor: Prof. Paolo Gaetani
Co-supervisor: Eng. Andrea Notaristefano

Thesis of:
Sami Tasmany, 10500590
Fabio Urnelli, 10495049

Academic year 2020-2021

Alle nostre famiglie

Abstract

Achieving low NOx emissions in gas turbines is fundamental for air quality. In order to meet pollutant emission regulations, modern combustors exploit lean premixed combustion to limit flame temperature, and hence NOx formation. However, this results in a strong unsteady heat release rate which produces unsteady temperature fluctuations, commonly known as entropy waves (EWs). Moreover, combustion air is swirled to get it thoroughly mixed with fuel, thus preventing local hot spots that can lead to significant NOx formation. These non-uniformities, i.e. swirled entropy waves, generated inside combustion chamber have strong impact on turbine stage aerodynamics and so it's crucial to investigate their convection through the stage. In the past years some studies have been already done, but some aspects have still to be addressed. This work aims at studying swirled entropy waves convection through an axial turbine stage working in both design and off-design conditions, by means of an experimental campaign carried out on the high-speed test rig at Politecnico di Milano. The facility features a combustor simulator called Entropy Wave Generator (EWG) equipped with a swirl generator. This device injects the disturbance axially upstream of the stator and two different clocking positions are investigated to study the effects of injection position. Along the turbine stage three measuring sections are defined (stator inlet, stator outlet and rotor outlet) and measurements are performed thanks to temperature and pressure probes, whose features are deeply described. The experimental results show that the injected swirl profile influences remarkably the aerodynamics and that EWs magnitude undergoes attenuation as they cross the stage.

Keywords: *Swirled entropy waves, Hot streaks, High pressure axial turbine, Turbine off-design operative conditions, Fast response pressure probe, FRAPP, 5-hole pressure probe*

Sommario

Per ragioni di inquinamento atmosferico, è necessario limitare l'emissione di NOx nelle turbine a gas. I requisiti imposti dalle autorità regolatorie possono essere soddisfatti grazie ai moderni combustori, che sfruttano una combustione magra premiscelata limitando così la temperatura di fiamma e quindi la formazione dei NOx. Tuttavia questa soluzione comporta un rilascio di calore instabile che causa fluttuazioni di temperatura nel flusso, comunemente chiamate entropy waves (EWs). Inoltre all'aria è impartito un moto di swirl così da favorire la perfetta miscelazione di aria e combustibile, evitando così la formazione di punti a temperatura più alta in camera di combustione che favorirebbero la formazione di NOx. Le disuniformità nel flusso causate dalle entropy waves e dallo swirl condizionano l'aerodinamica all'interno dello stadio di turbina ed è pertanto importante studiarne gli effetti. La campagna di test si è svolta nel Laboratorio di Fuidodinamica delle Macchine del Politenico di Milano sul banco prova denominato High-Speed Closed-Loop. Sono state utilizzate differenti sonde per caratterizzare il flusso a monte statore, valle statore e valle rotore.

Contents

List of Figures

List of Tables

Chapter 1

Introduction

Nowadays, control and reduction of pollutant emissions are fundamental for new products design and represent a topic of increasing concern to society and institutions. For this purpose, some studies on lean-burn combustors are being carried out to get lower emission of noxious substances, high efficiency and lower fuel consumption. However, low-NOx combustors show considerable increase in noise emission associated to combustion process, which is a big drawback since noise emission control is fundamental for civil product competitiveness [1]. This is due to lean premixed and stratified combustion that leading to an unsteady heat release rate, combined with a strong swirl motion to enhance mixing capability, produces significant non-uniformities and unsteadiness on the velocity and temperature [1, 2]. The latter are commonly referred as entropy waves.

The non-uniformities generated inside the combustion chamber are advected towards the turbine maintaining their intensity and strength [2], thus contributing to what is called indirect combustion noise (Appendix A). The highly unsteady flow approaching the first stage of the turbine and especially its swirling structures can strongly modify the efficiency of work extraction process within the turbine. In fact, vorticity disturbances interact with the wake and secondary flows strengthening or weakening the latter and , affecting the aerodynamic field and blade operations. So these non-uniformities have to be taken into account by turbine designers. A direct implication of the modified aerothermal field regards the blade heat transfer capability, hence it is fundamental to be able to predict the blades operating temperature in order to extend their life. As a consequence, during the design phase of blade cooling systems, the combustor non-uniformities have to be considered.

Given that the interactions of these unsteadiness with the first turbine stage are not negligible for the aforementioned reasons, an experimental campaign has been settled up. The aim of this campaign is to evaluate the effects of transport and diffusion of swirling entropy waves injected upstream of an axial turbine stage at design and off-design conditions. Past studies showed that a superimposition of the isolate cases considering either a swirl profile or a temperature perturbation leads to misleading results: they should be considered together since their effects are strongly non-linear [2].

Steady and unsteady experimental measurements are carried out through the turbine stage in the high-speed closed-loop test rig of the ”Laboratorio di Fluidodinamica delle turboMacchine” (LFM) at Politecnico di Milano. This test rig features: a centrifugal compressor which allows to set pressure at turbine inlet; heat exchangers where air is cooled down to the desired temperature; an axial turbine stage which is representative of a high-pressure stage and other auxiliary components. The mass flow rate of the plant is then imposed by its operating point, hence by the intersection on the compressor characteristic curve, the turbine characteristic curve and the plant one. In Chapter 2, a comprehensive description of the test rig is provided.

A combustor simulator device, called Entropy Wave Generator (EWG), is placed upstream of the stator. It is able to inject engine-representative entropy waves into the main turbine inlet flow (Fig. 1.1). Its outlet section is designed in such a way to produce a swirl profile that make rotate both some amount of mainstream air and the entropy wave.

The entropy wave is injected at stator blade midspan at two different circumferential position with respect to stator blade: leading edge and mid-pitch.In order to evaluate the influence of only injector presence on the main flow, also tests without entropy wave injection are performed. EWG working principles and details are discussed in Chapter 3.

The EWG mounted on the test rig seems to be, by the authors' knowledge, the first documented in literature that combines the production of an entropy wave with a swirl motion able to represent the harsh combustor-produced environment. Its design and commissioning have been developed by Notaristefano and Gaetani [3].

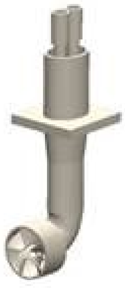

Figure 1.1: Entropy wave generator injector

Different probes are used to measure and characterize the flow quantities: a fast response thermocouple is chosen for carrying out thermal measurements, while for aerodynamic ones a five-hole probe and a fast response pressure probe are adopted. The temperature field achieved thanks to thermocouple results useful during the elaboration of data coming from the two other probes. The description of the probes used during experimental campaign is presented in Chapter 4. These probes are mounted on a stepping motor that allows to perform measurements at different radial positions inside the turbine annulus. Their circumferential position is fixed, so during tests, the stator blades and EWG injectors are rotated synchronously in circumferential direction, to simulate the azimuthal displacement of the probe within the blade channel. This is necessary to reconstruct the flow field. The measuring grid covers circumferencially two blade passages, that is about 32.73°, to have the full periodicity, being the combustor simulator pitch twice the stator one (one injector each two stator blades).

Three EWGs injectors (Fig. 1.2) are mounted on the test rig, thus it's necessary to carry out measurements in correspondence of the central one to satisfy the azimuthal periodicity [2].

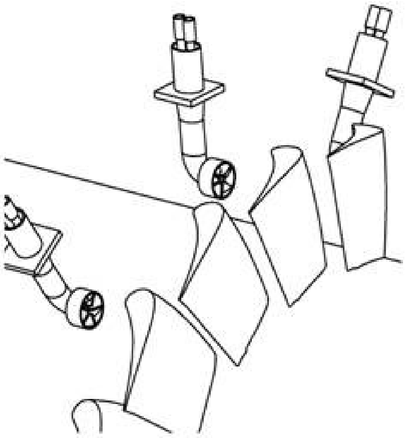

Figure 1.2: EWG injectors and stator blade representation

Measurements are performed at: stator inlet; stator outlet and rotor outlet. All the tests performed along the experimental campaign, together with information about test rig operating conditions, are summed up in Chapter 5. During experiments, the injectors can be aligned with the leading edge of the stator blades or with the vane mid-pitch so two clocking positions are taken into consideration. This allows to investigate the different effects of the injection position with respect to the stator blades. This could be significant during the design phase of the turbine-combustor interfacing. For each test, the operating condition, the clocking position and mounted probes are specified. Moreover the main steps that must be performed before starting the acquisition are shown, such as the setup of the whole EWG system.

The whole remaining part of this work is dedicated to the presentation and discussion of results from experimental campaign. Each measuring section is analyzed one by one in order to achieve detailed comprehension of transport and diffusion process through turbine stage of swirling entropy waves. The results from tests performed in different conditions, such as different plant operating condition or clocking position, are compared to highlight the effects of the non-uniformities introduced upstream of the stator. The main quantities of interest are losses, temperature and velocity fields, flow angles and vorticity. Thanks to these data it's possible to evaluate the effects of injected disturbs on the entire turbine stage.

As demonstrated in [4], the entropy waves can be proficiently simulated by considering a succession of hot streaks of different amplitude and this allows to reduce much computational cost for CFD analysis. This could be a great advantage since to perform a CFD analysis to study EW injected at 10Hz in an axial turbine stage, it would take about 15 days on 120 cores cluster. In particular 20 hours could be necessary to simulate a whole rotor revolution. Moreover the higher is the difference between the entropy wave injection frequency, the blade passing frequency and rotor rotational one, the higher will be the time requested for the analysis. In case of HS (Hot-Streak), it has been demonstrated that the time needed could decrease a lot, thus it is very favorable to consider it instead of EW. Given this premise, it's clear that it's worth to look also at HS condition, even if the best approximation of the phenomena occurring in gas turbines or engines is represented by pulsating thermal perturbations, so by entropy waves.

Throughout the campaign, some improvement and upgrade on the data acquisition and elaboration codes have been made. For example, a new executable file has been designed using Python to create acquisition grids for the fast response pressure probe. This allows to strongly reduce the time for grids construction and it ensures high-quality grids, thus decreasing the probability of discovering acquisition errors during elaboration phase. Regarding codes for data elaboration, that are in Fortran programming language, some modifications have been made to get more precise and reliable results. As an example, the code for elaboration of data coming from five-hole pressure probe has been extended to take temperature field from thermocouple as input. Further details will be given in next sections.

Chapter 2

High Speed Closed Loop Test Rig

In this chapter it is presented an overview of the test facility, i.e. the high-speed closed-loop test rig, in order to get basic knowledge about the plant components and its main technical features. The whole experimental campaign in this work is carried out on it and so it is essential to understand its configuration, working principle and characteristics.
The test rig at "Laboratorio di Fluidodinamica delle turboMacchine" of Politecnico di Milano (Italy), Fig. 2.1, was designed at the beginning of the 1980s with the purpose of research on turbomachines due to their importance in energetic and propulsive field. Over the years the plant has been upgraded to extend its research capabilities, which range from the analysis of operating characteristics of these machines to three-dimensional fluid dynamics measurements, and its versatility. Thanks to this plant, many research projects, some of which of international interest, have been developed in past years.

In order to facilitate the comprehension and explanation of the plant structure, the test rig can be subdivided into different circuits which are analyzed in the following pages one by one even if there are interactions among them.

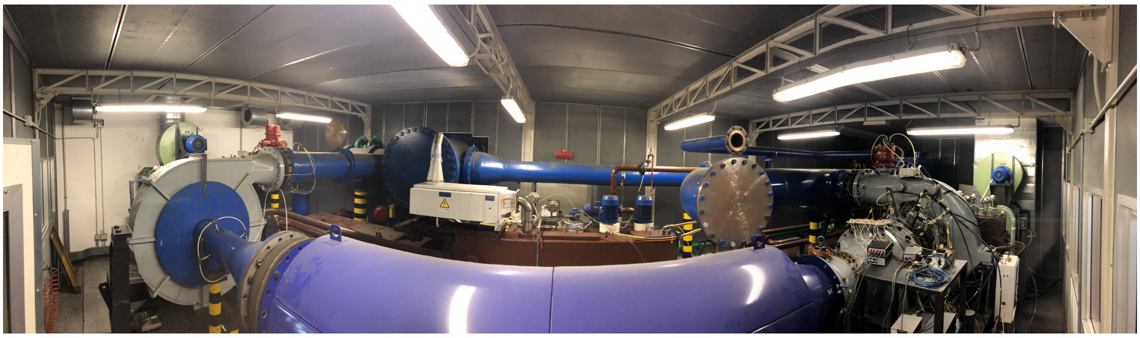

Figure 2.1: Plant

2.1 Air Circuit

The test rig is subdivided in two different air circuits: The main air circuit and the auxiliary air circuit.

2.1.1 Main air circuit

The main air circuit is the one responsible for the management of the working fluid through the machinery and through the main Loop Components, and it is composed by:

- Centrifugal Compressor
- Heat exchangers
- Venturi tube
- Valves for mass flow regulation
- Air filter
- Axial Turbine
- Silencer
- Piping system

From Fig. 2.1 it is possible to observe that the components responsible for air carriage are painted blue while the turbomachineries are painted grey. The main air circuit components and their arrangement can be observed instead from the scheme in Fig. 2.2.

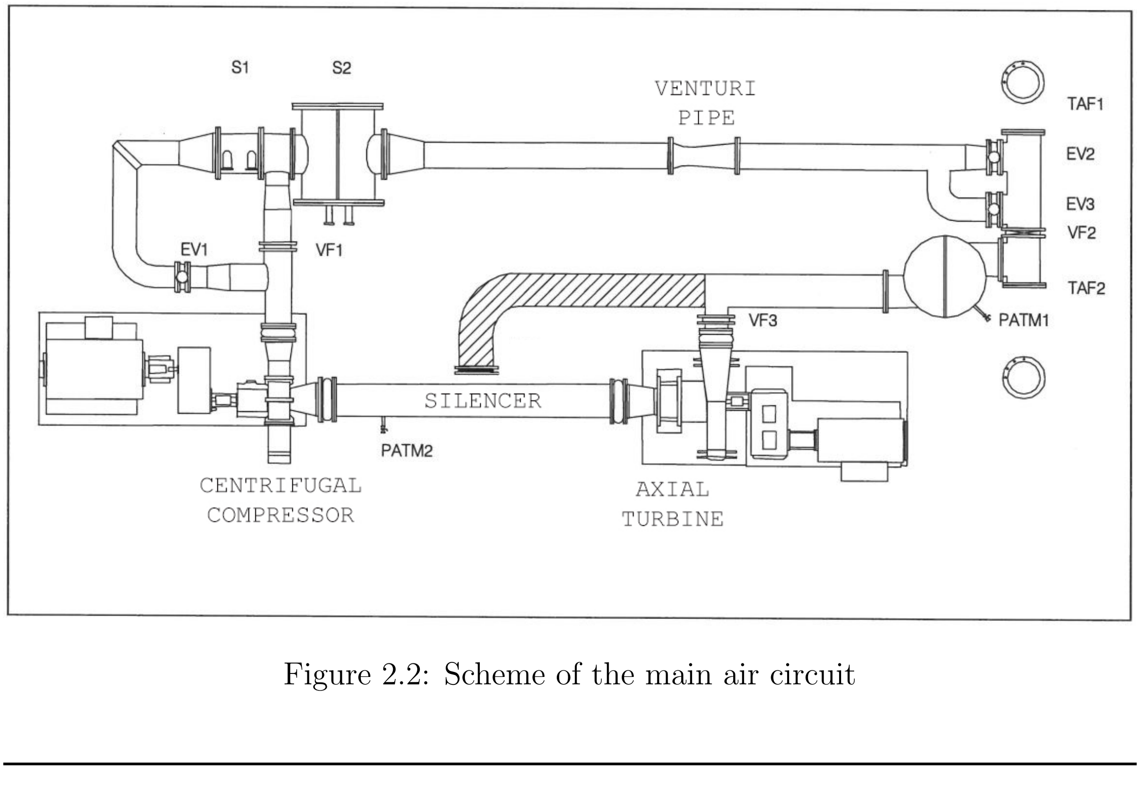

Figure 2.2: Scheme of the main air circuit

As a consequence of the plant complexity its working conditions are various. Those conditions are strictly dependent on the way the operator decides to arrange the different components of the system. Actually the different configurations relies on the possible combination of some crucial components:

- Flanged valves VF1,VF2,VF3
- Flanged caps TAF1,TAF2
- Valves for connection to atmospheric pressure PATM1,PATM2
- Electrically controlled throttle valves EV1,EV2,EV3
- Heat exchangers S1,S2

The configuration used during this study presents:

- Opened VF1,VF2,VF3
- Flanged caps TAF1,TAF2 are closed
- PATM1 closed and PATM2 opened
- Fully opened EV1, EV2,EV3
- S1 and S2 both active

As a result in this configuration the air flow rate processed by the centrifugal compressor gets divided onto the two branches, one of VF1 and one of EV1, Figs. 2.3a and 2.3b. However in this situation due to the huge pressure drop across the S1 heat exchanger almost all of the air flow rate is constrained to pass through the valve VF1. Anyway for the sake of the researches of interest at the moment, the fact that the heat exchanger S1 gets practically bypassed is not really a problem, since the heat exchanger S2 alone has enough capability to cool down the flow.

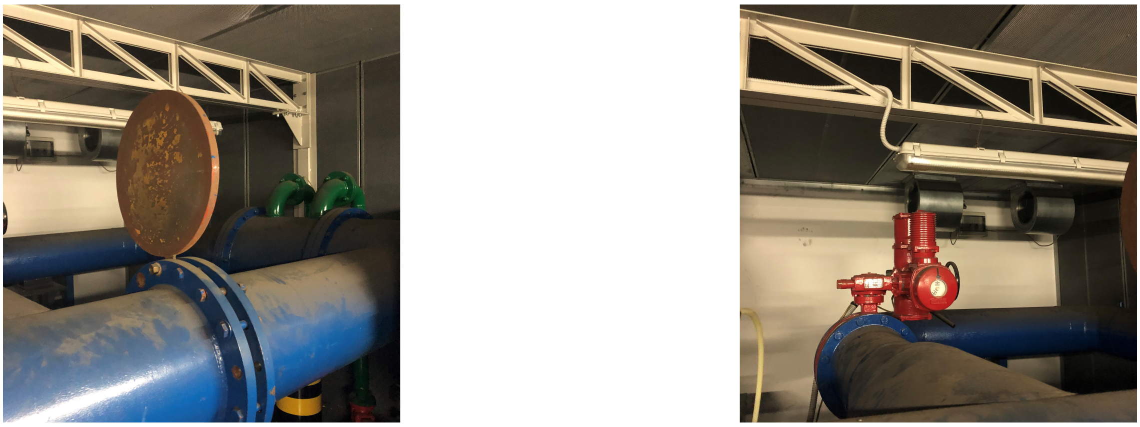

(a) VF1.

(b) EV1.

Figure 2.3: Valves on the plant

Another consequence of this configuration is that, being PATM1 closed and PATM2 opened the turbine works at a pressure higher than the environmental one; this is beneficial because in the opposite case, PATM1 opened and PATM2 closed, the turbine would work entirely at pressure below the ambient one and, being the oil for lubrication, across bearing outlet at ambient pressure it would naturally tends to flow towards the air system, affecting the measurement instrumentation.

2.1.2 Thermodynamic cycle

It can be interesting to understand the thermodynamic cycle that the air undergoes inside the closed loop. Since the test rig is equipped with many sensors, there is not the need of determining thermodynamic points analytically thus the cycle is analyzed in a qualitative way. The test bench cycle is a closed cycle working with air, which can be considered to be a perfect gas with constant specific heat. Even if there is a point in contact with atmosphere (PATM2), this is a closed cycle because the mass flow rate is constrained by the compressor operating condition which is fixed during each single test. Fig. 2.4 shows a simplified scheme of the plant.

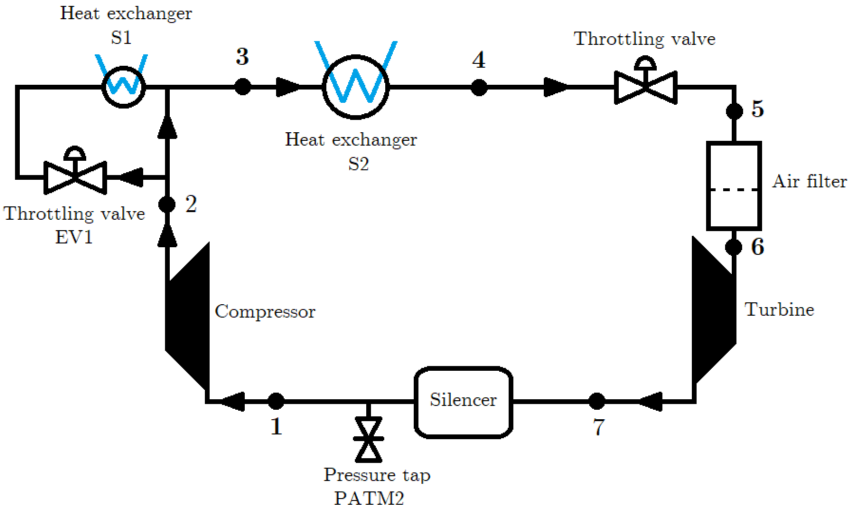

Figure 2.4: Plant simplified scheme

In Fig. 2.5 the thermodynamic cycle followed by air in the plant is reported on h-s (enthalpy - entropy) plane.

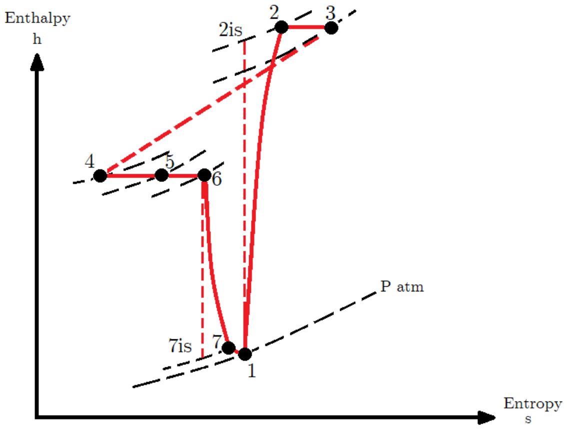

Figure 2.5: Thermodynamic cycle

The air enters the compressor at point 1 at atmospheric pressure due to PATM2, then it reaches point 2 at the exit. During compression the entropy increases since the machine is not ideal. Then air reaches the heat-exchanger S2 inlet at point 3 and, due to pressure losses across ducts, its pressure at point 3 is lower than the one at 2 while its enthalpy remains constant. As the air passes through the heat exchanger S2 further pressure drop occurs and enthalpy and entropy decrease due to heat transfer. Then air flows through EV2 and EV3 leading to an increase of entropy at constant enthalpy, thus to a pressure decrease. The same happens when it passes across filter directed towards turbine inlet at point 6. Since expansion process is not ideal, enthalpy at turbine outlet is higher with respect to one in isentropic case. Pressure at turbine outlet is slightly lower than the atmospheric one and then increases up to atmospheric value at silencer outlet due to its divergent shape.

2.1.3 Centrifugal compressor

The centrifugal compressor, like other fluid-dynamic machines, achieves the pressure raise by a transfer of energy to the flowing fluid stream. The working fluid, air in this case, enters axially into the rotating impeller with backward blades, that form the flow passages together with the hub and the casing. The increase in static pressure that occurs inside the impeller is due to the work done on fluid by centrifugal force and due to the diverging passages along the flow path which cause relative velocity to decrease. As the fluid flows through the blade passages towards the impeller outlet, it gains momentum thus absolute velocity increases. The kinetic energy of the flow leaving the impeller is then converted into static pressure inside the diffuser. In this case a vaned diffuser is adopted. Finally, a volute is used to smoothly collect the pressurized flow from the diffuser exit into a discharge duct. The compressor in the test rig is a single-stage compressor with a 16 backward blades impeller made of aluminum alloy coupled with a bladed diffuser with 19 vanes (Figs. 2.6a and 2.6b).

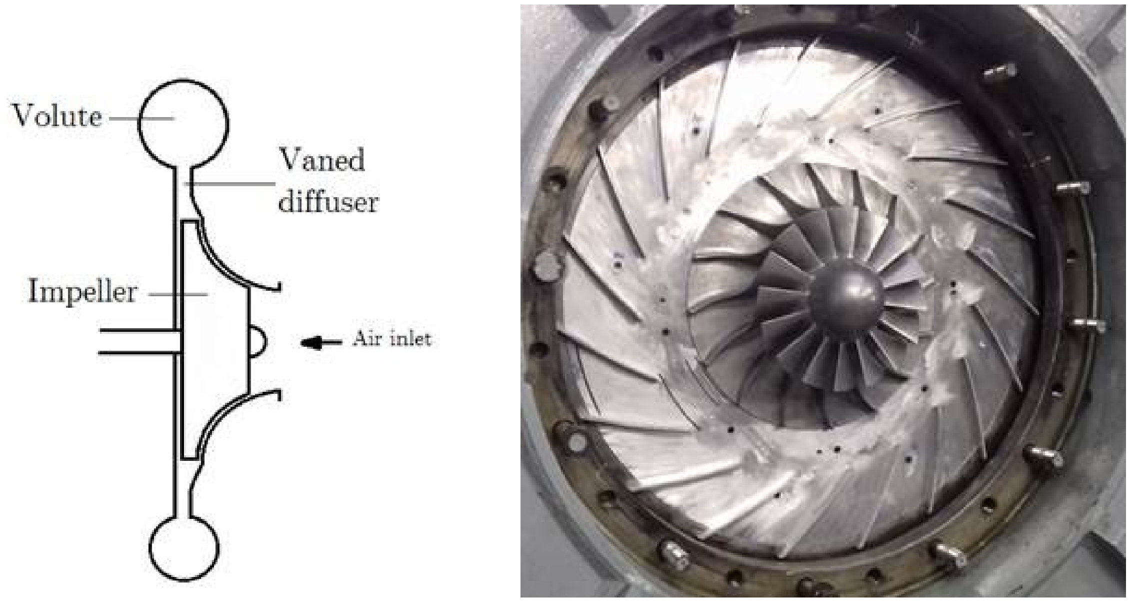

(a) (b)

Figure 2.6: Centrifugal compressor

The impeller, that has been manufactured by milling process, is characterized by an external diameter equal to 400mm and it is mounted in cantilever configuration on a forged steel shaft. From Figs. 2.6a and 2.6b it's clear that it rotates in clockwise direction. The impeller trailing edge and vaned diffuser inlet are 50mm apart, thus this vaneless region also contribute to recover energy from fluid. Both the diffuser and the impeller are enclosed in a carbon steel case, Fig. 2.7.

Figure 2.7: Case of centrifugal compressor

The shaft that drives the impeller is connected to an electric motor through a gear box (see Fig. 2.8) with two multiplication ratios and four parallel axes. Thermocouples are mounted at the bearings of the shafts to monitor temperature values.

Table 2.1: Centrifugal compressor data

	$Impeller$	$Vaned\,diffuser$
Diameter [mm]	400 (external)	440 (inlet)
Blade height [mm]	17.4	17
Geometric angle at output [°]	-24	-
Max. rotational speed [rpm]	20000	-
Number of blades	16	19

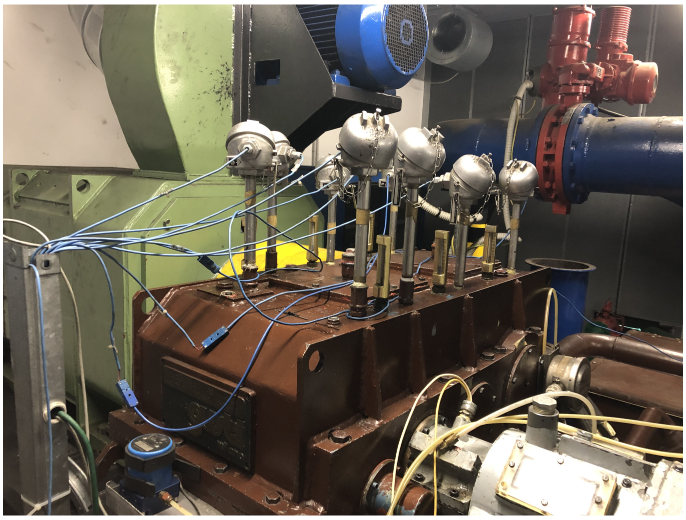

Figure 2.8: Compressor side multiplier

The DC motor, an AEG GC 45 SK, is characterized by a rated power of $800kW$ and nominal voltage of $600V$. The motor rotational speed is manually regulated by a potentiometer from control pulpit. The whole system can be observed in Fig. 2.9.

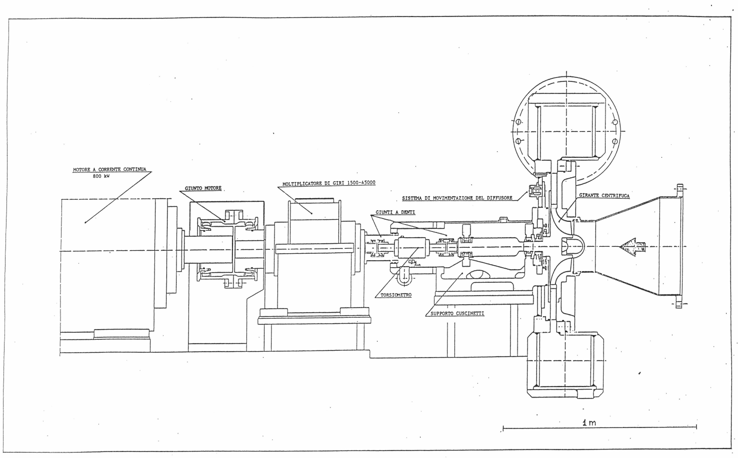

Figure 2.9: Centrifugal compressor side actuation system

In Fig. 2.10 are reported the compressor characteristics curved for three different rotational speeds.

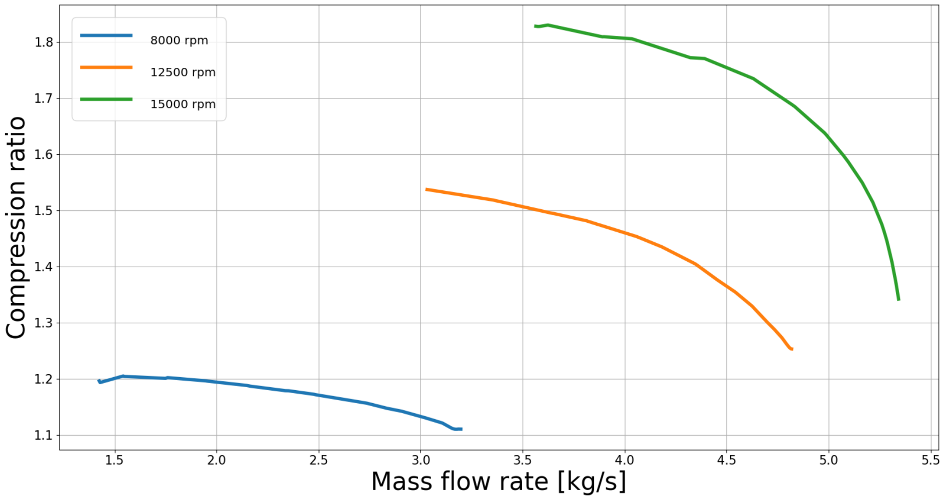

Figure 2.10: Centrifugal compressor characteristic curves

2.1.4 Axial turbine

The axial turbine is the component which flow has to be investigated during this study. In fact its characteristics have a key role in affecting the flow that have to be measured. Measurements are carried out downstream of the nozzle and downstream of the rotor.

Table 2.2: Blades geometric characteristics

Blades	**Number**	σ	**Aspect Ratio**	ϵ_{hub}	ϵ_{mid}	ϵ_{tip}
Stator	22	1.20	0.83	72.5 °	75.2 °	77.5 °
Rotor	25	1.25	0.91	124.6 °	115.3 °	93.2 °

$\sigma = \frac{blade\,cord}{blade\,spacing}$ = solidity (in tab calculated at mid-span), ϵ = geometrical blade deflection

The geometry of the blade is peculiar, Fig. 2.11: stator blades are leaned of 12° towards the pressure side; rotor blades are twisted and bowed towards the suction side. In order to get a wider comprehension about leaned geometry refer to Appendix B.

The average diameter of the machine is $D_m = 350\,mm$ and the blade height is $h = 50\,mm$, the rotor tip clearance is about $0.6mm$ of the blade height and the axial gap between stator trailing edge and rotor leading edge is equal to the vane axial cord $\frac{gap}{c_x,v} = 1$.

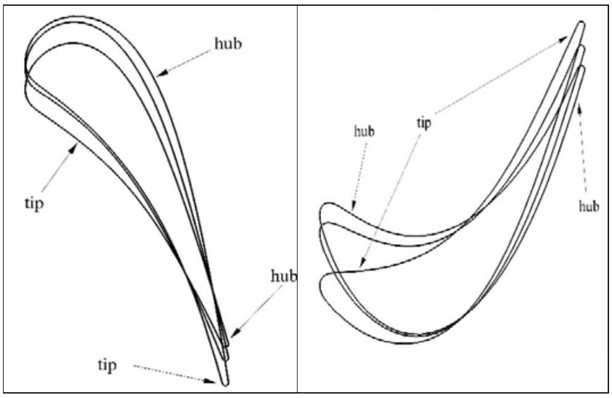

Figure 2.11: Turbine blade to blade view

Anyway the flow before entering in the statoric blade row passes through a centripetal inlet guide vane (IGV) and through a 400 mm long duct. Between the two aforementioned components there's a flow straightener with honeycomb shape. The meridional view of the whole equipment can be observed in Fig. 2.12.

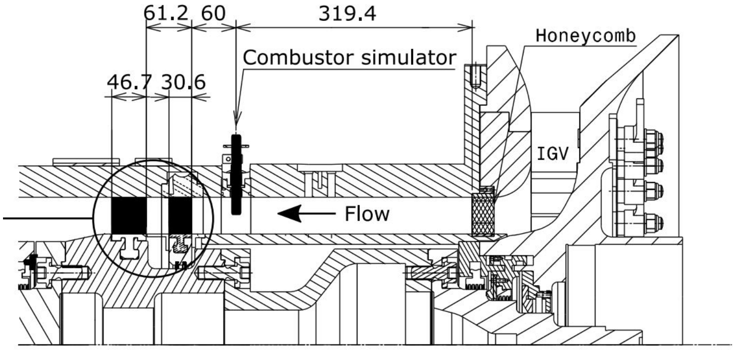

Figure 2.12: Meridional view

The turbine considered is representative of a high pressure gas turbine designed for transonic conditions [4]. The design conditions are:

- $\beta = 1.4$ (expansion ratio)
- $n = 7000\,rpm$ (angular velocity)
- $\dot{m} = 3.78\,kg/s$ (mass flow rate)
- $T_{int_0} = 323\,K$ (turbine inlet total temperature)

2.1.4.1 How is the turbine controlled?

The axial turbine is actuated thanks to a system composed by an electric actuator and a gearbox; its variable subjected to control is the angular velocity. In such a way, in most of the operative conditions, when the turbine is producing useful energy, the electric actuator works as a generator, while whenever the flow alone is not able to provide the required angular velocity through the interaction with blades, the electric actuator no longer works as a generator and instead works as a motor. In Fig. 2.13 it can be observed a scheme of the turbine system.

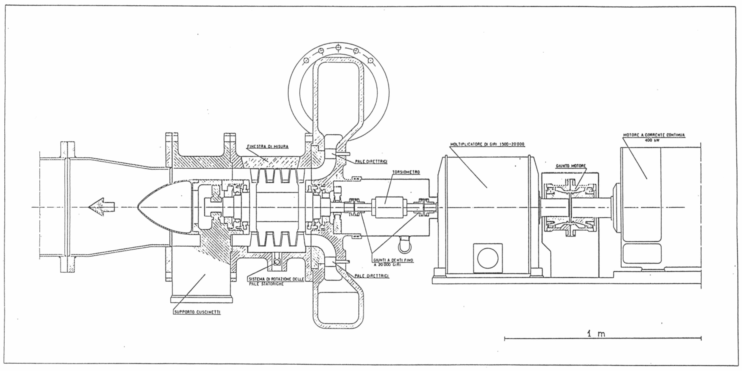

Figure 2.13: Axial turbine side actuation system

The gearbox mounted on the turbine side is similar and similarly monitored as the one mounted on the compressor side. The only differences among the two regard the gear ratios. The electric actuator, an AEG GC 45 SK, is characterized by a rated power of 400 kW and its rotational speed is manually regulated by a potentiometer from control pulpit.

2.1.5 Silencer

The silencer, Fig. 2.14, connects the two turbomachines and it has been specifically designed to damp the noise produced by the compressor that propagates upstream toward the turbine. This component, that has been placed to substitute a previously present duct, avoids noise propagation towards the turbine section thus allowing to get there correct acoustic measurements. This was the aim of the RECORD project, which focused on core noise reduction in propulsion systems for air transport.

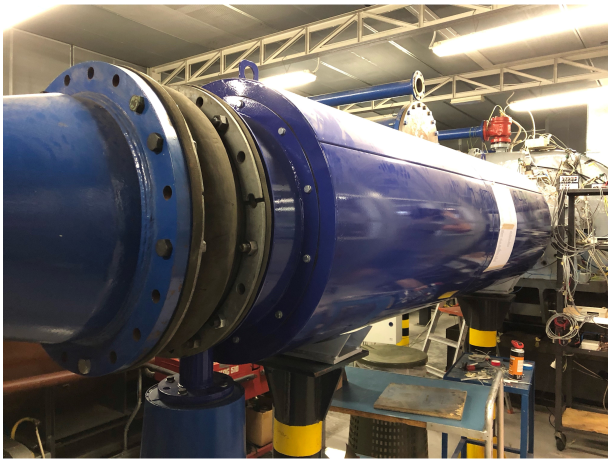

Figure 2.14: Silencer

2.1.6 Auxiliary air circuit

The plant is even equipped with an air system necessary to supply auxiliary components. The involved system is composed by: the auxiliary turbine that powers an Emergency Oil Pump (EOP); the oil sealing and the oil nebulizers for torque meters. The most critical part of this system is the one dedicated to the air supply for the EOP.
In fact the EOP,Fig. 2.15 , is responsible of pressurizing the oil whenever its measured pressure is lower than a certain value. Once the emergency pump is activated, the whole plant gets shot down, hence the EOP is responsible of keeping the oil pressure to an acceptable value during the time required for the machines to stop.
The air dedicated to this circuit is drawn from a network of vessels of the laboratory and distributed at about $7\,bar$ to the involved organs. Thanks to filters, capable of cleaning the air from impurities and thanks to pressure regulators, the air comes to the auxiliaries at the required conditions. The air for the EOP nominal working pressure is $5\,bar$ and, whenever the distributed pressure is detected to be at a value lower than this the plant go towards stop.

Figure 2.15: EOP

2.2 Oil circuit

Even the oil managing system is subdivided in a main oil circuit and two identical secondary circuits.

2.2.1 Main oil circuit

The oil system is fundamental for the plant operation and constantly guarantees that the whole system of machinery works under mechanically safe conditions. In fact this system covers two very important tasks: The lubrication of machines bearings, of the bearings of their multipliers and of the joint among torque meters and machines; the cooling action on the same lubricated components.

2.2.1.1 Critical aspects

This system is without any doubt the most critical for what concerns the safety of the plant. In fact if , for any reason, there would be a lack of oil supply to the interested parts of the plant the temperature of those would rise quickly exposing the components to conditions that promotes mechanical failure.
The rise in temperature would be caused both by the absence of a coolant effect and by the absence of lubrication effect which would induce friction between two different metallic parts and the consequent energy dissipation due to joule effect.

2.2.1.2 Description of the circuit

The oil is stored in a tank, Fig. 2.16, which is equipped with 4 different pumps.
In particular $4000\,l$ of oil are stored in a vessel which contain some heat resistance necessary to heat up the oil at plant start. The pumps that draw the oil for the tank have each a well defined role. A primary pump (POP) is the one used during ordinary operations, the auxiliary pump (AOP) is a pump similar to the primary one which is placed there in case of primary pump failure, the EOP which is described in the auxiliary air circuit part and an additional pump placed downstream of the other three (POS) which is necessary to reach an oil pressure high enough for ideal working conditions.

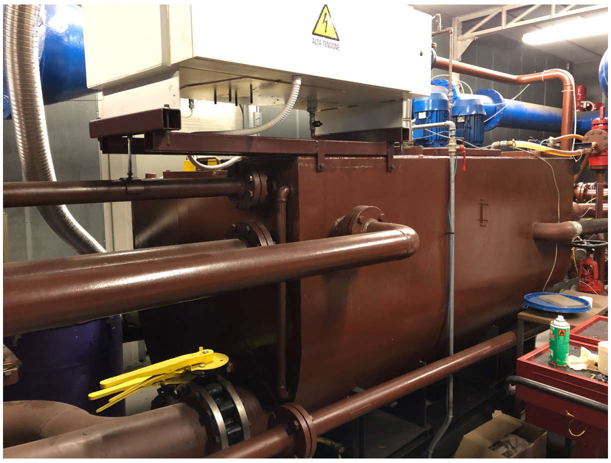

Figure 2.16: Oil tank

The oil drawn from the tank is then delivered to two heat exchangers (SOH1,SOH2) with nominal power of $78kW$, which are necessary to cool down the oil and keep it in a temperature range needed for operation. In order to keep the viscous characteristics optimal the oil must work in a temperature range from $40°C$ to $55°C$. The oil as stated before have to be warmed up at startup or in cold conditions and it also need to be cooled down at regime since it would come back from the machinery with a high temperature. In addition the oil tank is equipped with two aspirators, the aim of those aspirators is:

- Remove the oil vapor produced during working conditions

- Help de-emulsification of air dissolved in the oil
- Depressurize the tank and hence the return lines so that even the pressure at bearing would be lower and in this way the system experience less oil leakages across the sealings.

After passing through the heat exchangers the oil is delivered to the machines thanks to two separate branches both equipped with filters to avoid impurities in the downstream part of the circuit. In a second moment the oil that has passed from the machines and from the respective gearboxes is gathered thanks to gravity in an oil collection tank. From the collection tank the oil is then returned to the initial tank. Pressure and temperature of oil are measured at different location across the circuit to guarantee safety conditions.

2.2.2 Secondary oil circuits

The two secondary systems are the one responsible for lubrication at torque meters. Each system is composed by a tank and a pumping and mixing system. Those secondary oil circuits are powered by the auxiliary air. Therefore oil is emulsified with air before being atomized onto the torque meters bearings.

2.3 Water circuit

The water circuit supplies water to the heat exchangers that have two main functions: lower the temperature of the air at compressor outlet and lower the temperature of the oil before it reaches the components that need lubrication, such as the bearings. After performing its cooling effect water is returned to a cooling tower and there it releases the absorbed thermal power. This circuit is not as critical as the oil one because a lack of cooling water allows to switch off the plant without having serious damages to components. However it's important to maintain the oil temperature in its correct range in order to not alter lubrication capability and cause hazardous situations. In the air-water heat exchanger S1 air flows through a series of tubes, while water is in contact with external surfaces of the tubes. However high pressure loss occurs as air passes through it, even if it is characterized by higher heat transfer efficiency. The air-water heat exchanger S2 is cross-flow type with aluminum fins and brass tubes within which the water flows. It has lower efficiency but ensures a lower pressure drop because it is designed to work with higher mass flow rate values. The two oil-water heat exchangers, Figs. 2.17a and 2.17b, are counter-current type with a nominal power of about $78kW$. In order to control the thermal power exchanged is possible to vary the input water flow into the heat exchangers.

Heated water reaches a forced draught cooling tower,Fig. 2.18, within which water temperature is reduced.

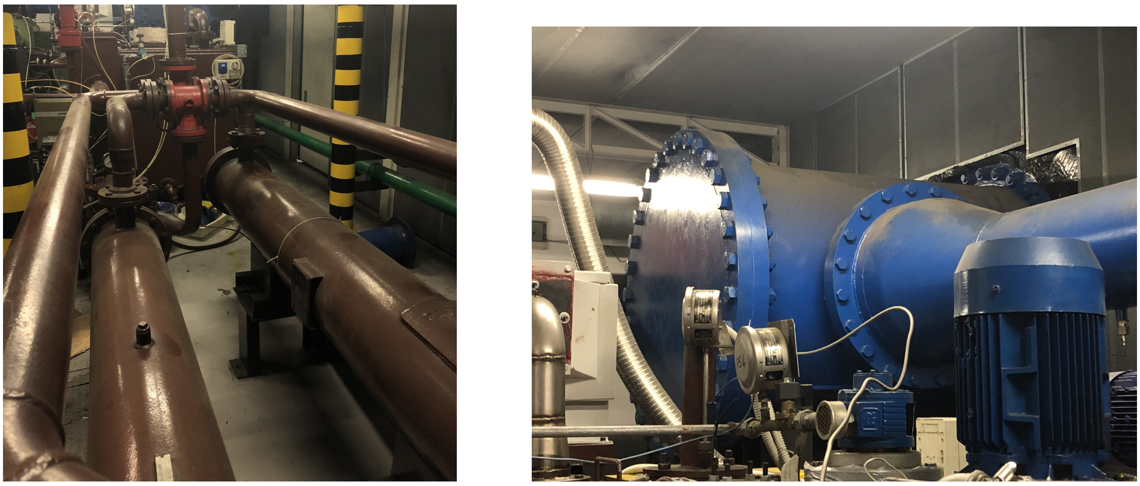

(a) (b)

Figure 2.17: a. Oil heat exchanger, b. air-water heat exchanger S2

Figure 2.18: Wet cooling tower

2.4 Electromechanical panel and Pulpit

Being the plant very complex and being the time available for preventing damages such tight if something is not working properly, it is necessary to continuously watch over it and to be always able to quickly act onto it in such a way to be capable to return in any case to safe conditions. In order to ensure a quick response, sensors along the plant allow to monitor operation and critical parameters, such as temperature, pressure, vibrations, speed and torque. The test rig is controlled at three different levels, by the electromechanical panel, by the software that accounts for the running of the test bench and by the operator. In particular the electromechanical panel is responsible for powering all the electromechanical devices which contribute to the working of the plant. This panel is placed in a closet having a series of light bulbs and push-button switches that operate on some relays. Moreover it receives signals from manostats and thermostats around the plant thus acting on some relays depending on the implemented logic. In Fig. 2.19 electromechanical panel is shown:

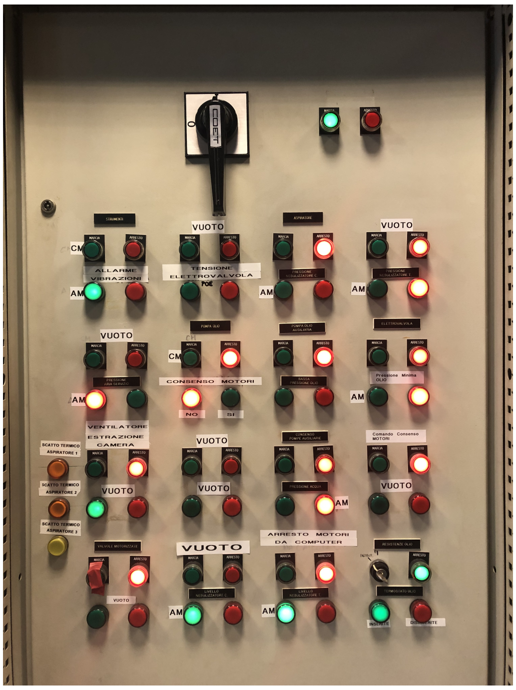

Figure 2.19: Electromechanical panel

Connected to this panel there is also the control pulpit that allows operator to set compressor and turbine rotational speed by acting on two potentiometers. Moreover from the pulpit it is possible to monitor current and voltage supplied to electric motor both for compressor and turbine. Fig. 2.20 shows the control pulpit.

Figure 2.20: Control pulpit

As can be seen in the figure above, each analog indicator related to turbine shows the same range of values both in left part of the quadrant and in the right one: the pointer is rotated in the left quadrant if electric motor of turbine is working as a brake, thus as a generator, while it is rotated in the right one if electric motor absorbs current to make the turbine to rotate at the desired speed.

Chapter 3

Swirl and entropy wave generator

In this chapter it is reported a description of the system used for generation of entropy waves and swirling flow. This system is responsible of generating flow features at the inlet of the turbine stage similar to the one found in premixed-mixture lean burn gas-turbines [3].
This system represents the core of this study since it allows to show a possible interaction among combustion chamber and turbine. In fact, usually turbine flows and performances get studied in isolated manner, which means that the inlet flow does not face any disturbance neither in terms of temperature nor in terms of velocity. Uniform inlet flows are in fact useful to study the turbine behavior as a stand alone component and without any interaction.
However in real gas-turbines applications, for the sake of compactness, low pollutant emissions and low fuel consumption, this kind of interactions are getting less and less negligible.
In light of this the ”Entropy wave generator” system has been developed and employed at Politecnico di Milano, in particular at ”Laboratorio di Fluidodinamica delle turboMacchine”. Even if a single system is responsible of both the generation of the thermal disturb and of the aerodynamic disturb, in this chapter the authors have decided to analyze their generation in two different sections.

3.1 Entropy waves

Entropy waves are fluctuations in entropy content of the flow in time, generated at a given location in combustion chamber. These are caused by the large heat release rate (HRR) fluctuations. This behavior, for long observed in gas-turbines, is strictly related to the combustion characteristics at burner, see Appendix A. Those fluctuations in combustion chamber are advected by the flow, diffused and so they act on the turbine stage as a thermal disturb non uniform in space and unsteady in time.
In conclusion, one of the main entropy waves properties is indeed their frequency. The here described system features components responsible for thermal disturb frequency control.

3.1.1 Simulation of thermal disturb

Entropy waves are simulated thanks to a system able to deliver hot pressurized gases at the inlet of the stator blades. This system is here described and represented in Fig. 3.1.

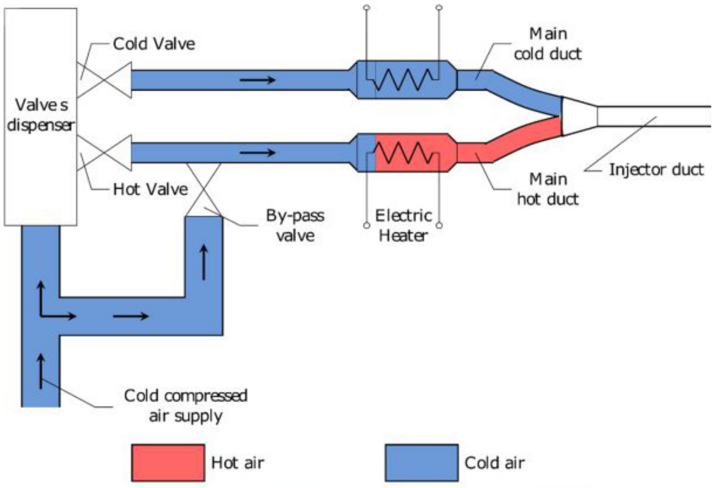

Figure 3.1: Entropy wave generator (EWG) schematic

- A flow of compressed air is delivered to the system coming from an external pressurized net.
- The pressurized flow has available two different paths: a path controlled by two automotive methane injectors; a bypass path controlled by a manually actuated valve.
- If the manually actuated valve is closed the air path would pass from the two methane injectors path and it would be alternatively delivered, depending on how the injectors get actuated, to two different ducts, one for each valve.
- The two ducts, or branches, downstream of the injectors features an electric heater each. One branch, the cold one, has the heater switched off while the other, the hot one, has the heater switched on.
- The presence of the heater in the cold branch is justified by the necessity to have similar pressure losses in both branches.
- Once the air passes through the two branches it gets delivered to the turbine stage inlet thanks to a specially designed injector that conveys both ducts.
- If the manually actuated valve, labeled as bypass valve, gets opened, the whole air flow would pass through the hot branch changing the nature off the thermal disturb. In this case the thermal disturb faced by the turbine would be constant in time and labeled as ”Hot Streak” (HS).

- More than one system for entropy wave generation is employed at the same time on the test bench. In fact one single injection throughout the whole turbine inlet annulus would not be representative of the conditions at the outlet of an aero-engine combustion chamber and in addition it would for sure not simulate a periodic flow at the blade vanes of interest for this study.
  In order to simulate a periodic flow at the turbine vanes investigated by this study, it is necessary at least to inject the thermal disturb at three different azimuthal adjacent positions, Fig. 3.2. The test bench provides actually 11 housings for injectors, hence one injector every two stator blades but for the present study only the sufficient three EWGs injectors(Fig. 3.2) are mounted on the test rig, thus it's necessary to carry out measurements in correspondence of the central one to satisfy the azimuthal periodicity [2].
- The outlet of the injectors are placed 50mm upstream the stator leading edge[2].
- Mass flow rate managed by this system is measured thanks to a calibrated nozzle

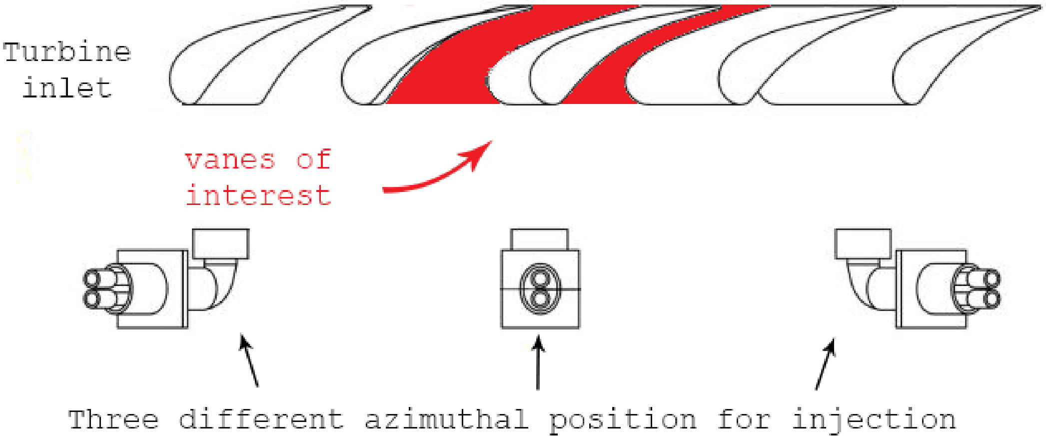

Figure 3.2: Entropy wave generator (EWG) schematic

3.1.1.1 Control of EW system

Thermal disturbances generated by this system depends on how the generation of the disturb is controlled. Actually the parameters on which it is possible to act are: The pressure of air delivery; the target temperature downstream of the electric heater, hence the power supplied to the electric resistance and the frequency of the injectors. De facto even the manually actuated valve should be gathered in this set.
The pressure at which the air is delivered is regulated manually and checked thanks to a labview software Section 5.3.5.
The temperature target is regulated thanks to an electro-mechanical control panel, Section 5.3.5.1.

The frequency of the injectors and their duty cycle is controlled thanks to a labview software too. The influence of those parameters on the working conditions of the whole system have been studied by Notaristefano A. and Gaetani P. in [3].

3.1.1.2 Methane injectors working principle

It remains still necessary to clarify the physical principle behind the methane injectors actuation.
The injectors openings are controlled by mean of a solenoid valve which, like in automotive applications would need two kind of current based signals to work properly. In fact at opening, to move the valve from rest position to operative position, a high current short duration signal through the solenoid valve is necessary. Then for the holding time, during which the valve has to stay opened a lower current level is required.
The two current conditions are obtained by means of a single DC circuit, Fig. 3.3, that features two different electro-mechanical relays.

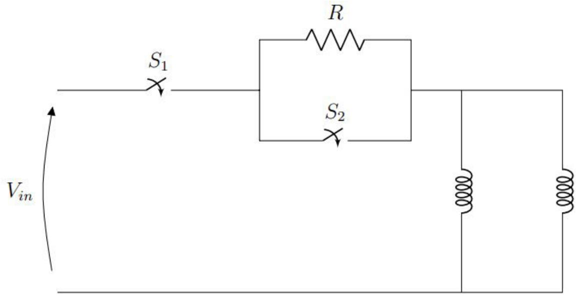

Figure 3.3: Methane injector valves actuating circuit

- The relay labeled as S_1 is the one responsible for the activation of the circuit, as long as it stays opened neither of the two opening injector condition can be achieved.
- When only S_1 relay is closed, current is able to flow through the circuit but with the only possibility of passing through the resistance R.
- When both the relays, S_1 and S_2, are closed the current is no longer forced to pass through the resistance R, instead it passes through the closed circuit created by S_2
- Comparing the two conditions with S_2 opened or closed, it is clear that given a constant voltage supply V_{in} the two inductances faces higher current with S_2 closed and lower current with S_2 opened.
- The control of the two relays is obtained by an "arduino board" that receives input frequency from a labview software and actuates the relays as output. This solution has been arranged because of the greater precision in controlling injectors frequency compared to the one obtained with a direct control from labview.

3.2 Swirling flow

Vortical structures such as swirl are necessary in low temperature lean-burn combustors. Since, in order to avoid incomplete oxidation and hence un-burned hydrocarbons emission, which results in dangerous emissions and lower extracted heating value, the fuel and air content need to be well mixed.
In order to simulate the swirling structure found at the inlet of novel gas turbines a study concerning the geometry of the aforementioned injector has been carried out by Notaristefano A. and Gaetani P. [3].
The parameters taken into consideration were the magnitude of swirl imposed to the free stream as well as to the entropic stream, the distortion in total pressure field and the symmetry of the flow.

3.2.1 Swirling injector

From the study aforementioned a particular injector geometry has been chosen as the most suitable among different kinds. The same geometry has been used during this thesis work, Fig. 3.4.

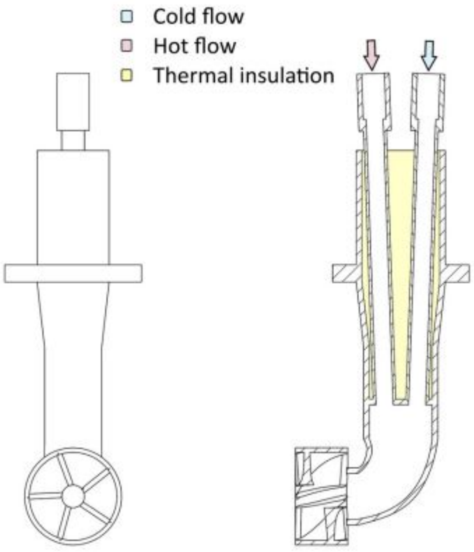

Figure 3.4: EWG injector scheme geometry

This injector head has simply the role of imposing a given angle to the flow of ejected gases and to the free stream flow passing in its neighboring zones. As a result the flow is deflected in a rotating manner around the injector outlet axis thanks to a set of 5 static blades housed in the injector head.
The vortical structure obtained is then advected, and modified by the flow, together with the entropy wave throughout the turbine stage.

Chapter 4

Instrumentation for flow characterization

In this chapter the measurement systems are analyzed with a brief deepening about their working principles and their calibration.
In particular for aerodynamic measurements the used probes are: a 5-hole probe and a Fast Response Pressure Probe (FRAPP). Instead for thermodynamic measurements the test campaign has relied on a fast response thermocouple.

4.1 FRAPP

The FRAPP probe, which has been object of research and development at "Politecnico di Milano" since 1998, contributed undoubtedly to the improvement in measurements of flow downstream of turbomachinery rotors thanks to its rigidity, reliability and promptness. Th FRAPP concept comes from the coupling of fast-response piezoelectric pressure transducers and aerodynamic directional pressure probes [5]. As a result of several studies a final development of a probe with dynamic response up to $100\,kHz$ have been reached.

4.1.1 FRAPP description

The current probe designs imposes a cylindrical shape, Fig. 4.1, for the 2D reconstruction of flow and a spherical shaped probe for 3D flow reconstruction. The first one have been used during this test campaign while the second one is not of interest for the study here reported. The cylindrical probe features only one pressure sensor in order to enhance its miniaturization and hence reduce its intrusiveness.
However three different pressure readings are necessary to reconstruct a two dimensional flow in terms of direction, and in terms of total and static pressure. As a result, the probe has to be rotated about the cylinder axis at three different angular positions, in such a way that the pressure tap can simulate a 3-holes probe. The probe results insensitive to pitch angle variation in the range of ±10° . Anyway this procedure prevents real-time unsteady measurements to be performed, since the

different pressure readings are acquired at different times. This prevents real-time unsteady measurements to be performed (phase-resolved flow) and excludes, in a first time, all the possibilities to detect non deterministic (turbulent) fluctuations. However in case of unsteady turbomachinery flows, this is not a severe limitation as one is typically interested in the periodic component of the flow unsteadiness [5].

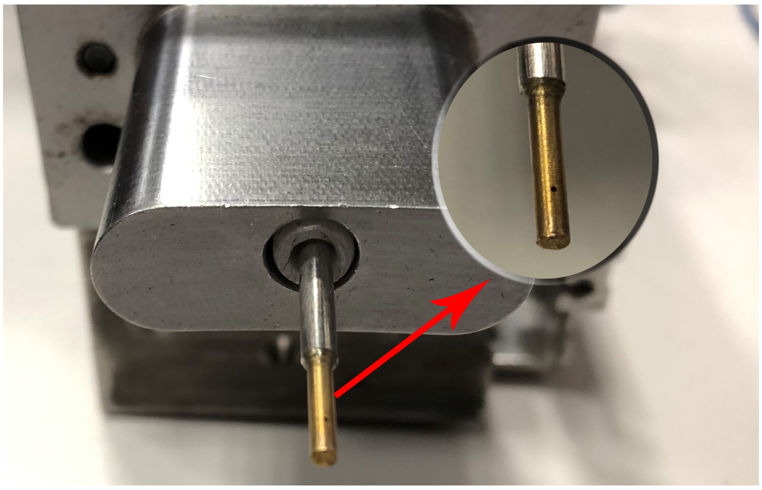

Figure 4.1: FRAPP picture with magnification on the hole region

At the same time a probe with three or more sensors would be able to accomplish this but, it has been observed that, due to the relatively large probe head of a 3 hole probe, a larger error would be introduced compared to hot wire and laser-doppler measurements [6].
The pressure tap connects the cylinder lateral surface to the transducer, located at the cylinder axis as it can be observed in Fig. 4.2.

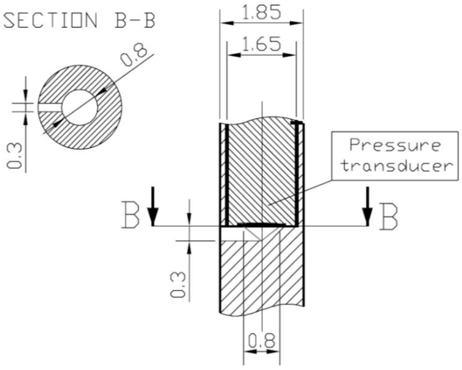

Figure 4.2: FRAPP scheme [5]

However an interesting application of the single-hole FRAPP is the acquisition of pressure fluctuations by aligning the pressure tap axis with the phase-averaged flow direction.
Actually thanks to this kind of acquisitions it can be estimated the turbulence intensity when the unresolved flow angle fluctuations stay within a ±9° range. This

range fall in the so called insensibility region. In this region, which cover a range of angles of about ±10° Yaw around the probe tap, the transducer outputs result not sensible to a variation in angles, Fig. 4.3. It is assumed that the instantaneous component of the pressure signal acquired at that angular position represents the effective unresolved fluctuation of the total pressure [6]. This effect can be considered as a consequence of the smooth cylindrical probe surface.

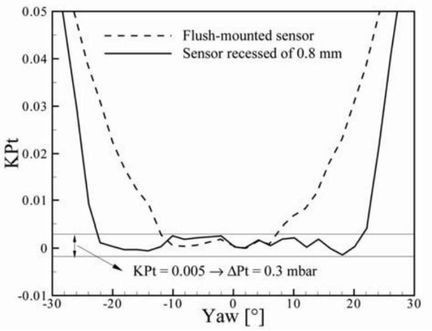

Figure 4.3: FRAPP angle sensibility for two different probe cavity design [6], the dashed line refers to the FRAPP used during this study

4.1.1.1 What is the dynamic behavior of the FRAPP?

The here considered device can be approximated to a line-cavity system, that connects the probe tap to a pressure sensor and its transfer function, obtained by means of a low pressure shock tube, has a bandwidth of 80 kHz, which satisfies the requirements to analyze both the phase-resolved and the turbulent flows downstream of a turbine rotor. The experimental transfer function is obtained thanks to a step input in pressure with an amplitude similar in magnitude to the fluctuations present in turbomachineries. Those perturbations are typically small enough to not activate relevant non linear effects in the dynamics of the line-cavity system. Plus the system seems to very well follow the response of an ideal second order system with a natural frequency at about 35 kHz as it can be observed in Fig. 4.4.

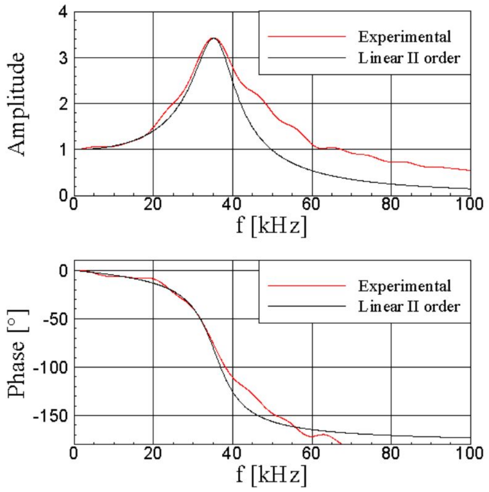

Figure 4.4: Experimental FRAPP transfer function compared to a second order ideal transfer function [5]

As a result of the very similar behavior an analytic model can be applied to derive meaningful pieces of information starting from the signals produced by the probe. A model for a second order system of a line-cavity arrangement has been considered as in [7].

$$\zeta = \frac{16\mu L}{d_t^2 \rho c}\sqrt{\frac{V}{V_t} + \frac{1}{2}} \tag{4.1}$$

$$\omega_n = \frac{c}{L\sqrt{\frac{V}{V_t} + \frac{1}{2}}} \tag{4.2}$$

- $\zeta = damping\, ratio$
- $\omega_n = natural\, frequency$
- $c = speed\, of\, sound$
- $V = cavity\, volume$
- $V_t = line\, volume$
- $L = line\, length$
- $\mu = dynamic\, viscosity$
- $\rho = density$
- $d_t = line\, diameter$

4.1.1.2 How is the FRAPP used?

Once the dynamic behavior of the probe is defined it is possible to understand how the deterministic component of the flow are calculated, in terms of Yaw angle, static pressure and total pressure.
A set of three coefficients, which are functions of static pressure, total pressure, YAW angle and are parametric with respect to the Mach number, have been derived during calibration of the probe in a dedicated wind tunnel. Those coefficients, reported below, are necessary then, during measurements, to reconstruct from an unknown flow both the pressures and the Yaw angle.

$$KYaw = \frac{P_L - P_R}{P_T - P_S} \quad KP_T = \frac{P_T - P_C}{P_T - P_S} \quad KP_S = \frac{P_S - 0.5(P_R + P_L)}{P_T - P_S}$$

Those kind of coefficients are employed since the FRAPP works virtually as a three hole probe. As a result the different pressures that appear in the coefficients are linked to the three, already mentioned, rotations performed about the probe axis. P_C, P_L and P_R are the pressures detected in three different moments which corresponds to the aformentioned three different angular positions needed to reconstruct any generic flow using the FRAPP.

- P_C pressure detected by the probe tap while oriented in a reference direction considered as central
- P_R pressure detected by the probe tap while rotated to the right of a given angle with respect to the reference central direction
- P_L pressure detected by the probe tap while rotated to the left of a given angle with respect to the reference central direction

P_T and P_S are relatively the total pressure of the flow and the static pressure at probe tap location. The experimentally calculated trends of the coefficients are reported in Fig. 4.5.
During calibration in fact the coefficients are considered unknowns and they can be derived, thanks to the knowledge of: the static pressure at probe location, the total pressures of the flow and the direction of the streamlines relative to the probe tap axis.
Those coefficients are derived for different conditions in which the direction considered as central is repeatedly changed. For each change in central direction the values of P_C, P_L and P_R are detected and the associated coefficient calculated.

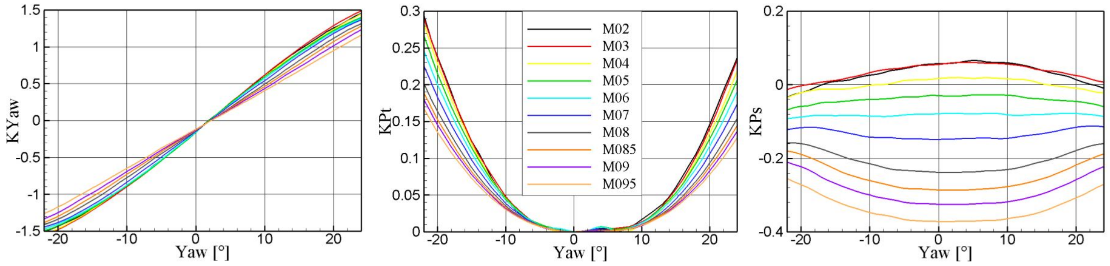

Figure 4.5: Experimentally derived trends for FRAPP coefficients parametric with respect to the Mach number

During experimental measurements the situation is opposite. In fact there is no knowledge of the static and total pressure, which indeed turned into unknowns together with the Yaw angle. In this case the knowledge of the calibration derived probe coefficient trends is crucial.
However in this step, necessary to reconstruct the 2D flow parameters starting an iterative procedure is required. This starts from the pressure values perceived at the three angular positions:

- First guess on static pressure and total pressure:$P_{S_{guess1}} = \frac{P_L+P_R}{2}$, $P_{T_{guess1}} = P_C$
- Calculation of $KYaw$ starting from the two first guesses: $P_{S_{guess1}}$, $P_{T_{guess1}}$

$$KYaw_{guess1} = \frac{P_L - P_R}{P_{T_{guess1}} - P_{S_{guess1}}}$$

- Once $KYaw_{guess1}$ is known, it is necessary to calculate a first guess for Mach number:

$$M_{guess1} = \sqrt{\frac{2\left[\left(\frac{P_{T_{guess1}}}{P_{S_{guess1}}}\right)^{\frac{\gamma-1}{\gamma}} - 1\right]}{\gamma - 1}} \tag{4.3}$$

- If the value obtained for the Mach number does not belong to the set at which the coefficients functions have been extrapolated during probe calibration, an interpolation, based on such known set, would be necessary. In such a way a coefficient function valid for the calculated Mach can easily be obtained.
- Once the curves at M_{guess1} are ready and since the $KYaw_{guess1}$ is known it become possible to derive a first guess value for the Yaw angle, Fig. 4.6: Yaw_{guess1}

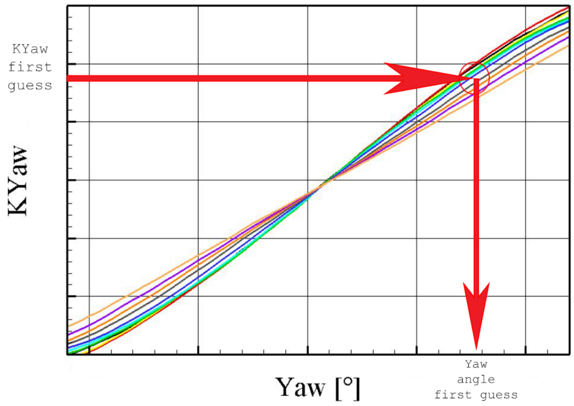

Figure 4.6: Graphical representation of the step used for deriving Yaw angle from KYaw coefficient

- Given the knowledge of Yaw_{guess1} it is possible to derive other two coefficients $KP_{T_{guess1}}$ and $KP_{S_{guess1}}$.
- Once the two coefficients have been calculated, thanks to their own definition and to the knowledge of the pressure readings P_C, P_L and P_R, it is possible to find a second guess value for both static and total pressures by solving a linear system of two equations.

$$\begin{cases} KP_{T_{guess1}} = \frac{P_{T_{guess2}} - P_C}{P_{T_{guess2}} - P_{S_{guess2}}} \\ KP_{S_{guess1}} = \frac{P_{S_{guess2}} - 0.5(P_R + P_L)}{P_{T_{guess2}} - P_{S_{guess2}}} \end{cases} \tag{4.4}$$

- At this point two new guess values are available for static and total pressure, hence the cycle described can restart from those values with a second iteration
- These steps are repeated until the difference among two successive iterations results stays below a certain threshold tolerance.

As a result, after the iterative process based on the three pressure readings obtained by the three different rotations, it is possible to derive the two pressures and the Yaw angle of the flow.
However this procedure is applicable only within angles of ±23 ° around the probe central tap direction. This constrain is due to the fact that onset of separation occurs on a cylindrical surface at ±67°, Fig. 4.7, from the stagnation point and that the three rotations of the probe have a phase displacement of 45°,Fig. 4.8.

- Maximum angle of sensibility: $\gamma = \pm 67°$
- Phase displacement angle: $\alpha = 45°$

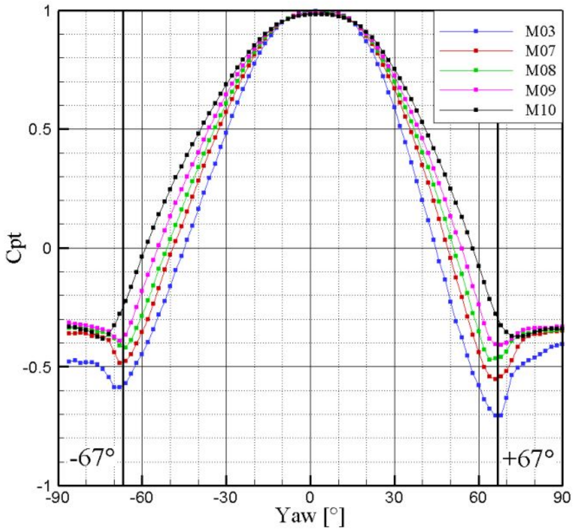

Figure 4.7: Trend of pressure coefficient on the surface of a cylinder as a function of the angular position, parametric on Mach number. The thrend outside the ±67° highlights separation

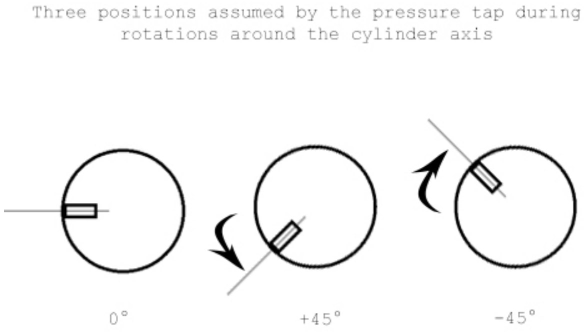

Figure 4.8: Representation of the angular step used during measurement

Given γ angle, the range of pressure tap orientation around the unknown flow direction which guarantees not to face any separation is equal to $2\gamma \approx 135°$.
This range, once divided in three different sectors, gives the maximum applicable angular step: $\left(\frac{2\gamma}{3}\right) = 45°$.
The chosen phase displacement among different rotations, α coincides with this number.
As a result, given γ and α, it is possible to understand for which angular position difference between the central tap direction and the flow direction, one of the two virtual pressure taps associated with the right and left rotations would face separation, Fig. 4.9 and Fig. 4.10. This angular difference is called "angular functioning field" Θ.

$$\Theta = \pm(|\gamma| - \alpha) \tag{4.5}$$

In case of separation the pressure tap reading goes beyond the calibration field causing a not correct flow reconstruction.

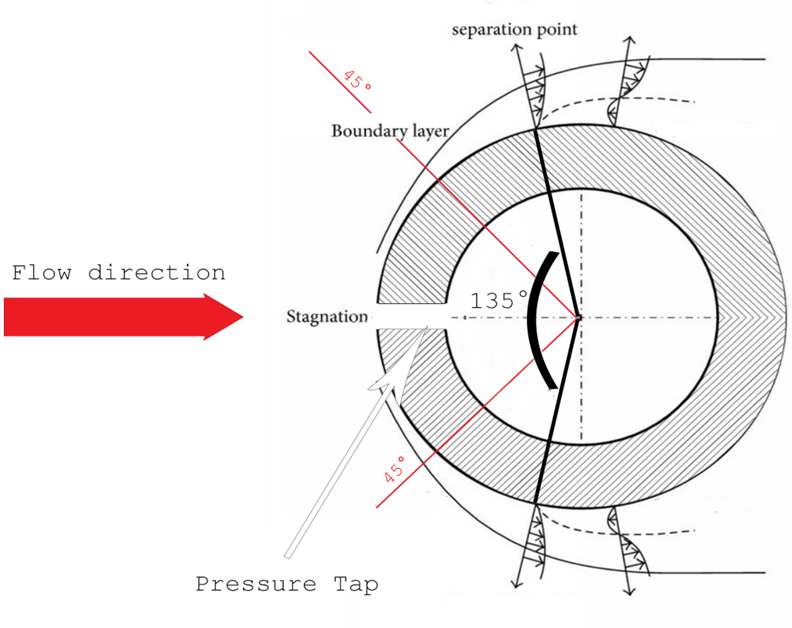

Figure 4.9: Representation of the FRAPP flow separation with pressure tap aligned with the flow; It can be observed that both rotation at 45° stays within the separation limits

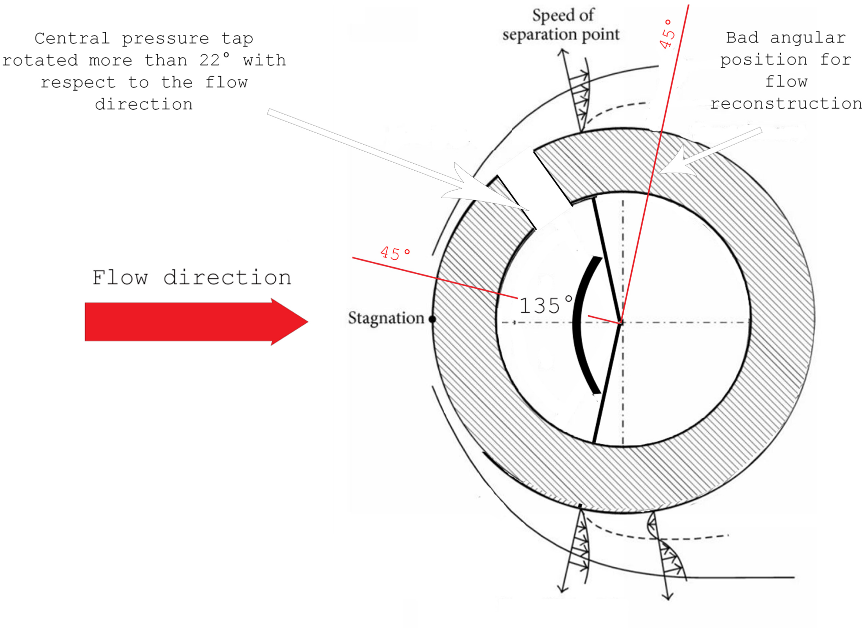

Figure 4.10: Representation of the FRAPP flow separation with pressure tap rotated more than 22° with respect to the flow direction; It can be observed that one of the two rotations at 45° necessary to reconstruct the flow ends up in a region of flow separation

4.1.2 How does acquisition work?

The first step to perform while analyzing a highly angled flow, like the one at the outlet of a machinery rotor, is to understand whether or not the deterministic flow stays within ±22 ° range around a central direction at each time. As a consequence during measurements, since the flow direction is at first unknown, it is necessary to perform, for each measuring point a set of rotations which takes into account the possibility of going out of calibration field.

Hence, the rotations imposed to the probe for each measuring point are, even at first try, more than three; this is done just to be able to reconstruct the flow at points with high angled directions. In fact, during this study downstream of the rotor of the axial turbine, the probe is at first positioned with the pressure tap aligned with the axial machine direction.

Then from this starting position, considered as 0°, the probe tap is rotated to other four angular position, ±45° and ±90°. At each angular position the signal transmitted by the probe is sampled at a frequency of $500kHz$ for $0.6s$. Then the aforementioned procedure is repeated for every position of interest downstream of the rotor.

In this way and thanks to a procedure called 'phase averaging', based on the knowledge of the rotor angular velocity, the 2D periodic flow is reconstructed at each point and for each stator-rotor blades relative position, Fig. 4.11 shows the output file results of this procedure. This set of rotations creates the so called "coarse" grid, which is able to give information on the static pressure, on the total pressure and on the yaw angle at all the points of measure for a given time interval. However this "coarse" grid is not able to give information about the non deterministic unsteadiness of the flow, hence turbulence.

It is important to keep in mind that in an highly angled flow,for some points the set of five rotations could be not satisfactory, and for a correct flow reconstruction it would be necessary to add rotations at ±135°.

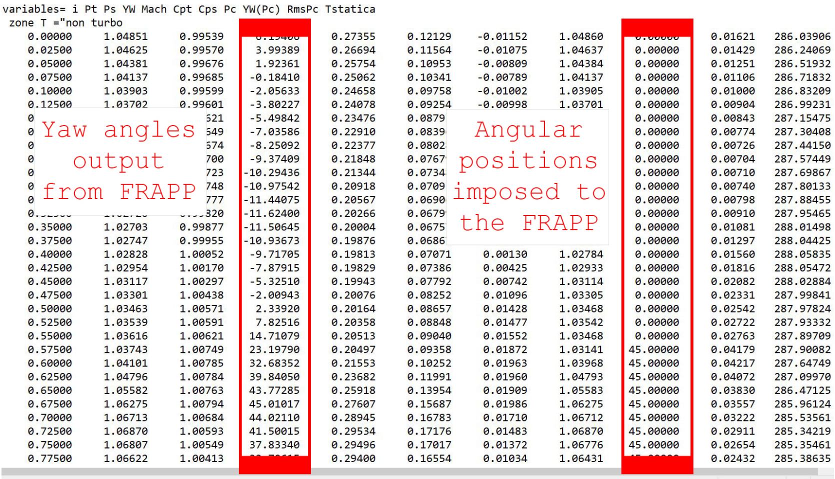

```
variables= i Pt Ps YW Mach Cpt Cps Pc YW(Pc) RmsPc Tstatica
 zone T ="non turbo
   0.00000    1.04851    0.99539               0.27355    0.12129   -0.01152    1.04860               0.01621  286.03906
   0.02500    1.04625    0.99570    3.99389    0.26694    0.11564   -0.01075    1.04637    0.00000    0.01429  286.24069
   0.05000    1.04381    0.99676    1.92361    0.25754    0.10953   -0.00809    1.04384    0.00000    0.01251  286.51932
   0.07500    1.04137    0.99685   -0.18410    0.25062    0.10341   -0.00789    1.04137    0.00000    0.01106  286.71832
   0.10000    1.03903    0.99599   -2.05633    0.24658    0.09758   -0.01002    1.03905    0.00000    0.01000  286.83209
   0.12500    1.03702    0.99601   -3.80227    0.24078    0.09254   -0.00998    1.03701    0.00000    0.00904  286.99231
   0                          521   -5.49842    0.23476    0.0879                           0.00000    0.00843  287.15475
   0                          549   -7.03586    0.22910    0.0839                           0.00000    0.00774  287.30408
   0                          574   -8.25092    0.22377    0.0802                           0.00000    0.00726  287.44150
   0                          700   -9.37409    0.21848    0.0767                           0.00000    0.00704  287.57449
   0                          723  -10.29436    0.21344    0.0734                           0.00000    0.00710  287.69867
   0                          748  -10.97542    0.20918    0.0709                           0.00000    0.00740  287.80133
   0                          777  -11.44075    0.20567    0.0690                           0.00000    0.00798  287.88455
   0.                         320  -11.62400    0.20266    0.0679                           0.00000    0.00910  287.95465
   0.35000    1.02703    0.99877  -11.50645    0.20004    0.0675                           0.00000    0.01081  288.01498
   0.37500    1.02747    0.99955  -10.93673    0.19876    0.0686                           0.00000    0.01297  288.04425
   0.40000    1.02828    1.00052   -9.71705    0.19813    0.07071    0.00130    1.02784    0.00000    0.01560  288.05835
   0.42500    1.02954    1.00170   -7.87915    0.19829    0.07386    0.00425    1.02933    0.00000    0.01816  288.05472
   0.45000    1.03117    1.00297   -5.32510    0.19943    0.07792    0.00742    1.03114    0.00000    0.02082  288.02884
   0.47500    1.03301    1.00438   -2.00943    0.20076    0.08252    0.01096    1.03305    0.00000    0.02331  287.99841
   0.50000    1.03463    1.00571    2.33920    0.20164    0.08657    0.01428    1.03468    0.00000    0.02542  287.97824
   0.52500    1.03539    1.00591    7.82516    0.20358    0.08848    0.01477    1.03542    0.00000    0.02722  287.93332
   0.55000    1.03616    1.00621   14.71079    0.20513    0.09040    0.01552    1.03468    0.00000    0.02763  287.89709
   0.57500    1.03743    1.00749   23.19790    0.20497    0.09358    0.01872    1.03141   45.00000    0.04179  287.90082
   0.60000    1.04101    1.00785   32.68352    0.21553    0.10252    0.01963    1.03968   45.00000    0.04217  287.64749
   0.62500    1.04796    1.00784   39.84050    0.23682    0.11991    0.01960    1.04793   45.00000    0.04072  287.09970
   0.65000    1.05582    1.00763   43.77285    0.25918    0.13954    0.01909    1.05583   45.00000    0.03830  286.47125
   0.67500    1.06275    1.00794   45.01017    0.27607    0.15687    0.01986    1.06275   45.00000    0.03557  285.96124
   0.70000    1.06713    1.00684   44.02110    0.28945    0.16783    0.01710    1.06712   45.00000    0.03222  285.53561
   0.72500    1.06870    1.00593   41.50015    0.29534    0.17176    0.01483    1.06870   45.00000    0.02911  285.34219
   0.75000    1.06807    1.00549   37.83340    0.29496    0.17017    0.01372    1.06776   45.00000    0.02654  285.35461
   0.77500    1.06622    1.00413               0.29400    0.16554    0.01034    1.06431               0.02432  285.38635
```

Figure 4.11: Example of file output from "coarse" grid acquisition and phase averaging for a single point of measure

4.1.3 How to derive information on turbulence?

In order to derive information on turbulence, the approach employed with the FRAPP, is the one based on measurements of total pressure fluctuations at each location of interest.

Hence, to perform this kind of measurement it is necessary the knowledge of the deterministic flow direction, from ”coarse” grid, and it is necessary to rotate the probe in such a way that the flow stays within its insensibility region.

As a result, once the flow direction as a function of time is known for each point of measure, the angular positions at which it is necessary to rotate the probe to fall in the insensitivity range are easily calculated.

In the present study it has been chosen to use angular position spaced of 9° one from the other: ±9°, ±18°, ±27°, ±36°, ±54°, ±63°, ±72°, ±81°, and so on.

Each of the aforementioned intermediate angle is considered as valid angle for a given measuring point whenever the flow has been detected, from the ”coarse” grid, to stay in a range of ±4.5° around it. The angular grid, onto which the signal from the transducer gets sampled, and which is constructed using this procedure is referred as ”refined”.

Using a Python code developed by the Authors it is possible to construct automatically those ”refined” grids, Fig. 4.12, starting from the output files from the ”coarse” grid measurements.

First and last radial position of the set of acquisition points

Step between two different points of acquisition in radial direction

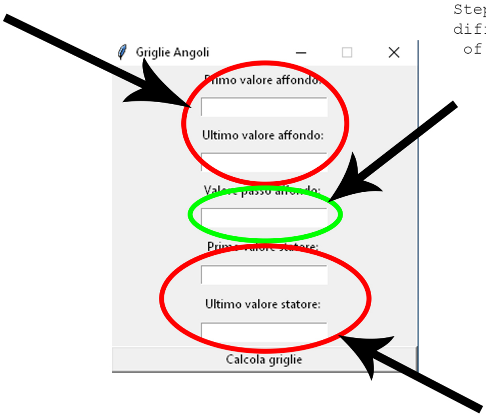

First and last circonferential positions of the set of acquisition points

Figure 4.12: Screenshot of the Python code user interface for ”refined” grid generation

4.2 Thermocouples

Thermocouples are by far the most widely used device for temperature measurements thanks to their good accuracy, high reliability, high flexibility they can cover and the various applications they can be used in. Essentially these devices allow to get measurements from a voltage difference output that by means of calibration functions can be directly linked to temperature values. These functions are usually linear and are calibrated with respect to a certain reference temperature. The accuracy and precision of the calibration equation could be improved with an adequate higher degree polynomial equation [8]. An electromotive forces inside the thermocouple originates from temperature gradients along the thermoelements which are the key components of this sensor. In particular, its working principle is based on the thermoelectric effect called Seebeck effect: when two different metal wires are connected to each other forming a closed circuit and one of two junctions is heated, then a non-zero potential difference at the cold junction extremities can be measured. This is mainly due to the rearrangement of the electrons along the wires due to the temperature change [9, 10]. A simplified representation of the junctions is shown by Fig. 4.13.

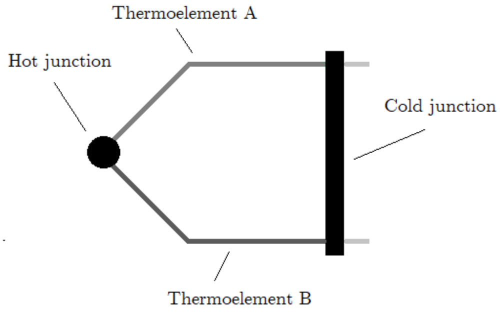

Figure 4.13: Thermocouple - Schematic

In general, the electromotive force generated in the circuit is function of materials characteristics and temperature difference between cold side and hot side.

$$V_{AB} = f\left[A, B, T_{hot\,side}, T_{cold\,side}\right] \tag{4.6}$$

Let's consider the scheme in Fig. 4.14, which represents the equivalent circuit of a typical thermocouple:

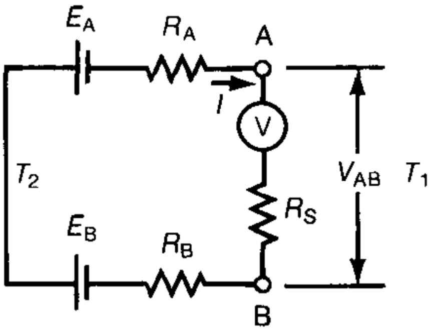

Figure 4.14: Equivalent thermocouple electrical circuit [9]

The voltage difference between the ends of cold junction (at T2) is given by:

$$V_{AB} = E_A - E_B - I(R_A + R_B + R_S) \tag{4.7}$$

Where:

- E_A and E_B are the electromotive force generated in thermoelement A and B respectively. They are represented as two batteries.
- I is the current flowing in the circuit.
- R_A and R_B are the electrical resistances associated to the two thermoelements.
- R_S is the resistance of the resistor due to the presence of the voltmeter.

If the thermoelectric current flows from A to B at the cold junction, then A is called the positive thermoelement and B the negative thermoelement of the thermocouple and vice versa depending on current flow direction.
The response of a thermocouple material to a temperature gradient is referred to as its Seebeck coefficient $\left(\frac{\mu V}{°C}\right)$, and for each standard material this value has been specified by documentary standards [11].
In Fig. 4.15 the Seebeck coefficients S of some common elements are enlisted:

Material	Seebeck Coeff. *	Material	Seebeck Coeff. *	Material	Seebeck Coeff. *
Aluminum	3.5	Gold	6.5	Rhodium	6.0
Antimony	47	Iron	19	Selenium	900
Bismuth	-72	Lead	4.0	Silicon	440
Cadmium	7.5	Mercury	0.60	Silver	6.5
Carbon	3.0	Nichrome	25	Sodium	-2.0
Constantan	-35	Nickel	-15	Tantalum	4.5
Copper	6.5	Platinum	0	Tellurium	500
Germanium	300	Potassium	-9.0	Tungsten	7.5

*: Units are µV/°C; all data provided at a temperature of 0 °C (32 °F)

Figure 4.15: Seebeck coefficients [12]

Seebeck coefficients are functions of temperature. The output voltage difference can be calculated as follows:

$$V_{AB} = \int_{T_{hot\,side}}^{T_{cold\,side}} \big[S_A(T) - S_B(T)\big]\, dT \tag{4.8}$$

Where:

- S_A and S_B are the Seebeck coefficients of thermoelements A and B respectively.
- $T_{hot\,side}$ is the temperature to be measured.
- $T_{cold\,side}$ is the temperature of the cold junction.

Once the voltage difference is known, it is possible to find the unknown temperature. However, it is necessary to know the temperature at cold side because thermocouples can only measure temperature differences. If the cold end of the device is not at reference temperature, which is universally set equal to $0°C$, cold junction compensation is adopted to compensate for the missing voltage, otherwise reference functions and tables cannot be used. In fact, those tables are obtained with the cold side at reference temperature. In the past, ice bath was used to set the temperature of cold junction equal to the reference one.

Up to here the two junctions in thermocouple have been distinguished between cold junction and hot one, thus implying measurements in which flow temperature is higher than the reference one. For the sake of completeness, it's important to notice that thermocouples may be used also to measure temperatures below the reference one, so it's better to call the junction exposed to flow to be characterized as “measuring junction”.

Some further considerations about thermocouples:

1. Seebeck coefficient changes after exposure to temperatures above approximately $200°C$ in most thermocouple alloys. When using noble-metal thermocouples alloys, these changes are typically less than 0.1% while in case of bare-wire base-metal thermocouples they can be greater than 10% [11].
2. The variations in performance among thermocouples of the same nominal type during use are often linked to structural or chemical changes in the alloys and can be caused by contaminants for example [11].
3. Measured temperature may be affected by thermal power absorbed by some thermocouple parts, such as extension wires
4. Irregularities in thermoelement materials, such as inhomogeneities, can lead to measurement errors thus great effort is spent by manufacturers to achieve high-quality elements [11].
5. When mounting the thermocouples, care must be taken in order to avoid bending and flexing of thermoelement wires because deformation may affect accuracy of measurements [9].

6. In some applications it could be necessary to protect the device from negative effects of the environment or to prevent contamination and ensure long life.

4.2.1 Thermocouple types

Available thermocouples are grouped depending on materials used as thermoelements to realize the wires and on application. The thermocouples that have been standardized are identified by letters:

- Type J: Iron as positive thermoelement and Constantan (45Ni-55Cu) as negative thermoelement. This is the most widely used thermocouple and it is suitable for applications in vacuum, oxidizing, reducing and inert atmosphere at temperatures up to $760°C$.

- Type T: Copper as positive thermoelement and Constantan (45Ni-55Cu) as negative thermoelement. This is the most used thermocouple for cold applications since it guarantees high stability at sub-zero temperatures and so it is suitable for cryogenic measurements. Because of the low oxidation resistance of copper it should not be used above $370°C$.

- Type K: Chromel (90Ni-10Cr) as positive thermoelement and Alumel (95Ni-2Al-2Mn-1Si) as negative thermoelement. This thermocouple is the most used for hot applications thanks to its reliability and accuracy at high temperatures. The maximum operating temperature is about $1260°C$, it is recommended for use in oxidizing atmosphere and should not be used in environments containing sulfur unless protected.

- Type E: Chromel (90Ni-10Cr) as positive thermoelement and Constantan (45Ni-55Cu) as negative thermoelement. These thermocouples are characterized by the highest thermal electromotive force produced per degree (see Fig. 4.16) and can be used for power generation applications such as thermopiles. They may be used only in oxidizing or inert atmosphere at temperatures up to $870°C$.

- Type B: both positive and negative thermoelements are Platinum alloys, 60Pt-30Rh and 94Pt-6Rh respectively. It has the highest temperature limit of all the standard thermocouples since it can be used at temperatures up to $1700°C$.

- Type N: Nicrosil (84.3Ni-14.2Cr-1.4Si-0.1Mg) as positive thermoelement and Nisil (95.5Ni-4.4Si-0.1Mg) as negative thermoelement. These thermocouples represent an alternative to Type K with the advantage to be more stable at high temperatures.

- Type S: Platinum alloy (90Pt-10Rh) as positive thermoelement and Platinum as negative thermoelement. It is suitable for very high-temperature measurements and it is recommended for use in oxidizing and inert atmosphere. It can be used in lower temperature applications because it ensures high accuracy and stability.

- Type R: Platinum alloy (87Pt-13Rh) as positive thermoelement and Platinum as negative thermoelement

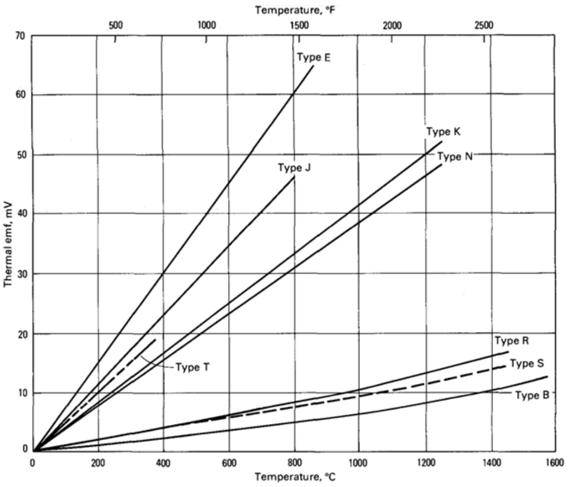

Figure 4.16: Emf vs temperature - Comparison of different thermocouple types [9]

To connect thermocouple wires to temperature measuring and control instrument, extension wires are used. The main reason these wires are adopted is that thermoelement materials could be very expensive, such as in case of Pt-Rh alloy wire for example.

4.2.2 Measuring junction configurations

Thermocouple measuring junctions are available in different configurations (see Fig. 4.17):

a. Grounded junction: when the junction is integral part of the metallic sheath tip. This allows to protect the wires from corrosive or contaminant species in the environment, to use thermocouple in high pressure applications and to achieve longer lifespan

b. Ungrounded junction: when the junction is electrically insulated from the outside metallic sheath, which is still acting as shielding element.

c. Exposed junction: when the junction extends beyond the protective metallic sheath. This configuration guarantees very fast response time but it makes the thermocouple not recommended for measurements in case of high pressure applications or aggressive environment.

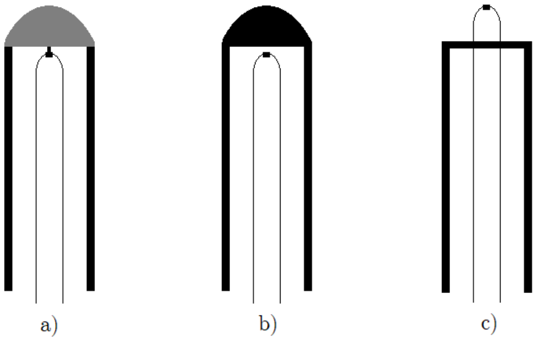

Figure 4.17: Junction types

A key parameter is the ”response time” because it gives an idea about how quickly the sensor responds to temperature changes. Configuration of measuring junction has a strong impact on response time as so as the wires diameter: heat transfer processes require much more time when ungrounded junction and bigger diameter wires are used. Fig. 4.18 shows the trend of response time as function of wires diameter in the three configurations:

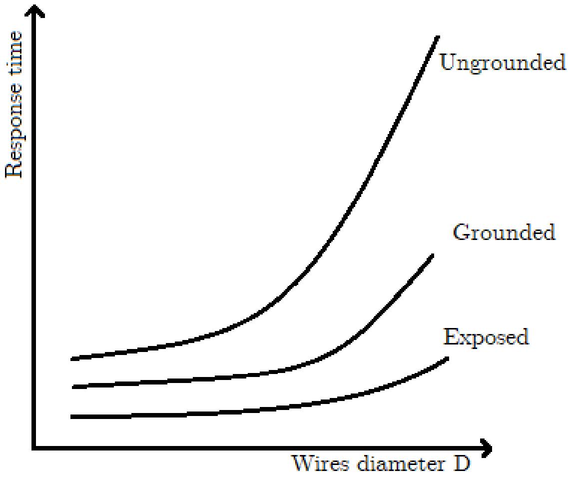

Figure 4.18: Thermocouple response time as function of wire diameter and junction type

4.2.3 First-order system modeling

The transient response of a thermocouple can be modeled using first-order differential equation. In general, the dynamic behavior of a first-order system is governed by the following equation:

$$a_1 \frac{dy(t)}{dt} + a_0 y(t) = f(t) \tag{4.9}$$

where y(t) is the response of the system (the output) to some forcing function f(t) (the input).

Dividing by a_0, Equation (4.9) becomes:

$$\frac{a_1}{a_0}\frac{dy(t)}{dt} + y(t) = \frac{1}{a_0}f(t) \tag{4.10}$$

The ratio between a_1 and a_0 has the dimension of a time and it is called "time constant" of the system, while $\frac{1}{a_0}$ is called "gain".

$$\tau = \frac{a_1}{a_0} \tag{4.11}$$

$$K = \frac{1}{a_0} \tag{4.12}$$

If a step input is considered, such as a sudden variation of temperature in thermocouple case, the solution of first-order differential equation is:

$$y(t) = y_\infty\left(1 - e^{-\frac{t}{\tau}}\right) \tag{4.13}$$

with $y(0) = 0$ as initial condition.
The picture below (Fig. 4.19) illustrates the transient response of a first-order instrument to a step input:

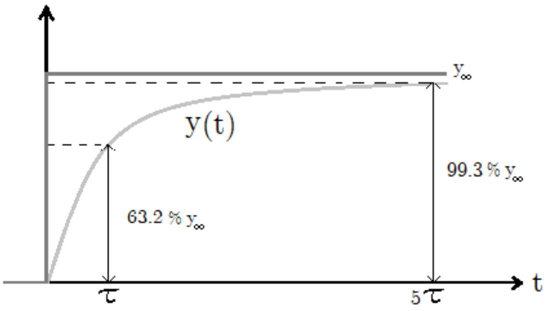

Figure 4.19: Graphical representation of the step used for deriving Yaw angle from KYaw coefficient

When $t = \tau$, the output value has reached 63.2% of its final value, while when $t = 5\tau$ it becomes equal to 99.3% of the final value [13]. The response time is defined as the time needed by sensor to detect 99.3% of the step change and it is clearly only function of the time constant. Regarding the thermocouple, a simplified model based

on heat transfer can be used to analyze transient response to a step input. It can be reasonably assumed that the dominant heat transfer process is convection and that the thermal power given off by the fluid must equals the thermal power absorbed by the thermocouple measuring junction. Hence ,the following equation is valid:

$$hA(T_\infty - T) = mc\frac{dT}{dt} \tag{4.14}$$

where T_∞ and h are the fluid temperature to be measured and its convection heat transfer coefficient respectively, A is the area of measuring junction exposed to the

fluid, m the mass of junction and c its specific heat.
Writing Equation (4.14) in similar form to Equation (4.10):

$$\frac{mc}{hA}\frac{dT}{dt} + T = T_\infty \tag{4.15}$$

where the time constant is $\tau = \frac{mc}{hA}$.
Solving this differential equation allows to determine measured temperature trend over time.

4.2.4 Thermocouple for flow characterization

The thermocouple used during experimental campaign for flow characterization is a S type one with exposed junction, that ensures very fast response time and high accuracy. Junction size is equal to $25.4\mu m$ and it has been chosen as a trade-off between mechanical resistance and dynamic properties. However, due to those characteristics it can be easily damaged in presence of strong aerodynamic loadings. Those loadings cause stresses at the junction to overcome their critical limit and thus induce failure.
The probe is characterized by a 1^{st} order instrument response with a time constant of $2.4ms$, measured during calibration in a shock tube. Temperature measurements are compensated applying the transfer function. The extended uncertainty of this probe is $\pm 0.3K$.
The need of very prompt probe is due to the will of catching the temperature unsteadiness associated to entropy waves frequencies. In fact, if response time is slow compared to rate of change of temperature to be measured, it's not possible to faithfully represent temperature fluctuations. Moreover, the temperature field obtained by means of the fast thermocouple is necessary for the elaboration of data coming from the other probes, i.e. five-hole pressure probe and FRAPP, thus it is very important to get accurate results.
In Fig. 4.20 the measuring junction of fast thermocouple used during experiments is shown:

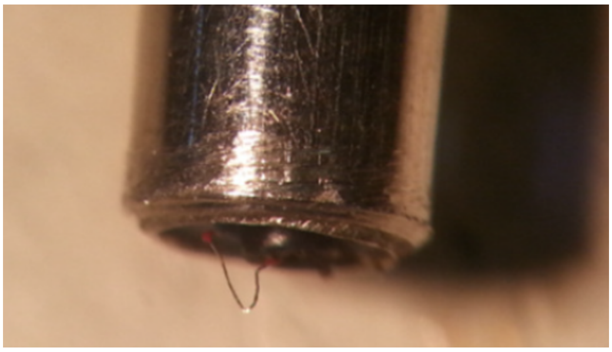

Figure 4.20: Detail of the fast thermocouple used for experimental campaign

4.3 5-hole steady probe

Five-hole pressure probe is a device used in experimental fluid-dynamics and aerodynamics for measurements of Mach number, inflow angles and static and total pressure values. Since it can be used for three-dimensional flow studies, this type of probe is very useful when the purpose is to investigate the flow field within turbomachines cascades. It represents an alternative to hot-wire anemometry for determining flow direction and for carrying out steady measurements of the average aerodynamic field. Moreover, it overcomes the main problem of pitot-static tube which requires the flow to be aligned with the probe to guarantee good accuracy.
The five-hole pressure probe (Fig. 4.21 [14]) consists in three parts:

1. The head, that is where the five pressure taps are located. They are called up, down, left, right and central tap depending on the position. The five holes are connected through tubes to the pressure transducers. These are used to measure the flow stagnation and the static pressure at probe location.

2. The stem, which must be characterized by high stiffness to avoid vibration and misalignment during measurements.

3. The outreach, that is used to keep the pressure taps far enough from the stem which could affect significantly the results. In general, inserting a probe into a gas stream has consequences on the measured quantities so it's crucial to reduce the impact of instrumentation. For example, when Mach number is close to 0.9, a reduction of flow area by only 1% causes the flow to choke.

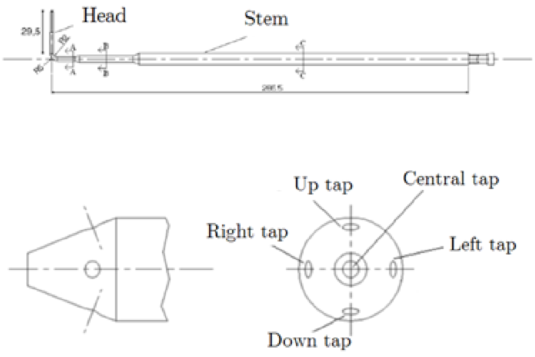

Figure 4.21: Five-hole pressure probe parts

The reference system associated to the probe is represented by triad $x_p\,, y_p\,, z_p$ (see Fig. 4.22). It's possible to define two fundamental quantities:

- Yaw angle: angle between the projection of absolute velocity on $x_p - y_p$ plane and x_p axis

- Pitch angle: angle between the projection of absolute velocity on $x_p - z_p$ plane and x_p axis

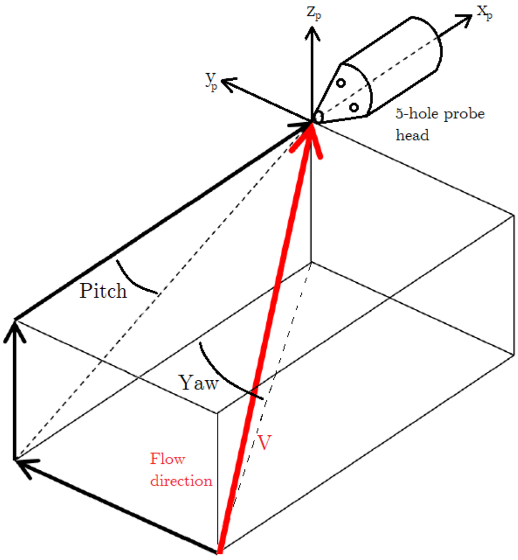

Figure 4.22: Pitch and yaw angle

Prior to the beginning of measurement campaign, the probe must be calibrated. Calibration consists in subjecting the probe to a known flow field and measuring pressures at the five holes while the probe is positioned at predefined angular positions relative to the flow (different combinations of yaw and pitch angles). During calibration Mach number of the flow is set at different values. Once the tests have been completed, data reduction process is carried out: the collected data are used to obtain calibration matrices. These matrices are built up starting from some dimensionless pressure coefficients that are defined as it follows:

$$K_{yaw} = \frac{p_l - p_r}{p_T - p_S} \tag{4.16}$$

$$K_{pitch} = \frac{p_u - p_d}{p_T - p_S} \tag{4.17}$$

$$K_{pt} = \frac{p_T - p_c}{p_T - p_S} \tag{4.18}$$

$$K_{ps} = \frac{p_S - 0.25(p_l + p_r + p_u + p_d)}{p_T - p_S} \tag{4.19}$$

- p_l pressure reading of the left tap
- p_r pressure reading of the right tap
- p_u pressure reading of the up tap
- p_d pressure reading of the down tap
- p_T stagnation pressure at the probe location
- p_S static pressure at the probe location

The obtained calibration matrices, which have been found for a set of Mach number, allow to relate the pressure values read by the five pressure taps at a specific point to yaw angle, pitch angle, total pressure and static pressure values that characterize the flow in that specific position.

The geometry of the head must be designed in such a way not to promote flow detachment, in fact if one of the pressure taps would face detached flow the calibration matrices would no longer be reliable.

When the probe is used in unknown flow field, an iterative cycle (Fig. 4.23) is needed to find quantities of interest. For a given position:

- As first guess assume the local total pressure equal to the pressure measured by the central tap and the static one equal to the average of pressure values measured by the four peripheral taps. So Mach number is derived assuming isentropic flow and perfect gas, while the yaw and pitch coefficients can be calculated.

- Entering the calibration matrices with yaw/pitch coefficients and Mach number allow to derive the associated yaw and pitch angles. Since calibration matrices have been obtained for a finite set of Mach number values, bilinear interpolation among this set of matrices is required to find yaw and pitch associated to a Mach number equal to the calculated one.

- Being total pressure coefficient and static one functions of Mach, yaw and pitch angles, then it's possible to derive K_{pt} and K_{ps} from calibration matrices using the calculated Mach number, yaw and pitch.

- Since K_{pt} and K_{ps} are now available, total pressure and static pressure are calculated by rewriting Equations (4.18) and (4.19). If they are different from the two values given as input, they must be imposed as new first guess and cycle restarts. Cycle stops when output values are equal to input ones.

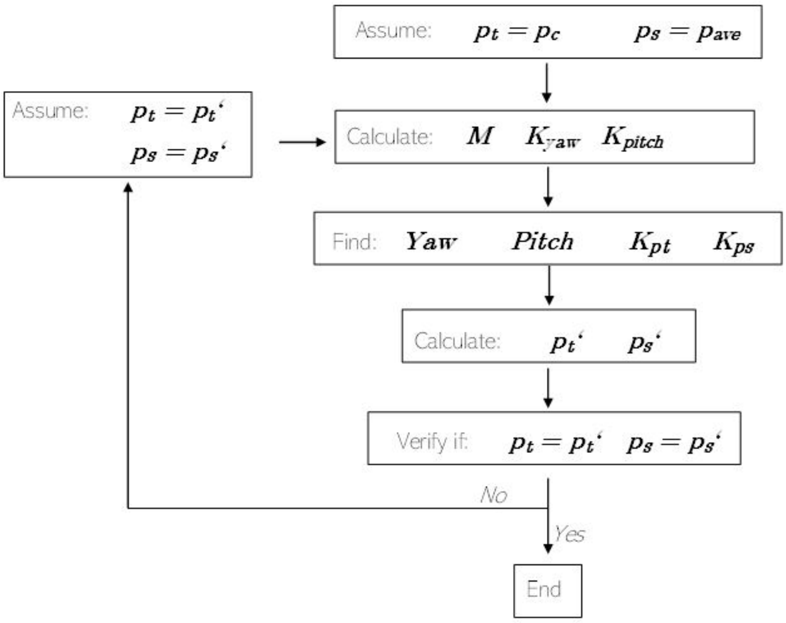

Figure 4.23: Scheme of the iterative cycle for five-hole pressure probe

In Figs. 4.24–4.27 calibration matrices of the five hole probe used during experimental campaign are reported for a given Mach number value ($M = 0.2$) as an example:

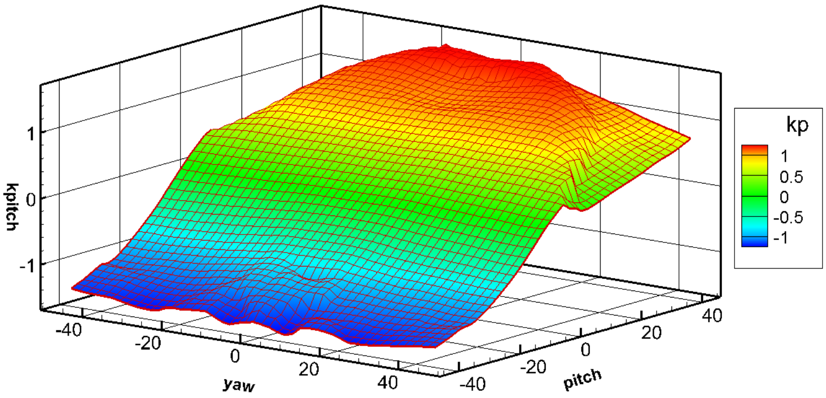

Figure 4.24: Pitch coefficient - calibration matrix representation

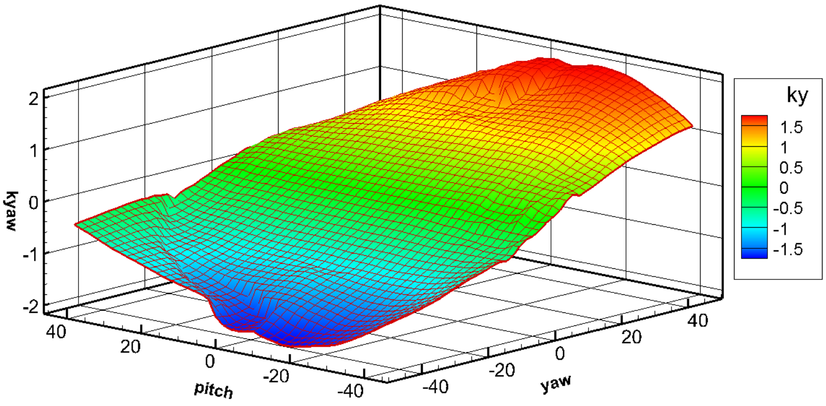

Figure 4.25: Yaw coefficient - calibration matrix representation

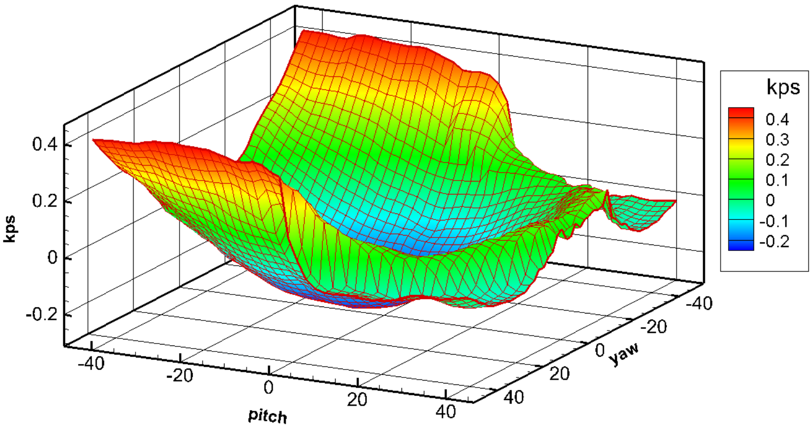

Figure 4.26: Static pressure coefficient - calibration matrix representation

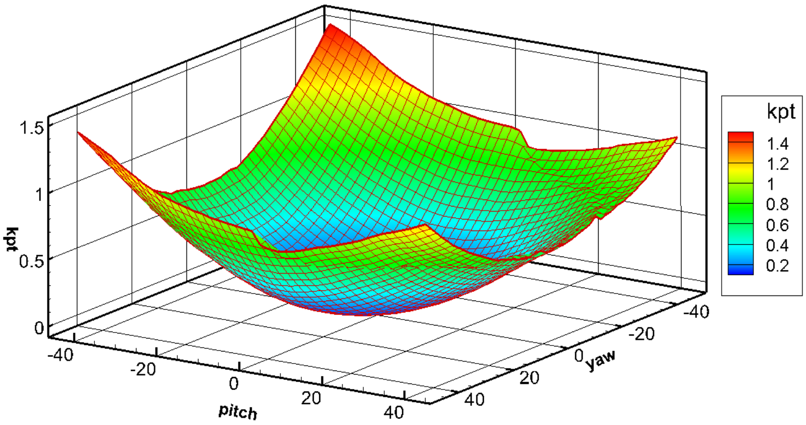

Figure 4.27: Total pressure coefficient - calibration matrix representation

Since from five-hole pressure probe measurements it's possible to get the local Mach number, then the velocity of the flow in each point is equal to:

$$v = M\sqrt{\gamma R T_{static}} \tag{4.20}$$

From Equation (4.20) it's clear that it's necessary to know the temperature field to compute the velocity. Temperature data can be obtained from measurements with fast thermocouple (see Section 4.2.4).
Velocity components are calculated by means of following relations:

$$v_r = v\, sin(\beta) \tag{4.21}$$

$$v_t = v\, cos(\beta) sin(\alpha) \tag{4.22}$$

$$v_a = v\, cos(\beta) cos(\alpha) \tag{4.23}$$

Notice that the reference frame of the machine is different with respect to the one of the probe because there could be a phase displacement between the axes of the two reference frames. During data acquisition for the characterization of the flow downstream the stator, an angle equal to 82.6° between x_p (axis of the central tap) and the axial direction of the machine has been set.
This value has been chosen to be sure of being inside the calibration range. Fig. 4.28 shows the phase displacement between the five-hole probe central tap axis and the machine axis.

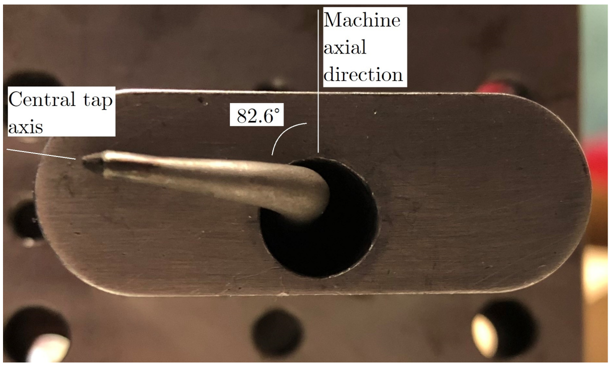

Figure 4.28: Five-hole pressure probe orientation with respect to machine axial direction

Flow angles alpha and beta, i.e. the angles in the frame associated to the machine, are calculated thanks to an algorithm which requests as input the yaw and pitch angles, in addition to the phase displacement between the two reference systems. In particular alpha is the angle between the projection of velocity in blade-to-blade plane and the machine axis, while beta is the angle between absolute velocity and its projection in blade-to-blade plane.
One of the five-hole pressure probes used during experimental campaign is characterized by head diameter equal to $2.1mm$. The diameter of each hole is $0.3mm$, the

lateral taps are located on a surface that is inclined of 22° with respect to central tap axis. In Fig. 4.29 technical drawings of the five-hole probe are shown.

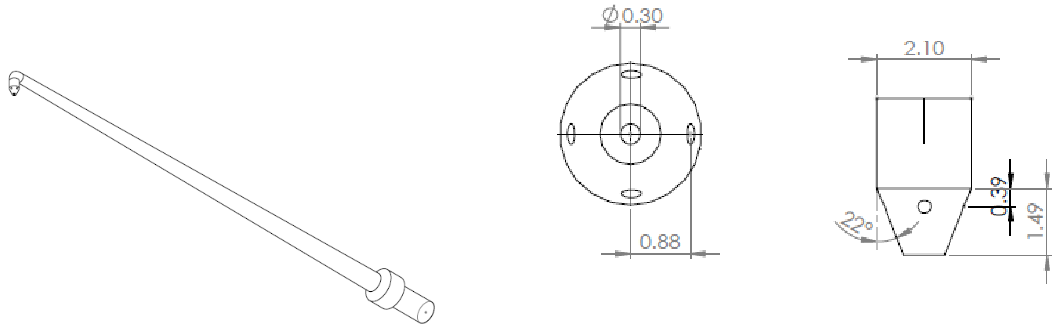

Figure 4.29: Drawings of 5-hole pressure probe used upstream of the stator

Chapter 5

Test campaign

In this chapter details on plant operating conditions are given: the tests are performed for different operating conditions in order to characterize the flow in different situations. Moreover, a summary of the tests carried out for this work is provided to get an overview of the test campaign. All measurements take place inside the turbine stage since the purpose of this work is to investigate the effect of entropy waves on flow quantities.

5.1 Plant operating conditions

From one operating condition to another one, rotational speed of both compressor and turbine are changed, thus the compression ratio provided by compressor and consequently the expansion ratio that features the turbine, in addition to variations in the turbine inlet total temperature. In fact, given the working principle and control strategy of the plant, the expansion ratio is directly determined by the compression ratio from compressor which is set by acting on its impeller rotational speed. The turbine rotational speed is set thanks to the dedicated potentiometer which control the electric motor on the turbine side. The latter, as already mentioned, behaves as a brake when the desired rotational speed is lower than the one that it would naturally reach due to the flow action. Plant is controlled to get the desired conditions at the turbine side, which means a specific expansion ratio, rotational speed and total inlet temperature.

The operating conditions enlisted in Table 5.1 have been chosen in such a way to get the same rotor incidence at blade midspan to make results comparable. Same incidence is obtained by imposing the same peripheral speed coefficient kp, so the same velocity triangle shape in the two operating conditions. It is defined as it follows:

$$k_p = \frac{u}{v_1} \tag{5.1}$$

where u is the peripheral speed at midspan and v_1 the absolute velocity at stator outlet.

Taking OP3 as reference condition, the peripheral speed coefficient has been calculated and it has been used to determine the necessary v_1 in OP2. From the absolute

Table 5.1: Plant operating conditions

	$OP3$	$OP2$
Rpm compressor [rpm]	12340	15035
Compression ratio β_{comp}	1.44	1.81
Expansion ratio β_{turb}	1.4	1.76
T_t turbine inlet [$°C$]	40	50
Rpm turbine [rpm]	7000	8740

velocity of flow downstream the stator, it is possible to derive the expansion ratio that is needed and, consequently, the compression ratio the compressor must provide. From experiments it has been found that expansion ratio is about 0.97 times the compression ratio due to some pressure losses that occur in ducts. Thanks to this preliminary analysis, it is possible to link the turbine rotational speed and the compression ratio, for fixed turbine peripheral speed coefficient and degree of reaction. This allows to have an idea about the requested compressor rotational speed for the chosen rotational speed of turbine in OP2. Then, starting from this analysis, the optimal rotation speed of both turbine and compressor have been determined by mean of tests in order to be sure to have same rotor mid-span incidence in OP3 and OP2. The higher the turbine rotational speed, the higher the expansion ratio that is necessary to guarantee the satisfaction of the constraint. An upper limit to turbine rotational speed is represented by the electrical power that is needed to keep it at the set value so its value has been chosen taking into consideration this aspect too.

Fig. 5.1 compares the trend of the incidence as function of radial position in the two operating conditions. It can be noticed that in both cases the trend is almost the same, so the same velocity triangle shape is achieved. What is interesting in studying this higher compression ratio reached in OP2 is the possibility, when k_p is kept constant, to analyze the effects given by a change in Mach and Reynolds numbers.

In addition to these two operating conditions, two more have been tested. They are variants of OP3 and they have been called OP3L and OP3U respectively (Table 5.2): L stands for loaded, while U for unloaded. In the first case, the rotational speed of turbine has been reduced leading to higher blades loading and, in the second one it has been increased. Different loading conditions significantly affect the flow field, as it will be seen in the next chapters. Fig. 5.2 shows the incidence in these two last operating conditions compared to OP3.

Table 5.2: Plant operating conditions

	$OP3$	$OP3U$	$OP3L$
Rpm turbine [rpm]	7000	8240	5000

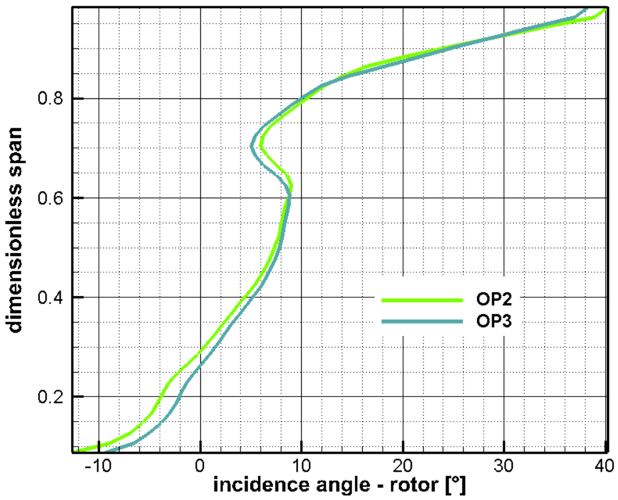

Figure 5.1: Incidence angles in the two clean operating conditions

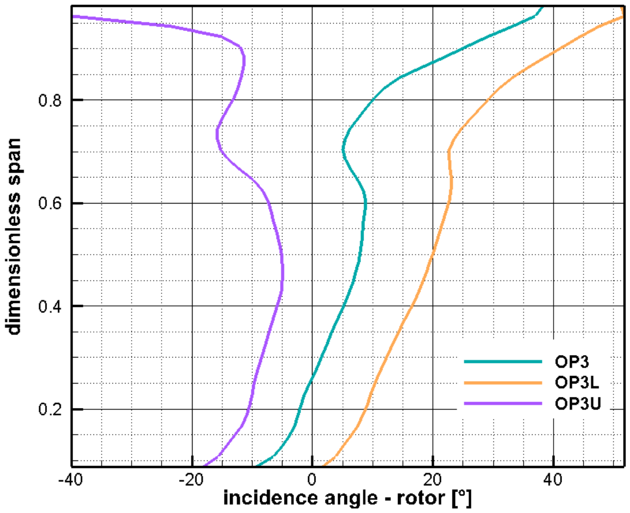

Figure 5.2: Incidence angles in the three OP3 conditions

5.2 Test list

Tables 5.3–5.5 enlist the tests carried out during experimental campaign. They are grouped according to the turbine stage section where they have been performed, Fig. 5.3: upstream the stator (T1), downstream the stator (T2) and at rotor outlet (T3).

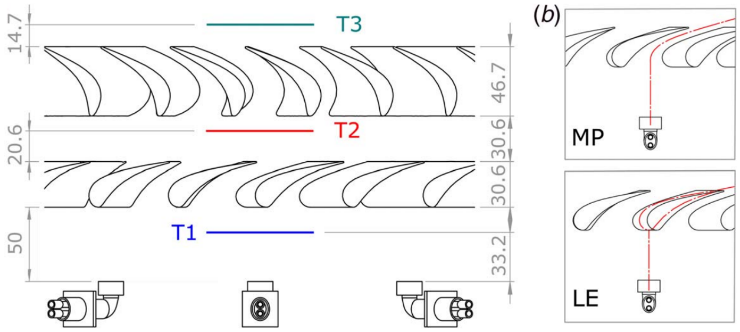

Figure 5.3: Scheme representing the three sections of measurement together with their axial position

For each test, the plant operating condition and the probe installed are specified. The tests called "Clean" have been performed to characterize the flow in absence of disturb injection and of the swirler, while the ones called "No injection" (Noinj) have been carried out to evaluate the effect of the injector presence on the main flow. Regarding the tests when injector is mounted, its circumferential position (clocking position) is specified: "LE" (leading edge) when swirler axis is aligned with the leading edge of stator blade and "MP" (mid pitch) when it crosses the middle of the blade channel. For those tests during which entropy wave generator is switched on, the injection frequency is given, otherwise the acronym HS is used for tests featuring "hot streak".

Table 5.3: Stator inlet

OP condition	**Type**	**Clocking position**	**Probe**
OP3	HS	-	T_{fast}, 5-holes
OP2	No injection	-	5-holes
	HS	-	T_{fast}, 5-holes
	$10Hz$	-	T_{fast}, 5-holes
	$100Hz$	-	T_{fast}, 5-holes

For stator inlet:T_{fast} acquisition time = 15 minutes; 5-holes acquisition time = 22 minutes

Table 5.4: Stator outlet

OP condition	Type	Clocking position	Probe
OP3	Clean	-	5-holes
	HS	LE MP	T_{fast}, 5-holes
OP3L	Clean	-	5-holes
OP3U	Clean	-	5-holes
OP2	Clean	-	T_{fast},5-holes
	No injection	LE MP	5-holes
	HS	LE MP	T_{fast}, 5-holes
	$10Hz$	LE MP	5-holes, FRAPP
	$100Hz$	LE MP	5-holes

For stator outlet:T_{fast} acquisition time OP3 = 47 minutes; T_{fast} acquisition time OP2 = 35 minutes; 5-holes acquisition time = 54 minutes; FRAPP acquisition time = 60 minutes

Table 5.5: Rotor outlet

OP condition	Type	Clocking position	Probe
OP3	Clean	-	T_{fast}, FRAPP
	HS	LE MP	T_{fast}, FRAPP
OP3U	Clean	-	T_{fast}, FRAPP
	No injection	LE MP	T_{fast}, FRAPP
	HS	LE MP	T_{fast}, FRAPP
	$10Hz$	LE MP	T_{fast}, FRAPP
	$100Hz$	LE MP	T_{fast}, FRAPP
OP3L	Clean	-	T_{fast}, FRAPP
	No injection	LE MP	T_{fast}, FRAPP
	HS	LE MP	T_{fast}, FRAPP
	$10Hz$	LE MP	T_{fast}, FRAPP
	$100Hz$	LE MP	T_{fast}, FRAPP
OP2	Clean	-	T_{fast}, FRAPP
	No injection	LE MP	T_{fast}, FRAPP
	HS	LE MP	T_{fast}, FRAPP
	$10Hz$	LE MP	T_{fast}, FRAPP
	$100Hz$	LE MP	T_{fast}, FRAPP

For rotor outlet:T_{fast} acquisition time = 37 minutes;FRAPP acquisition time dependent on the angular grid (OP3 = 137 min, OP3U = 120 min, OP3L = 142 min, OP2 = 128 min).

Note to the reader: the frequency of EW at 100Hz refers actually to a disturb injected at 112Hz. This notation has been chosen by the Authors in accordance to past reports on the same topic.

5.3 Procedure to start acquisition on the high speed test rig

In this chapter it is described the procedure necessary to correctly and safely start the acquisition of turbine stage flow data. It is important to keep in mind that some of the steps described hereafter, if performed in the wrong way, could lead to both hazardous situations and failure of the instrumentation.
As long as different kind of tests require slightly different procedures the guidelines here proposed will try to satisfy the whole set of possible bench configurations employed at the moment.

5.3.1 Ambient pressure measurement

The first step to carry out is the measurement of the environmental pressure at the test site via a barometer, Fig. 5.4. This pressure converted in millibar [$mbar$] would then be submitted to the bench Labview software.

Figure 5.4: Barometer used for atmospheric pressure measurement

It is important to measure the environmental pressure since as reference pressure it plays a major role in the correct interpretation of data coming from the pressure transducers.

5.3.2 Zeroing system transducers

Wait for the transducers to be on for at least 30 min and hence to reach their thermal equilibrium. Then, from the Labview software, Fig. 5.5, it is possible to record a whole set of values coming from the pressure transducers mounted on the system. This passage is necessary to have a correct measurement of the pressures values once the test has started. It is important to record the zeros when the system is not working yet.

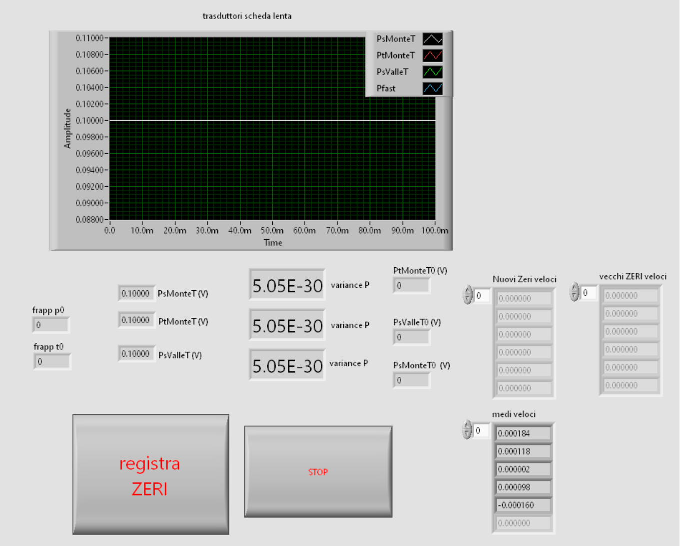

frapp p0: 0
frapp t0: 0

PsMonteT (V): 0.10000
PtMonteT (V): 0.10000
PsValleT (V): 0.10000

variance P: 5.05E-30
variance P: 5.05E-30
variance P: 5.05E-30

PtMonteT0 (V): 0
PsValleT0 (V): 0
PsMonteT0 (V): 0

Nuovi Zeri veloci: 0
0.000000
0.000000
0.000000
0.000000
0.000000
0.000000

vecchi ZERI veloci: 0
0.000000
0.000000
0.000000
0.000000
0.000000
0.000000

medi veloci: 0
0.000184
0.000118
0.000002
0.000098
-0.000160
0.000000

Figure 5.5: Zeros routine Labview

5.3.3 Electric motors

As soon as the previous steps have been completed it is necessary to turn on the actuators, Fig. 5.6, and to adjust the probes, the stage nozzle and the Entropy Waves Generator (EWG) to their useful starting position.

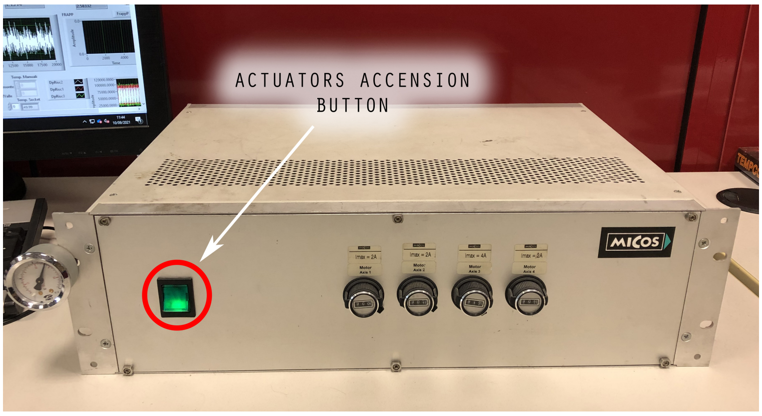

Figure 5.6: Motor activation button

The information related to the positions imposed by the actuators at this step would be then used by the acquisition software during the tests.

5.3.3.1 How does the Labview software work for electric motors?

The electric motors Labview interface presents, as it can be seen in Fig. 5.7, two values for each motor: the first value is actually an entry value required to move the motor to a given position; the second value is an output and gives back the current position of the motor.

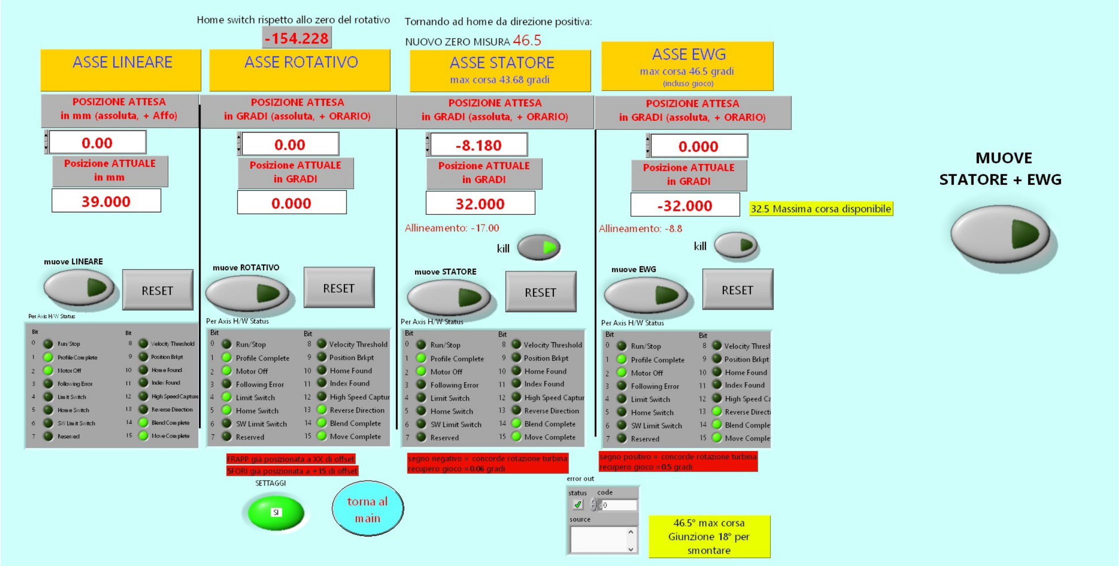

Home switch rispetto allo zero del rotativo -154.228

Tornando ad home da direzione positiva:
NUOVO ZERO MISURA 46.5

ASSE LINEARE
POSIZIONE ATTESA in mm (assoluta, + Affo): 0.00
Posizione ATTUALE in mm: 39.000

ASSE ROTATIVO
POSIZIONE ATTESA in GRADI (assoluta, + ORARIO): 0.00
Posizione ATTUALE in GRADI: 0.000

ASSE STATORE
max corsa 43.68 gradi
POSIZIONE ATTESA in GRADI (assoluta, + ORARIO): -8.180
Posizione ATTUALE in GRADI: 32.000
Allineamento: -17.00

ASSE EWG
max corsa 46.5 gradi (incluso gioco)
POSIZIONE ATTESA in GRADI (assoluta, + ORARIO): 0.000
Posizione ATTUALE in GRADI: -32.000
32.5 Massima corsa disponibile
Allineamento: -8.8

FRAPP già posizionata a XX di offset
5FORI già posizionata a +15 di offset

segno negativo = concorde rotazione turbina
recupero gioco = 0.06 gradi

segno positivo = concorde rotazione turbina
recupero gioco = 0.5 gradi

error out
status ☑ code 0
source

46.5° max corsa
Giunzione 18° per smontare

Figure 5.7: Labview of motors page

However, it is important to highlight that every time that a position is given as input or it is received as output, the value associated to it has necessarily only a direct meaning in a relative frame of reference imposed by the user. In fact as it can be seen from the software at each current position it can be associated a zero reference value thanks to the reset button.

As a consequence of the useful usage of relative frames of references, the instrumentation controlled by electric actuators need to be also equipped with a set of switches.

Those switches are positioned at known positions to always have absolute reference to come back to between different tests. The aforementioned switches once triggered stop the actuator and give back a signal to the software that light up the "limit switch" light.

5.3.4 Import grid for acquisition points

In order to control the position of the probes during the acquisition it is fundamental to load some information that comes from txt files constructed in advance, Fig. 5.8.

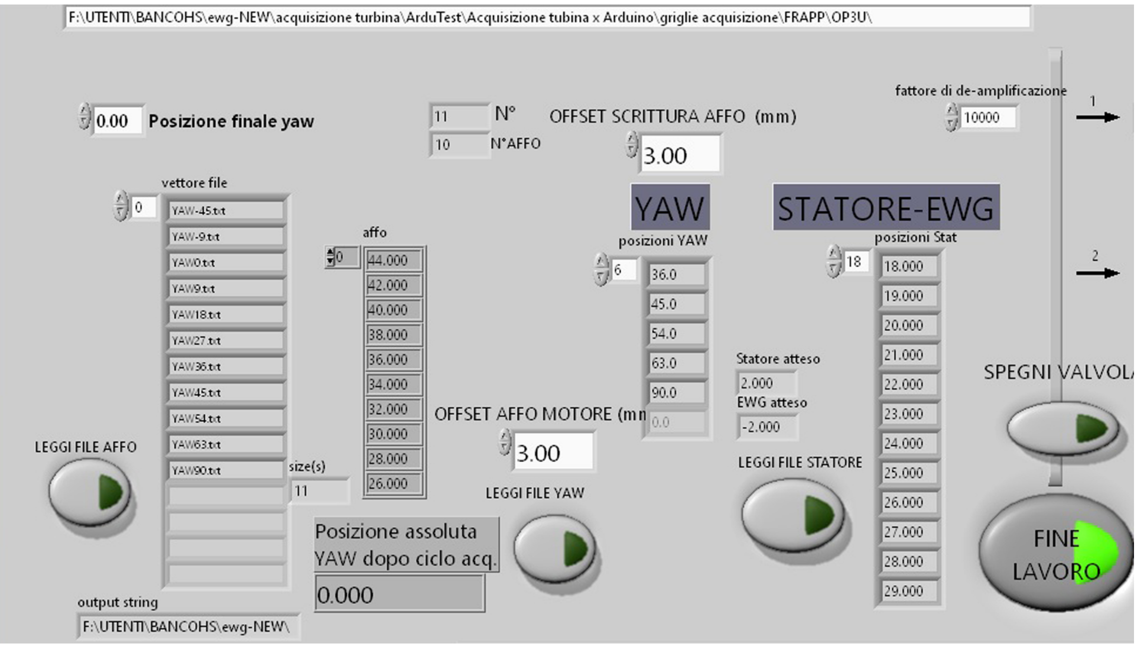

F:\UTENTI\BANCOHS\ewg-NEW\acquisizione turbina\ArduTest\Acquisizione tubina x Arduino\griglie acquisizione\FRAPP\OP3U\

0.00 **Posizione finale yaw**

11 N°
10 N°AFFO

OFFSET SCRITTURA AFFO (mm): 3.00

fattore di de-amplificazione: 10000

vettore file: 0
YAW-45.txt
YAW-9.txt
YAW0.txt
YAW9.txt
YAW18.txt
YAW27.txt
YAW36.txt
YAW45.txt
YAW54.txt
YAW63.txt
YAW90.txt

size(s): 11

affo: 0
44.000
42.000
40.000
38.000
36.000
34.000
32.000
30.000
28.000
26.000

OFFSET AFFO MOTORE (mn: 3.00

posizioni YAW: 6
36.0
45.0
54.0
63.0
90.0
0.0

Statore atteso: 2.000
EWG atteso: -2.000

posizioni Stat: 18
18.000
19.000
20.000
21.000
22.000
23.000
24.000
25.000
26.000
27.000
28.000
29.000

Posizione assoluta YAW dopo ciclo acq.: 0.000

output string: F:\UTENTI\BANCOHS\ewg-NEW\

Figure 5.8: Labview grid import section

This step could have slight differences among different probes.

5.3.5 EWG system setup

This step is required whenever the test features the injection of a disturb upstream of the stage. However when the test is focused on the only effect of a swirled flow without any thermal disturbance the steps described below are not performed and the test can be consequently started.

In order to obtain any kind of disturb it is required to interact with an external air feeding system. In case of thermal disturb the feeding system is coupled even with a system of thermal resistances.

In order to pressurize the system for delivery of the aerodynamic disturb it is necessary to activate two different key operated switches from an external panel, Fig. 5.9.

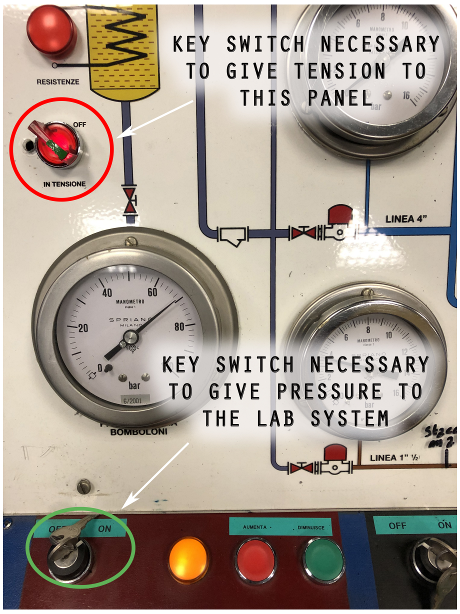

Figure 5.9: Key-switches for pressurization system

After the two switches have been activated a system of external pressurized air, stored in vessels at about 80 *bar*, is connected to a system of pipes internal to the laboratory.

It is necessary at this point to act upon a part of this system to deliver the pressurized air to the High Speed Test Rig: in order to do so the two valves in Figs. 5.10a and 5.10b should be moved. It have to be taken into account that sudden variations in pressure along the pipes could be dangerous, hence the valves must be slowly opened and slowly closed.

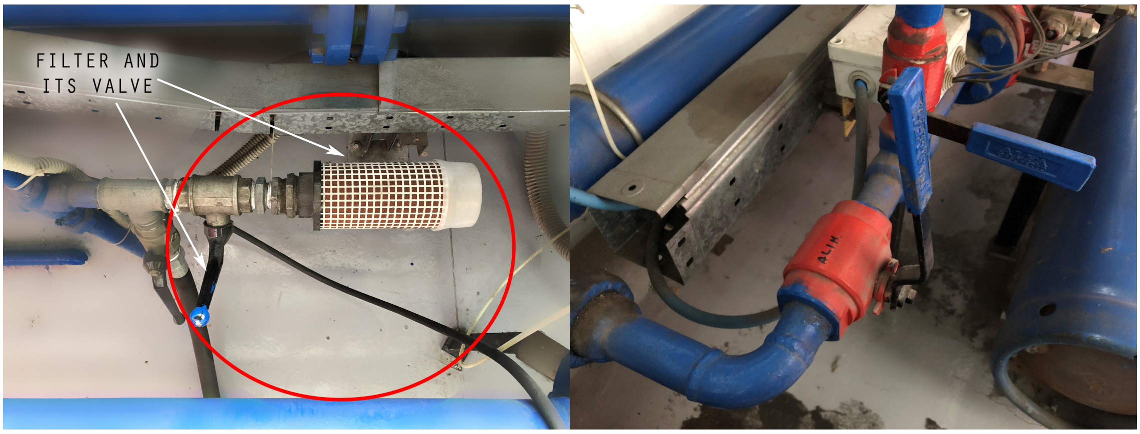

(a) Filter and its valve.

(b) Main valve.

Figure 5.10: Valves on the pressurization system

The internal circuit maximum air pressure can be controlled thanks to two buttons on the same panel used for the key-switches, Fig. 5.11.

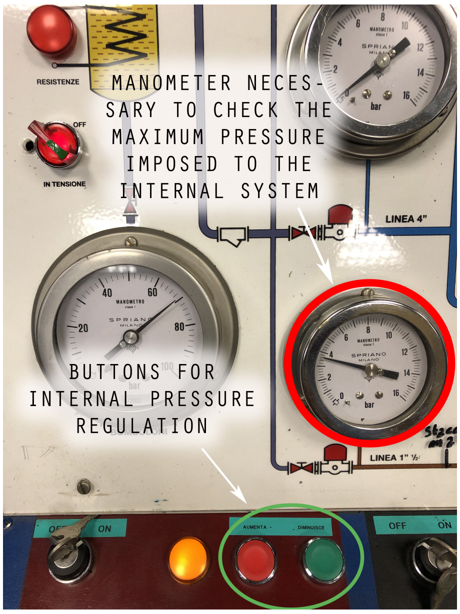

Figure 5.11: Pressure control buttons

Once the pressurization system is ready, the pressure value at the stage entrance (feeding pressure) can be corrected thanks to another kind of valve positioned near the test bench, Fig. 5.12.

Figure 5.12: Compressed air valve at test bench

However the system mounted on the machine casing features two different possible air path for delivery, extensively described in Section 3.1.1. As a result, if the disturb needs to be pulsated, it is necessary to activate from the Labview software the set of valves, Fig. 5.13, and to close the bypass branch. Instead if the disturb needs to be continuous the bypass branch of the valve set have to be opened and the set of pulsating valves deactivated.

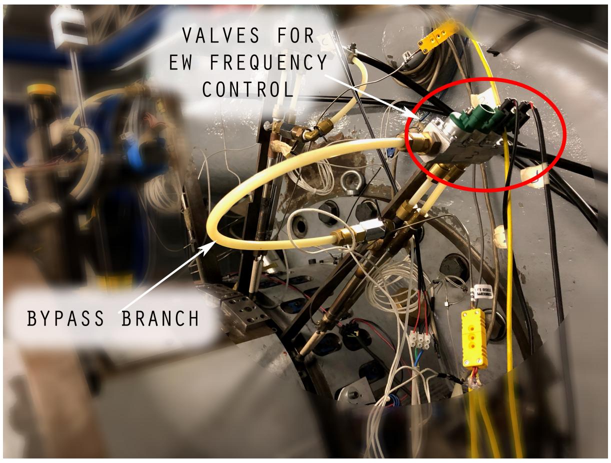

Figure 5.13: Valves on delivery system and Labview button

The relative value of pressure, referred to the turbine inlet pressure detected by the system, can be observed from the Labview software, Fig. 5.14.

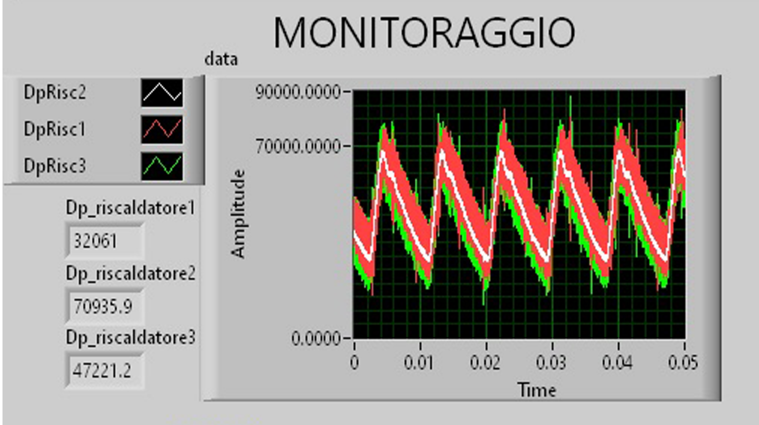

Dp_riscaldatore1
32061
Dp_riscaldatore2
70935.9
Dp_riscaldatore3
47221.2

Figure 5.14: Relative pressure trend from Labview

As a general rule, the compressed air valve at the test bench, Fig. 5.12, should never be opened when the valves, Fig. 5.13, are deactivated and the bypass branch is close at the same time. This is done to avoid any damage at the system for air delivery. The air delivery path needs to be set up in such a way that the flow of compressed air gets constantly or periodically heated up by getting in contact with a heat source, in this case an electrical resistance, Fig. 5.15.

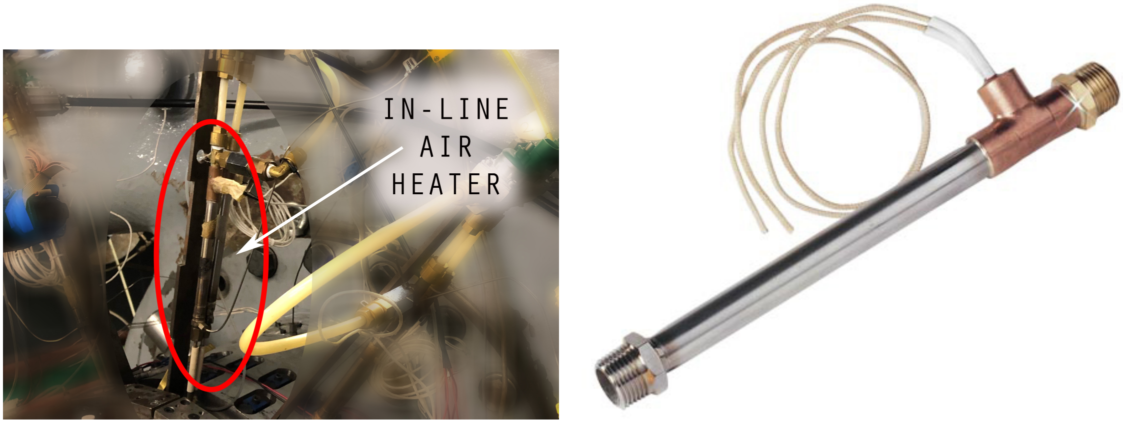

Figure 5.15: In-line air heater

This resistance need to be controlled by an external system featured at the test bench. A very important constrain to keep in mind is that the electrical resistance, in absence of an air flow, would burn off. As a result, the resistance can be activated only when the compressed air is already flowing. The procedure to activate the resistance is the following:

- Give current to the resistance circuit thanks to a physical switch, Fig. 5.16a.
- Activate resistance from the Labview software, Fig. 5.16b.
- Increase the set point temperature thanks to a physical interface, Fig. 5.16a.
- The pressure of the flow in contact with the resistances is constantly monitored by transducers; if the difference between this pressure and the one detected upstream of the turbine is lower than zero, Labview control system would prevent the power to be supplied supply to the resistances.

Once the temperature has reached its steady state value, it is necessary to check out again from the Labview software the value of the relative pressure. As a result of the heat introduction the previously checked relative pressure value have necessarily changed. Finally after having adjusted the injection relative pressure to the desired value the test can start.

5.3.5.1 EWG parameters for current experimental campaign

Labview user interface allows to set different parameters: the valves frequency corresponding to the EW fluctuation frequency and the valves duty cycle. Given the total period to complete a cycle of cold-hot injection, it is possible to define the amount of this period dedicated to hot injection as well as the one dedicated to the cold injection. Those two fractions of period are specified in the duty cycle field in Table 5.6.

The first of the two numbers refers to the hot period, while the second refers to the cold period. Cold injection time lasts more than the hot one.

Δp = maximum difference between feeding pressure and pressure upstream of the stator inlet

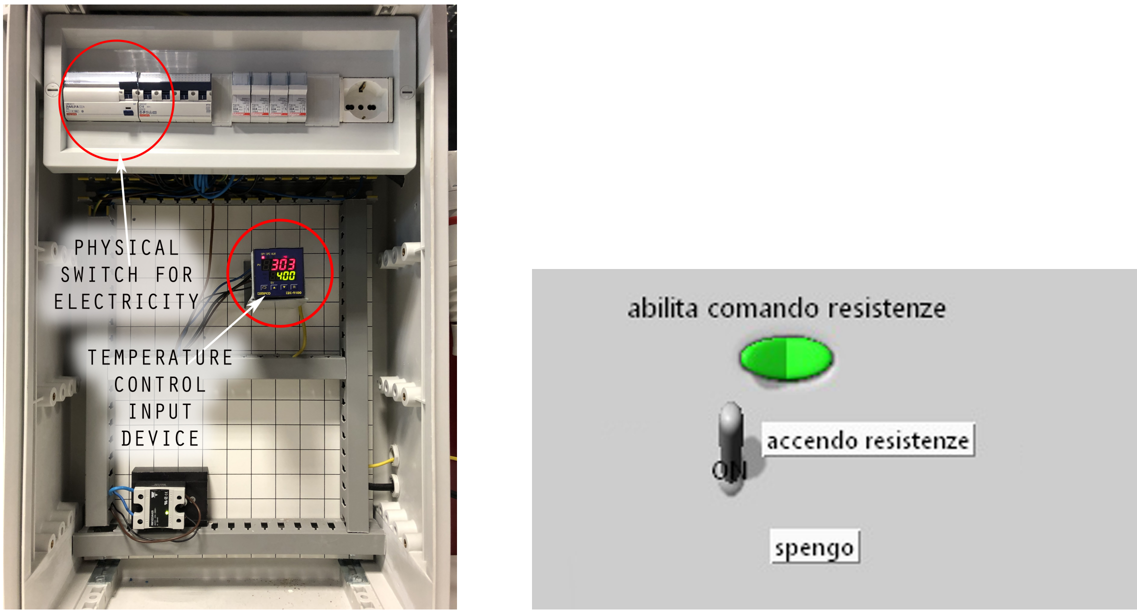

(a) (b)

Figure 5.16: Panel for resistance control

Table 5.6: Plant operating conditions

	OP3		**OP2**	
	Duty-cycle	Δp [bar]	Duty-cycle	Δp [bar]
EW $10Hz$	40-60	1.2	40-60	1.5
EW $100Hz$	35-65	0.7	35-65	0.9
HS	-	0.7	-	0.9

Chapter 6

Stator inlet measurements

In this section the measurement results obtained during the experimental campaign are reported for the stator inlet section. Since a crucial point of the analysis carried out is the comparison among results obtained in different plant operating conditions, also measurements obtained during previous experimental campaign are here reported [15].
As a result, since the knowledge of the injector behavior and its effects on the inlet flow are fundamental for the the whole stage study understanding the first step that has been carried out, is the research of the injector operating condition. Applying those conditions OP2 flow field displays similar effects as the ones observed in OP3, during previous experimental campaigns. The schemes representing the measuring points coordinates inside the inlet annulus section are called "Grids" and for stator inlet they are reported in Figs. 6.1a and 6.1b.

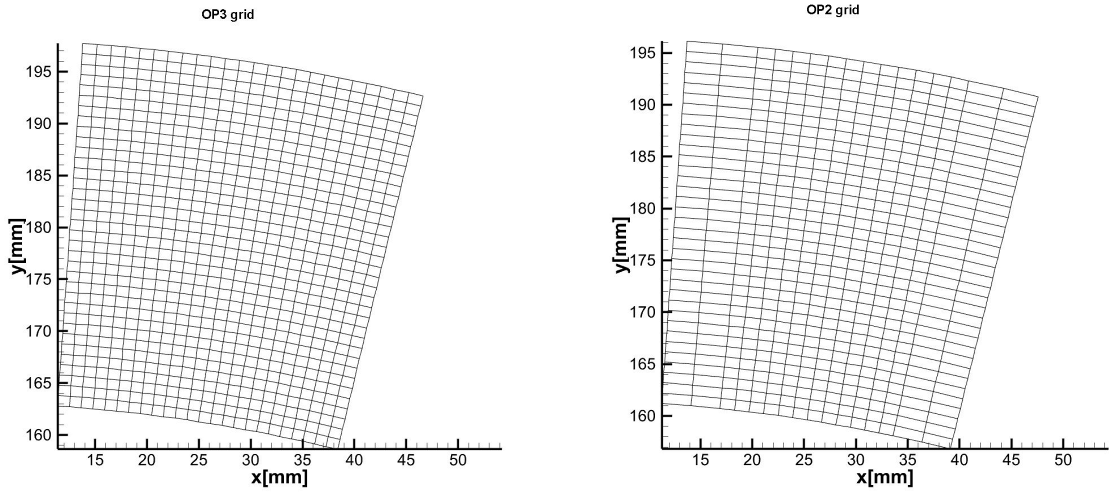

(a) (b)

Figure 6.1: a. Measuring grid for OP3 stator inlet, b. Measuring grid for OP2 stator inlet

As it can be observed there are some differences in the measuring points locations among grids. From those differences some problems could arise in the comparison between different operating conditions; problems of this kind have been solved thanks to interpolations. Interpolation of data on grids different from the acquisition one is discussed in Section 7.1.

In general this chapter gathers all the pressure and temperature fields of interests together with some circumferential mass averaged values plotted against a dimensionless span, defined as:

$$Dimensionless\ span = \frac{R_m - R_{hub}}{h_{blade}}$$

R_m is the radius at which the measure is performed, R_{hub} is the radius of the machine hub and h_{blade} is the height of the blade. The two radii refer to the center of the machine annulus.

6.1 Procedure for circumferential mass average

In this section it is discussed the procedure used to obtain the circumferential averages weighted on mass starting from the values obtained at measuring points.

The averaging procedure is based on the association of a punctual value of mass flow rate to each measuring point. As a consequence it is necessary to have knowledge of local axial velocity v_a, local density ρ and a value representing an area associated to the measuring point A. In next paragraphs it is reported a procedure to derive those three quantities starting from the data of the probes.

6.1.1 Axial velocity and density

The calculation of axial velocity and density is possible via the knowledge of the local Mach number, correctly derived thanks to the 5-holes probe, and the knowledge of the local total temperature, which could be instead measured by the fast thermocouple. In case no heat is introduced in the flow and no work gets extracted too, the total temperature is considered to be equal, for each point, to the one measured upstream of the injector.

Some problems, related to errors in measurements, could arise using the thermocouples but this topic will be discussed in Section 7.2, where possible corrections identified by the Authors are exposed. Given that the working fluid is air the following values can be assumed:

$$R_{air} = 287\frac{J}{kgK}$$

$$\gamma_{air} = 1.4$$

The procedure for axial velocity calculation follows these steps: at first it is computed the static local temperature value, from the knowledge of total local temperature and local Mach number.

$$T_{static} = \frac{T_{total}}{1 + \frac{\gamma_{air}-1}{2}M^2} \tag{6.1}$$

Thanks to the knowledge of the static temperature it is possible to calculate the local density and the local speed of sound for air.

$$\rho = \frac{p_{static}}{R_{gas}T_{static}} \tag{6.2}$$

$$a_s = speed\,of\,sound = \sqrt{\gamma_{air}R_{air}T_{static}} \tag{6.3}$$

Given the local speed of sound it is possible, via the local Mach number, to compute the absolute value of the velocity.

$$v = local\,velocity = Ma_s \tag{6.4}$$

Since the flow angles, referenced to the machine axis are known, as explained in Section 4.3, it is possible to compute the axial component of the local velocity.

$$v_a = v\,cos(\beta)cos(\alpha) \tag{6.5}$$

Once both ρ and v_a are known the only left component for the mass flow rate is the associated area A.

6.1.2 Point associated area

The calculation of the associated area comes from geometrical considerations on the grids. In particular each point of the grid have to be associated to an area based even on the spacing between it and its neighboring points. The wider the gap, the larger the area. In this passage it is introduced an error due to interpolation since the values obtained at a single point, from measurement, are assumed to be uniform throughout the associated area. The reasoning behind the area calculation is here reported and a representation of the an example of area is shown in Fig. 6.2.

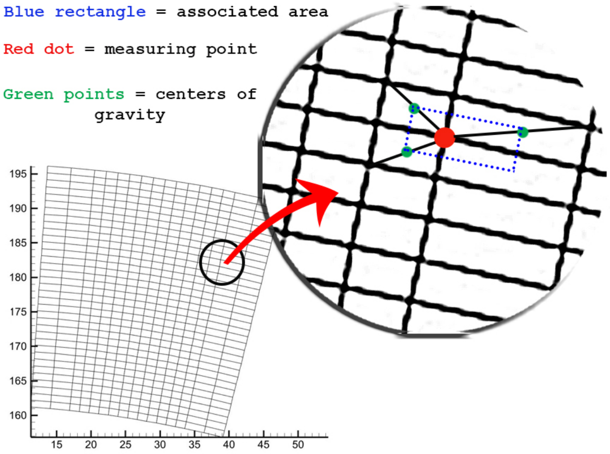

Figure 6.2: Scheme representing the area associated to a single point, Blue rectangle

The whole procedure is based on the computation of the coordinates of the geometrical centers of gravity for the cells surrounding the point of measure considered.

The calculation of the centers of gravity for the surrounding cells is carried out by considering the coordinates associated with the middle point of the cells diagonals. Once those coordinates are known, it is possible to compute the distances among the centers of gravity and hence the area of a rectangle surrounding the point of measure. This approach ensures continuity among the different areas of different cells, hence compatibility. However this approach could be even improved by considering annular sectors instead of rectangles, but for the case studied by the Authors no differences in results are observable. In the end it is possible to evaluate the punctual values of mass flow rate for each measuring location in grid:

$$\dot{m} = \rho v_a A \tag{6.6}$$

6.1.3 Circumferential average procedure

Once the mass flow rate is known for each point of the grid it is possible to carry out a circumferential average, weighted on mass. This means that, for a given radial coordinate, the measured values are all, at first, multiplied by the associated local mass flow rate, and then summed with each other. The obtained value is then divided by the summation of all the punctual associated mass flow rate values calculated for the corresponding radial coordinate. Considering the two indexes i and j, with $i = radial\,coordinate$ and $j = angular\,coordinate$ the procedure can be represented as:

$$\bar{K}(\tilde{i}) = \frac{\sum_{j=1}^{n} K(\tilde{i},j)\dot{m}(\tilde{i},j)}{\sum_{j=1}^{n} \dot{m}(\tilde{i},j)} \tag{6.7}$$

$\tilde{i}$ is a given radial position, $K(i,j)$ is the punctual value of an extensive measured value, $\dot{m}(i,j)$ is the punctual value of mass flow rate, $\bar{K}(\tilde{i})$ is the circumferential mass average of the extensive quantity at a given radial position. The angular coordinate j in Equation (6.7) is considered to vary from 1 to n.

This procedure is repeated for each radial coordinate and the trend of circumferential averages in radial direction can be then observed.

For intensive values, such as static pressure p_{static}, the circumferential average is computed based on area weight, as a result the Equation (6.7) would be simply modified and instead of $\dot{m}(i,j)$ it would present $A(i,j)$, which is the punctual value for the associated area.

6.2 OP3

Here are reported the results obtained at stator inlet for the three different injection conditions of interest, EW at $10Hz$, EW at $100Hz$ and HS.
Those measurements have been performed during previous experimental campaigns. By the way any data analysis carried out on those measures have been fully revisited and upgraded by the Authors. During $10Hz$ EW conditions, it has been imposed to the injected flow a pressure of $1.2bar$ above the main stream one, and a duty cycle of $40-60$. During $100Hz$ EW conditions, it has been imposed to the injected flow a pressure of $0.7bar$ above the undisturbed flow one and a duty cycle of $35-65$. Those values have been decided during past experimental campaigns focused more on swirling entropy waves generations by EWG (see [16]). In particular pressure values have been chosen as a trade off between injected flow penetration effect and total pressure losses [16]. For what concerns the duty cycle, the set values come from considerations on the hot flow behavior during injection. As a matter of fact, the hot flow withstands an acceleration compared to the cold one due to its lower density, hence it would tend to approach the previously injected cold stream and mix with it. Then the cold injection period is set longer than the hot one in order to guarantee a well balanced temperature oscillation of the injected entropy wave.
During HS condition the relative pressure of injection is the same used in the case of $100Hz$ EW and clearly no duty cycle is present.
In the following figures it is presented the total temperature field and the total pressure field downstream of the injector.
All fields presented in those figures refer to what an observer would see when placed downstream of the injector at measuring plane and facing the injector itself. Flow angles reported in circumferential averages follow instead the convention reported in Fig. 6.3.

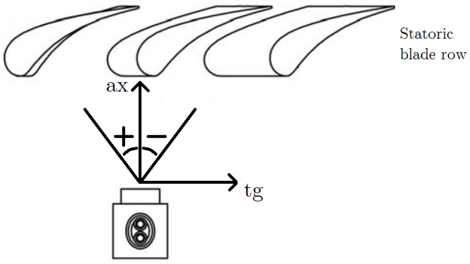

Figure 6.3: Stator inlet flow angle sign convention

6.2.1 Thermal field

In Fig. 6.4 it can be observed the temperature average field obtained thanks to the thermocouple. All the three injector working condition are reported. Actually by looking at the mean values of temperature no particular observation can be done on the nature of the pulsated thermal disturb.
However it is glaring that in each one of the reported fields the regions which result

affected by an average temperature increase, compared to the undisturbed flow, are slightly shifted radially with respect to the injector outlet location.
In fact the injector outlet is located at a radial position corresponding to the blade midspan while the average temperature field highlights a core of high temperature at a slightly higher radial position. This shift is considered to be caused by the way in which the hot flow interacts with the blades in the terminal part of the injector.

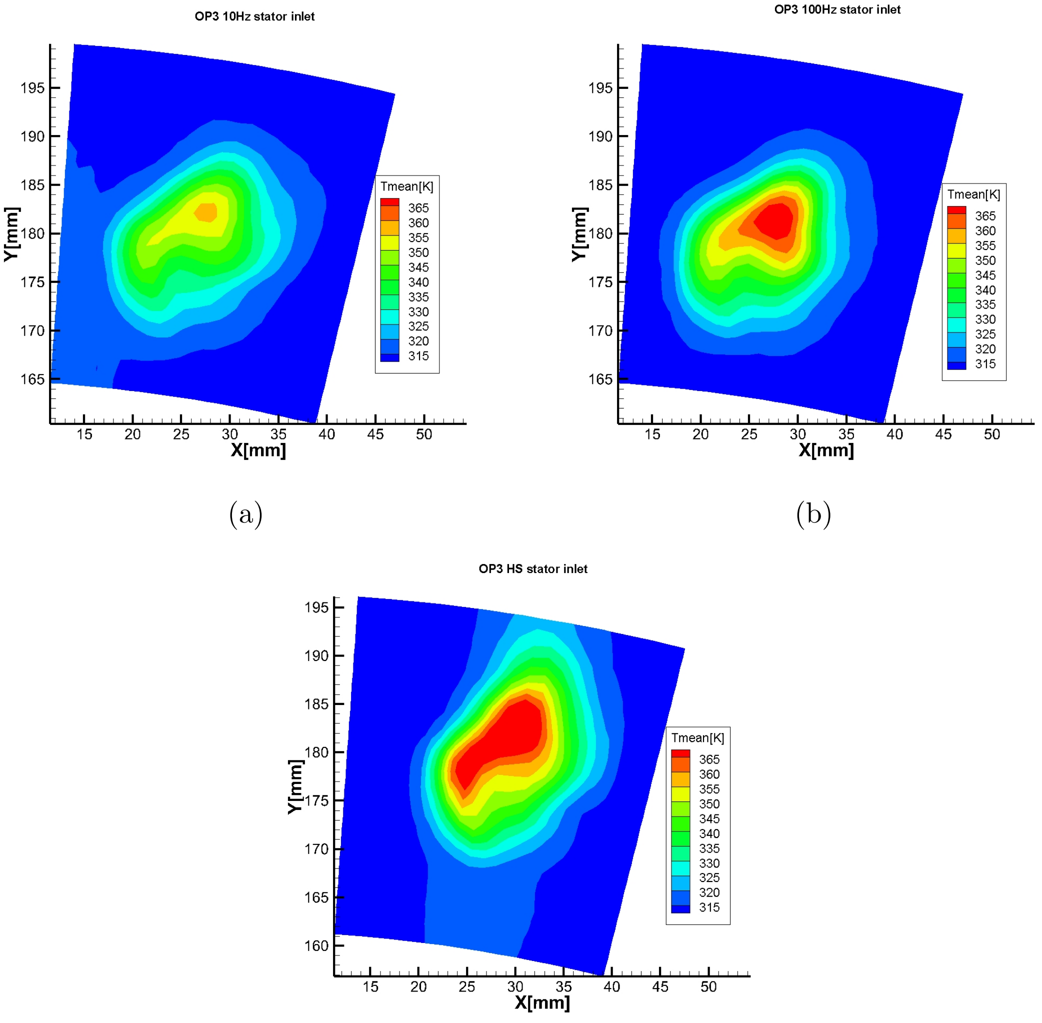

(a) (b)

(c)

Figure 6.4: Average temperature fields in OP3 10Hz (a), 100Hz (b) and HS (c) downstream of the injector

In the case of entropy waves, to understand where the pulsating disturb has migrated it is convenient to look at the difference in temperature perceived in time at a given location during acquisition. A step necessary to perform this difference is the phase averaging of the detected signal based on the frequency of the injected disturb. From the averaged signal it is then possible to perform a difference between the highest averaged temperature registered at a certain point and the lowest registered at the same point. By observing this quantity, labeled as $T_{peak-peak}$, it can be found the

location of maximum pulsation together with its intensity.
Fig. 6.5 reports the $T_{peak-peak}$ fields for the two entropy waves frequency cases. From those two fields it is possible to notice that even the pulsation, together with the average field undergoes a outward shift in radial direction with respect to the injector outlet position.
Another important fact, highlighted by the figure reporting the $T_{peak-peak}$ field, is the huge difference in magnitude that is observable between the two different cases. This is supposedly due to the fact that the mixing among cold and hot injected flows at a frequency of $100Hz$ happens in a narrow region inside the injector and close to its outlet; moreover even inside the injector itself the heat exchange by conduction covers a relevant role.

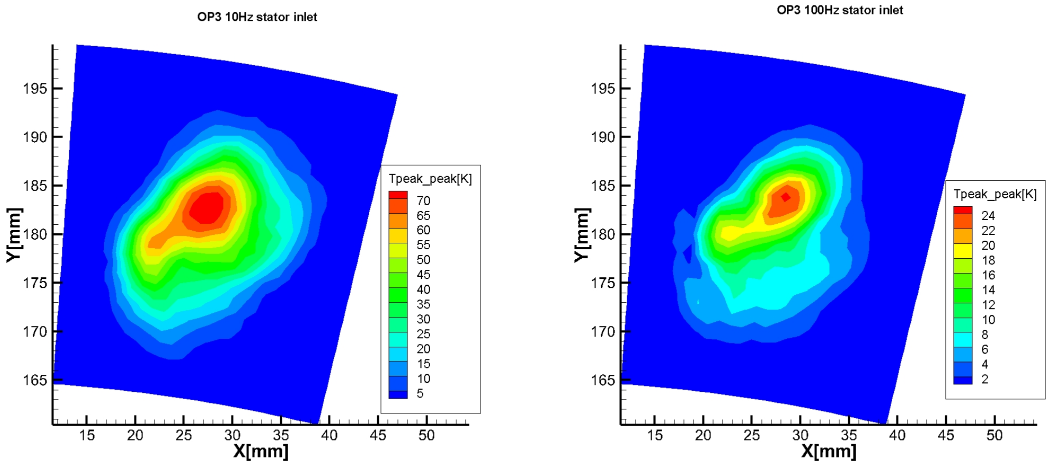

(a) (b)

Figure 6.5: $T_{peak-peak}$ fields in OP3 $10Hz$ (a), $100Hz$ (b) downstream of the injector

Another way to easily look at the position and intensity of the disturb is by looking the circumferential averages of the observed fields. In fact in Fig. 6.6, it can be observed that in case of hot streak the thermal disturb is found at about 70% of the blade-span.

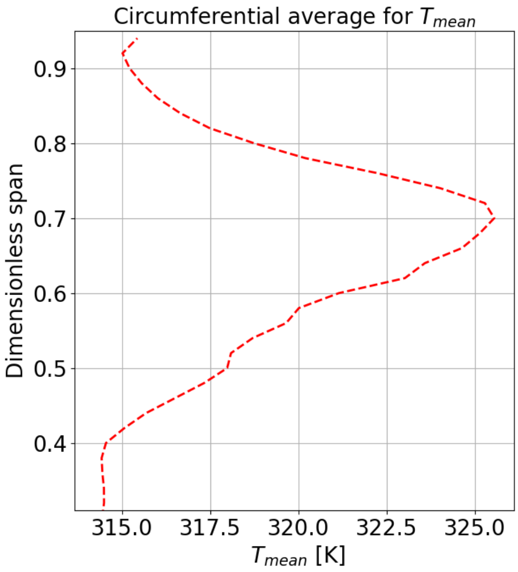

Figure 6.6: Circumferential average weighted on mass flow of the α angle and of the average temperature downstream of the injector in case of HS

Instead in Fig. 6.7 it can be observed that in case of entropy waves the disturb is detected at about 65% of the blade-span for both cases. In addition it can be observed how the disturb results much more intense in the $10Hz$ case compared to the $100Hz$ one.

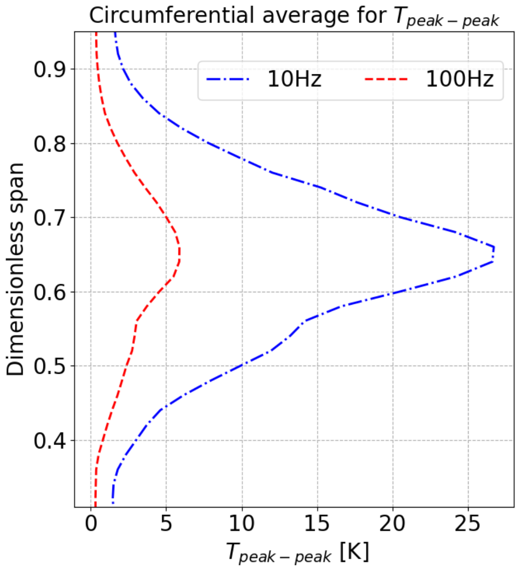

Figure 6.7: Circumferential average weighted on mass flow of the α angle and of $T_{peak-peak}$ downstream of the injector in case of EW

A clear conclusion derived from those data just presented is that the thermal disturb, both in the case of EW and HS, enters the stator at a radial position different from the one of the injection, hence where the swirler is located.

6.2.2 Aerodynamic fields

In Fig. 6.8 it can be observed the pressure average fields registered by the 5-hole probe for each measuring point. The reported fields feature streamtraces to highlight the behavior of in measuring plane velocity. These local values of velocity are extracted thanks to both the data from the 5-hole and the data from the thermocouple. All the three injector working conditions are reported.

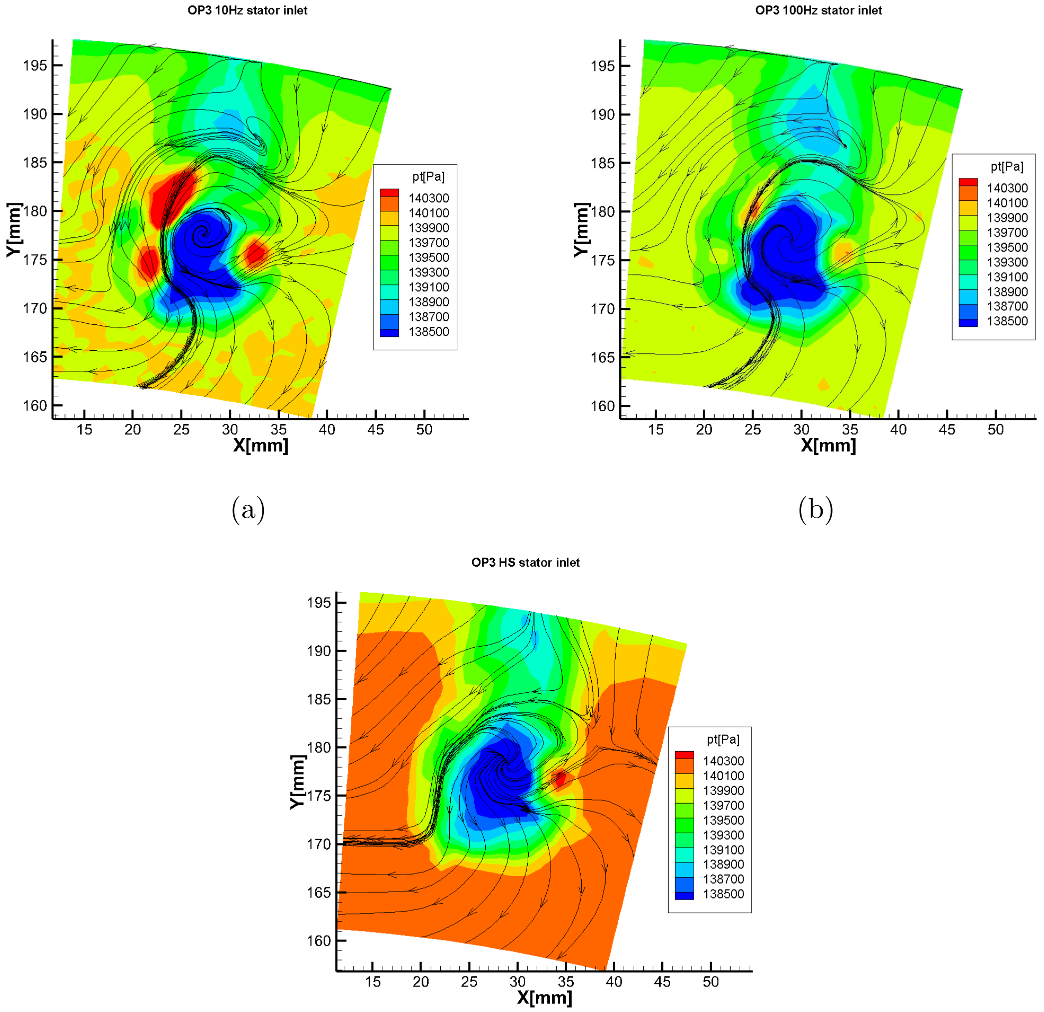

(a)

(b)

(c)

Figure 6.8: Pressure fields and streamtraces of in plane velocity in OP3 $10Hz$ (a), $100Hz$ (b) and HS (c) downstream of the injector

By looking at the pressure values comparison some similarities among the three different cases can be observed. By way of example only one of the three fields is here analyzed to highlights those similar regions, Fig. 6.9.

The regions of lower pressure, associated with a higher introduction of losses, coincides with: the boundary layer region near the machine case, the injector stem wake region which introduces additional losses, and the losses associated to the vortical structure introduced by the swirler of the injector. The vortex core, highlighted even by the shape of the streamtraces, represents the region with higher losses, hence higher irreversibility.

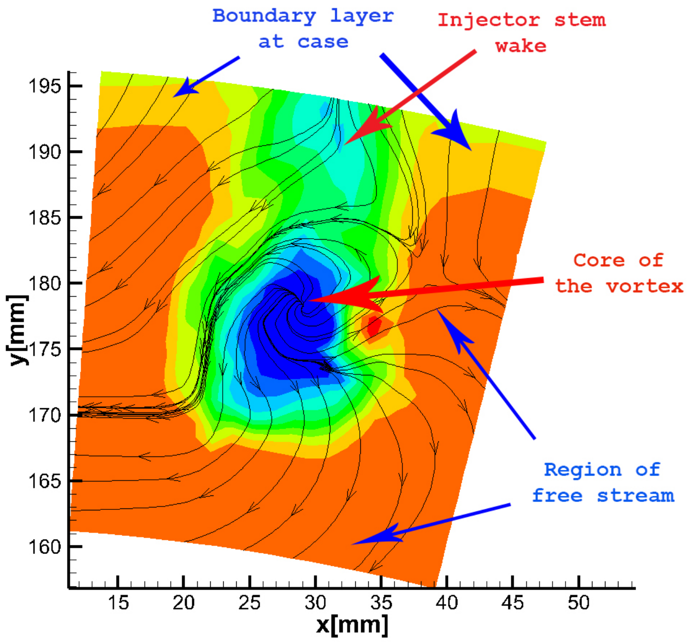

Figure 6.9: HS pressure field downstream of the injector

The position of the higher aerodynamic disturb is then assumed to be the vortex core, which in case of HS is located at about 62% of blade-span, while for both the entropy wave conditions it is located at about 60% of blade-span. Fig. 6.10 reports the circumferential mass averages of the absolute flow angle for the three conditions here considered.

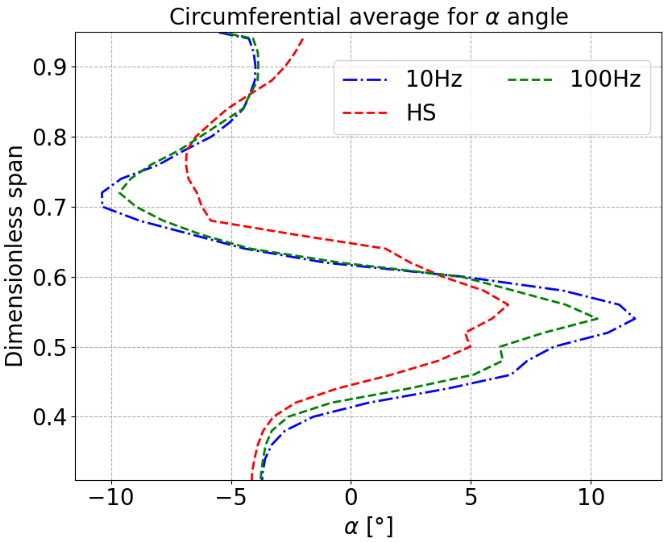

Figure 6.10: Stator inlet α angles in different EWG working conditions

6.3 OP2

The operating conditions for OP2 have been chosen on the basis of a morphological comparison with the OP3 temperature fields. Both measurements and analysis on data in OP2 have been performed by the Authors. Three different injection operating conditions have been considered for OP2. The effects on temperature fields of the three injector conditions for HS can be observed in Fig. 6.11.
During $10Hz$ EW conditions, it has been imposed to the injected flow a pressure of $1.5bar$ above the main flow one, and a duty cycle of $40-60$.
During $100Hz$ EW conditions, it has been imposed to the injected flow a pressure of $0.9bar$ above the main flow one and a duty cycle of $35-65$.
During HS condition the relative pressure of injection is the same used in the case of $100Hz$ EW and clearly no duty cycle is present.

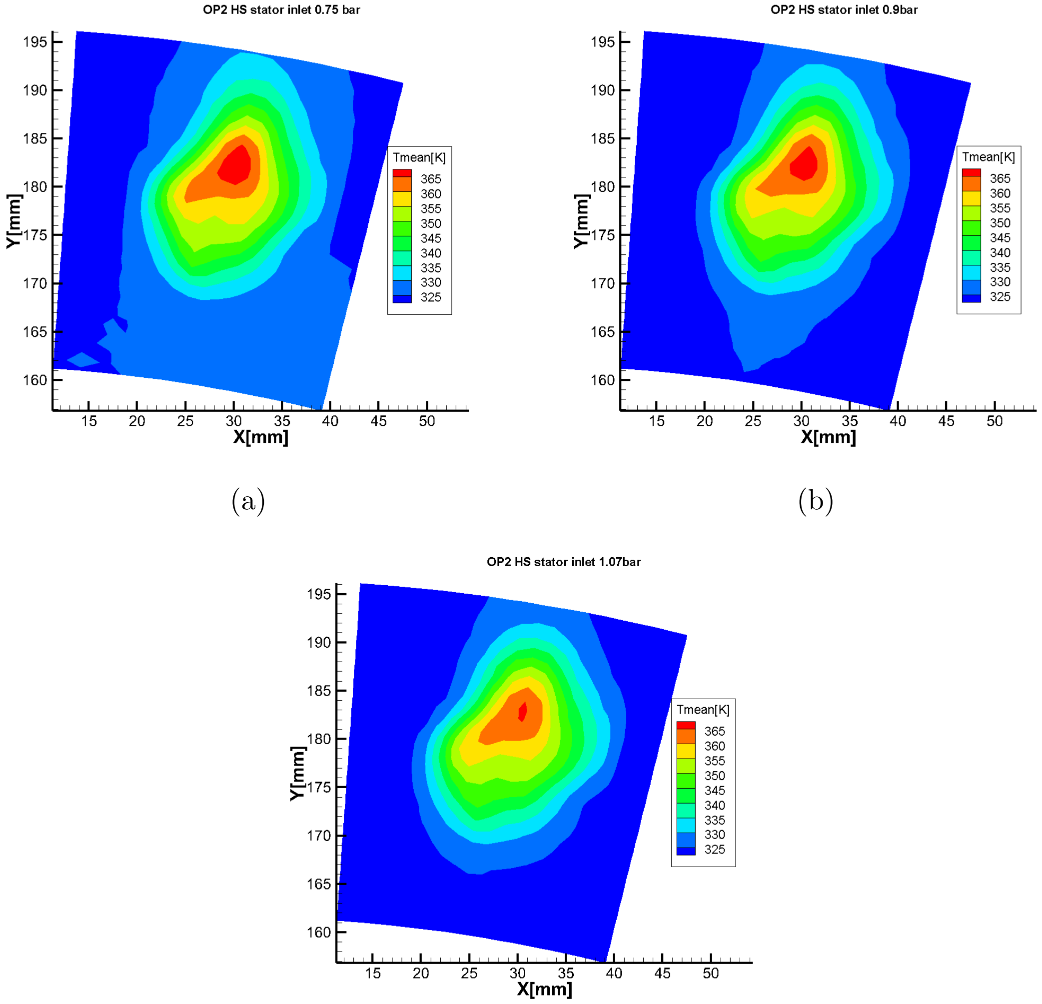

(a)

(b)

(c)

Figure 6.11: Temperature fields for HS downstream of the injector in three different injection conditions: $0.75bar_r$ (a), $0.9bar_r$ (b), $1.07bar_r$ (c)

The chosen operative condition among the three is the one with $0.9bar_r$ of injection pressure.

While the HS case is here reported, for entropy waves a simple scaling factor based on the turbine expansion ratio has been applied to the injection pressure. Anyway starting from the figures above, it is possible to notice how the OP2 average temperature field presents always a smaller region at high temperature compared to OP3, even if the first one has a free stream temperature which is about $10°C$ higher. In addition the maximum value found in the T_{mean} field is higher for OP3 than for OP2. This effect is the direct consequence of the change in working conditions of the EWG. EWG gives the same amount of power both in OP3 and OP2, but OP2 case presents higher pressure and hence higher density. As a result OP2 feels a lower average heating effect. This sort of inversion of temperature can be easily seen by the field obtained by performing a punctual difference among the T_{mean} field in OP3 and the T_{mean} field in OP2, Fig. 6.12.

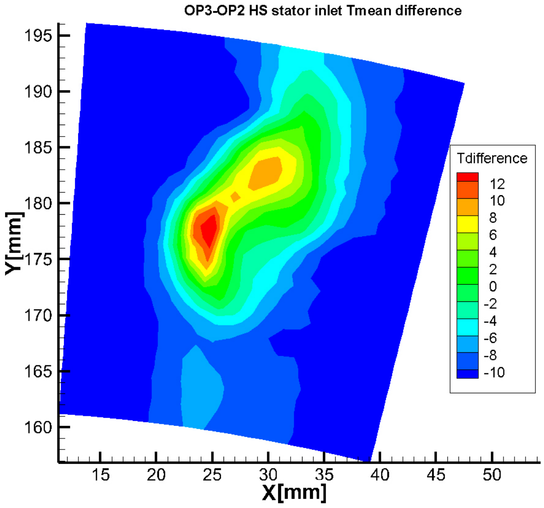

Figure 6.12: T_{mean} difference between OP3 HS and chosen OP2 HS condition

6.3.1 Thermal field

Fig. 6.13 reports the temperature average fields obtained by measurement in OP2. Even in this case all the three injector working conditions are present.

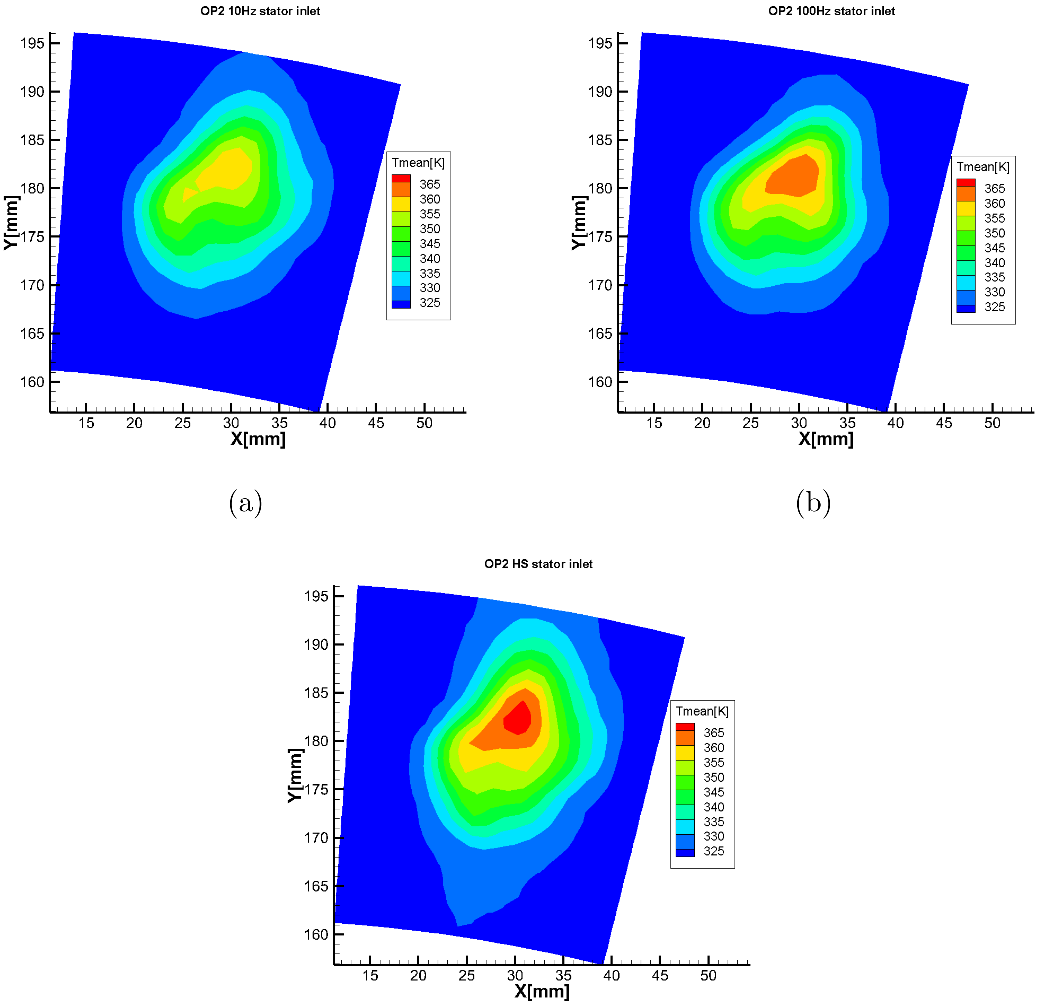

(a) (b)

(c)

Figure 6.13: Average temperature fields in OP2 $10Hz$ (a), $100Hz$ (b) and HS (c) downstream of the injector

Even for OP2 it is convenient to look at circumferential averages, Figs. 6.15 and 6.16, in order to understand the radial position of the thermal disturb, which from the figure above clearly seems once again shifted with respect to the midspan injection position.

Plus, as it happened in OP3, the average temperature increases passing from $10Hz$ to $100Hz$ and to HS. For completeness here in Fig. 6.14 are reported the fields for $10Hz$ and $100Hz$ of $T_{peak-peak}$.

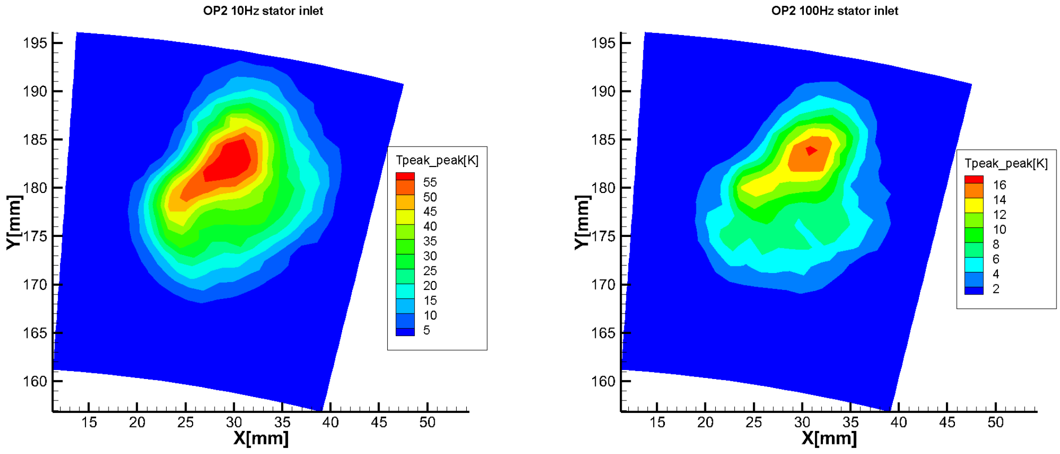

(a) (b)

Figure 6.14: $T_{peak-peak}$ fields in OP2 $10Hz$ (a), $100Hz$ (b) downstream of the injector

Fig. 6.15 shows the circumferential average for both EW conditions based on the $T_{peak-peak}$ field, while Fig. 6.16, shows the circumferential average for HS condition based on the T_{mean} field.
Once again it can be stated that, the EW thermal disturb migrates at about 65% of blade-span in both $10Hz$ and $100Hz$ cases. Even the thermal disturb introduced by HS migrates once again at about 70% of blade-span.

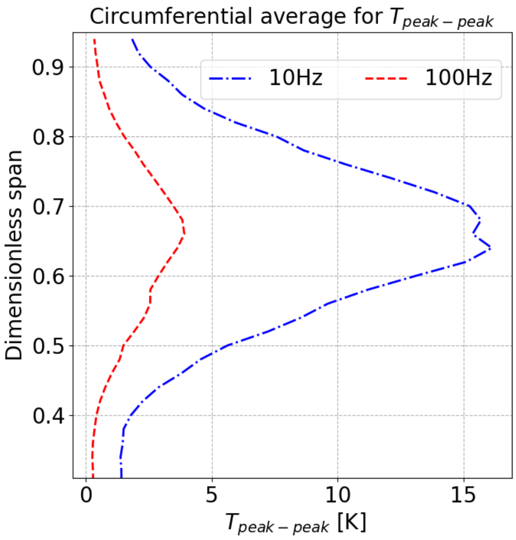

Figure 6.15: Circumferential average weighted on mass flow of the α angle and of $T_{peak-peak}$ downstream of the injector in case of EW

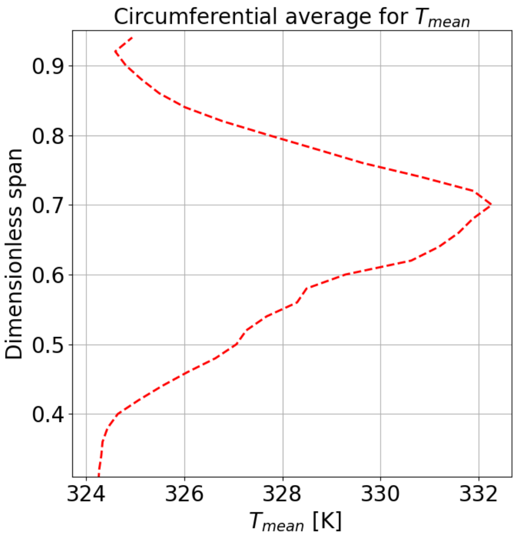

Figure 6.16: Circumferential average weighted on mass flow of the α angle and of T_{mean} downstream of the injector in case of HS

6.3.2 Aerodynamic fields

Here are reported the measurements obtained in OP2 for what concerns the aerodynamic disturb. Hence, the injected swirling structure can be observed in Fig. 6.17 together with the total pressure fields, for the four considered injection conditions, EW, HS and the condition of aerodynamic disturb only (No-injection). Those maps downstream of the injector have been obtained with the same procedure used for OP3.

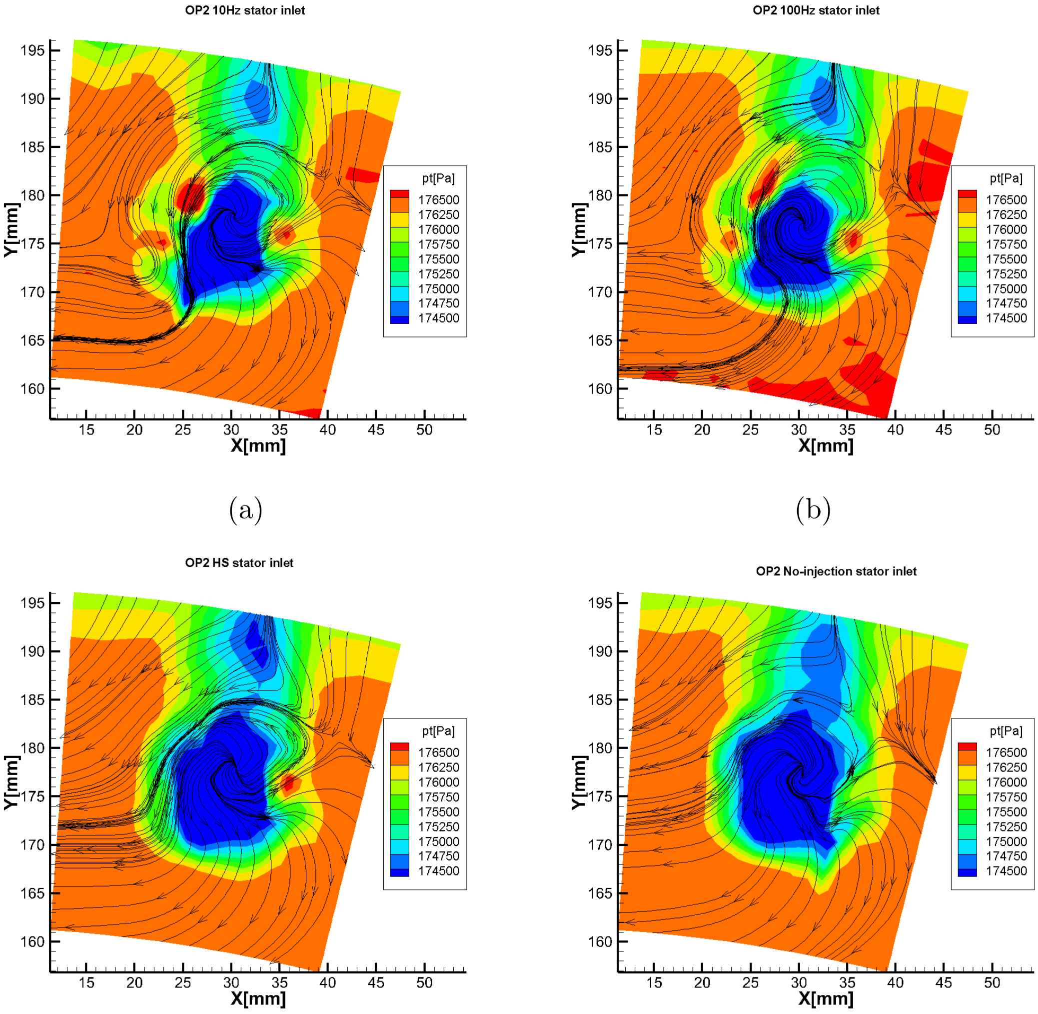

(a) (b)

(c) (d)

Figure 6.17: Total pressure fields in OP2 10Hz (a), 100Hz (b), HS (c) and noinj (d) downstream of the injector

For all the four cases the center of the swirling structure is found at about 61% on blade-span. Even in this case the swirling structure in HS is the one with the higher radial shift. Also in OP2 all the fields present the same macro-regions of losses highlighted during the analysis of OP3 data: boundary layer at case, injector stem wake and core of the vortex. The fact that similarities among 10Hz and 100Hz exist, leads one to think that even the flow throughout the stage would show analogous patterns. Moreover this is even suggested by the absolute flow angle circumferential averages.

Fig. 6.18 reports the circumferential mass averages for the absolute flow angle in all the four considered conditions.

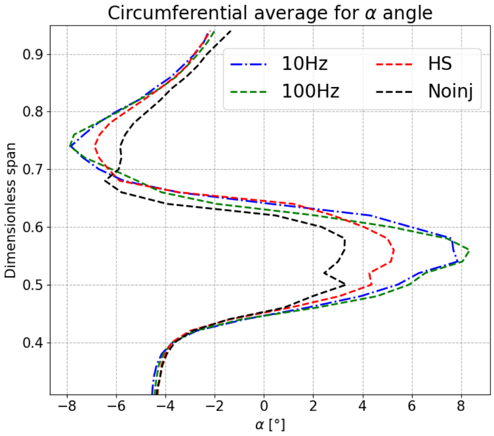

Figure 6.18: Circumferential average weighted on mass flow of the absolute flow angle for all the cases in OP2

In both OP3 and OP2 it can be seen that the absolute values of the circumferential average of α angle result to cover a narrower range in HS cases than in both the EW cases. In addition EW values present α trends very similar among the two cases of $10Hz$ and $100Hz$ for both operative conditions OP2 and OP3.

A valid motivation for this could be found in the functioning principle of the EWG injector itself. In fact during the HS cases only one of the two air delivery channels is used, while the EW cases features the usage of both the channels available for air delivery, Fig. 6.19.

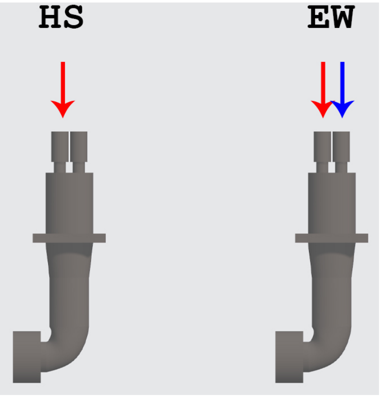

Figure 6.19: Scheme that represents the two working different injector flows: left HS, right EW

As a result, this difference causes a change in air behavior while flowing through the very last part of the injector. In turn air withstand a better swirling action by the blades of the injector in EW than in HS, implying a weaker action on the flow deflection and hence α. To fully isolate the effect given by the injector swirler on the main flow, measurements have been carried out even for the no-injection case. No-injection case highlights a further reduction in terms of α angles, compared to the HS case, when the injector is not supplied with air at all. This is shown in Fig. 6.16. It can be observed that No-injection case has a strong reduction of the range covered by the positive angles, while the negative angles range stays about the same as the one in HS. This fact suggests a non symmetrical behavior of the injector even in No-injection case. This behavior is considered valid even in OP3.

6.4 Unsteady thermal field

In this section it is presented a scheme, derived from the phase averaging of the obtained temperature data based on the frequency of injection. This is useful to qualitatively understand how the temperature pulsation is perceived at the measuring plane. Fig. 6.20 reports different time instants based on phase averaging reconstructions carried out on the temperature data downstream of the injector.
As a result of phase averaging, it can be observed that during one period of injection the temperature follows a cycle of oscillation between a maximum value and a minimum value. This result coming from the measurements downstream of the injector confirms that the system works as expected. In addition, even if it cannot be observed directly from the figure below, the reconstructed disturb frequency follows closely the frequency imposed by the valves.

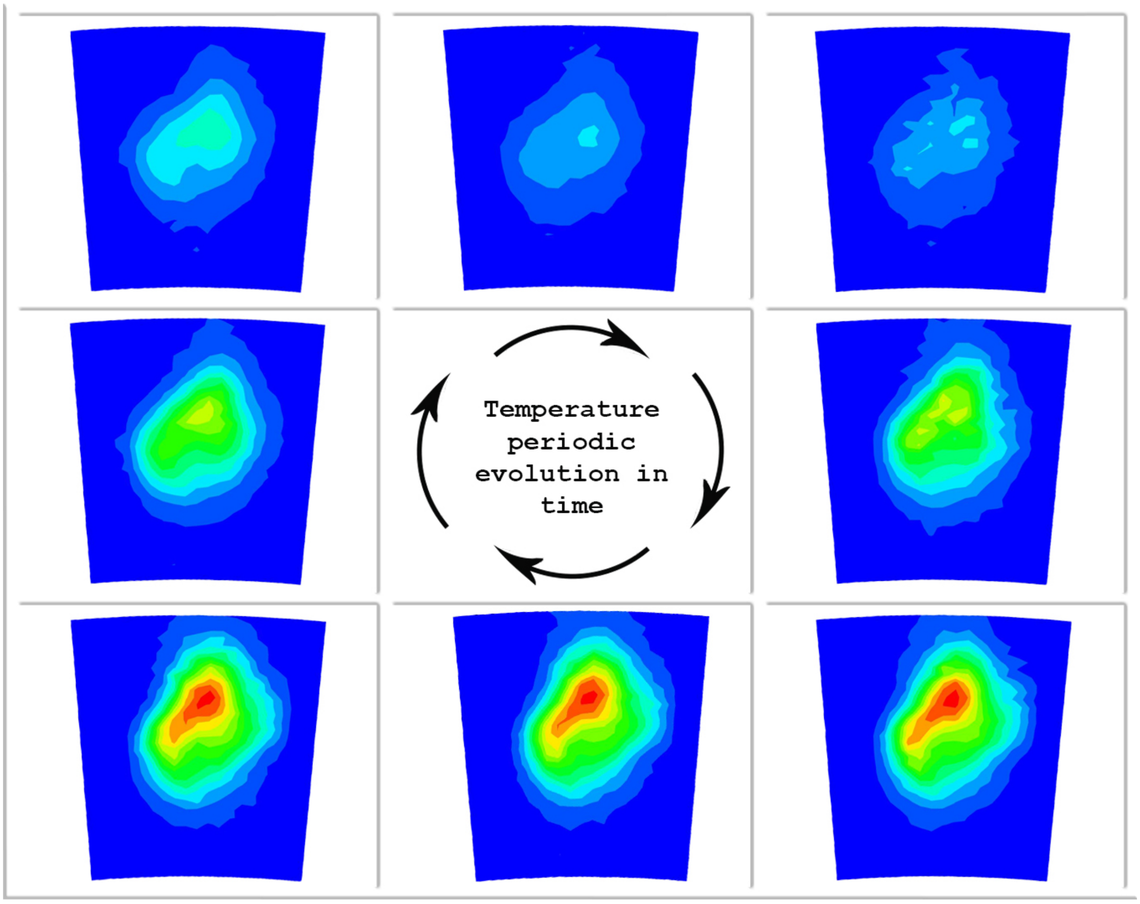

Figure 6.20: Representation of entropy waves oscillation from data collected at the measuring plane for EW 10Hz in OP2 condition

This kind of representation would have no meaning in case of HS, since no oscillation is imposed to the thermal disturb by the EWG.

Chapter 7

Stator outlet measurements

In this chapter, the results of the measurements carried out at stator outlet are discussed. First of all, a section is dedicated to the measurement grids (Fig. 7.1) of both thermocouple and five-holes pressure probe because some steps have to be done to make data from the first probe useful for data elaboration coming from the second one. Then the aerodynamic field in the tests called Clean is presented: this allows to have a clear idea about the magnitude and trend of the main flow quantities when there are no perturbations at stator inlet. This is fundamental for analyzing the effects of the swirled EWs injected upstream on the flow at stator exit. The last two parts of this chapter are focused on thermal and aerodynamic fields analysis respectively, in the two plant operating conditions.

Measurement results from thermocouple data elaboration aims to highlight how the temperature non-uniformities generated upstream by the EWG evolves through the stator. In particular, migration and attenuation of EW depending on injection frequency and position are discussed. In this way it is also possible to have an idea about which secondary flows it interacts with, by looking at its position at stator outlet. As it will be shown, the temperature perturbation is found mainly at the center of blade passage, which corresponds to the isentropic region in the Clean case.

Thanks to 5-holes pressure probe, the steady flow field exiting the stator is measured. The flow fields in Clean condition (no disturbances), Noinj condition (only swirl profile is injected), with EWG switched on (injection of temperature disturbance combined with swirl motion) and HS condition are compared with special attention to total pressure loss coefficient defined as:

$$Y = \frac{p_{t,u} - p_t}{p_t - p_s} \tag{7.1}$$

where $p_{t,u}$ is the average total pressure upstream the stator, p_t and p_s the total and static pressure measured by the probe.

Finally, the FRAPP allows to measure the time evolution of total, static pressure and flow angles. In fact, to achieve a more comprehensive investigation of the flow field downstream the stator, it becomes interesting to perform also an unsteady analysis since further unsteadiness is introduced by the upstream injected disturb. The time-dependent pressure signals coming from FRAPP are phase-averaged on the EWG valve period with the maximum injection pressure chosen as trigger. This procedure is necessary to isolate the frequency of the phenomenon of interest, i.e. the one of injected perturbation, and eliminate all other components with different frequency and noise. So the phase-averaged results allows to investigate the effects of time periodic injected disturbance on the unsteady flow field at rotor inlet. The phase-averaging is applied only to $10Hz$ case because it has been chosen as representative for EW injection condition. In fact in $100Hz$ case fluctuations of relevant quantities shows very low amplitude as demonstrated in [17]. During test campaign, FRAPP has been mounted at stator outlet measuring section only for tests OP2 $10Hz$ LE and OP2 $10Hz$ MP because the results in plant condition OP3 for same injection frequency and positions have been already discussed in [17].

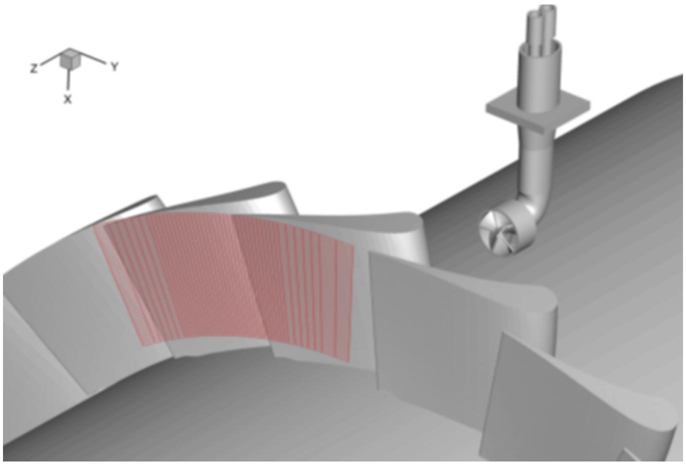

Figure 7.1: Example of measuring grid downstream the stator

7.1 Acquisition points grids

Tests performed with different probes and for different clocking positions lead to discrepancies among acquisition grids coordinates points. Anyway the whole set of measuring grids is located on the same radial-tangential plane downstream of the statoric row.

7.1.1 Differences among MP, LE and Clean for the same probe

The first difference analyzed is the one concerning the same probe in different clocking conditions. In fact, among different clocking positions, any probe is virtually moved throughout its acquisition grid. This acquisition grid is kept usually with same shape for each clocking condition but it presents always a different angular range. This means that among different operative conditions the same probe covers a different angular sector inside the same machine annulus. Fig. 7.2 helps in visualizing the different grids.

This effect is given by the necessity to capture the disturb in its entire extension, hence the stator vanes to be investigated from downstream result slightly different when the disturb is injected at different angular positions upstream.
This effect introduce complexity when the different clocking positions results need to be compared among each others because acquisition grids are shifted. A solution to this problem comes from the assumption that, by measuring throughout two entire vanes, and by arranging the system according to the description in Section 3.1.1, the observed portion of annulus downstream of the stator would present periodicity between the leftward boundary and the rightward boundary.
Considering this assumption it is possible to simulate a larger angular range, for each case considered, just by creating a copy of the acquired measurement results and by attaching it to one of the two boundaries thanks to a rotation. The knowledge of a doubled angular range grid for each map is useful since the grids associated to different clocking positions never differs of more than few degrees, Table 7.1. In this way the doubled solution presents a region which overlaps perfectly the others non doubled solutions, hence it could be compared to the others as if it would have the same angular range just by means of interpolation.

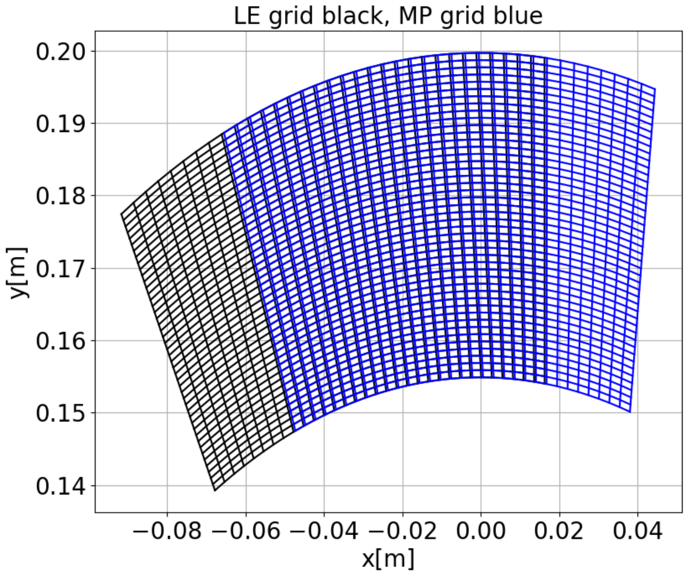

Figure 7.2: Comparison between grids obtained in two different conditions

Table 7.1: Starting angular position of the statoric row all referenced to the same zero

	Clean	MP	LE
Stator starting position [°]	46.5	46.655	38.475

7.1.2 Differences among 5-Holes and other probes

The difference here reported is highlighted by the authors just for completeness, since its understanding results necessary for a correct data elaboration, in particular at the outlet of the stator row. Given that to fully reconstruct the velocity field at a measuring section, it is necessary to couple data extracted from the 5-holes probe and from the fast response thermocouple. Values from both the probes need to be associated with the same coordinates of measuring points. This connection, among data from different probes to the same grid points, is not simple to be carried out, even in case of same operating conditions and same clocking position. In fact, while the used thermocouple sensor stays always at the same angular coordinate during its radial movement from case to hub, the 5-hole probe pressure taps do not, since its central tap axis is not orientation in axial direction, Fig. 4.28. This effect is due to the 5-holes probe outreach and its necessity to be aligned with the flow direction. In fact where the flow has a great tangential component, like at the outlet of a turbine stator row, the tip of the outreach follows a trajectory different from the one followed by the stem axis, as represented in Fig. 7.3.

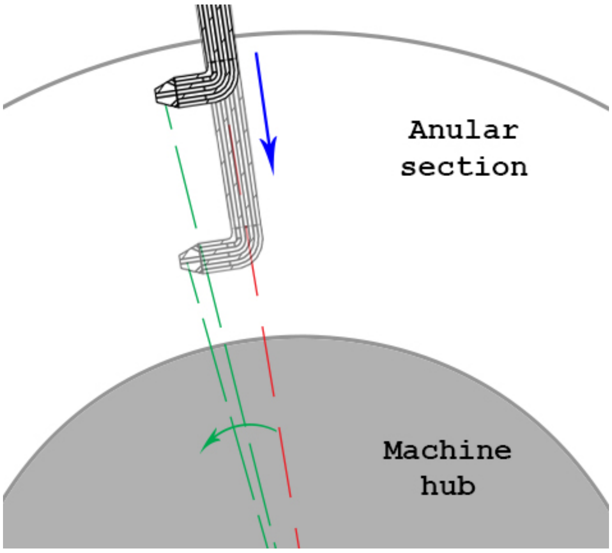

Figure 7.3: Scheme of 5-holes probe, tip angle in green, stem angle in red

Since thermocouples sensor follows instead a trajectory with a direction equal to the one followed by the 5-holes stem axis, this results in two different grids of acquisition for the aerodynamic field and for the thermal field, Fig. 7.3. Anyway, once the two grids coordinates are well defined, it is possible to face the problem of having thermal data associated to a certain set of point and aerodynamic data associated to another, just by interpolation of one field onto the grid of the other.

During this thesis work the chosen approach has been the one based on the interpolation of data coming from thermocouple onto the grid coordinates of the 5-holes probe.

7.2 Temperature measurement errors and correction

As anticipated in Section 6.1.1 a particularly difficult quantity to be correctly measured at the stator vanes outlet is the local total temperature. In absence of thermal disturb its value has to remain equal to the one measured upstream, as a result its measurement results completely trivial. However, when the thermal disturb is introduced upstream of the stator, the evaluation of points at vane outlet, affected by this disturb, needs to be carried out via direct measurements, hence by the introduction of a thermocouple.

Unfortunately, because of the nature of the thermocouple physics and because of the high Mach number, a tangible error is committed during those measurements.

In general any immersion device, like thermocouples, can indicate only its own temperature, which however it is never equal to the gas one, in case no precaution is adopted. As a consequence, during experimental campaigns, each temperature measurement would require a certain degree of correction to ensure a very small difference between the measured temperature and the gas one.

Error in measurement at steady state is actually caused by four well defined phenomena:

- Heat transfer to or from the probe by radiation
- Heat transfer by conduction
- Conversion of kinetic energy to thermal energy in the boundary layer around thermocouple
- Heat transfer from the boundary layer to the junction by convection

Hence to easily correct this measuring error, the environmental conditions have to be well known. This is not really possible in the studied case. As a result any applied correction has an intrinsic uncertainty directly related to the environmental conditions uncertainties.

In addition, the aforementioned sources of error interact with each other in a non linear manner whenever the flow presents extremely unfavorable environments.

For example a high velocity flow would face a viscous dissipation when brought to rest near the probe and, due to the convective heat transfer losses, the temperature perceived by the probe is lower than the gas total one. So the effects of viscous dissipation and convective heat loss result to be closely coupled [18].

In fact, measurements performed by thermocouples give at each point of measure an intermediate value between total and static temperature, and each point of interest is subjected to an error different from the one committed in the other locations. Hence the topic of temperature correction is fundamental to keep physical consistency with the conservation of energy, Appendix C, and the individuation of a correct approach is not obvious at all. As a result a-posteriori data correction has to be carried out on the output temperature measured by the probe.

Multiple correction methods have been taken into consideration during this thesis; among all the methods only two has been in the end considered good enough. The two methods has been respectively used one in OP3 and the other in OP2, because the set of data available slightly differs among operating conditions. In fact OP2 presents a lack in temperature data at the outlet of the stator, since the employed thermocouple failed under severe aerodynamic conditions at the beginning of the thermal OP2 measurement campaign. Clearly for both operative conditions the temperature correction has been carried out on HS and EW data, while in Clean an No-injection conditions no correction has been necessary.

7.2.1 Correction in OP3

The method employed to correct temperature data in OP3 is based on the thermal field knowledge downstream of the stator during No-injection disturb conditions. This knowledge is not available for OP2, see Section 7.2.2. Since the error in thermocouple measurement is strictly related to the aerodynamic behavior of the flow, it has been assumed that the map of local errors (calculated point by point) observed in No-injection could be considered somehow similar to the one done in the other injection conditions. The maps of errors are calculated as the point by point difference between the measured temperature in No-injection condition and the imposed upstream total temperature of $T_{total} = 313K$. This procedure is based on the assumption of total temperature conservation, hence possible heat exchange between streamlines at different Mach numbers is neglected. This error is defined as:

$$error = (T_{total} - T_{measured}^{Noinj}) \tag{7.2}$$

The so called errors map has been calculated for both MP and LE cases and it has been applied to all the available cases of HS and EW.

Thanks to this procedure the corrected total temperature values can be calculated as follows:

$$T_{total}^{HS} = T_{measured}^{HS} + error \tag{7.3}$$

$$T_{total}^{EW} = T_{measured}^{EW} + error \tag{7.4}$$

By looking at the flow regions where the thermal disturb is not supposed to migrate, it has been possible to understand whether or not the correction was well performed.

7.2.2 Correction in OP2

OP2 data have been corrected following a different approach. Their correction relayed on the usage of the so called "recovery factor", RF:

$$RF = \frac{T_{measured} - T_{static}}{T_{total} - T_{static}} \tag{7.5}$$

Starting from $T_{measured}$, which is the one detected by the probe, it is possible, by imposing a value of the RF, to derive a new value of the T_{total}. This is possible since the correct value for the ratio of static and total temperatures is known thanks to the knowledge of Mach number, hence the total and static pressure ratio which is correctly measured by the aerodynamic probe (5-holes).

$$RF = \frac{\frac{T_{measured}}{T_{total}} - \frac{T_{static}}{T_{total}}}{1 - \frac{T_{static}}{T_{total}}} \tag{7.6}$$

$$\Longrightarrow$$

$$T_{total} = \frac{T_{measured}}{RF(1 - f(M)) + f(M)} \tag{7.7}$$

$f(M)$ is simply the temperature ratio expressed as a function of Mach number measured by the 5-holes probe.

$$f(M) = \frac{T_{static}}{T_{total}} = \frac{1}{1 + \frac{\gamma_{air}-1}{2} M^2} \tag{7.8}$$

Since to perform this correction it is necessary to associate the measured temperature and the measured mach number to the same coordinate point, it is clear that a form of interpolation of data coming from different probes is required. In fact the first step performed, before starting any calculation, has been a bi-linear interpolation of data coming from the thermocouple on the acquisition grid of the 5-holes probe.

Anyway during this thesis work an additional step has been introduced to this kind of correction procedure. In fact, since the thermocouple has an error which is location dependent, the usage of a constant RF throughout the whole thermal field would not for sure be correct. As a consequence it has been introduced a dependence of the local RF on the local Mach number. In particular RF has been implemented as a linear decreasing function of Mach, Equation (7.9), since the gap between the measured temperature and the total one is expected to rise as the Mach increases, because of the nature of the thermocouple behavior.

$$RF = RF_{input} + \frac{R1 - RF_{input}}{M1 - M0}(M_{local} - M0) \tag{7.9}$$

RF is the local recovery factor, RF_{input} is a global value imposed for recovery factor, M_{local} is the local value of Mach number from 5-holes probe and $M0$, $M1$ and $R1$ are values used to tune the correction method and obtain the most suitable result. Fig. 7.4 represents the linear trend of the recovery factor.

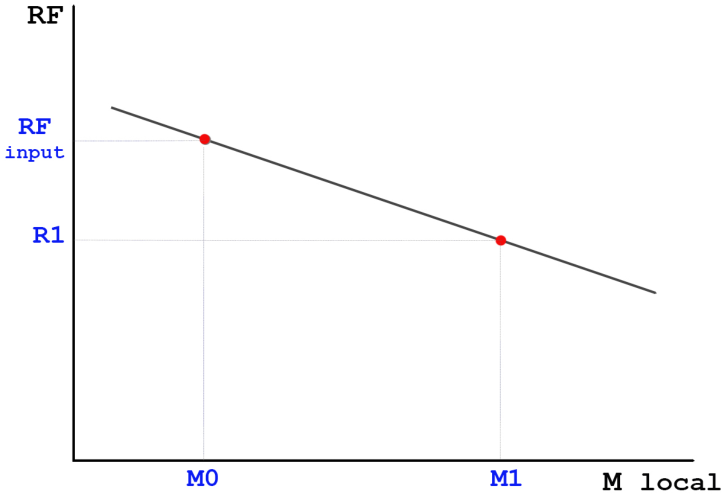

Figure 7.4: Recovery factor imposed law graphical representation

7.3 Measurements in Clean conditions

The aerodynamic field in Clean configuration is obtained using the 5-holes pressure probe, that is the only probe used to characterize the flow in this configuration downstream the stator. Pressure loss coefficient Y, Mach number M, the absolute flow angle at stator outlet α and the streamwise helicity hel_{sw} have been chosen as most representative quantities.

For further information about streamwise helicity hel_{sw} refer to [19]. The maps related to the test OP3 in Clean configuration are shown in Fig. 7.5. A black line is used to highlight the wake position and PS stands for pressure side, while SS for suction side.

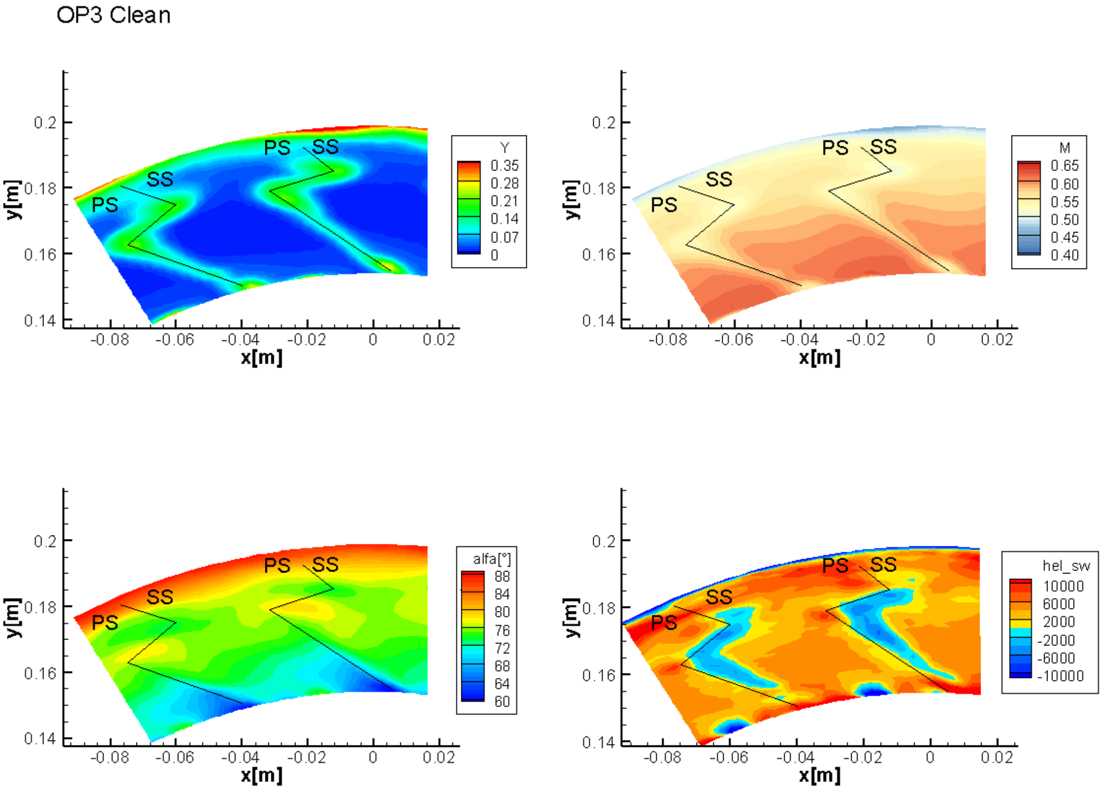

Figure 7.5: OP3 Clean maps

The same maps can be realized for OP2 in Clean condition, and they are showed in Fig. 7.6.

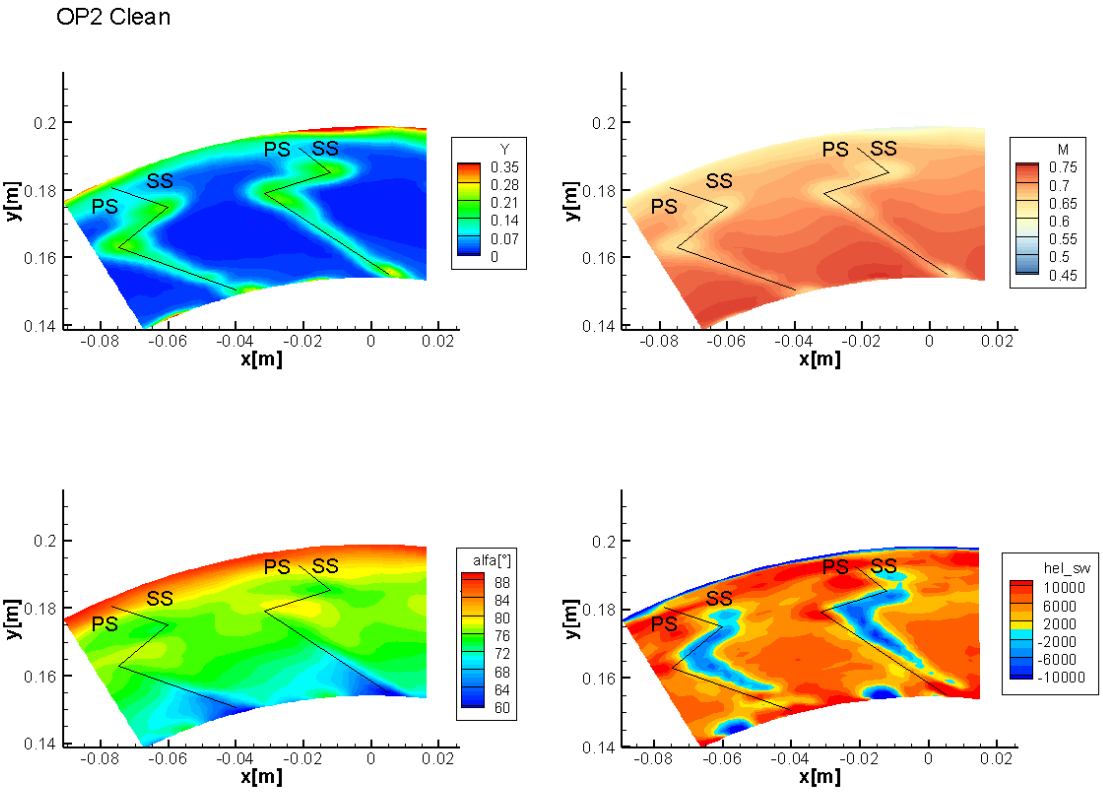

Figure 7.6: OP2 Clean maps

Knowing the streamwise helicity in Clean case allows to carry out a comparison with the helicity fields in the other configurations (Noinj, EW 10Hz, EW 100Hz). In this way it's possible to get an idea about the effects of swirled entropy wave on vortical structures downstream the stator and about the location where it affects more the aerodynamic field. By convention helicity is positive if vortical structures rotate clockwise, while negative if they rotate counterclockwise, for an observer placed downstream of the stator at the measuring plane looking towards stator blades cascade.

As it can be seen from the maps the helicity field is mainly positive, especially in the isentropic region within blade passage and this is due to blade leaned geometry. Near the wake region, helicity is negative due to the viscous interaction between the wake flow and vortical structures within blade passages that produces vortical structures which rotate counterclockwise (shed vortices). Leakage at hub due to the clearance slot in the blades trailing edge gives rise to a region with negative helicity, as expected. In the OP2 condition, streamwise helicity values are higher in magnitude with respect to the ones in OP3.

Looking at pressure loss coefficient maps, it's not possible to say if total pressure losses are higher in OP3 or in OP2. For this purpose, a map which shows total pressure loss coefficient difference between OP3 and OP2 is created (Fig. 7.7). This map shows that there are no big changes in total pressure loss coefficient in the two operating conditions, in fact the ΔY is almost zero in the whole map. The regions in which some differences are present highlight higher losses in OP3: this is in accordance with the fact that the Reynolds number in OP2 is greater due to an increase in both velocity and density at stator outlet. Consequentially, this causes a drop of the friction factor and hence losses, mainly in the blade boundary layer and at casing. The only region that shows high variation in losses among the two operating condition is located at the hub and in particular it is the one affected by the hub leakage vortex. This leakage vortex changes its position due to different blade loading conditions in the two cases leading to two distinct nuclei of higher loss coefficient difference, one positive and one negative. Moreover there is a tangential shift of the wakes between OP3 and OP2, and this causes the presence of the two regions where ΔY is negative and positive.

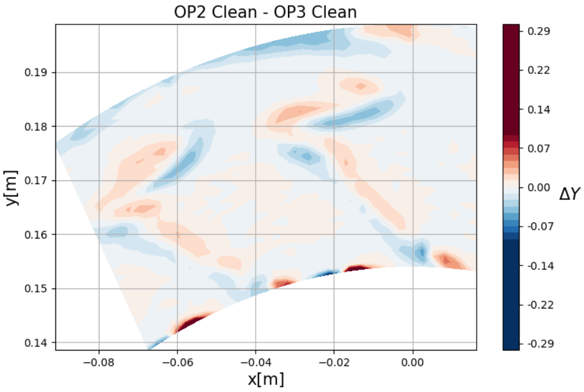

Figure 7.7: Map of ΔY between OP2 and OP3

Now it can be interesting looking at azimuthal mass averaged total pressure loss coefficient Y, absolute flow angle at stator outlet α (named “alpha” in the graphs) and the incidence (calculated as the difference between relative flow angle at measuring plane and the rotor blade geometric angle) as function of dimensionless span (Fig. 7.9). The black dashed line represents the trend of stator blade geometric angle at outlet and it is useful to compare it with the evolution of α. It’s important to notice that these angles are depicted according to the sign convention reported in Fig. 7.8. Given this premise, it’s clear that the wake shape is in agreement with the averaged stator outlet flow angle trend along the span.

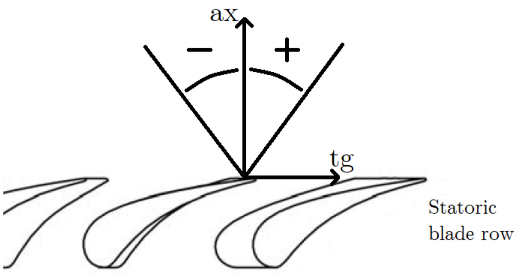

Figure 7.8: Stator outlet flow angles sign convention

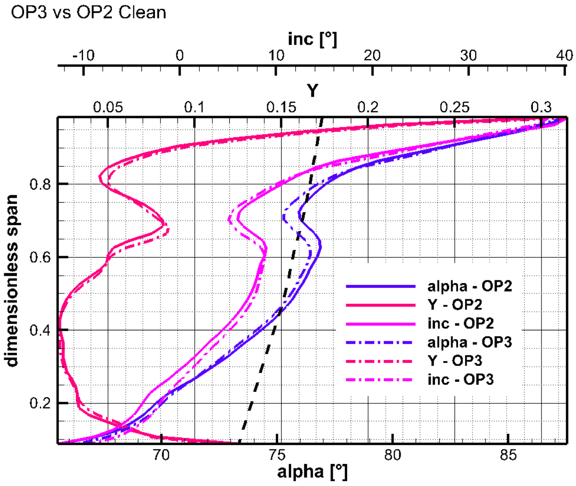

Figure 7.9: Circumferential mass averaged Y, α, inc (OP3 vs OP2 Clean)

As already seen, there is no appreciable difference in loss coefficients between the two operating conditions. The trend of stator outlet flow angle α is mainly governed by the blades leaned geometry (see Appendix B) which cause a great overturning at the tip (flow angle is higher than the one imposed by the blade, so the flow becomes more tangential) and a strong underturning at the hub (flow angle is lower than the one imposed by the blade), a region of underturning above the midspan and of overturning below. For the sake of comprehension a schematic representation of the main vortical structures is provided in Fig. 7.10. Between the two operating conditions, the values of α changes a bit in the region between 50% and 80% of the span: in OP3 the underturning is stronger while the overturning is lower with respect to OP2, in which the overturning region extents radially. The lower underturning in OP2 at about 70% of the blade span is due to the lower interaction between the tip passage vortex and the wake flow which leads to weaker shed vortex. This is consequence of the higher Mach number which causes secondary flows to be more stretched axially and less extended radially.

In order to visualize overturning and underturning regions in the annular sector, the difference between measured stator outlet flow angle and the geometric blade angle can be calculated. Fig. 7.11 and Fig. 7.12 shows the maps representing the results from this calculation for both OP3 and OP2. Where the difference value is higher than zero, it means that those are overturning regions, otherwise they are underturning regions if it is lower than zero.

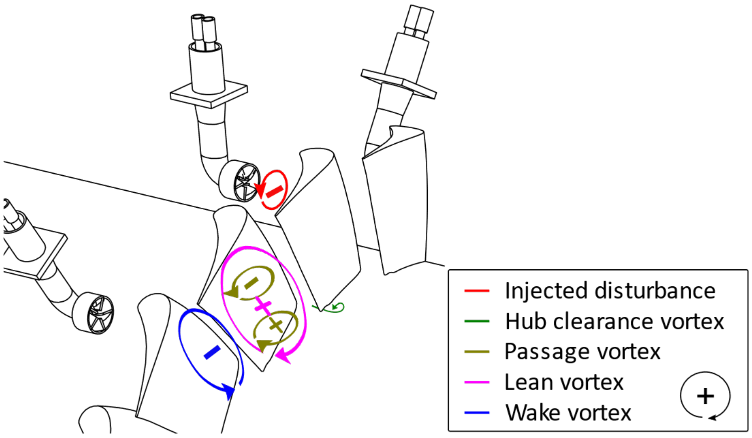

Figure 7.10: Schematic representation of vortical structures downstream of the stator

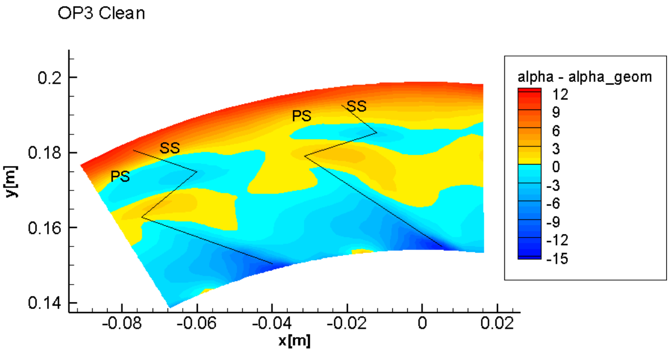

Figure 7.11: Difference maps between measured absolute flow angle and blade geometric angle at trailing edge in OP3 Clean

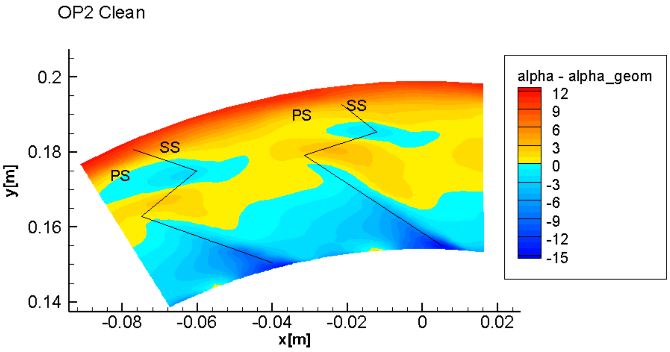

Figure 7.12: Difference maps between measured absolute flow angle and blade geometric angle at trailing edge in OP3 Clean

For what concern the Mach number, it is greater in OP2 condition due to higher expansion ratio. The trend of averaged Mach number trend along the span is similar, as shown in Fig. 7.13. The circumferential averaged mass flow rate trend is depicted in Fig. 7.14 and it confirms the expected behavior for leaned geometry blades. In OP2 condition mass flow rate is higher due to turbine characteristic curves.

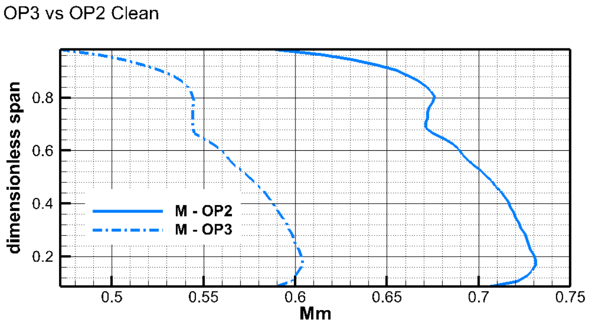

Figure 7.13: Circumferential mass averaged Mach number (OP3 vs OP2 Clean)

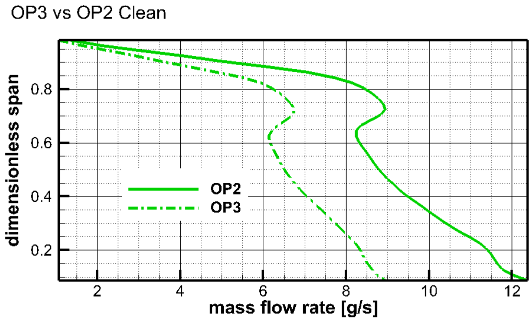

Figure 7.14: Circumferential averaged mass flow rate (OP3 vs OP2 Clean)

7.4 Thermal field analysis

The most useful quantity for this analysis is the peak-to-peak temperature $T_{peak-peak}$, which represents the remaining temperature oscillations after the passage through stator blades and that allows to quantify the surviving amount of the injected EW downstream of the stator. The first part is dedicated to OP3 condition, while the second one to OP2.

7.4.1 OP3

First of all, it's possible to look at the effects of injection frequency on the EW remaining magnitude at stator outlet. For given injection position, LE for example, it is found that the $T_{peak-peak}$ becomes lower with increasing the injection frequency (Fig. 7.15): at $10 Hz$ the maximum value of $T_{peak-peak}$ is 10.6 K, while at $100 Hz$ is 3.63 K. This trend is valid also for MP clocking position. The reduction in the temperature oscillation amplitude is due to the fact that, at higher injection frequencies, the hot and cold pulse are closer in space, thus significant mixing takes place. This creates a more homogeneous temperature of the flow and reduce much the magnitude of EW. The wake profile is given by the black line and it's useful to have reference about stator blade position (pressure side PS on left side and suction side SS on right side with respect to the line).

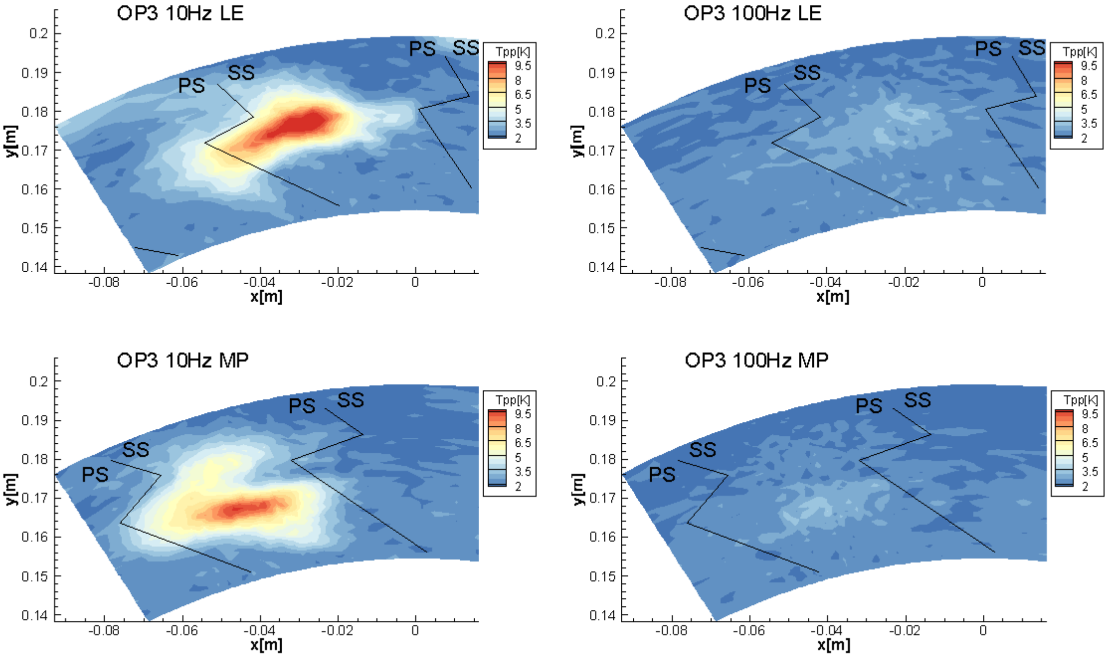

Figure 7.15: Comparison between $T_{peak-peak}$ maps in 10 Hz and 100 Hz cases

Since the most representative results are obtained in $10Hz$ case, the comparison of results between different clocking position is based on single injection frequency value, i.e. $10Hz$. Looking at the map related to the LE injection case, it can be seen that EW does not propagate below midspan, however it is transported towards wake region thus affecting the wake temperature. This is due to the entrainment of the EW in the blade boundary layer. The two injection conditions lead to different profiles in radial direction: the EW in MP injection case results more stretched and this is mainly due to interaction with secondary flows in blade passage which enhance the mixing. From Fig. 7.15 it's clear that a transport in azimuthal direction towards the pressure side occurs in both LE and MP tests. It can be justified by the interaction of the EW with tip passage vortex [2].
If circumferential average weighted on mass flow rate is performed, the following graph (Fig. 7.16) is obtained:

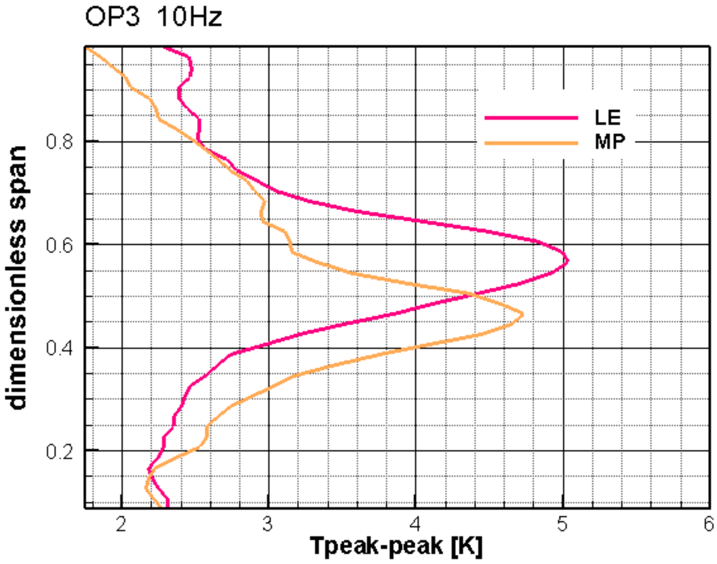

Figure 7.16: Circumferential mass averaged $T_{peak-peak}$ in case of injection frequency set equal to 10 Hz for the two injection positions

In LE case the averaged maximum value is reached at about 57% of blade span while in MP case it is reached at about 47% of blade span. In MP case the maximum value of averaged $T_{peak-peak}$ is less than in LE case and this is due to the mixing and spreading of the EW over the whole channel that leads to higher attenuation of EW. In both cases it can be noticed that the maximum $T_{peak-peak}$ is at a lower radial position with respect to the one upstream stator, that was at about 65% of blade height. The EW is transported downward because of the blades leaned geometry, however in MP case radial displacement is higher due to stronger interaction with secondary flows.

As conclusion, it's possible to state that the clocking position (LE and MP) influences the peak magnitude, its radial position and the diffusion of EW within the blade passage.

Given that in OP3L and OP3U flow conditions at stator inlet and outlet remain almost the same, the considerations valid for OP3 can be extended to these two operating conditions.

Thanks to a phase average on data coming from fast thermocouple, it is possible to visualize the time evolution of thermal field (Fig. 7.17) with injection frequency set equal to $10Hz$. As example the case LE is reported. It is interesting to notice that, at each snapshot the phase averaged temperature field, Fig. 7.17, presents traces of the disturb even in the hub region. These are instead not visible on the $T_{peak-peak}$ map. The difference among those fields is supposedly caused by the interaction between the injected pulsating thermal disturb and the blade boundary layer (BL). In fact this viscous interactions damps the temperature fluctuations, hence creating a wake zone at constant temperature in time in the hub region.

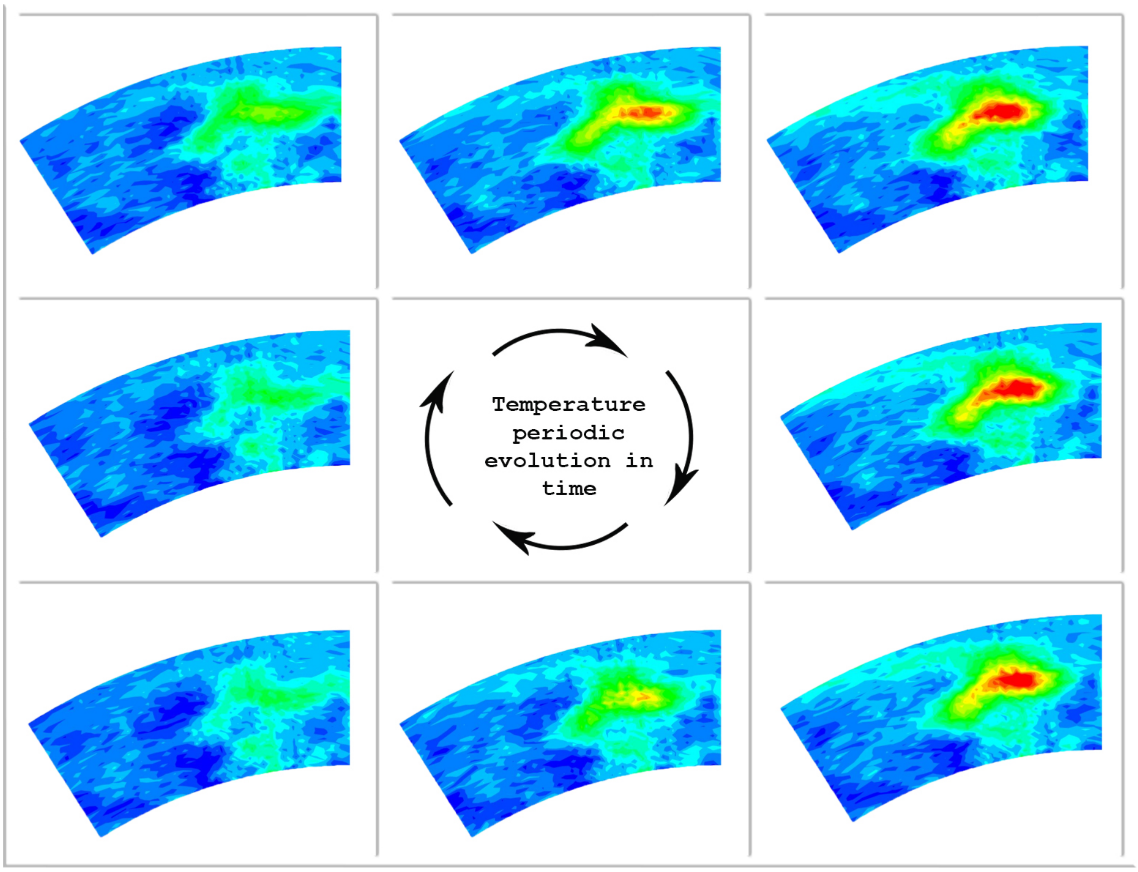

Figure 7.17: Mean temperature field evolution in time for OP3 $10Hz$ LE

When the EWG is set to generate a hot-streak, the temperature field analysis cannot be based on $T_{peak-peak}$ because the temperature of injected disturbance is kept constant. To understand its evolution through stator, the total temperature maps become useful. As it can be seen in Fig. 7.18, the hot-streak survives better when the clocking position is LE rather than MP. This behavior can be directly linked to the interaction with secondary flows, so the consideration about EW attenuation and thermal diffusion are still valid also with HS. For what concern the LE case, the hot-streak distributes inside the wake along almost all the blade span. Downstream of the stator, the temperature increase is about $8.9K$ at maximum (LE) that corresponds to a 2.84% rise with respect to undisturbed temperature.

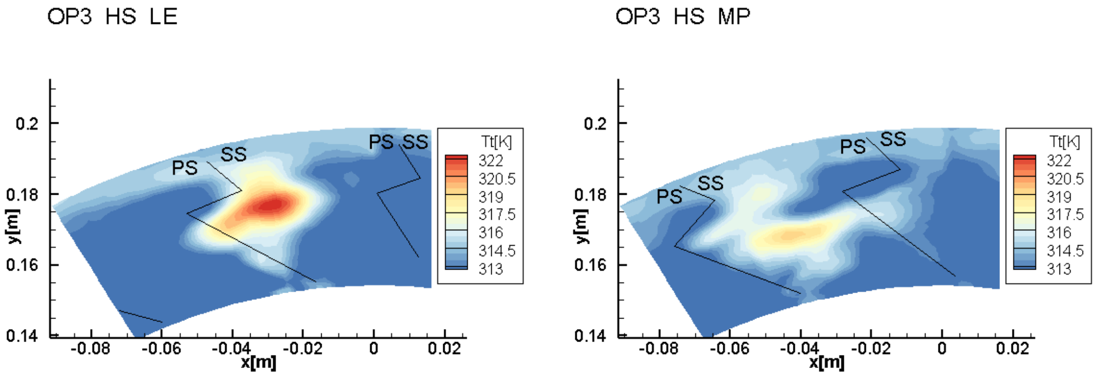

(a) (b)

Figure 7.18: Temperature fields for the two injection positions (OP3)

7.4.2 OP2

In OP2 condition, the EW migration towards hub and attenuation depending on injection position is expected to be in agreement with what happens in OP3. However, the analysis based on $T_{peak-peak}$ cannot be performed because of the lack of data. In fact, measurements at stator outlet using thermocouple with EWG switched on have not been done because the aerodynamic field is such strong to cause the thermocouple measuring junction to fail. An attempt has been made, however the thermocouple broke. Given that the cost of instrumentation is not negligible and that the same thing would have been occurred again with new probe, another attempt has not been done. Regarding the stator outlet measuring section, the thermocouple survived only the time needed for HS tests.

As already explained the temperature values given by fast thermocouple may be not correct and some strategies should be adopted to get reliable results. For tests in OP2 condition, the correction strategy allows to get temperature field maps so that it's possible to see at least where HS migrates through stator. In Fig. 7.19 the thermal field is shown for the two injection positions. If they are put in comparison, it's clear that in MP injection case the attenuation is greater and the transport in azimuthal direction is more pronounced. These effects are due to the stronger interaction with secondary flows which promote the mixing.

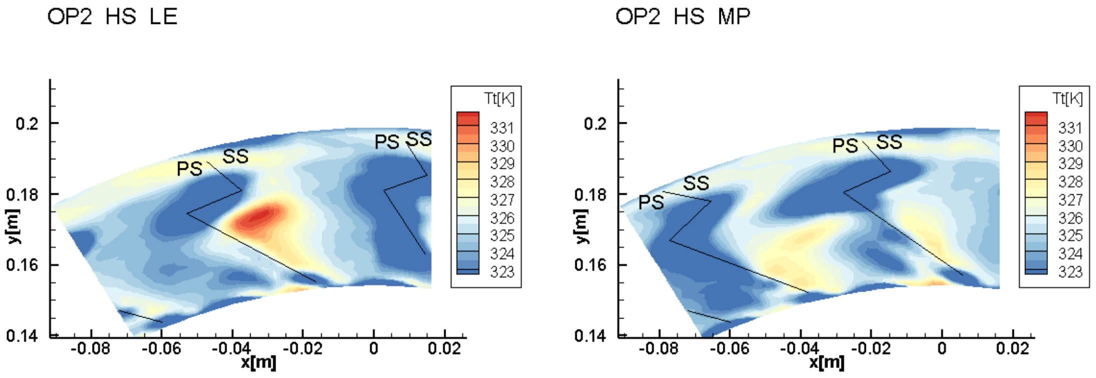

(a) (b)

Figure 7.19: Temperature fields for the two injection positions (OP2)

7.5 Aerodynamic field analysis

Thanks to the available data, it's possible to compare the results in different conditions, such that the effects on aerodynamic field of the introduced perturbation can be discovered. In the next pages the most representative and explanatory maps are reported in combination with azimuthal mass averaged graphs. The analysis starts looking at OP3 plant operating condition, then it focuses on the OP2.

7.5.1 OP3

7.5.1.1 Total pressure loss coefficient

The loss coefficient maps for the two injection positions with injection frequency set equal to $10Hz$ and $100Hz$ are reported in Fig. 7.20. The steady loss coefficient fields do not show significant changes for a fixed injection position. This can be seen also from mass averaged loss coefficient trend (Fig. 7.21): the curves related to the tests at $10Hz$ and $100Hz$ perfectly overlap, so the losses do not change with varying injection frequency for fixed clocking position. These similarities can be related to the flow fields upstream of the stator, which do not show appreciable differences among $10Hz$ and $100Hz$, Section 6.3.2. The same occurs to stator outlet flow angle α and to the incidence angle curves, which result to be equal in both $10Hz$ and $100Hz$ tests for a given injection position. For these reasons, when analyzing the results of tests with EWG switched on, the ones with injection frequency equal to $10Hz$ have been chosen as representative of the swirled EW injection cases. On the contrary, evident differences exist if the trend of those quantities is compared based on the injection position, as it can be observed in Fig. 7.22.

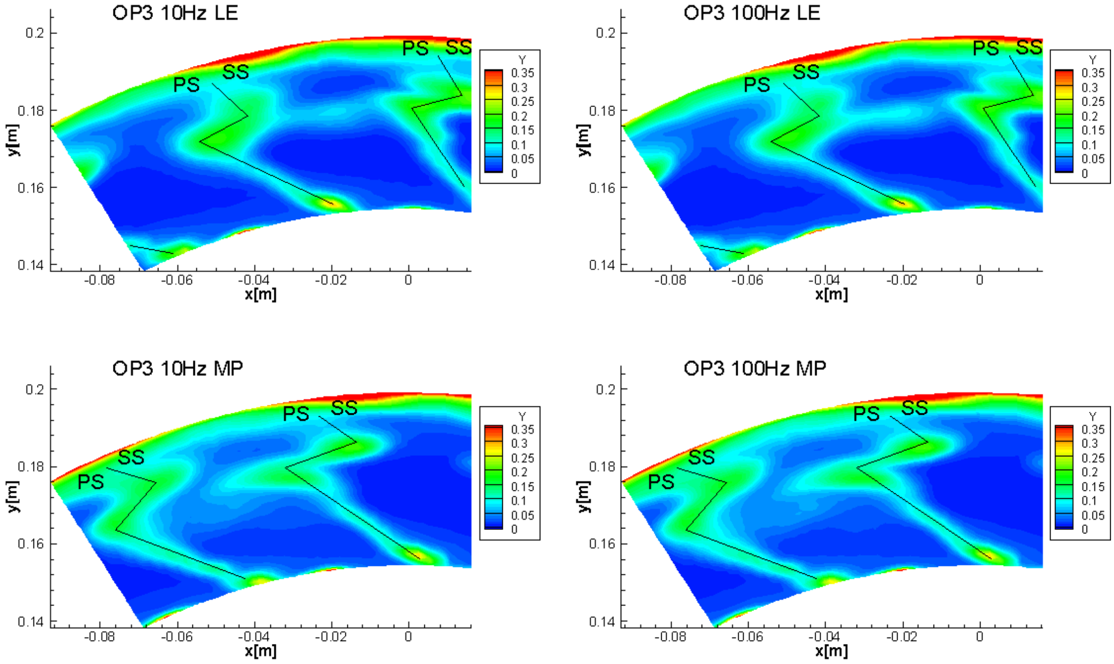

Figure 7.20: Loss coefficient maps for OP3 10Hz LE, OP3 10Hz MP, OP3 100Hz LE and OP3 100Hz MP

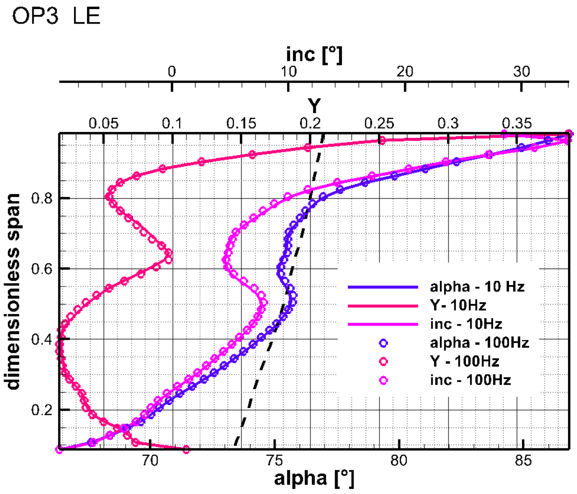

Figure 7.21: Circumferential mass averaged loss coefficient, stator outlet flow angle and incidence in OP3 10Hz LE and OP3 100Hz LE

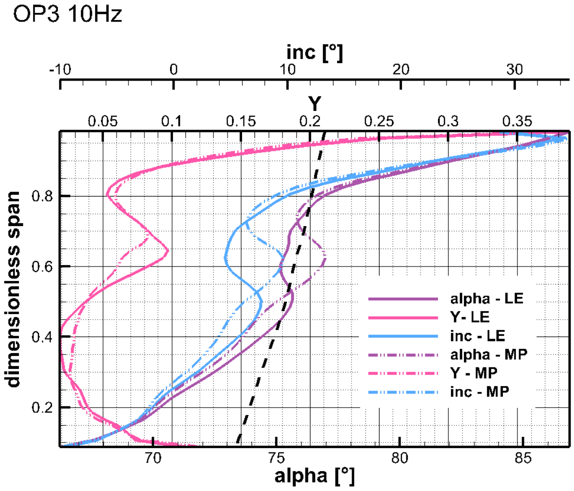

Figure 7.22: Circumferential mass averaged loss coefficient, stator outlet flow angle and incidence in OP3 $10Hz$ LE and OP3 $10Hz$ MP as function of blade span

Referring to Fig. 7.20, the higher losses region above blade midspan remains more localized in LE case than in MP, even if a thin zone of non-zero losses detaches from suction side and propagates circumferentially in the middle of the channel. The partial stagnation of the injected perturbation on the LE leads to weaker flow perturbation and the injected swirled EW moves radially towards the tip due to a sort of climbing on the suction side blade surface, thus it interacts less with secondary flows. In MP case the region affected by higher losses is wider due to the greater interaction between swirled EW, the wake and secondary flows. These variations in the maps between LE and MP injection positions translate into different values of circumferential mass averaged loss coefficient as it can be seen in Fig. 7.22. For both clocking positions significant differences in morphology can be noticed with respect to the map associated to Clean test Fig. 7.5, so the injection of swirled entropy wave strongly affects the flow field downstream the stator especially in the region close to the midspan. In addition to notable changes in the wake zone morphology, the isentropic region within the blade channel that was present in the Clean case does not exist anymore. The regions close to the hub and tip do not change the loss intensity meaning that they are dominated by the casing boundary layers and hub leakage, hence the effect of the introduced perturbation is negligible. In order to better comprehend the impact of perturbation injection on losses, it can be interesting looking at the results in Noinj and Clean conditions and compare them with the $10Hz$ tests. From Fig. 7.23 it can be seen that loss coefficient values in $10Hz$ and Noinj cases are almost the same since the curves overlap both for LE and MP injection position respectively. The pressure loss coefficient maps in $10Hz$ and Noinj condition are provided in Fig. 7.24 for both the injection position. They are very similar, consequently the circumferential mass averaged coefficient follows very similar trend for a given clocking position. This implies that the temperature perturbation is not the main responsible for the losses increase. In fact, given that the loss coefficient values are higher on vast majority of the blade heigh if compared to the ones in the Clean test, the conclusion is that the injected swirl profile represents the biggest contribution to losses increase.

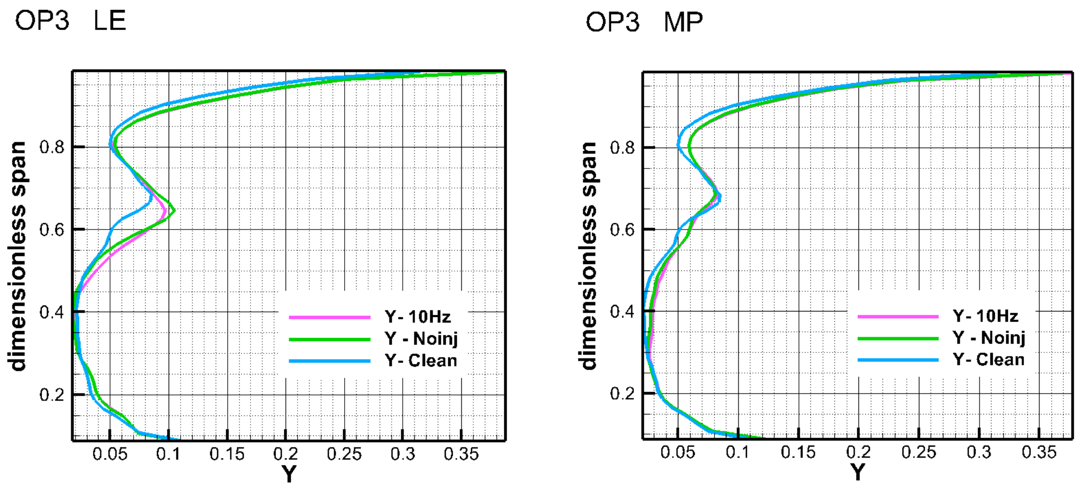

(a) (b)

Figure 7.23: Circumferential mass averaged loss coefficient for OP3 test with EWG switched on with injection frequency set equal to $10Hz$, in Noinj and Clean conditions for the two injection positions

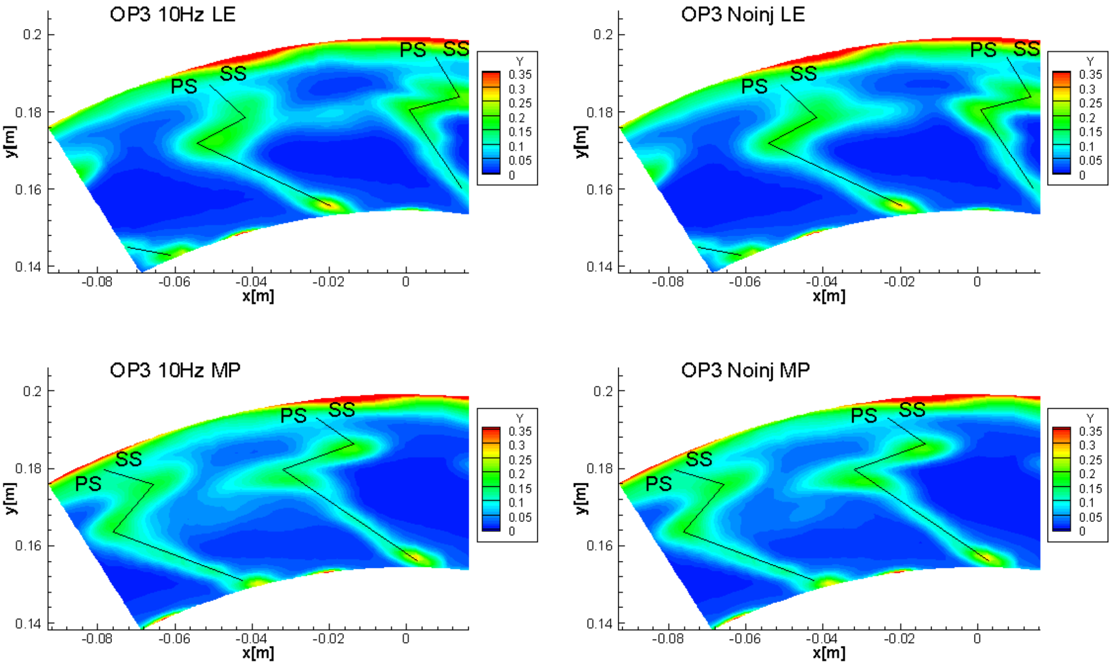

Figure 7.24: Loss coefficient maps for $10Hz$ LE, $10Hz$ MP, Noinj LE and Noinj MP in OP3

In order to provide further proofs about the bigger impact of the swirl profile rather than EW on losses, the maps in Fig. 7.25 and Fig. 7.26 have been created to make possible comparing the relative changes between the cases Clean and Noinj with Noinj and $10Hz$ tests. As expected, higher values of ΔY are found when Clean loss coefficient map is subtracted point by point to Noinj map. The regions where the peak values of ΔY are reached can be related to both tangential and radial shift of the wake and of other zones in the flow field.

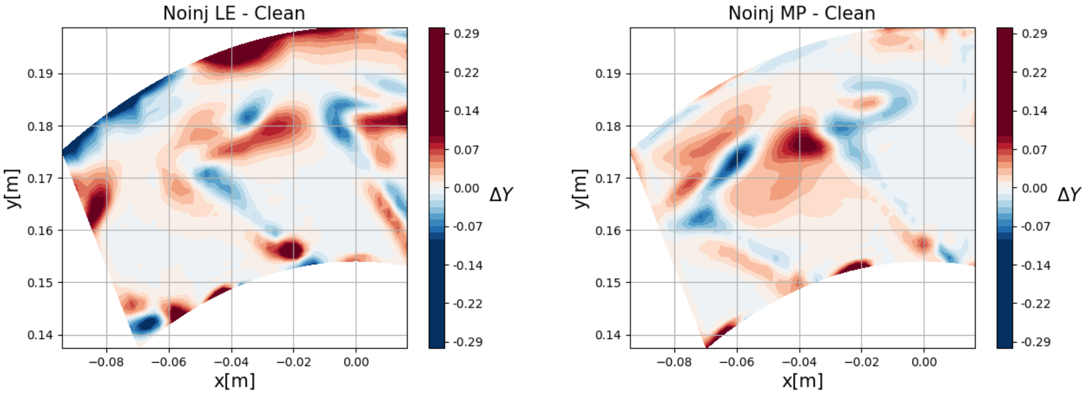

(a) (b)

Figure 7.25: Loss coefficient variation ΔY between Noinj and Clean for the two injection positions (OP3)

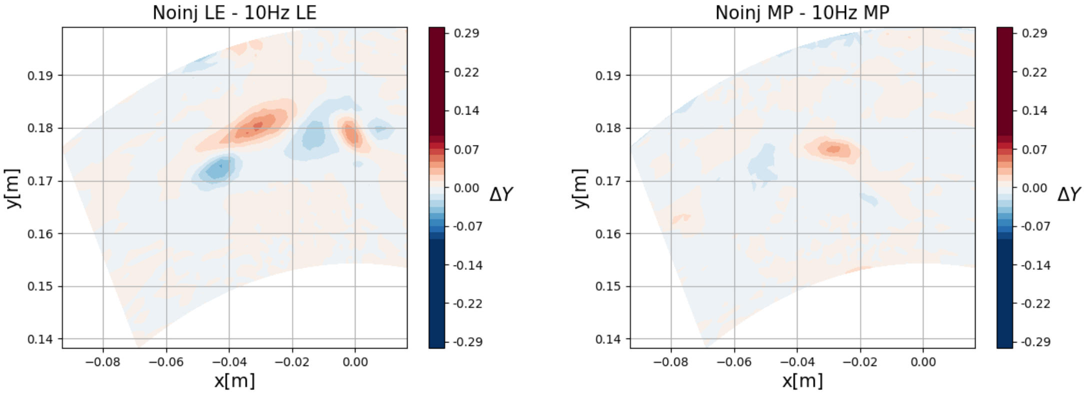

(a) (b)

Figure 7.26: Loss coefficient variation ΔY between Noinj and $10Hz$ tests for the two injection positions (OP3)

Regarding the HS injection condition, the trend of loss coefficient is very similar to Noinj and $10Hz$ cases (Fig. 7.27) and so the same considerations are valid. The slightly different behavior in some regions may be related to the fact that the perturbation has higher enthalpy content that leads to higher velocity. Thus the swirled perturbation may interact in different manner with secondary flows producing little changes on vortical structures downstream of the stator and consequently on losses.

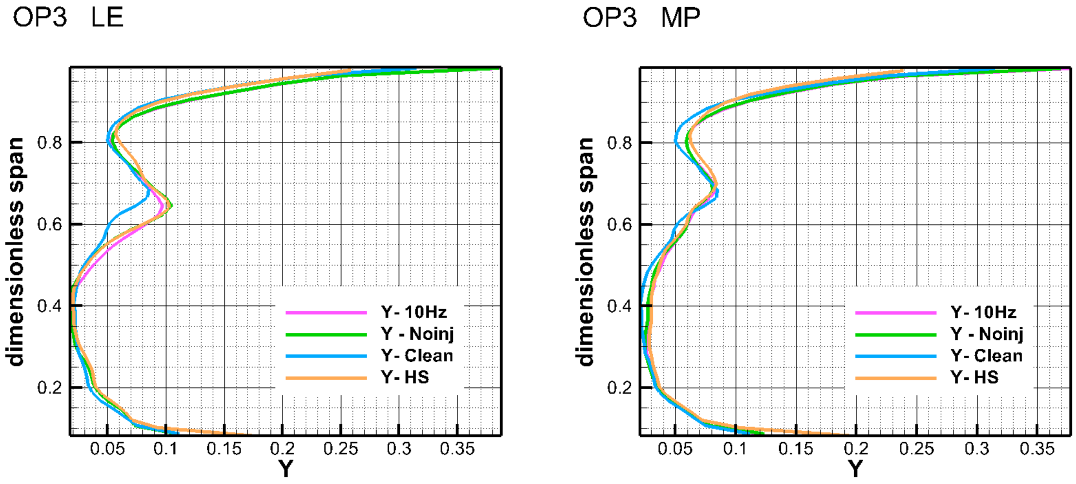

(a) (b)

Figure 7.27: Circumferential mass averaged loss coefficient for OP3 with EWG switched on with injection frequency set equal to 10 Hz, in Noinj, Clean and HS conditions for the two injection positions

Fig. 7.28 provides a detail of the total pressure loss coefficient trend for both the clocking positions in different injection conditions with the purpose of sum up all the discussed cases and achieve better idea about its evolution.

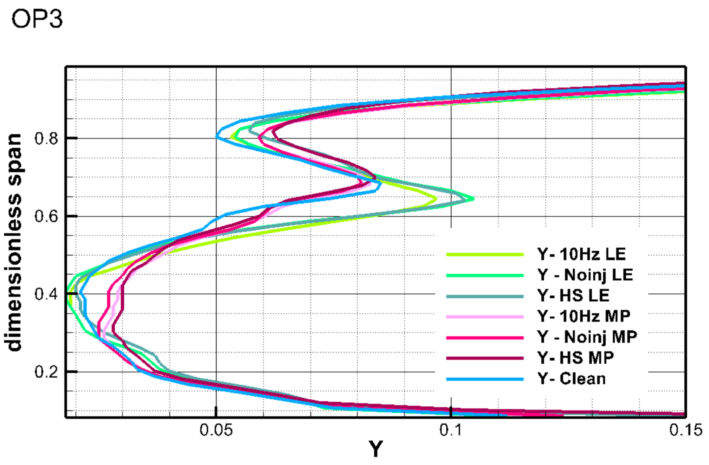

Figure 7.28: Detail of circumferential mass averaged loss coefficient for OP3 in different configurations

Thanks to a modification on circumferential mass average algorithm implemented on Fortran, it's possible to get the overall mean value of loss coefficient in each test for the two injection positions. The loss coefficient is calculated point by point and multiplied by the mass flow rate associated to the area around that point, then all these terms are summed up. The summation is divided by the total mass flow rate to find the mean value weighted on mass flow rate. Table 7.2 shows the calculated loss mean coefficients.

Table 7.2: Percental mean loss coefficients in different injection setups (OP3)

Clean		**10Hz**	**100Hz**	**Noinj**	**HS**
5.1	**LE**	5.9	5.8	5.8	6.1
5.1	**MP**	5.7	5.7	5.6	6.0

The Clean case is the one that ensures lowest loss coefficient, while HS is characterized by the highest values and in between there are $10Hz$, $100Hz$ and Noinj (the latter has lower losses). So the swirl profile injection causes an increase of losses and the combination with EW produce a further increase. No clear trend can be highlighted by looking at injection frequency, however about injection position becomes evident that higher losses are achieved for LE injection rather than MP.

7.5.1.2 Absolute flow angle

Now the analysis can focus on absolute flow angle at stator outlet. The maps of α for EW injection at $10Hz$ and Noinj tests are reported in Fig. 7.29. Notice that $100Hz$ maps are not shown because they are very similar to $10Hz$ ones. Close to the hub and at the tip region the flow angle values seem not to change significantly with respect to Clean case (Fig. 7.5), however little variations are found above midspan. Given that at about 60% of blade heigh in $10Hz$ MP and Noinj MP maps angle values look similar to ones in Clean case, it's expected to find still overturing close that radial position. In $10Hz$ LE and Noinj LE cases not clear conclusions can be found by looking only at these maps.

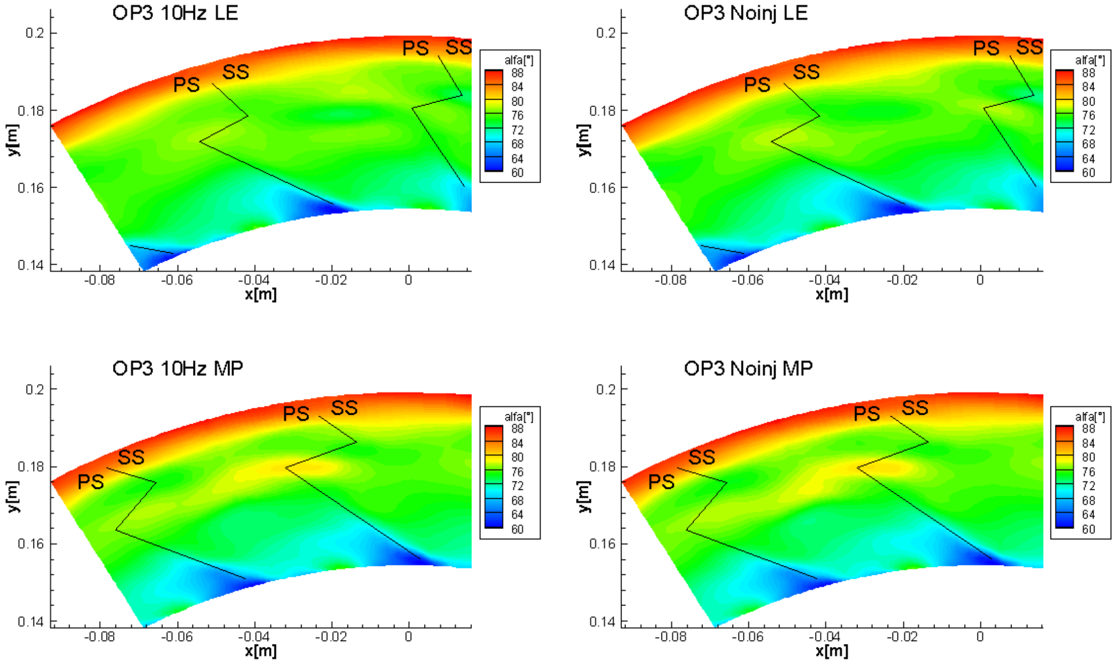

Figure 7.29: Absolute flow angle maps for 10Hz LE, 10Hz MP, Noinj LE and Noinj MP (OP3)

In order to better understand the relative changes between 10Hz, Noinj and Clean tests results, some maps (Fig. 7.30) containing the difference point by point of α obtained by subtracting the Clean values to 10Hz and to Noinj results have been built up. This has been done thanks to a Python code developed by the authors. In this way it is possible to compare the different tests and highlight variations in flow angles values with Clean condition chosen as reference. Where the $\Delta\alpha$ (difference between α values) is greater than zero, it means that flow has become more tangential than in Clean case and more axial where $\Delta\alpha$ is lower than zero.

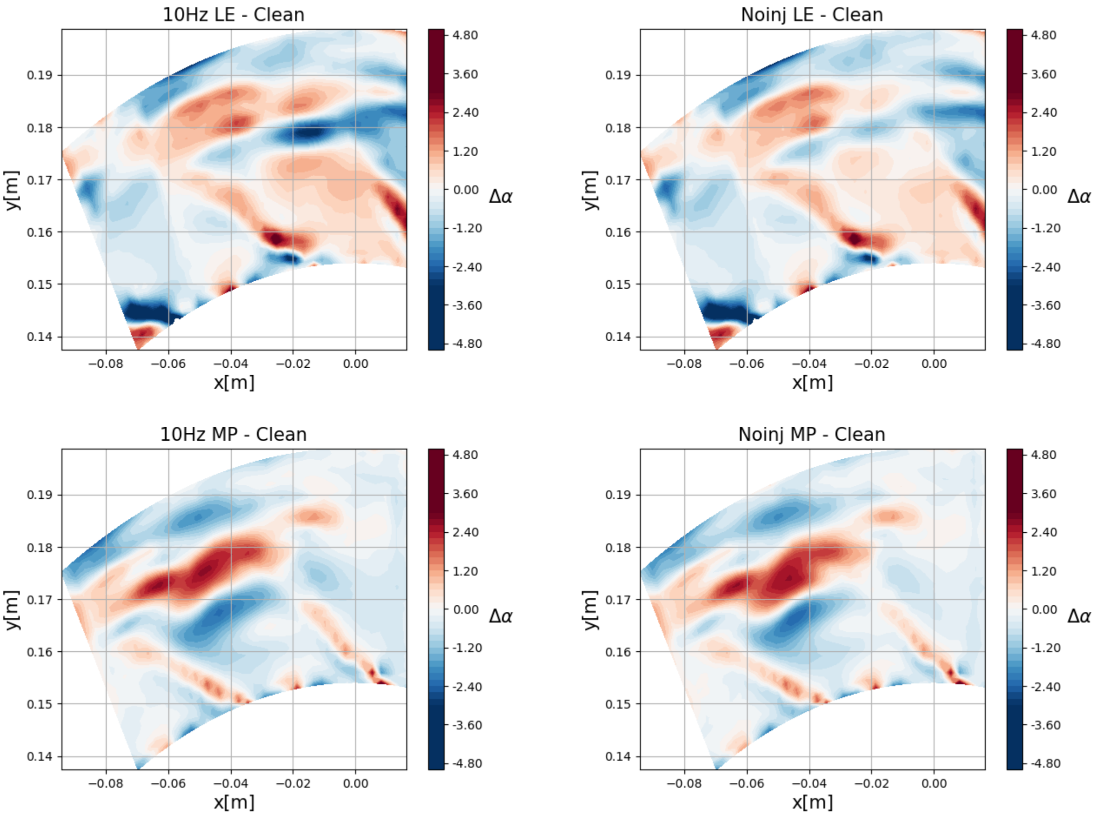

Figure 7.30: $\Delta\alpha$ calculated from $10Hz$ LE - Clean, $10Hz$ MP - Clean, Noinj LE - Clean, Noinj MP - Clean (OP3)

For sake of completeness, also the $\Delta\alpha$ maps (Fig. 7.31) between Noinj and $10Hz$ results are provided to see relative changes between these two tests.

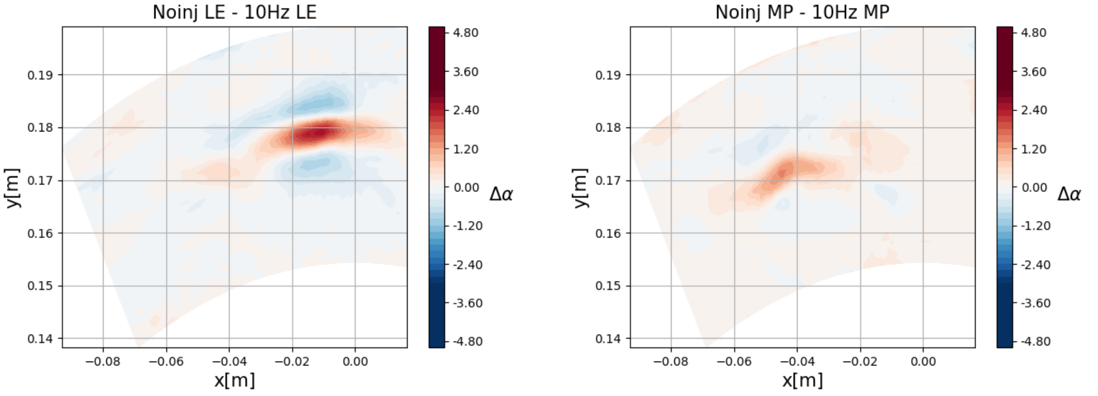

(a) (b)

Figure 7.31: $\Delta\alpha$ calculated from Noinj LE - $10Hz$ LE and Noinj MP - $10Hz$ MP (OP3)

The spanwise profiles of azimuthal average weighted on mass flow rate of the absolute flow angle α at stator outlet are shown in Fig. 7.32. In the figure, the results in Clean, Noinj and perturbation injection at $10Hz$ conditions are represented for the two injection positions. Looking at MP case, it's clear that both $10Hz$ test results and Noinj ones differ from Clean one but they show very similar values between them two. Also for LE injection, Noinj and $10Hz$ results are different from Clean ones but in this case the values in $10Hz$ and Noinj tests don't follow the same trend as in MP injection. Regardless of whether the injected disturbance is, the swirl profile interacts (more or less depending on injection position) with secondary flows within the blade channel leading to significant changes of the angles trend close to mid-span region with respect to Clean case.

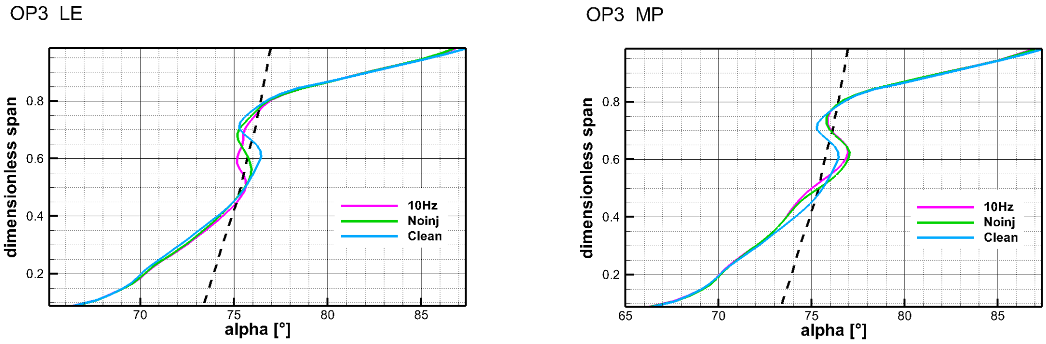

Figure 7.32: Circumferential mass averaged stator outlet absolute flow angle for both clocking positions in $10Hz$, Noinj and Clean cases (OP3)

Regarding the LE case, the only injection of swirl profile causes the underturning region above midspan to become wider while the overturing region below becomes narrower and less pronounced. When also EW is injected, this overturning region is not present anymore and it is replaced by an underturning one, in which local maximum flow angle is reached at about 60% of blade span. This significant change is assumed to be caused by the interaction between the swirl profile, that moves radially towards the tip on blade suction side due to sort of climbing, and the tip passage vortex pushed towards midspan by leaned geometry. The results of the interaction between the branch of swirl profile and branch of the tip passage vortex is that at the measuring section the flow angle profile changes significantly, leading to strong underturning instead of overturning that is present in Clean case. The great difference between $10Hz$ and Noinj profiles may be due to the flow angle at stator inlet which shows a very different range of values because the swirl effect seems to be enhanced by pulsating disturb injection. This causes the flow to enter the stator cascade more tangential than in Noinj case (where only part of upstream injector air is swirled) and so interaction between swirl profile, blade and secondary flows necessarily is subjected to changes.

For what concern the MP case, the intensity of underturning at 75% of the span is reduced, while the one of overturning below increases with respect to Clean case. Moreover at 45% of blade span, the underturning becomes stronger. This common trend in $10Hz$ and Noinj is directly linked to the swirl profile that is injected upstream stator at about 50% of the span and that rotates clockwise (according to the point of view of α mass averaged graph). It makes the values of alpha increase

between 50% and 75% of blade span and decrease between 30% and 50% of the span, thus affecting significantly the stator outlet absolute flow angle.
It's important to notice that these results from circumferential mass averages perfectly match with the maps in Fig. 7.30 and Fig. 7.31.
The analysis of the results in the HS injection case (Fig. 7.33), that regarding the losses are similar to ones of the tests with swirled EW injection, gives the following stator outlet absolute flow angle trends:

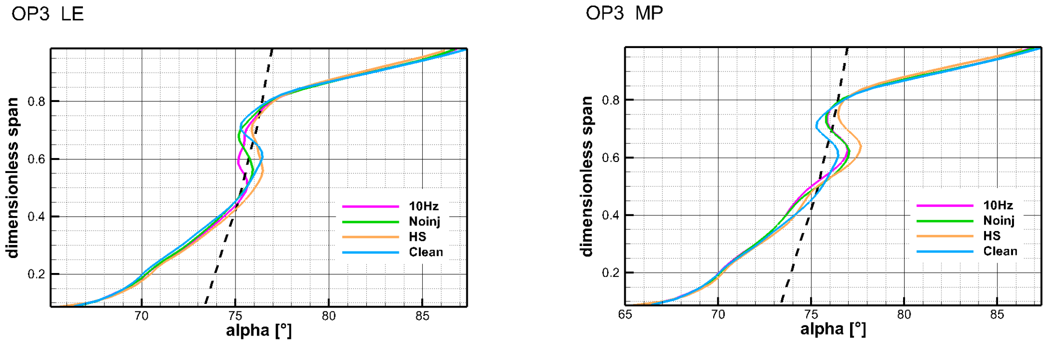

Figure 7.33: Circumferential mass averaged stator outlet absolute flow angle for both clocking positions in $10Hz$, Noinj, HS, Clean cases (OP3)

It can be noticed that in case of hot streak injected at LE, the trend of α is more similar to the one of Noinj case rather than to $10Hz$, even if underturning zone is less pronounced and overturning one is wider in comparison with the Noinj profile. This similarity can be probably related to the analogous profiles of flow angle at stator inlet Fig. 6.18. In MP case the underturning above midspan is further reduced and overturning becomes stronger. Fig. 7.34 shows the maps of $\Delta\alpha$ for HS injection in the two clocking positions. The profiles in Fig. 7.33 find a confirm in the $\Delta\alpha$ fields.

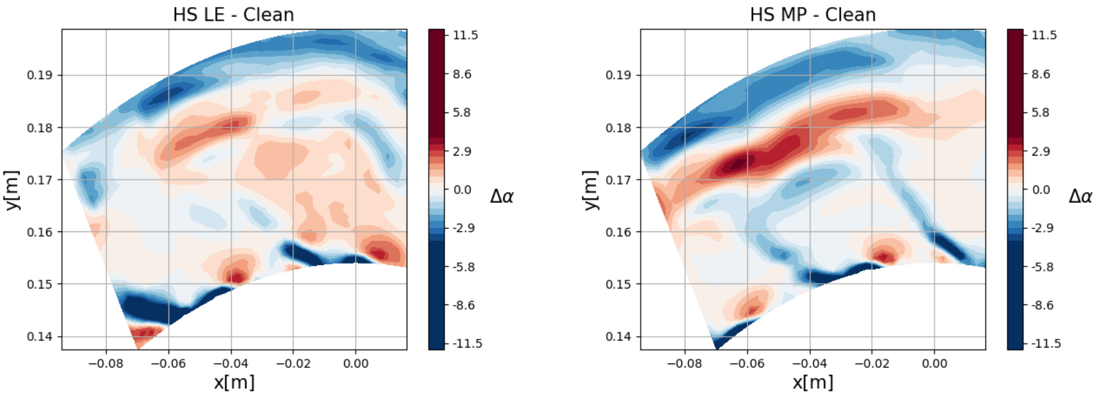

Figure 7.34: $\Delta\alpha$ calculated from HS LE - Clean and HS MP - Clean (OP3)

7.5.1.3 Relative flow angle and incidence

It's worth to remember that any change in absolute flow angle α produces a relative flow angle β variation leading to differences in incidence on rotor blades. Moreover a hotter flow injection, that has higher enthalpy content, should reach higher velocity values and consequently higher relative flow angles. For these reasons, it becomes interesting to look at the evolution of β (labeled "beta" in the graphs) and at the trend of incidence (labeled "inc" in the graphs) along the blade span with changing the injection setup (Figs. 7.35 and 7.36). The black dashed lines in Fig. 7.35 represent the rotor blade geometric angle trend along the dimensionless span. As for absolute flow angle, also for relative flow angle β the most evident changes among the different tests are found around midspan, especially above. In particular it can be seen that the HS injection leads to higher relative flow angles which imply greater incidence on rotor blades. This effect is stronger for MP injection position, but it is present also for LE one. For what concerns $10Hz$ and Noinj cases, β is lower for LE injection and higher for MP position with respect to Clean results and this agrees with the evolution of α.

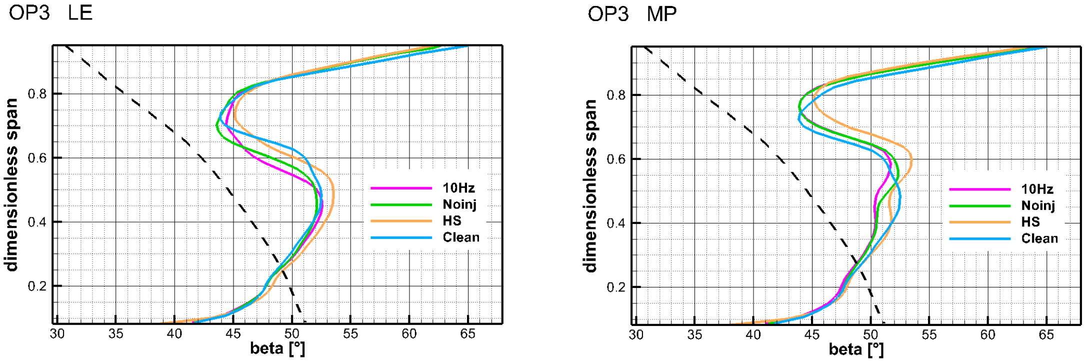

Figure 7.35: Relative flow angle β for both LE and MP injection positions (OP3)

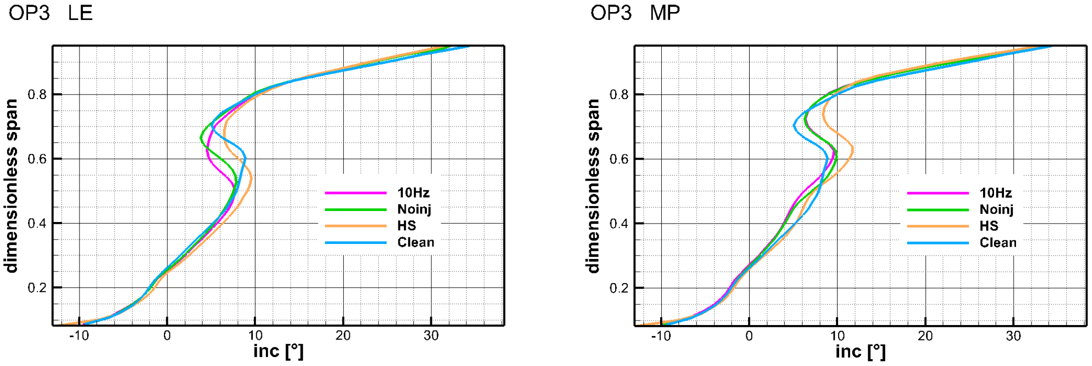

Figure 7.36: Incidence profiles for both LE and MP injection positions (OP3)

7.5.1.4 Streamwise helicity

In order to complete the analysis in OP3 condition, streamwise helicity maps for different injection conditions are analyzed and compared to the one obtained in Clean condition. In this way it is possible to see where the swirl profile affects most the vortical structures at the measuring section. Fig. 7.37 shows the streamwise helicity maps in Clean, Noinj LE and MP cases, while Fig. 7.38 shows the maps in Clean, $10Hz$ LE and MP. These tests have been chosen since they are considered to be the most representative. From these pictures it's clear that the swirl profile injection causes modification in vortical structures downstream the stator both for LE and MP clocking position. Given that the swirl profile is characterized by negative streamwise helicity (counterclokwise), it leads to a reduction in helicity within the blade passage (positive in Clean case). Looking at the LE case, the experiments show that the swirl profile remains on suction side interacting with boundary layer before being released at trailing edge where it merges with wake flow. The interaction with boundary layer leads to a decrease of streamwise helicity in the region highlighted by the ellipse and this effect is stronger in $10Hz$ case than in Noinj. Moreover the negative helicity wake region becomes much wider in LE injection case with respect to Clean and MP injection conditions. When injection takes place at MP position, the helicity within the blade channel decreases in the zone entrained by the circle, meaning that the swirl profile affects the vortical structures in that region. Moreover also the wake region results modified at the measuring section in comparison with Clean case, maybe due to the viscous interaction between swirled entropy wave and mainstream that causes an increase in helicity.

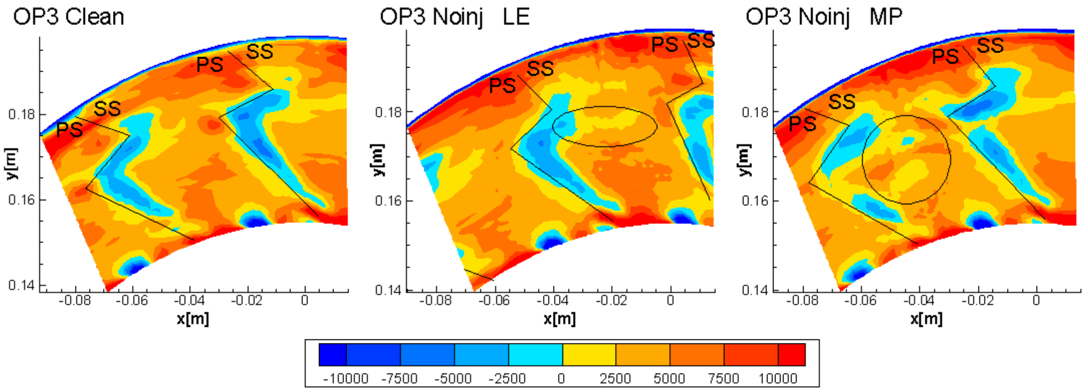

Figure 7.37: Streamwise helicity maps for the cases Clean, Noinj LE and Noinj MP in OP3

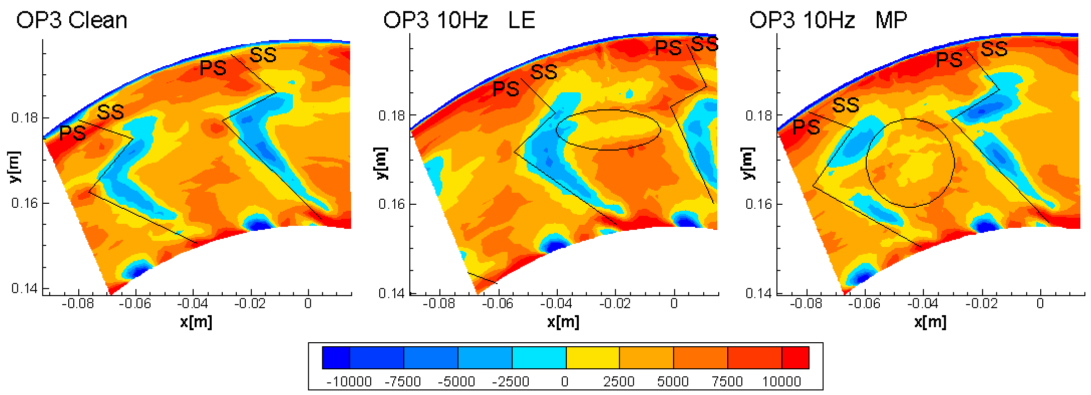

Figure 7.38: Streamwise helicity maps for the cases Clean, $10Hz$ LE and $10Hz$ MP in OP3

In MP case the breakdown of the negative vorticity regions, in correspondence of the wake, could be related to the blockage introduced by the swirl and the injector presence, which causes a redistribution of the flow that affects vorticity at measuring section.

7.5.2 OP2

7.5.2.1 Total pressure loss coefficient

As it has already seen for OP3 tests results, also for OP2 ones the losses and the other aerodynamic quantities don't show appreciable differences with changing injection frequency. This can be seen looking at Fig. 7.39 and Fig. 7.40. Moreover, the conclusion found in OP3 about the contribution to losses of the swirl profile is still valid: the main responsible for losses increase with respect to Clean case is the swirl profile injection rather than the EW. Fig. 7.41 and Fig. 7.42 show the trend of circumferential mass averaged loss coefficient over the dimensionless span and the maps of loss coefficient in Noinj and $10Hz$ conditions, respectively. For further details about loss coefficient evolution refers to OP3 section (Section 7.5.1.1) since the OP2 results are very similar both in morphology and values. Fig. 7.43 provides a detail of the total pressure loss coefficient trend for both the clocking positions in different injection conditions with the purpose of sum up all the relevant cases and achieve better idea about its evolution.

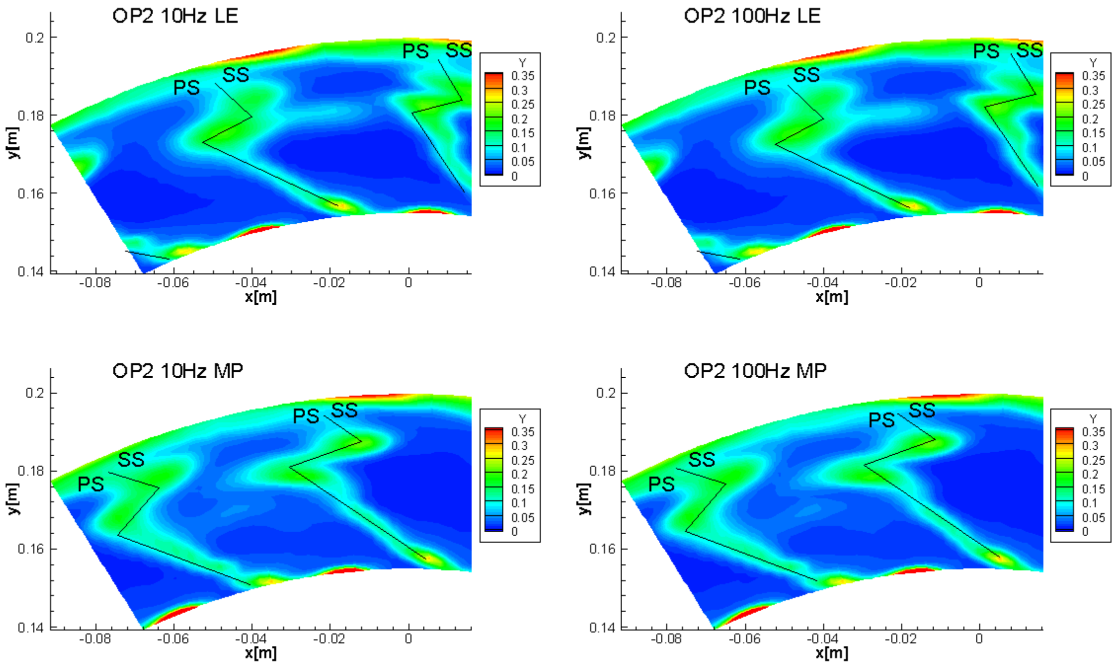

Figure 7.39: Loss coefficient maps for OP2 10Hz LE, OP2 10Hz MP, OP2 100Hz LE and OP2 100Hz MP

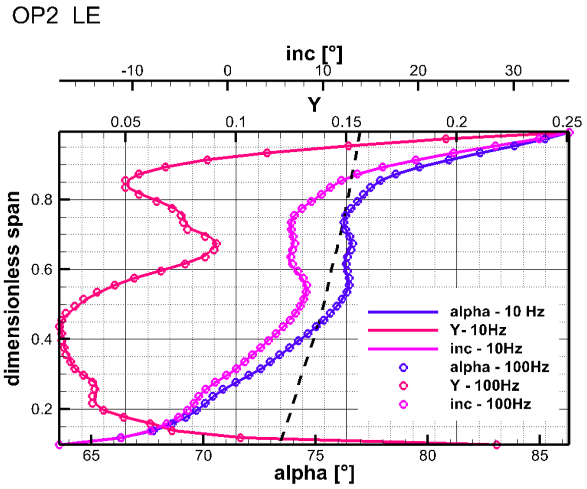

Figure 7.40: Circumferential mass averaged loss coefficient, stator outlet flow angle and incidence in OP2 10Hz LE and OP2 100Hz LE

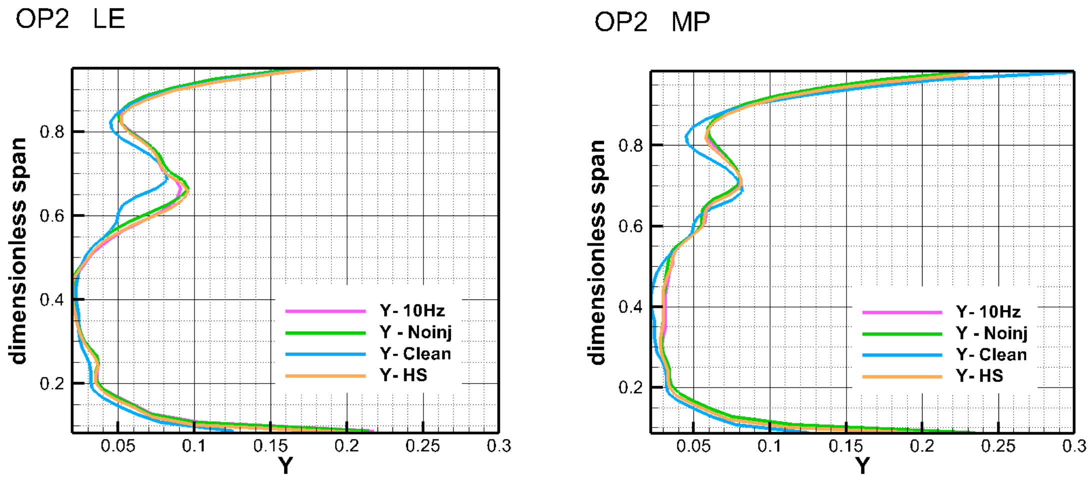

Figure 7.41: Circumferential mass averaged loss coefficient for OP2 with EWG switched on with injection frequency set equal to $10Hz$, in Noinj, Clean and HS conditions for the two injection positions

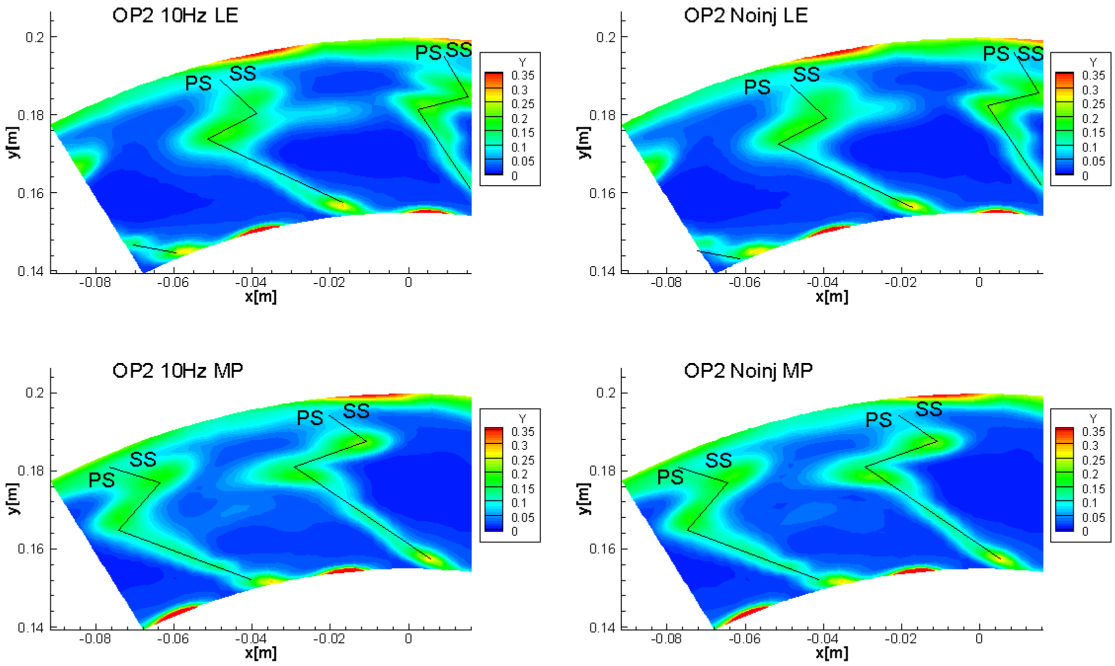

Figure 7.42: Loss coefficient maps for $10Hz$ LE, $10Hz$ MP, Noinj LE and Noinj MP in OP2

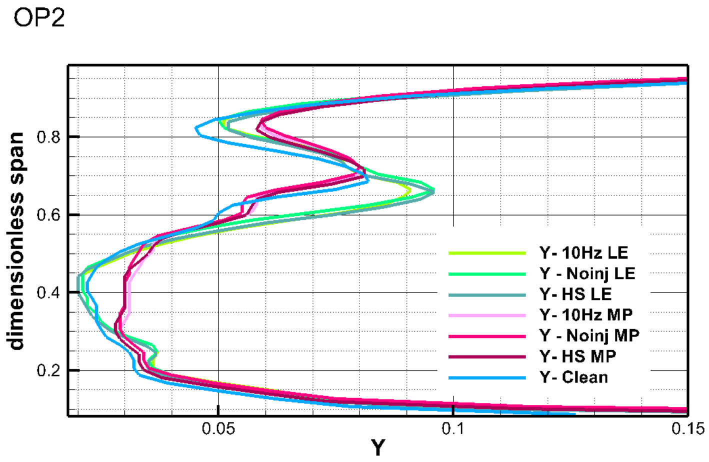

Figure 7.43: Detail of circumferential mass averaged loss coefficient for OP2 in different configurations

Thanks to the same algorithm used during OP3 analysis for estimating an overall loss coefficient in each test, it's possible to determine which injection configuration ensures highest losses. In Table 7.3 the calculated mass weighted loss coefficients are collected (expressed as percentages). As expected, the Clean case is the one characterized by lowest losses, while greatest values are reached with EW injection. The consideration about the influence of swirl profile injection on losses is further confirmed by the values of the coefficients: the difference between Clean case value and Noinj ones is higher than the difference between the latter and values obtained with EW injection. In OP2 increasing the injection frequency leads to slightly lower loss coefficients while, as in OP3, the injection position which gives little greater losses is LE. Although from these calculations it results that the difference between MP and LE values are very small, it must be kept in mind that the morphology of the wake significantly changes and this for sure affects the aerodynamics inside rotor.

Table 7.3: Percental mean loss coefficients in different injection setups (OP2)

Clean		**10Hz**	**100Hz**	**Noinj**	**HS**
5.0	**LE**	6.1	6.0	6.0	6.0
5.0	**MP**	6.0	5.9	5.9	5.9

7.5.2.2 Absolute flow angle

Now the analysis can focus on absolute flow angle α. In Fig. 7.44 the maps obtained in Noinj and $10Hz$ set ups are shown for both the clocking positions. If they are compared with Clean map in Fig. 7.6, no huge variations are visible even if above midspan it can be seen a general decrease of flow angle in LE cases, while an increase in the same zone in MP case. In order to get a proof to confirm this conclusion, it's possible to look also at Fig. 7.45 in which azimuthal mass averaged flow angle profiles in the different test configurations are compared with Clean case. The results for Noinj and HS tests are very similar for both injection positions, and in MP case also the $10Hz$ profile overlaps with those two profiles. However, when EW is injected at the LE, the overturning close to the 60% of blade span becomes weaker with respect to Clean case and this can be related to the interaction between the tip passage vortex and the swirl profile of the pulsating disturb. When injection takes place in correspondence of MP, the injected swirl causes an increase of overturning at about 65% of the span and an increase of underturning below midspan. In comparison with OP3, the variations given by disturb injection are more restrained, especially in LE case.

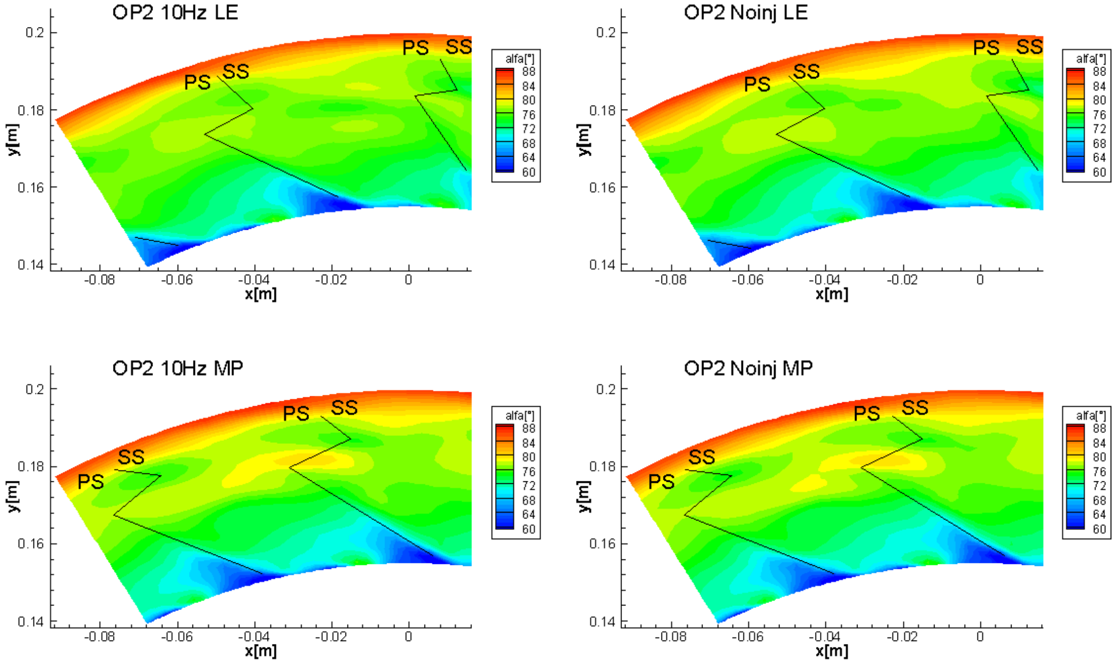

Figure 7.44: Absolute flow angle maps for $10Hz$ LE, $10Hz$ MP, Noinj LE and Noinj MP (OP2)

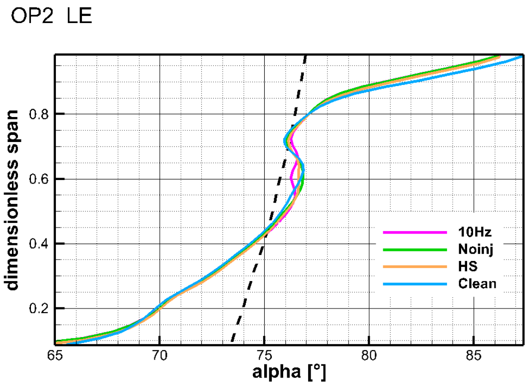

Figure 7.45: Circumferential mass averaged stator outlet absolute flow angle for both clocking positions in $10Hz$, Noinj, HS, Clean cases (OP2)

7.5.2.3 Relative flow angle and incidence

The relative flow angle β is strongly dependent on flow temperature and so only the results coming from HS tests for LE and MP clocking positions are considered between all the tests where thermal perturbation is injected. In fact, only in HS case the temperature field is available and so the corrected temperature values have been taken into account during 5-holes data elaboration. As already mentioned, in $10Hz$ and $100Hz$ tests, temperature fields are not available since the intensity of aerodynamic field led to the failure of the thermocouple measuring junction and so the values of β angles are not reliable. Fig. 7.46 shows the circumferential mass averaged relative flow angle (labelled as "beta"). The black dashed lines represent the evolution of rotor blade geometric angle along the dimensionless span. Fig. 7.47 shows the trend of the incidence angle (labelled as "inc") calculated as the difference between relative flow angle and blade geometric angle.

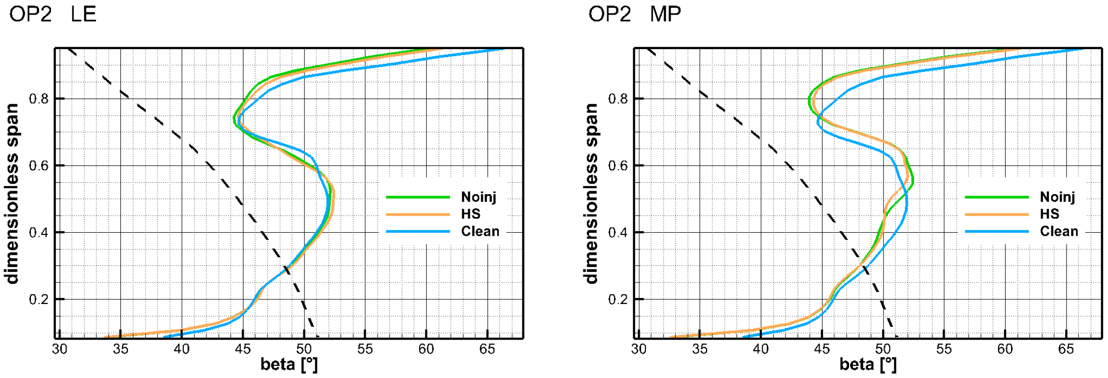

Figure 7.46: Relative flow angle β for both LE and MP injection positions (OP2)

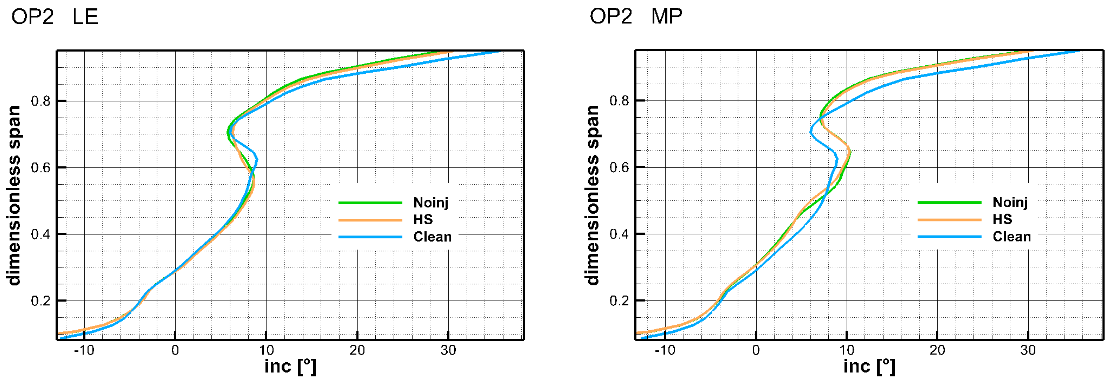

Figure 7.47: Incidence profiles for both LE and MP injection positions (OP2)

7.5.2.4 Streamwise helicity

Helicity maps are shown in Fig. 7.48 and Fig. 7.49. In the first picture the Clean case is compared with Noinj in the two injection position, while in the second one it is compared with HS results. The latter injection setup has been chosen instead of $10Hz$ because knowing absolute velocity is required in the calculation of streamwise helicity. In HS case the absolute velocity values are more reliable than in $10Hz$ because temperature data have been used during 5-holes data elaboration. As already seen in OP3 results analysis, in the LE injection case the swirl profile remains on suction side interacting with boundary layer before being released at trailing edge where it merges with wake flow. The negative helicity region in correspondence of the wake zone becomes wider in Noinj and HS cases with respect to Clean. When injection takes place at MP position, the helicity within the blade channel decreases in the zone entrained by the circle, meaning that the swirl profile affects the vortical structures in that region. This effect is stronger in HS injection case in which a negative helicity zone detaches from pressure side going towards suction side of adjacent blade.

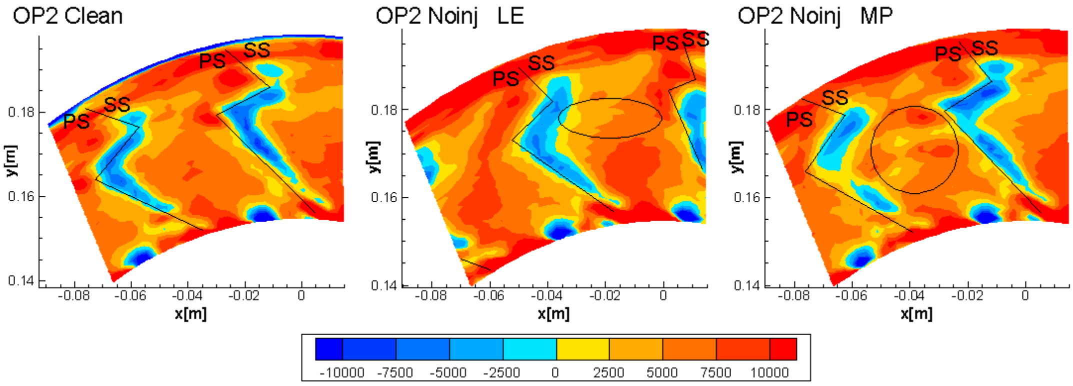

Figure 7.48: Streamwise helicity maps for the cases Clean, Noinj LE and Noinj MP in OP2

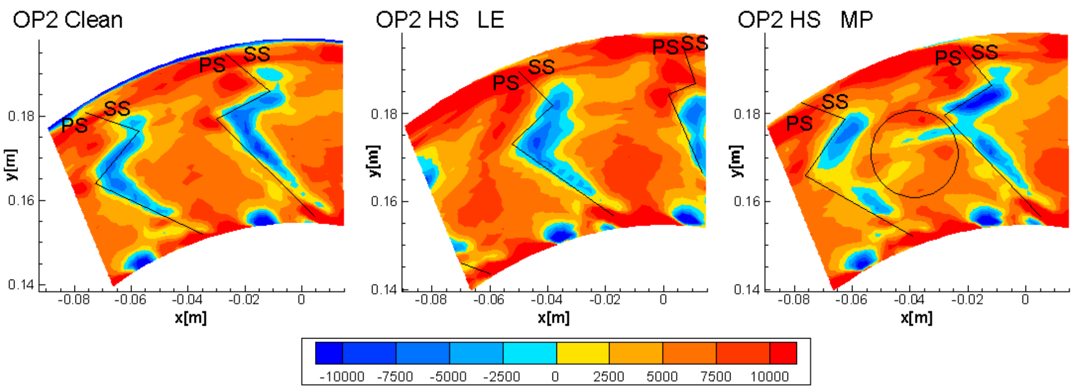

Figure 7.49: Streamwise helicity maps for the cases Clean, HS LE and HS MP in OP2

Also in OP2, the wake region helicity behavior in MP case is similar to the one seen in OP3, Section 7.5.1.4. In general comparing OP2 and OP3, it is possible to state that the swirling disturb effects have a lower impact in OP2. This could be traced back to the relatively higher helicity field characterizing OP2 condition.

7.5.2.5 Unsteady analysis

Thanks to FRAPP it's possible to perform unsteady analysis. Given that temperature field is not available, no graphical representations about velocity, relative flow angle and incidence can be realized. However temperature doesn't affect total pressure and absolute flow angle measured by the probe and so these are the quantities of interest. Fig. 7.50 and Fig. 7.51 show the peak-to-trough values of these variables at LE and MP respectively. Peak-to-trough values are calculated point by point as the difference between maximum value acquired in time and minimum one calculated in the same location, so they give an idea about fluctuation of quantities. In the LE case, the injected perturbation is transported on the blade surface, while in MP case it interacts significantly with secondary flows that reduce its strength at the vane outlet. This is the reason why in LE case, the peak-to-trough values are higher with respect to MP so the unsteadiness introduced by injected perturbation results somehow reduced for passage-aligned injection. In [17] OP3 have been analyzed and it has been demonstrated that maximum peak-to-trough values of total pressure and absolute flow angle are found nearby the maximum peak-to-trough total temperature region. However their spatial location do not match precisely because unsteadiness is also introduced by the swirl generator, in addition to one given by temperature perturbation. The same is expected to be valid also for OP2, even if it should be verified by using a fast response thermocouple capable of withstanding such aerodynamic loading. Thanks to phase-average procedure, the contribution of injected perturbation becomes clearer. Regarding LE injection case, the higher losses (thus lower total pressure) region that seems to detach from blade suction side above midspan (area inside the ellipse in Fig. 7.50) and the thickening of the wake around midspan are caused by swirled EW injection. In fact there is a spatial correspondence between maximum peak-to-peak values of both total pressure (labeled as ”Delta_pt”) and yaw angle (labeled as ”Delta_yw”), and the location where wake morphology changes or total pressure decreases (inside blade channel). The circle in Fig. 7.50 highlights the maximum peak-to-peak total pressure value, that is where the highest fluctuation is reached. Also for MP injection case (Fig. 7.51), a link can be established between the lower total pressure zone that originates from pressure side above midspan (identified by the circle) and injected disturbance. In fact, in the same location the maximum peak-to-peak value of total pressure and yaw angle can be found.

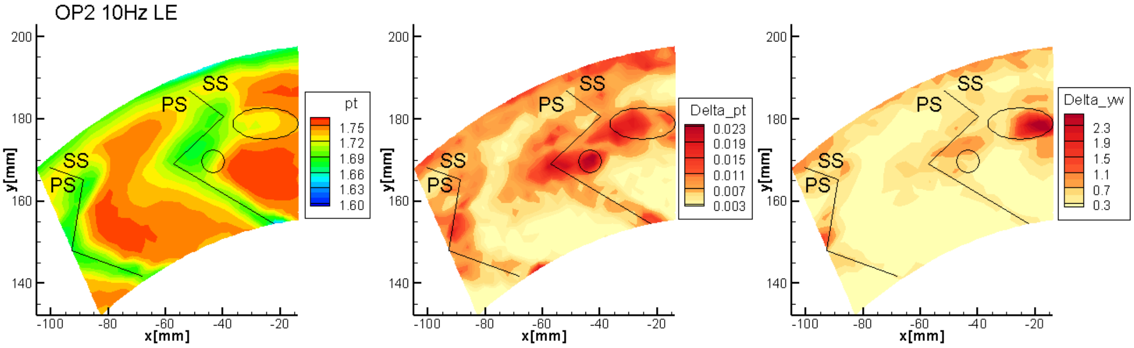

Figure 7.50: Phase-average results at stator outlet measuring section for LE injection: total pressure [*bar*], peak-to-peak total pressure [*bar*] and peak-to-peak yaw angle [°]

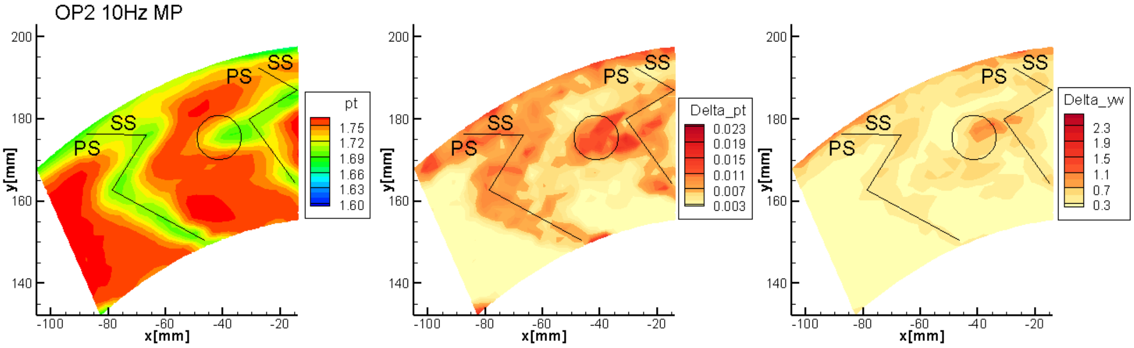

Figure 7.51: Phase-average results at stator outlet measuring section for MP injection: total pressure [*bar*], peak-to-peak total pressure [*bar*] and peak-to-peak yaw angle [°]

Chapter 8

Rotor outlet measurements

In this section it is reported the analysis of the flow features at the outlet of the rotor row.

Multiple flow characteristics could be of interest at the involved measuring section, T3, and while at stator outlet no differences have been highlighted among the OP3 cases at different loading, in this case the three different loading conditions, OP3 OP3L and OP3U have been extensively considered.

In fact the rotor behavior among those three conditions presents non negligible differences. As a consequence, together with the comparison of OP3 and OP2, OP3L and OP3U are here discussed.

A comparison among the cases in Clean condition results necessary at first to fully understand the flow behavior in absence of disturbances. In a second part the analysis is instead carried out on the differential effects observed on the whole set of operating conditions in presence of the considered aerodynamic and thermal disturbs.

Hence, all the different operating conditions, in terms of load and expansion ratio, have been analyzed in presence of EW, at $10Hz$ and $100Hz$, of HS and in Noinj conditions for both the MP and LE clocking positions. Both absolute and relative frame of reference are considered, however particular focus has been made on the latter to achieve an easier interpretation of flow features.

All data concerning rotor outlet measuring section are derived from FRAPP and T_{fast} measurements. The presented flow fields refer to what an observer placed downstream of the rotor and facing the rotor itself would see.

8.1 Absolute frame of reference and relative frame of reference

As stated before, measured quantities at the rotor outlet can be observed relaying on two different frames of reference. Those two frames are considered as 'Absolute' and 'Relative'. The absolute one is fixed with respect to the x-y-z axis of the machine, while the relative one rotates about the z axis with the same rotational speed as the one imposed to the rotor.

Probes used at rotor outlet measure values in the absolute frame as it could be observed from stator inlet and outlet. However absolute data at the outlet of the rotor can result to be tricky and of difficult interpretation, hence a particular data elaboration is useful to be able to observe measurements in the relative frame.
This data elaboration is based on the knowledge of the rotor angular frequency. This frequency is measured thanks to a signal triggered each time the shaft complete a full revolution. Thanks to the knowledge of this indicator it is possible to perform a phase averaging on the probe acquired data by associating them, at each given time, to the position of the rotoric vanes at the same moment.
Thanks to this procedure it is possible to observe flow features as the rotor perceive them.

8.2 Measurements in Clean conditions

As stated above the first analysis reported concerns all the measurements performed in 'Clean' conditions. It is interesting to look at values assumed by the circumferential mass averages of the outlet measured temperature fields and the circumferential mass averages of the deviation angle, Fig. 8.1. The deviation angle is defined as the difference between the local relative flow angle and the outlet geometrical angle of the rotor, which is constant along the span and equal to $-67.7°$.

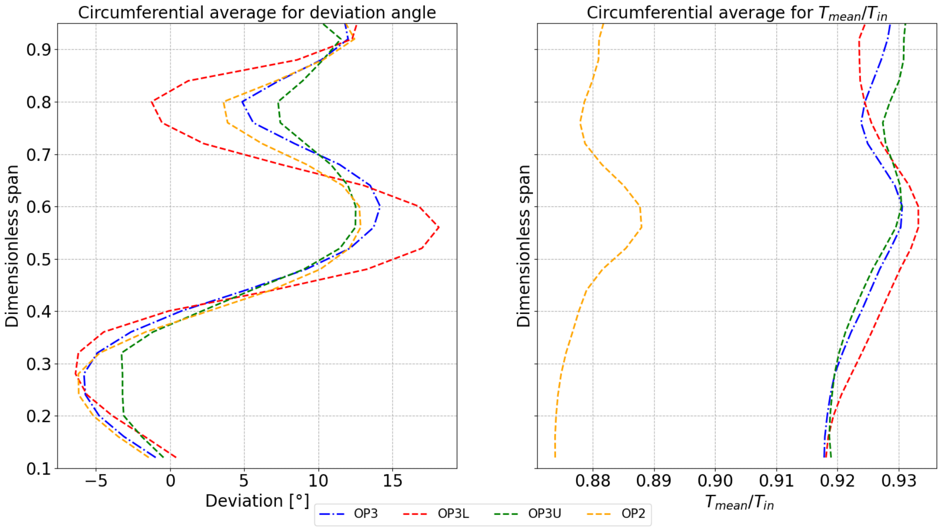

Figure 8.1: Circumferential averages weighted on mass flow rate for deviation angle and non-dimensional average total temperature at rotor outlet

Average total temperature is made non-dimensional dividing it by the total inlet temperature.
A positive deviation angle corresponds to a flow which is deflected, in relative frame, less than the blade geometric angle, hence, in correspondence of a positive deviation region, it is expected a poorer energy extraction from the flow with respect to regions with a negative deviation.

In fact, coupling the two graphs, it results glaring that, at radii where deviation is high, it corresponds a high non-dimensional temperature, which is consequential of a bad work extraction from the fluid. The same correspondence is observed with low deviation and low non-dimensional temperature.
However, circumferential values do not give substantial clues about mechanisms responsible for different degree of energy extraction nor about coordinates of the loss core at measuring plane. So it could be useful to observe the fields concerning a so called "relative total pressure coefficient" defined as:

$$cp_{tr} = \frac{p_{tr} - p_{sv}}{p_{tm} - p_{sv}} \tag{8.1}$$

And p_{tr} is the relative total pressure measured by the probe, p_{sv} is the static pressure downstream of the stage and p_{tm} is the average total pressure upstream of the turbine. Since the coefficient is defined in the relative frame of reference its value is related to the loss mechanisms present in the rotor vanes. cp_{tr} fields can be observed in Fig. 8.2.

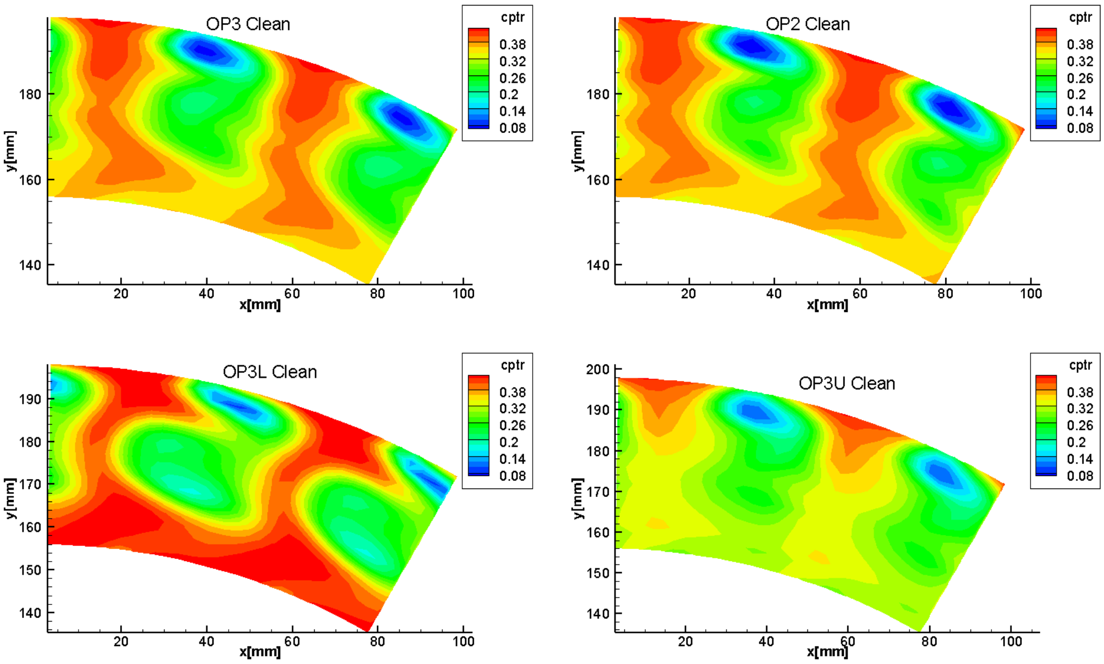

Figure 8.2: cp_{tr} fields in the four considered conditions

A first observation that can be done on the cp_{tr} fields concerns OP3 and OP2. In fact as shown above the two fields do not present huge discrepancies. As a matter of fact this is justified by the cinematic similitude at rotor among the two operative conditions. This behavior is similar to the one observed at stator outlet. One again to highlight the region of dissimilarities among the two fields it could be useful to plot the difference point by point of the two maps, Fig. 8.3.

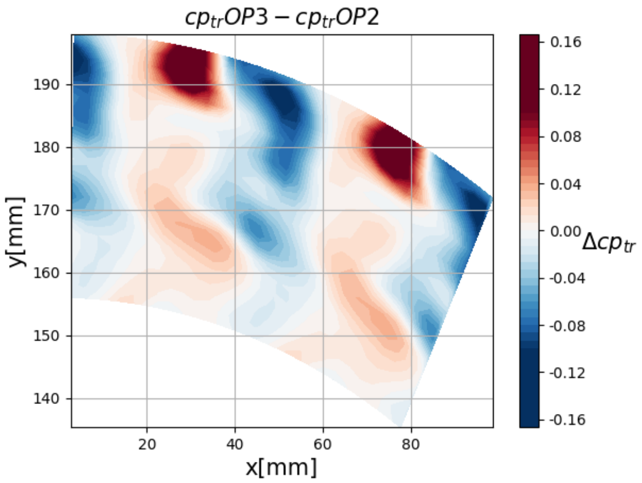

Figure 8.3: Difference of cp_{tr} fields in OP3 and OP2

From the figures above it can be remarked that, even if the two conditions of OP3 and OP2 present very similar patterns, a shift of the whole observed structure is present, hence the difference among the two maps is not negligible in some regions. Considering instead the comparison among OP3, OP3L and OP3U huge differences can be observed even at first sight. However, before doing any consideration on those differences, it is necessary to give a general overview on the regions found in those fields. As a result together with the cp_{tr} fields it is presented the deviation angle field. The different region of loss are described in Fig. 8.4 taking OP3 field as example.

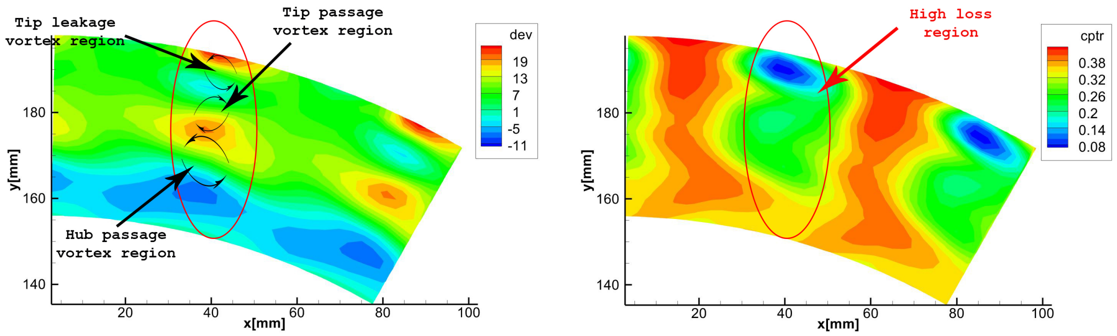

Figure 8.4: Deviation angle field (left) and cp_{tr} field (right) for OP3 case

It can be observed a core of low cp_{tr} value which denotes losses, Fig. 8.4. In particular inside the loss region (red ellipse in Fig. 8.4) a peak of losses is identified in the upper part. The examination of the same region in the deviation angle field suggests that, the peak in losses coincides with the core of a vortex present near the tip, the tip leakage vortex, which is characterized by a high underturning and a modest overturning.

Moving radially inward from the tip leakage vortex region other sources of losses can be identified. In this case losses coincides with the region in which are located the rotor passage vortexes. Once those regions of loss have been defined, it is possible

to notice their change among the different OP3 loading conditions.
However first in Fig. 8.5 it is reported the time evolution of one of the cp_{tr} maps.

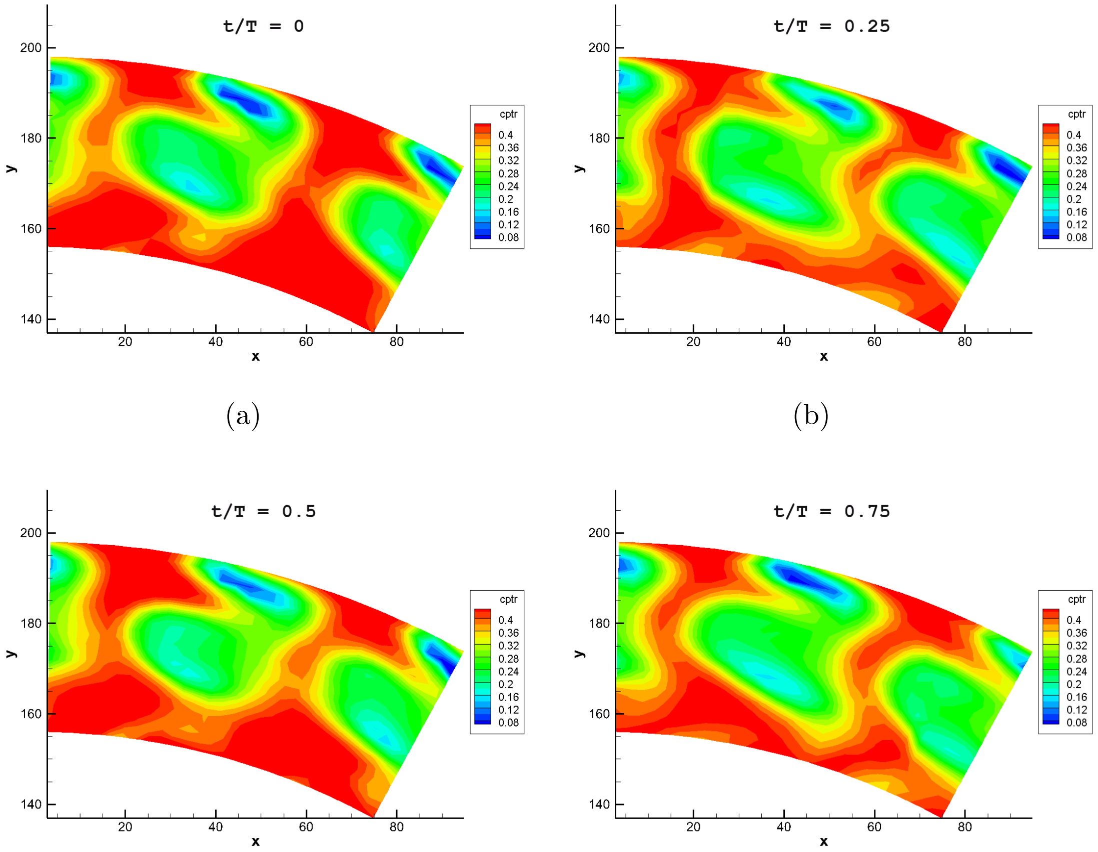

(a) (b)

(c) (d)

Figure 8.5: Reconstruction of cp_{tr} rotor downstream field in OP3L; 4 different relative positions stator-rotor represented ordered from (a) to (d); T = period considered for phase averaging

Since the loss core region does not present a sensible change in position over time and, being the fields reconstructed in the relative frame of reference, it is possible to associate them to the rotor wake together with the residual components of the rotor secondary flows. These are clearly expected to be the most influencing structures observable at the measuring plane.
In conclusion, it is possible to say that the rotor wake and the residual structured of the rotor secondary vortexes are overlapped at the measuring plane. However, while the wake region extends from tip to hub, the secondary structures do not, being pushed radially outward by the rotation effect. In the second place, all around the loss core is present a high cp_{tr} region. This high cp_{tr} region is coincident with the free stream expected position. More in general a structure of free-stream and loss exists all along the blade span, and a reduction of pitch-wise gradients moving from tip to hub is observed. This latter feature is fairly common downstream of axial flow turbomachinery rotors [20]. Now that the main features of the rotor downstream

flow has been shown, it is possible to carry on with the analysis of trends among the different operating conditions. A clear trend is the one concerning the change in shape of the loss region. In fact, the loss region changes shape with load and in particular, it passes from a radially extended shape at low load, to a more circumferential distribution at high load. As it can be seen from Fig. 8.2, in OP3U the loss region is extended from tip to hub, while in OP3L it no longer touches the hub and it is more extended in pitch-wise direction.

As a consequence, this region results well confined in OP3L. However even the remaining part of the flow has a sensible change. In fact, as the load is increased, the whole free stream region presents a sensible drop in losses magnitude together with a slight deformation; the free stream region at tip gets larger while at mid-span it gets thinner as a consequence of the loss region enlargement. The effect of load denotes in addition the almost complete disappearance of the rotor blade wake loss at hub in OP3.

A useful field, to understand where the hub region wake affects the flow field, is the α one in relative frame, Fig. 8.6.

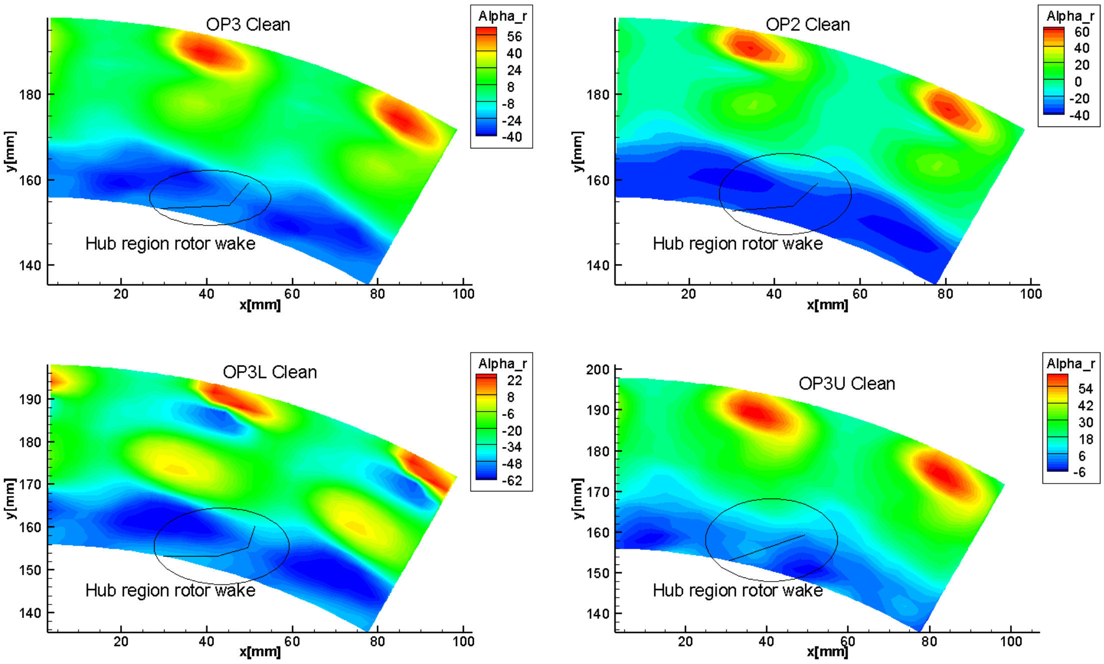

Figure 8.6: α fields in relative frame

In fact, as displayed in Fig. 8.7, considering constant the radial coordinate, a low momentum flow would present a higher value of α compared to a higher momentum one.

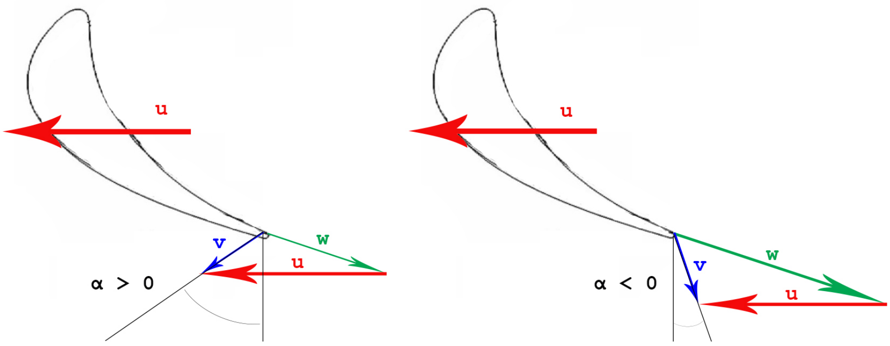

Figure 8.7: α difference based on the relative velocity magnitude, $|w|$

Instead for understanding where the wake is located it is necessary to look again at deviation fields which give information about the part of the loss region associated to the vortexes together with their strength.

Fig. 8.8, which is helpful in discern the vortexes from wake in the loss regions, shows contours of deviation angle together with iso-lines of cp_{tr} in Clean cases.

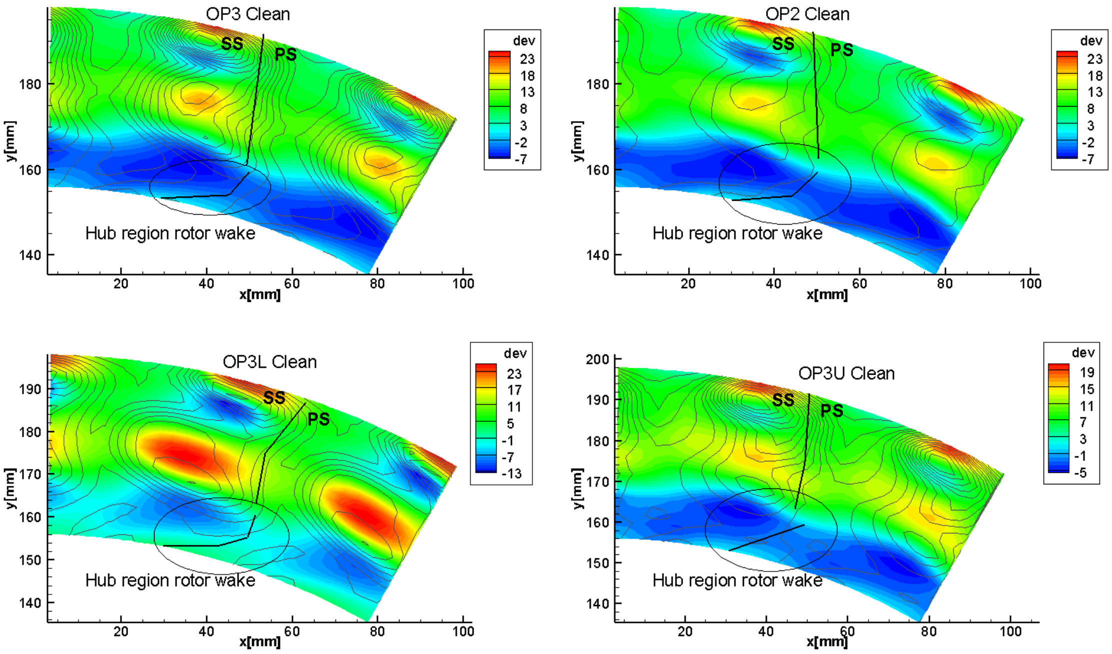

Figure 8.8: Deviation angle fields overlapped by cp_{tr} iso-lines with highlighted wake position

The wake itself is hence supposed to stay on the right of the tip passage vortex, which is affecting the flow downstream of the suction side. Starting from the right of the tip passage the wake is then supposed to occupy the region of loss, form tip to the already discussed hub region, where no effects of vortexes on deviation are observable.

In addition another interesting observation that can be done concerns the strength of the vortexes. In fact as it can be seen from Fig. 8.8, magnitude of deviation nuclei caused by the secondary flows of the rotor increases with the operating condition load. OP3U has weaker vortexes compared to OP3 while OP3L has stronger vortexes. Furthermore there's a slight increase in vortexes strength moving from OP3 to OP2. Anyway it is important to keep in mind that figures above reports average values, hence no hints about variations in time are present. So to understand where the regions most affected by variation in time are located, it is useful to look at different fields values, in particular, at the standard deviation calculated utilizing the different stator-rotor interaction relative positions Fig. 8.9. Fig. 8.9 shows fields for cp_{tr} standard deviation together with iso-lines of cp_{tr} itself.

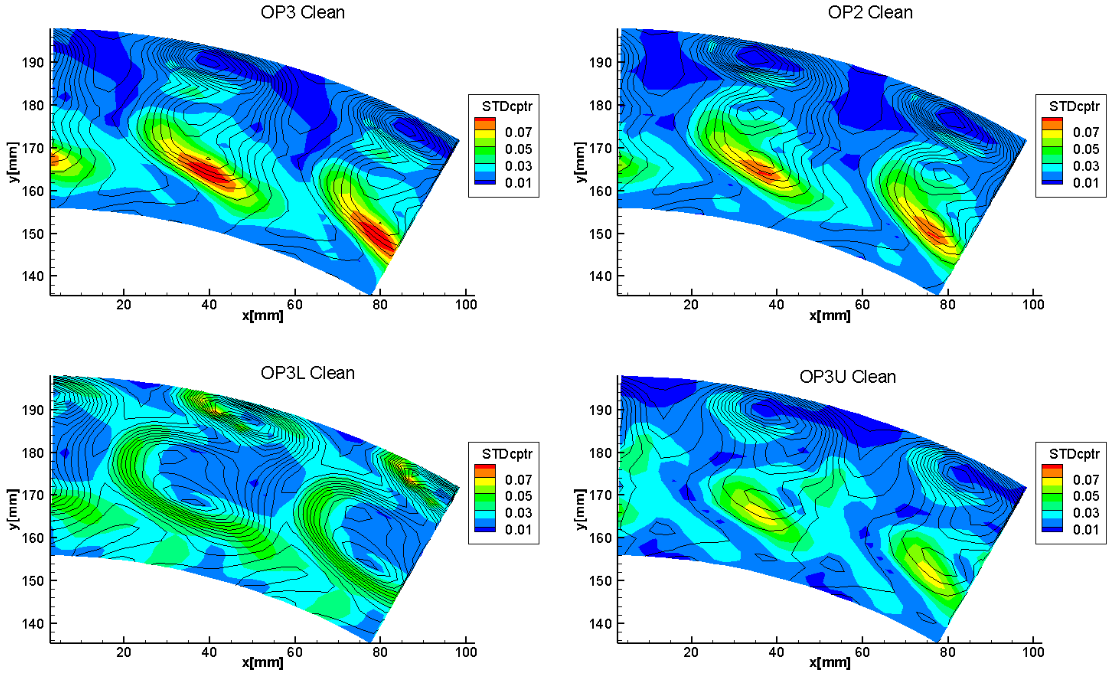

Figure 8.9: Standard deviation fields for cp_{tr}

Standard deviation fields denote a similar trend among three of the operating conditions, OP3, OP3U and OP2. In fact, those three fields highlight that the loss region presents high dispersion of values, in particular at its lower boundary, where it confines with the hub quasi-isentropic region. This is supposedly the remaining effect of the convected stator wake and secondary flows, which change behavior and position based on the relative rotor-stator location. This strong effect vanish in OP3L supposedly due to stabler vortical structures. However in OP3L a stronger variation is observable at the boundaries between vortexes and free stream regions. Anyway the strong variation of flow at hub region can be traced back to the non-uniform distribution of the stator wake along the span. In fact, while at tip region the stator wake is spread in circumferential direction, at hub it is well confined and easily distinguishable from the free stream region, see Chapter 7. To sum up, the observed unsteadiness at rotor outlet is linked to the spacial non uniformity at the outlet of the stator.

8.3 Measurements with disturbances

In this section the observable effects of the different injection configurations are presented and compared among each other. The first one to be taken into account is the one of the No-injection case. In a second moment it is analyzed the HS case and finally the EW cases.

8.3.1 No-injection

At first the circumferential averages for the 4 analyzed plant operating conditions are reported for No-injection. The reported effects are considered as the direct consequence of the presence of the injector and of the swirl.
Hence it results useful to compare the obtained data with the ones of Clean condition. In Fig. 8.10 and Fig. 8.11 both Clean and No-injection mass weighted circumferential averages are displayed for both MP and LE cases.

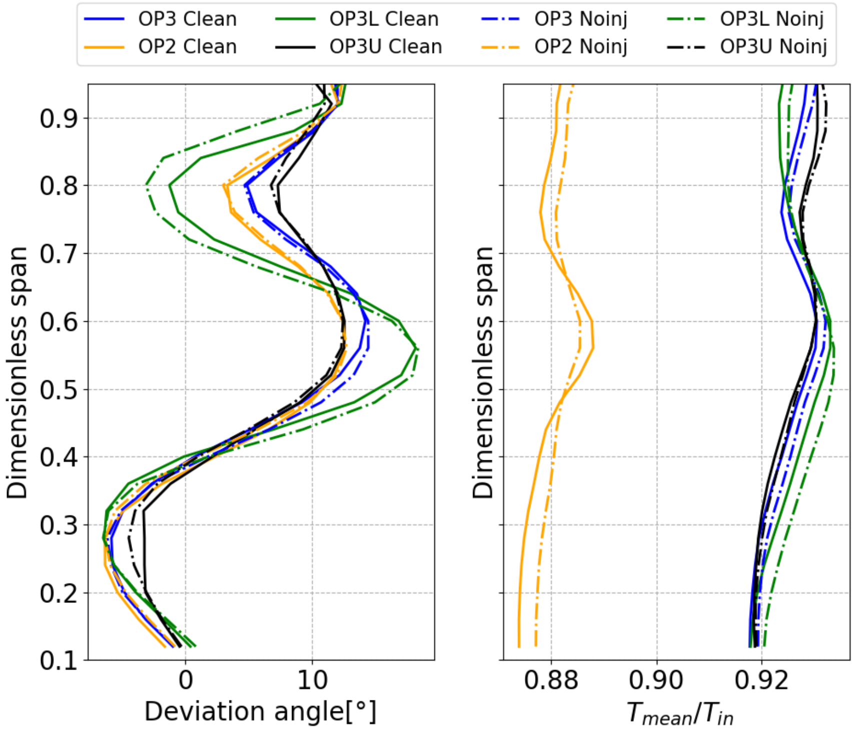

Figure 8.10: Circumferential mass averages in Clean cases and in Noinj leading edge cases

Among different plant operating conditions it holds the trend discussed in Section 8.2 for Clean tests. A first observable effect related to the presence of the injector is a slight increase of the outlet temperature, which could be blamed to the introduction of the injector aerodynamic disturb upstream of the stator. This aerodynamic disturb is supposedly affecting the whole stage reducing the work extraction compared to the Clean case.

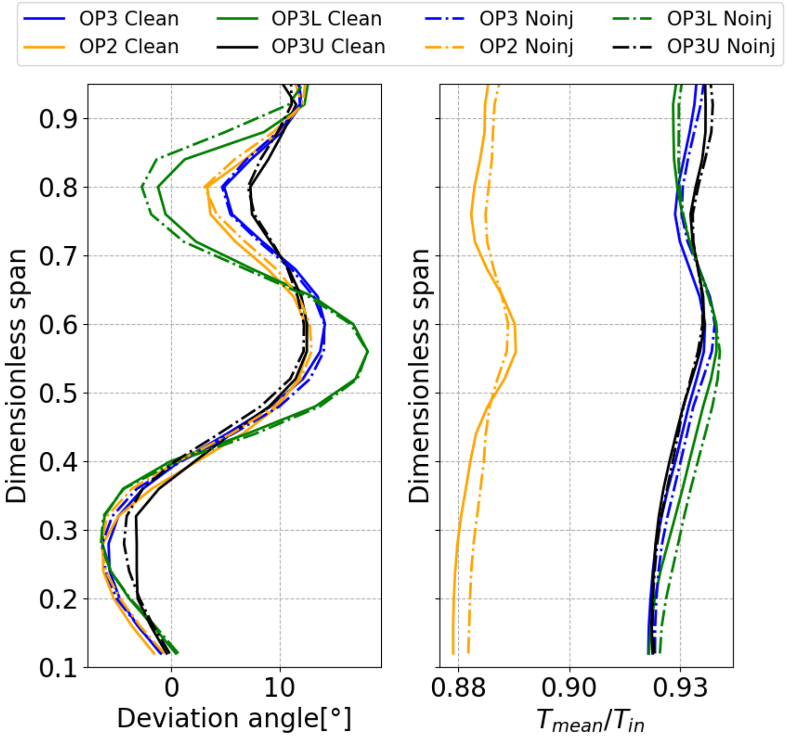

Figure 8.11: Circumferential mass averages in Clean cases and in Noinj mid pitch cases

By looking at circumferential averages of MP case the difference with Clean cases is reduced more than in LE. A useful value to be studied is the circumferential average of cp_{tr}, Fig. 8.12. In fact coupling the information on deviation angle and the information on cp_{tr} it is possible to understand at which radial coordinate it should be expected a high extraction of work and whether this extraction of work would be efficient or not. For what concerns the Clean conditions it is possible to couple the high value of cp_{tr} at hub region with the negative value of deviation. This means that the blade at this location is converting energy in a relatively efficient way and it is possibly extracting a relatively high amount of work. A similar trend is observed in No-injection cases for both deviation and cp_{tr}. It is interesting to notice that the introduction of swirl upstream of the stator increases the pressure losses observable at rotor outlet in design conditions (OP2 and OP3), while it decreases the pressure losses in off-design conditions (OP3L and OP3U). This trend is present both in MP and LE cases. In particular by looking at OP3L in LE case a huge tangible increase in cp_{tr} is present at 0.8 of the span. This peak at 0.8 of the span is coincident with a local minimum in deviation, Figs. 8.10 and 8.11. In addition, even by looking at deviation plot it is possible to notice a decrease in deviation in Noinj compared to Clean conditions during plant off-design. Instead once again the swirl introduction in design operative condition doesn't bring a great variation.

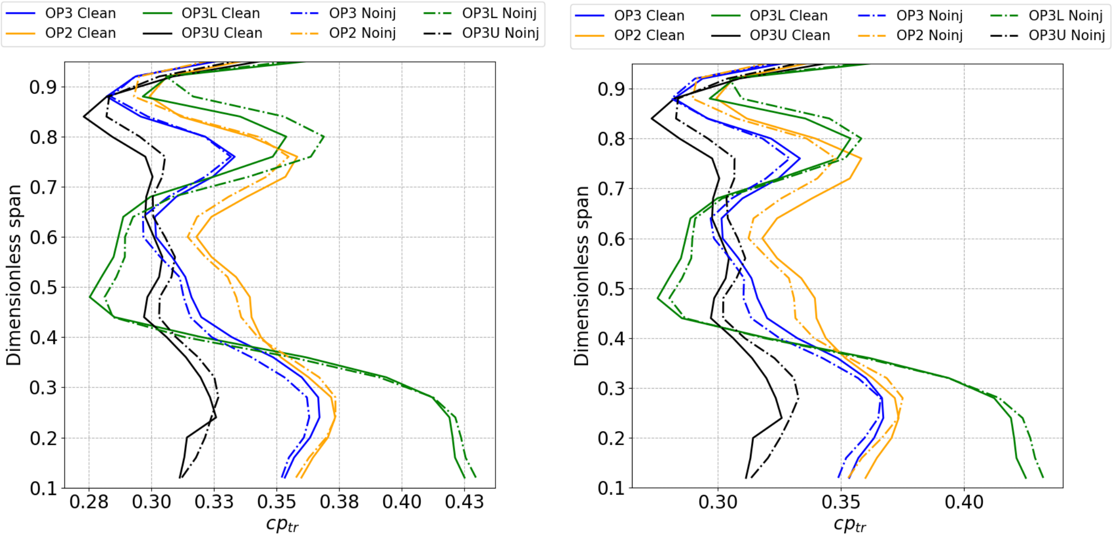

(a) (b)

Figure 8.12: Circumferential cp_{tr} mass averages in Clean cases and in Noinj LE cases (a), and in Noinj MP cases (b)

The good effect of swirl introduction on the OP3L off-design condition is observable even between 0.7 and 0.4 of the span. In fact in this range it is found that the minimum value of cp_{tr} increases and the maximum of the deflection stays the same.

8.3.2 Hot-streak

Here are reported the circumferential averages for HS in the 4 analyzed plant operating conditions. The direct comparison here presented is the one with the No-injection case, Figs. 8.13 and 8.14. This is done for highlighting the effects given by the introduction of a thermal disturb overlapped to the aerodynamic one. The choice of the HS over the EW cases is justified by the fact that the imposed aerodynamic disturb, upstream of the stator, is very similar to the one perceived in Noinj case.

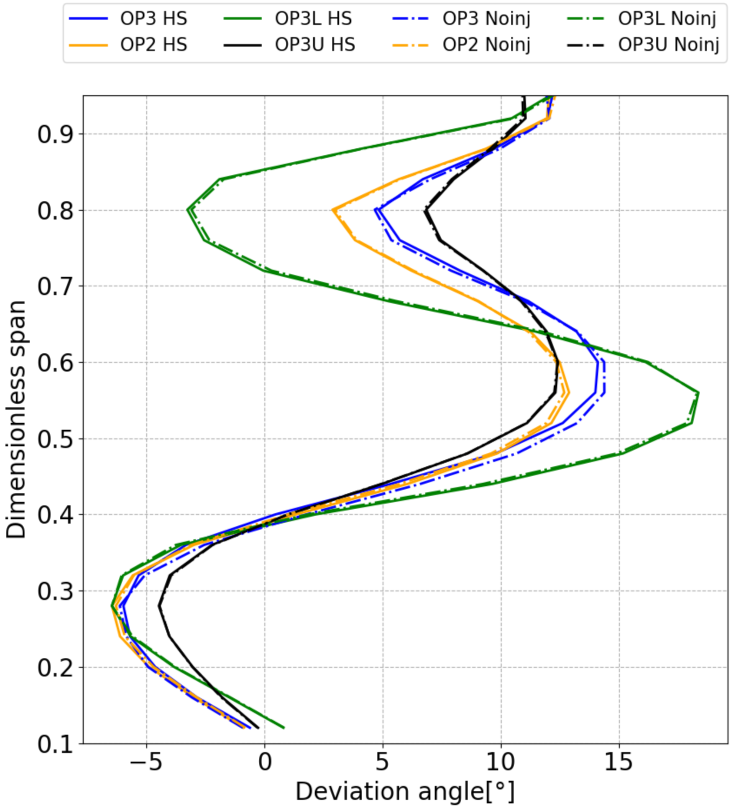

Figure 8.13: Circumferential mass averages in HS LE cases and in Noinj LE cases

It is highlighted by the plot of HS and Noinj at the same time that, given a completely overlapped deviation angle average trend for each plant operating condition, the two aerodynamic disturbs seem to not differ at the outlet of the rotor. In particular, for HS and Noinj it could be interesting to observe the point by point values, to highlight further differences.

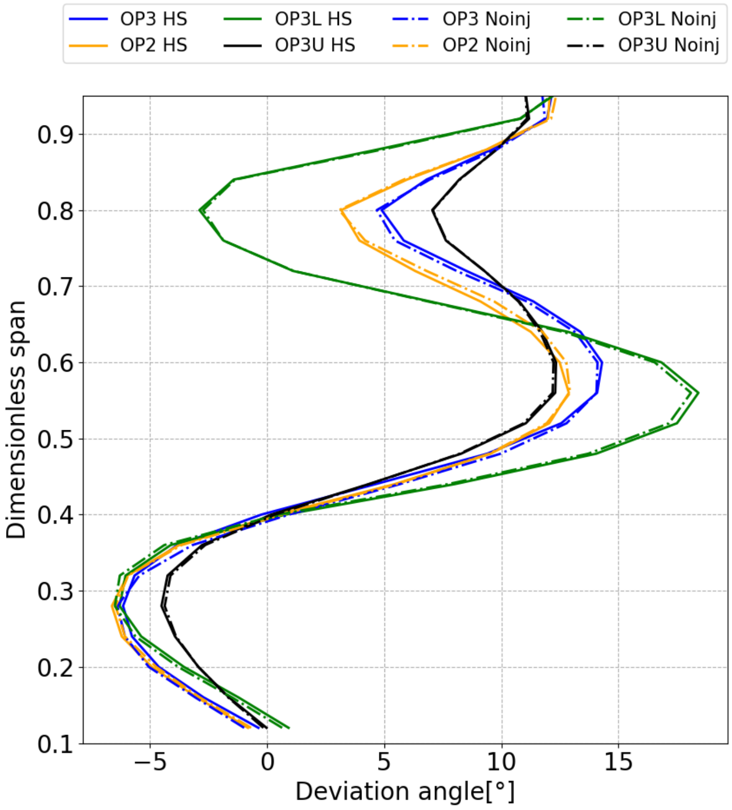

Figure 8.14: Circumferential mass averages in HS MP cases and in Noinj MP cases

Even in this case, in order to better characterize the energy conversion process performed by the rotor the analysis of the circumferential averages of cp_{tr} comes out to be useful. Fig. 8.15 reports the Noinj and HS cases compared for both LE and MP. In terms of deviation angles the discrepancies between HS and Noinj are tiny, the most important discrepancy among the 4 operating conditions involves OP3. Both MP and LE have very similar trends. OP3L seems to be the more stable operating condition among the four, since both the deviation and the cp_{tr} averages in HS and Noinj perfectly overlap. As a result in OP3L the beneficial effect with respect to the Clean condition still holds for HS both in LE and MP cases.

The introduction of a thermal disturb, or a slightly stronger swirled structure has however a different effect among the other operating conditions.

The other off-design condition, OP3U, presents instead an opposite trend among LE and MP. In fact with LE injection cp_{tr} average values are slightly reduced compared to the Noinj ones. Instead with MP injection cp_{tr} average values are slightly increased with a peak of increase at about 0.3 of the span.

In the case of OP2, design condition, the trend imposed by the simple swirl is reversed by the Hot streak introduction, in fact cp_{tr} average values are slightly higher for HS throughout the whole span.

Instead the other design condition presents different effects above mid-span and below mid-span. Below mid-span HS has the effect of increasing cp_{tr}, while above mid-span of decreasing it. In MP case the decreasing effect is stronger while the increasing one is weaker.

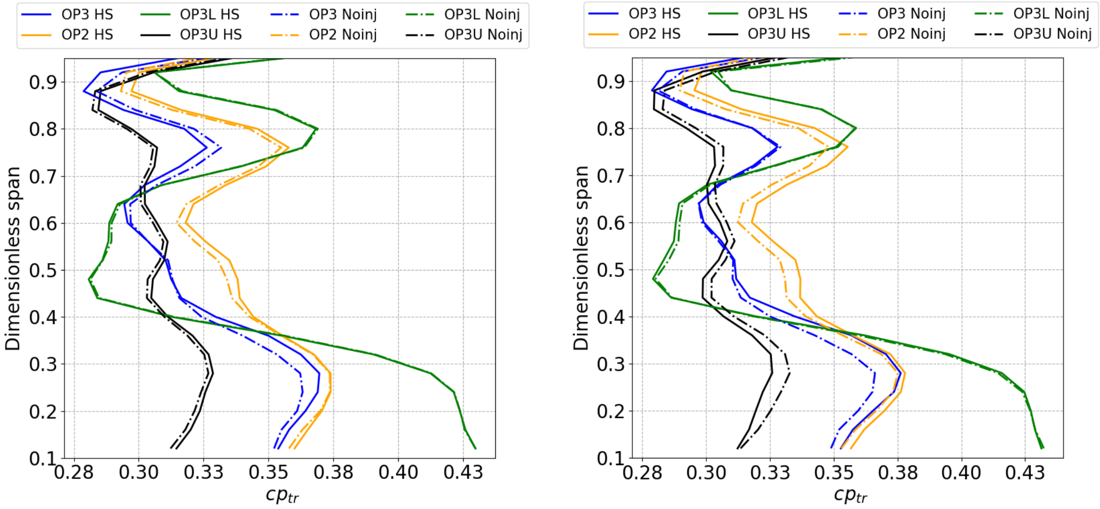

(a)

(b)

Figure 8.15: Circumferential cp_{tr} mass averages in HS LE cases and in Noinj LE cases (a), and in HS MP in Noinj MP cases (b)

8.3.3 EW $10Hz$ and $100Hz$

The effects on circumferential averages given by the pulsated disturbs are here analyzed. At first a comparison between $10Hz$ and $100Hz$ circumferential mass averages is reported, Fig. 8.16 presents deviation and cp_{tr} values.

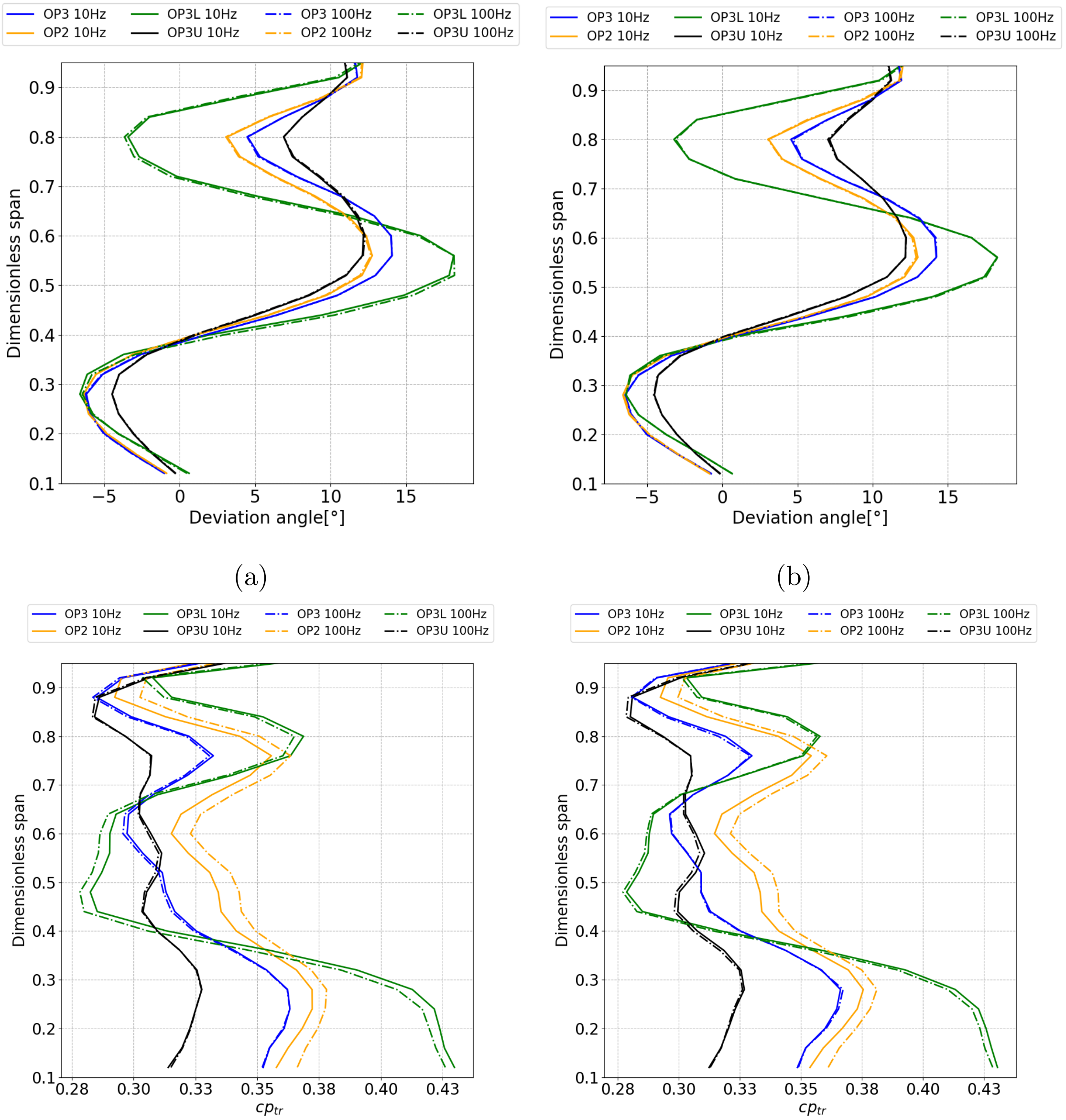

(a)

(b)

(c)

(d)

Figure 8.16: Deviation circumferential mass averages in $10Hz$ LE cases and in $100Hz$ LE cases (a), and in $10Hz$ MP and in $100Hz$ MP cases (b); cp_{tr} circumferential mass averages in $10Hz$ LE cases and in $100Hz$ LE cases (c), and in $10Hz$ MP and in $100Hz$ MP cases (d)

Deviation averages for $10Hz$ and $100Hz$ are overlapped almost perfectly in both LE and MP cases as already noticed at stator outlet for the absolute flow angle. Hence averages of cp_{tr} are useful to understand possible differences. The effects observed in cp_{tr} averages have same trend in both LE and MP cases but they presents slight discrepancies in magnitude. In fact, in both cases OP3 and OP3L, cp_{tr} average values stays about the same for 10Hz and 100Hz. In OP3L 100Hz presents a higher presence of losses throughout the whole span compared to 10Hz, while in OP2 the trend is opposite and 100Hz presents lower losses than 10Hz for the whole span. As a result of what seen in Fig. 8.16, a deviation comparison between EW and HS cases would take into account only one of the two frequencies, in fact Fig. 8.17 shows the comparison between 10Hz and HS.

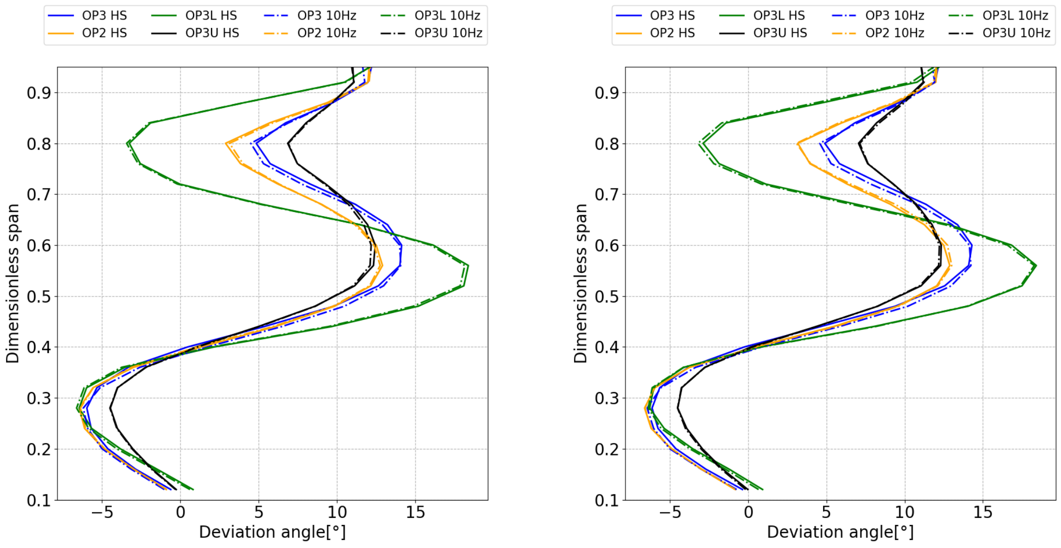

(a) (b)

Figure 8.17: Deviation circumferential mass averages in HS LE cases and in 10Hz LE cases (a), and in HS MP in 10Hz MP cases (b)

Neither by looking at the comparison among HS and 10Hz, which would be equal in case 100Hz were considered, any relevant difference is observable in deviation averages. Given that no conclusions can be drawn by looking at deviation, once again it is presented a comparison concerning cp_{tr}. Fig. 8.18 shows the comparative plot for cp_{tr} in case of HS and EW 10Hz and 100Hz. Those circumferential averages highlight how the 10Hz condition introduces very small changes compared to the HS one. In addition, in 10Hz condition during off-design operation almost nothing changes in terms of cp_{tr} averages. Even for 100Hz in off-design no big variations of cp_{tr} are observable. OP3 100Hz and 10Hz have decreasing effects in the lower channel region and increasing in the upper, both in LE and MP. Instead in OP2 the effects observed in 100Hz are basically beneficial compared to the HS case throughout the whole span, while in 10Hz they are cheapening.

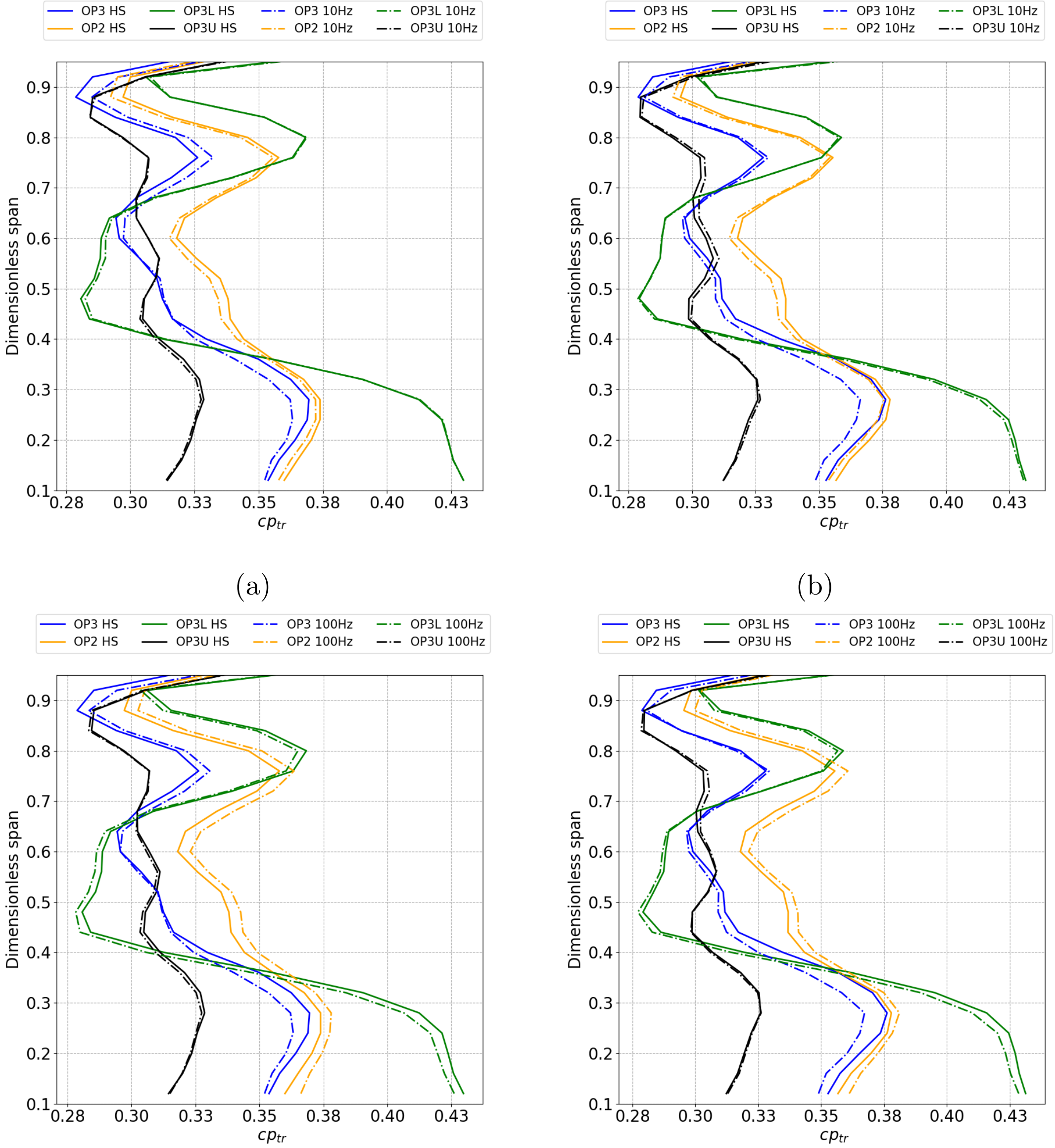

(a) (b)

(c) (d)

Figure 8.18: cp_{tr} circumferential mass averages in HS LE cases and in $10Hz$ LE cases (a), and in HS MP in $10Hz$ MP cases (b); cp_{tr} circumferential mass averages in HS LE cases and in $100Hz$ LE cases (c), and in HS MP in $100Hz$ MP cases (d)

8.3.4 Summary of circumferential averages

Now that all the circumferential averages for cp_{tr} have been presented it is possible to summarize some trends. First of all it is interesting to notice that for all the operating conditions the differences among trend observed in LE and MP are few. Basically between LE and MP differences in trends are present only for OP3U.

Trend observed in OP3: The swirl introduction by Noinj condition enhance the pressure losses for MP and LE; HS causes an increase, compared to Noinj, in losses above a certain span and it causes a decrease of them below it both for LE (about 0.5 of the span) and MP (about 0.7 of the span); both EW, compared to HS, cause a decrease in losses above the previously mentioned coordinates and an increase below.

Trend observed in OP2: No-inj causes a general loss increase compared to Clean both for LE and MP; HS introduces a general loss decrease compared to Noinj both for LE and MP; EW $10Hz$ causes a general loss increase compared to HS both for LE and MP; EW $100Hz$ introduces a decrease of losses compared to HS for both LE and MP.

Trend observed in OP3L: The swirl introduction by Noinj causes a general decrease of losses compared to Clean for both LE and MP; HS seems to have almost the same values of cp_{tr} circumferential averages of Noinj for both MP and LE; EW $10Hz$ does not seems to change significantly the loss profile compared to HS for both LE an MP; EW $100Hz$ slightly increases the losses compared to HS for both LE and MP.

Trend observed in OP3U LE: Noinj introduces a general decrease in losses compared to Clean; HS slightly decreases losses compared to No-inj; EW $100Hz$ slightly increases losses compared to HS; EW $10Hz$ has almost no effect on losses compared to HS.

Trend observed in OP3U MP: Noinj introduces a reduction of losses compared to Clean; HS increases losses compared to Noinj; EW $10Hz$ slightly decreases losses compared to HS; EW $100Hz$ slightly decreases losses compared to HS.

This analysis is made harder by the fact that no comparison with circumferential averages obtained upstream of the rotor can be carried out with ease. In fact the streamlines evolve through the rotor without keeping constant radii. Hence no conservation of relative total pressure happens even in isoentropic case.

Since the trend in OP3U seems weird it is interesting to look at maps comparing the two conditions of LE and MP.

8.4 OP3U maps

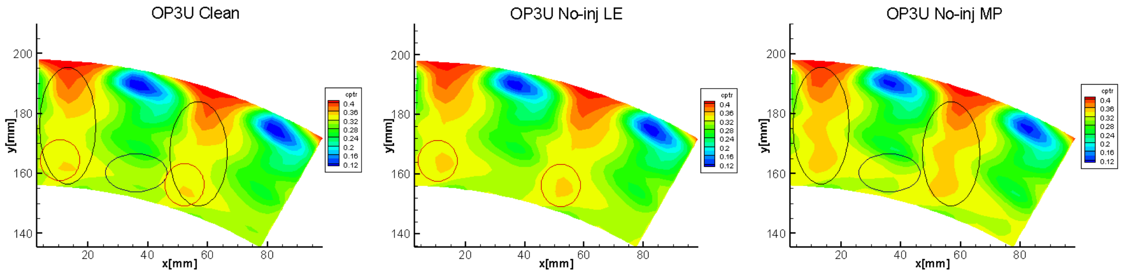

Figure 8.19: cp_{tr} fields for No-inj LE,MP and Clean

Fig. 8.19 shows the differences among Noinj LE and Noinj MP. By looking at the circled regions it is clear that both conditions present lower losses than the Clean case. In fact the circled region of low losses are in correspondence of the free stream and of the lower boundary of the loss region associated to rotor blade wake and residual secondary structures. Among the three maps the one that presents the lower level of losses, specifically in the regions just mentioned, is the MP one.

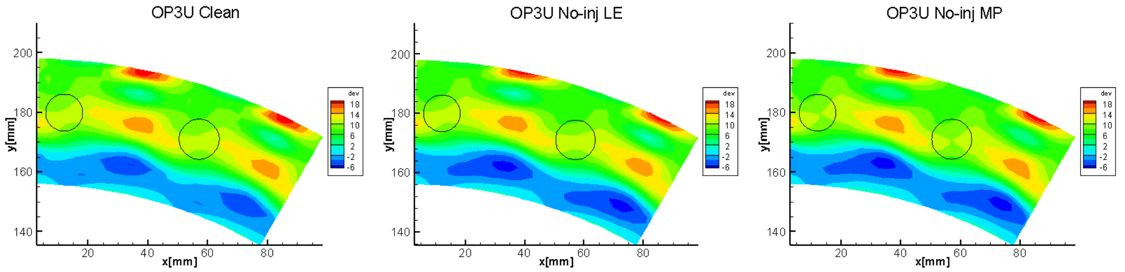

Figure 8.20: Deviation fields for No-inj LE,MP and Clean

Fig. 8.20 shows instead the deviation angle maps. In those maps is present a little but fundamental difference. The region around mid-span, that due to the passage vortexes actions is periodically subjected to a highly positive deviation, seems to present a better blade guided flow in both No-injection cases with respect to the clean condition. This effect is particularly visible in the circled regions, Fig. 8.20. As a result the effect of secondary vorticity seems to be decreased in the free stream by the injector actions.

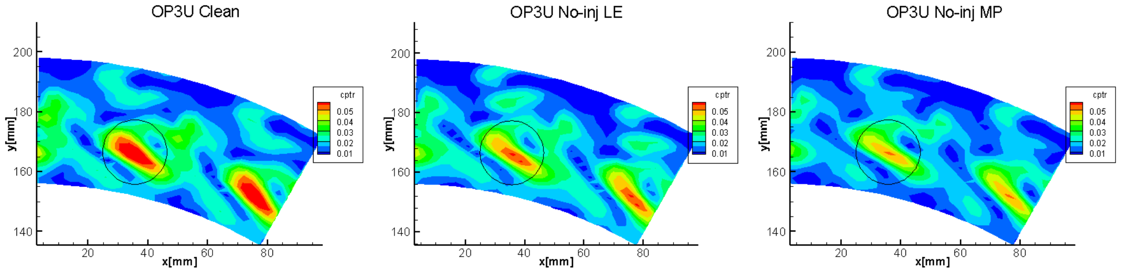

Figure 8.21: cp_{tr} standard deviation fields for No-inj LE,MP and Clean

Fig. 8.21 is useful to understand how the injector presence is affecting the variability of pressure losses. By looking at the circled region it is clear how in both LE and MP cases the injector reduces standard deviations throughout the whole field and in particular at the lower boundary of the loss core. Noinj MP presents a higher reduction with respect to Noinj LE.
By looking at discrepancies in circumferential averages between Noinj and HS, it is expected that the latter would have more similarities to Clean case than the former. In order to check this fact in Fig. 8.22 it is presented the cp_{tr} field for both OP3U MP and OP3U LE in HS case.

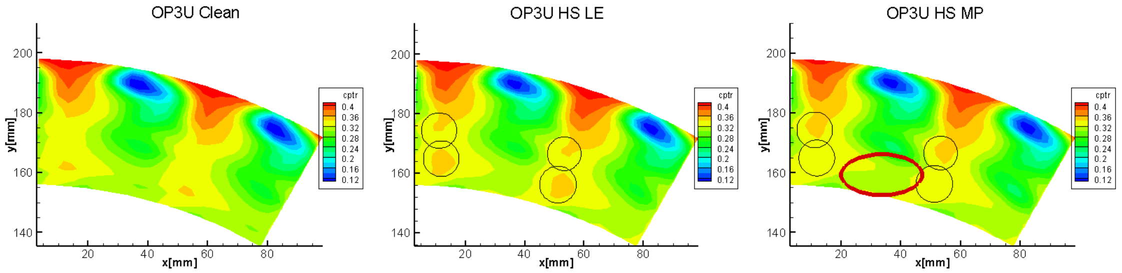

Figure 8.22: cp_{tr} fields for HS LE,MP and clean

As expected, once HS is imposed over the purely aerodynamic disturb, OP3U MP cp_{tr} field came back to a shape more similar to the Clean one, and to the OP3U HS LE one. As it can be observed, the free stream region came back to higher values of losses and the strange low loss region, observable in the ellipse in Fig. 8.19, is no longer present in Fig. 8.22 red ellipse. In addition by looking at the field of deviation angle even the free stream region supposed to be affected by a secondary vorticity weakening, present in Fig. 8.21, is no longer there in Fig. 8.23.

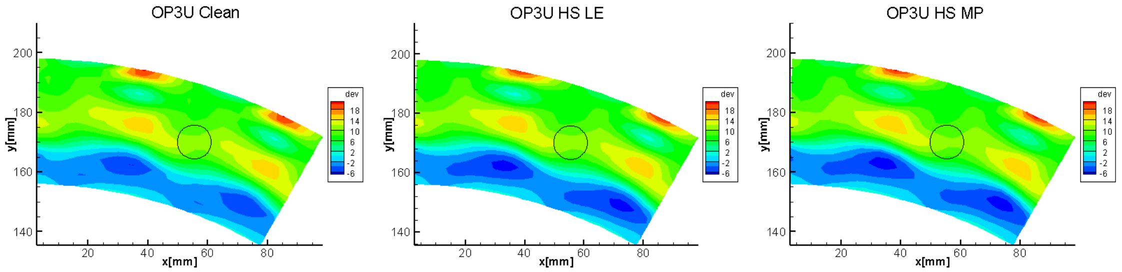

Figure 8.23: Deviation angle fields for HS LE,MP and clean

Since the opposite trend observed in circumferential averages between OP3U MP and OP3U LE is still present even when comparing HS to EW, fields for EW $10Hz$ LE and EW $10Hz$ MP are reported in Fig. 8.24. OP3U fields for $100Hz$ are expected to be similar to $10Hz$ ones because of the almost overlapped circumferential averages, as shown in Fig. 8.16. Hence fields for OP3U $100Hz$ are omitted in this section.

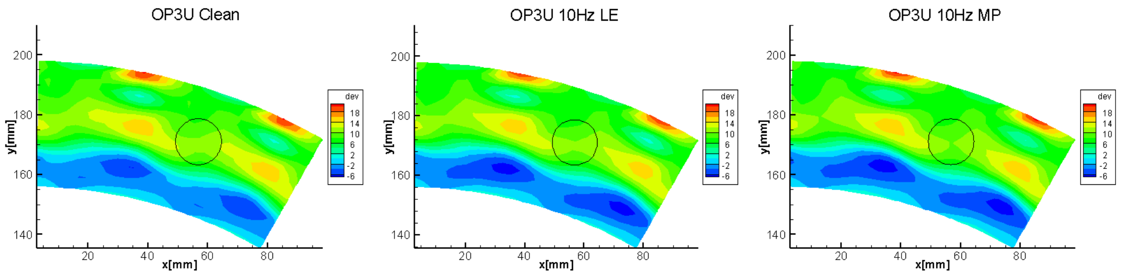

Figure 8.24: Deviation fields for $10Hz$ LE,MP and clean

As expected from the first field, reported in Fig. 8.24, concerning EW conditions a region of more positive deviation angle is once again present in OP3U MP field.

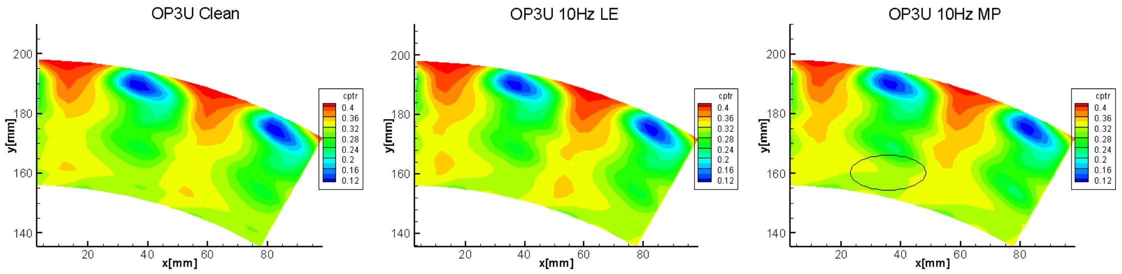

Figure 8.25: cp_{tr} for $10Hz$ LE,MP and clean

In Fig. 8.25 it is possible to observe how the change of conditions from HS to EW tends to brings back the flow features observed in Fig. 8.19. In fact by looking at the ellipse, in Fig. 8.25 OP3U MP, a thinning of the green loss region, compared to the one present in HS case, results glaring. As a result of this analysis it can be stated that the flow features seen for OP3U downstream of the rotor in the relative frame of reference change in accordance to what observed in circumferential averages. However these changes, in terms even of losses, clearly show a non linear behavior related to the strength of the swirl injected upstream of the stator.

The second interesting trend observed during the analysis of circumferential averages is the one of the other off-design condition, hence OP3L. Then OP3L is analyzed in the next section.

8.5 OP3L maps

Looking this time at the difference between OP3L Noinj MP and OP3L Noinj LE for cp_{tr}, a trend opposite to the one observed in OP3U is expected, since this is what have been observed in Fig. 8.12. In particular this time both LE and MP are expected again to have lower losses compared to Clean, but with LE performing a bit better than MP. In addition both MP and LE should present a sensible decrease in losses at about 0.8 of the span. Fig. 8.26 shows the maps of cp_{tr} for OP3L Noinj LE, MP and Clean.

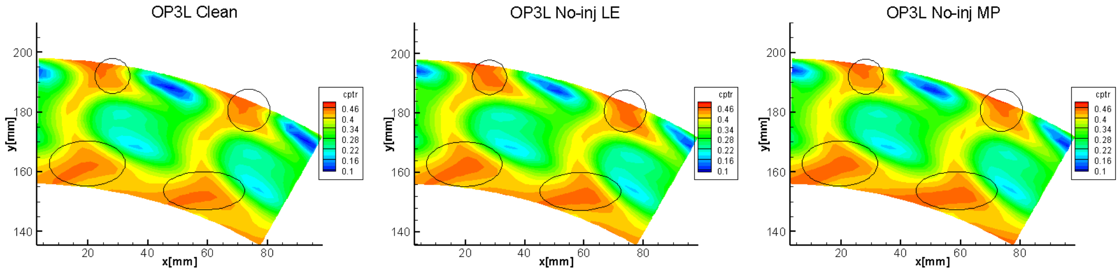

Figure 8.26: cp_{tr} for OP3L Noinj LE, MP and clean

Looking at Fig. 8.26 it is clear how the free stream zones at about 0.8 of the span (circled) present, as expected, a decrease of losses compared to Clean in both MP and LE, with LE performing a bit better. Plus, other regions of free stream near the hub, the ones in the ellipses, seem to get better cp_{tr} values for both cases, this time with MP performing a bit better than LE. These zones in ellipses confirm once again what reported in Fig. 8.12.

In addition Fig. 8.26 suggests that even in OP3L the presence of the injector leads to lower losses in the region of free stream. By looking at deviation fields, Fig. 8.27, instead a pattern, visible even in Fig. 8.23, is recognizable; the lower branch of the hub passage vortex gets strengthened.

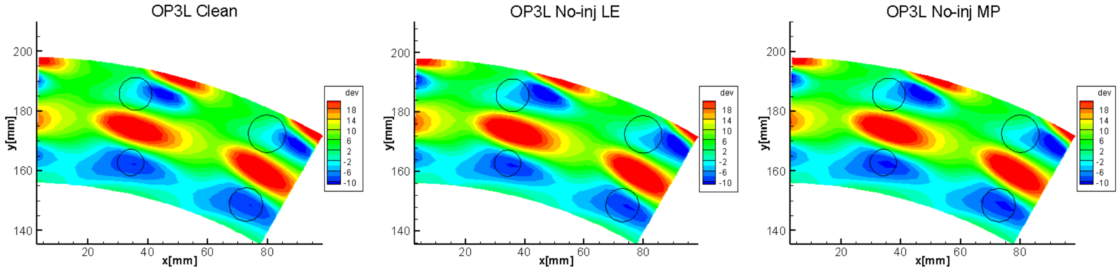

Figure 8.27: cp_{tr} for OP3L No-inj LE,MP and clean

In Fig. 8.27 even an effect on the lower branch of the tip leakage vortex is present. It could be interesting to look at the standard deviation fields for cp_{tr} too, Fig. 8.28. It is possible once again, comparing to the Clean case, to see a general decrease in flow variability in the relative frame both for MP and LE. Notably LE case has a stronger reduction at tip region (0.8 of the span) while MP case has a stronger reduction at hub where it is supposed to be present the lower part of the rotor wake.

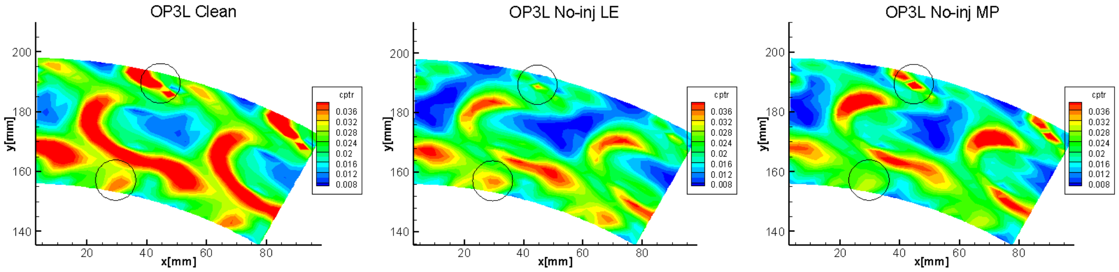

Figure 8.28: cp_{tr} standard deviation fields for OP3L No-inj LE,MP and Clean

Since no major changes, between the No-inj case and both HS and EW, have been observed in circumferential averages, Figs. 8.15 and 8.18, the sole presence of the injector is considered to be the most affecting source of disturb at measuring plane. Hence fields for EW and HS are omitted for the sake of brevity. The next sections would be dedicated to the analysis of in-design conditions.

8.6 OP3 maps

In this section it is reported the analysis of OP3 fields. Since OP3 is considered as a design condition and since circumferential averages suggest so, it is expected to notice a loss increase in all the non-Clean cases. Hence, once more, the fields concerning cp_{tr} are here reported, Fig. 8.29.

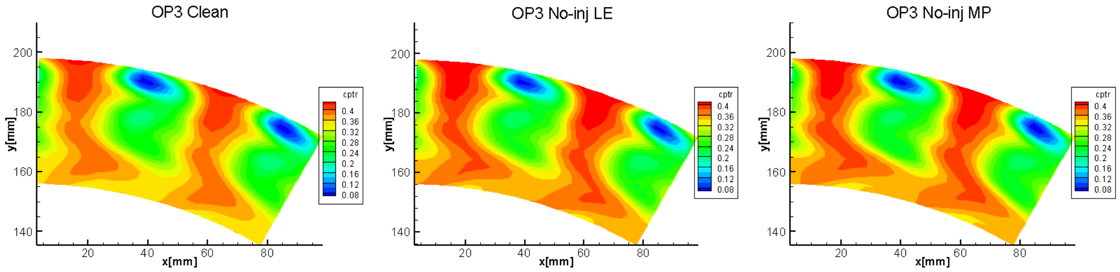

Figure 8.29: cp_{tr} fields for OP3 No-inj LE,MP and clean

What is observable from OP3 cp_{tr} fields seems not to be in accordance with the circumferential averages, Fig. 8.12. Actually the effects observed in circumferential averages depend even on the distribution of mass flow rate in the vanes. Hence, it is supposed that the region of loss in No-inj case, both for MP and LE, would present a higher mass flow rate than the analogous region in the Clean case. This can be confirmed by the point by point difference of the mass flow rate fields, which is shown in Fig. 8.30.

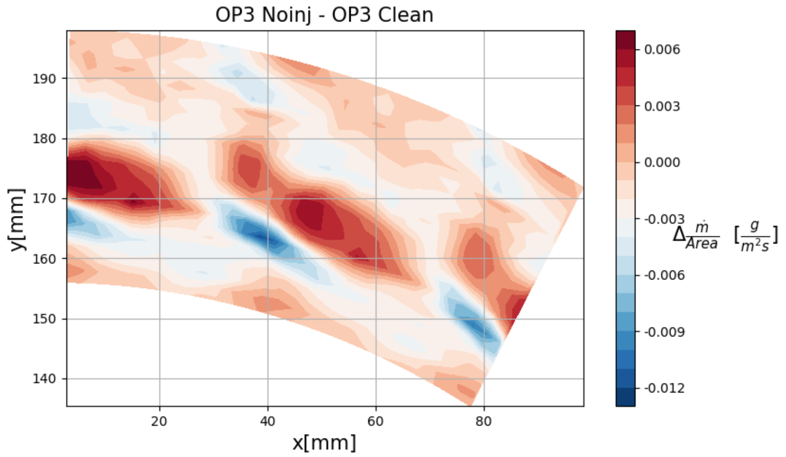

Figure 8.30: Point by point difference of relative frame mass flow rate maps for OP3 Noinj and OP3 Clean (Noinj minus Clean)

Even if No-inj has higher mass flow rate in the region of loss, the maps of cp_{tr} still show a decrease in absolute values of losses in the free stream region and in the region below the loss nucleus compared to the Clean case. This is the same behavior observed in off-design turbine operating conditions. In addition even the features observed previously for OP3U and OP3L in deviation fields are once again present, Fig. 8.31.

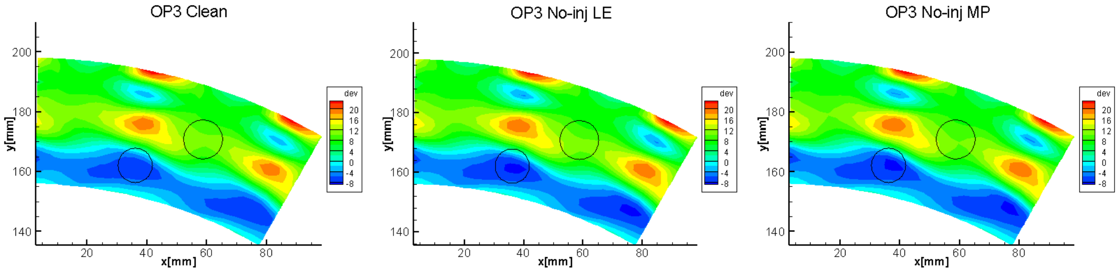

Figure 8.31: Field derived from the difference of the mass flow rate in OP3 No-inj and OP3 Clean

The same trend seen in OP3L and OP3U is once again present even for the standard deviation of cp_{tr}, Fig. 8.32. The introduction of the injector is still associated with a decrease in standard deviation values throughout the field.

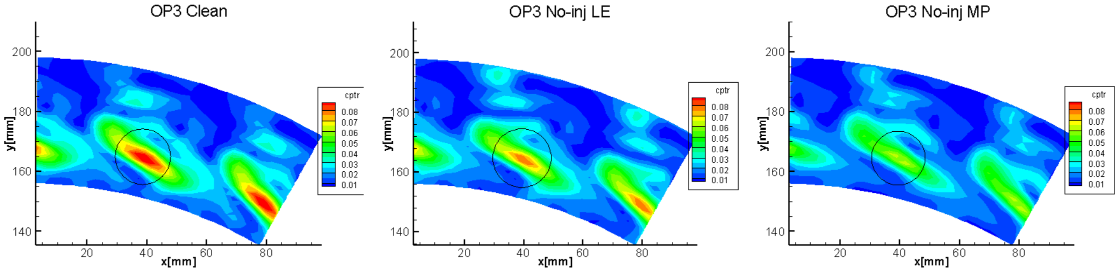

Figure 8.32: cp_{tr} standard deviation fields for OP3 No-inj LE,MP and Clean

In conclusion, independent of the operative condition, the presence of the injector seems to bring beneficial effects in terms of flow uniformity. This could be explained by the fact that, in presence of the injector, a larger region of losses is found at stator outlet. Hence a more uniform flow is there present at rotor inlet. This more uniform flow is perceived in relative frame as a less unsteady one and in turn it brings to a decrease in standard deviations. As a result, a less uniform stator inlet condition causes a more uniform rotor outlet one. This behavior is present both in design and off-design conditions. However during design operative conditions, due to the rearrangement of the mass flow rate, this beneficial effect do not contributes enough and the overall effect of the injector presence is seen as an increase of losses. In Fig. 8.33 are reported the fields for OP3 HS in order to understand whether or not the behavior observed in circumferential averages (Fig. 8.15) find confirmation.

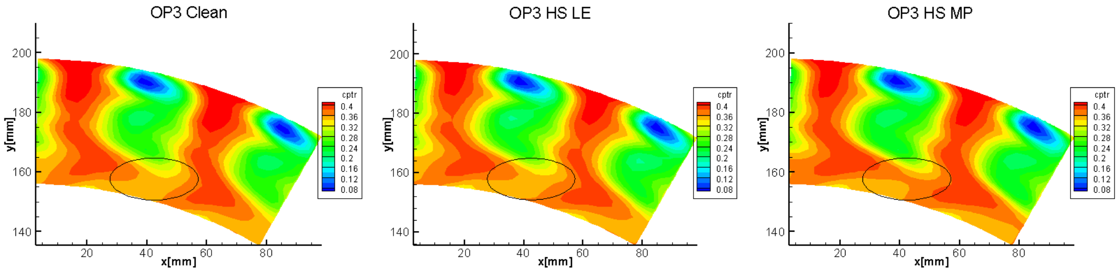

Figure 8.33: cp_{tr} fields for OP3 HS LE,MP and Clean

Looking at Fig. 8.33 the effects seen from the circumferential averages are confirmed. As a matter of fact both HS LE and HS MP case introduce a worsening effect above a certain span and an ameliorating one below it. In addition MP case presents once more the particular loss trend observed preciously in OP3L, see ellipse in Fig. 8.33.

8.7 OP2 maps

In this section are reported the maps for OP2. The analysis carried out in OP2 follows the one done for OP3, Section 8.6 since the cp_{tr} fields for No-injection case present similar peculiarities, Fig. 8.34.

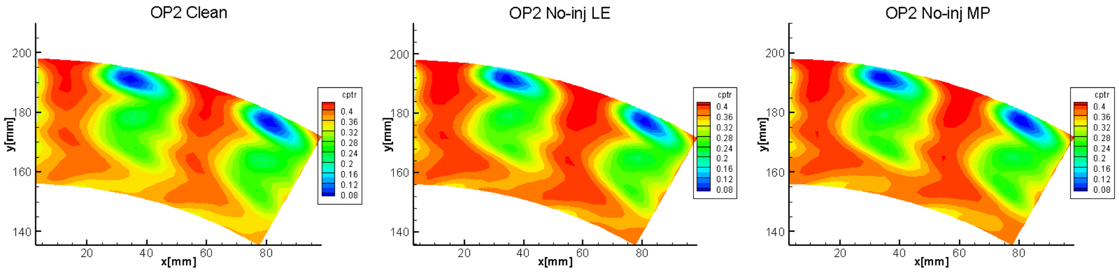

Figure 8.34: cp_{tr} fields for OP2 Noinj LE,MP and Clean

The same considerations done in Section 8.6 can be repeated here. Plus the direct observation of cp_{tr} fields would bring to the conclusion that the injector presence would be, in particular for MP, very beneficial from the point of view of losses. So in Fig. 8.35 the analogous plot of Fig. 8.30 is reported.

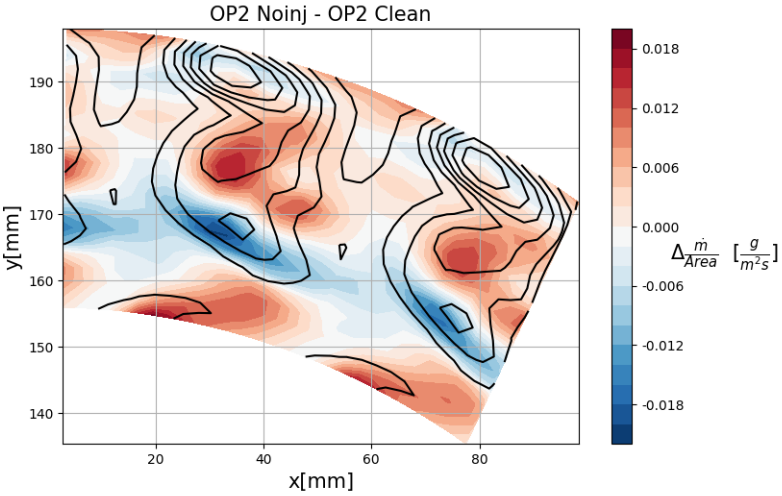

Figure 8.35: Point by point difference of relative frame mass flow rate maps for OP2 Noinj MP and OP2 Clean (Noinj minus Clean) with iso-lines at constant cp_{tr} for Noinj

Again comparing No-injection to Clean, the former displays a higher mass flow rate in high loss region while the latter presents higher mass flow rate in free stream regions. Anyway the effect given by the mass rearrangement induces in OP2 Noinj a region at 0.3 of the span with a lower flow rate compared to Clean, blue area in Fig. 8.35. The effect of this region could be even observed in Fig. 8.12 where the dotted yellow line shows higher cp_{tr} values, compared to the continuous one, right around 0.3 of the span.

Fig. 8.36 shows the cp_{tr} standard deviation field for OP2 Noinj LE,MP and Clean.

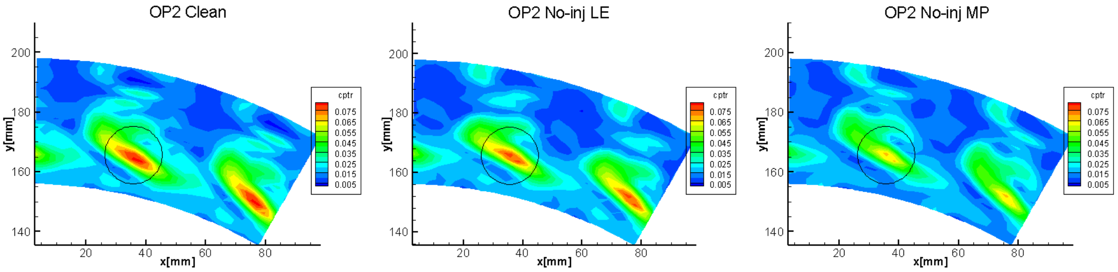

Figure 8.36: cp_{tr} standard deviation fields for OP2 Noinj LE,MP and Clean

Even OP2 confirms the trend mentioned in OP3 concerning the effect of the injector presence on the variability of the pressure field downstream of the rotor.

As a matter of fact OP2 Noinj behaves in a similar way to OP3 Noinj, however from the circumferential averages not each disturb condition seems to affect the two operating conditions of the turbine in the same way. Fig. 8.37 shows the cp_{tr} field for OP2 HS.

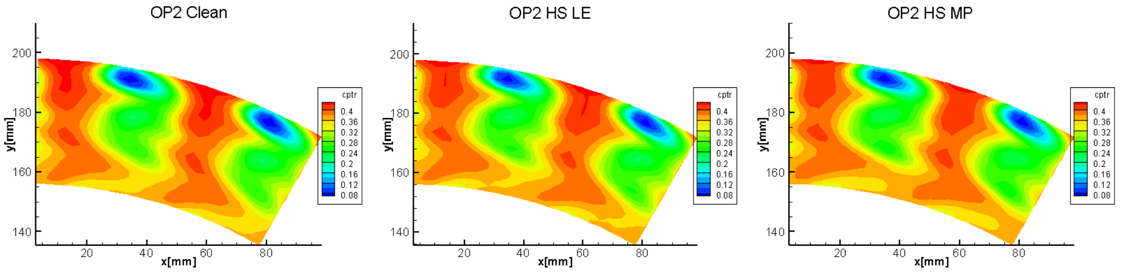

Figure 8.37: cp_{tr} fields for OP2 HS LE,MP and Clean

Comparing Fig. 8.37 and Fig. 8.35 it seems that HS case presents higher losses compared to No-injection. This result seems again to contradict what observed in circumferential averages Fig. 8.15. This inconsistency can be again solved by looking at the mass flow rate difference among the two maps. For example the point by point difference between mass flow rate field in HS and mass flow rate field in No-inj is represented in Fig. 8.38.

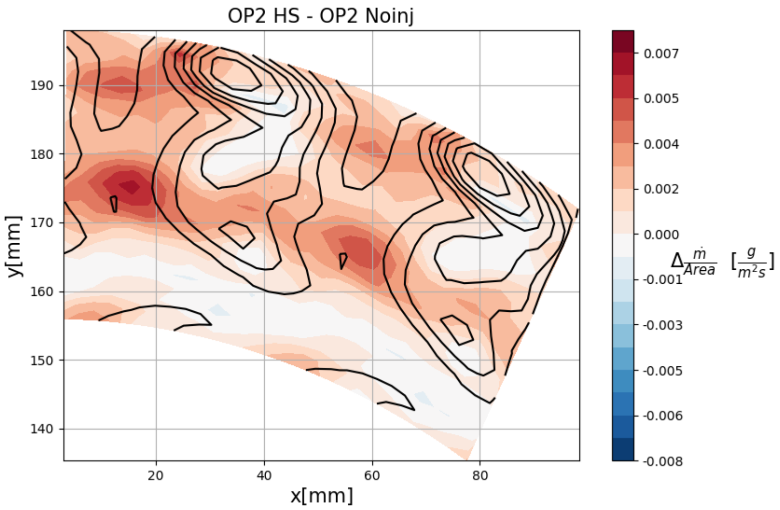

Figure 8.38: Point by point difference of relative frame mass flow rate maps for OP3 Noinj MP and OP2 Clean (HS minus Noinj) with iso-lines of constant cp_{tr} for HS

As it can be seen from Fig. 8.38 the mass flow rate gets rearranged differently. HS case in fact presents, when compared with Noinj, a higher mass flow rate in free stream zones, and a lower one in region characterized by losses.

8.8 Thermal field analysis

This section is dedicated to the analysis of the thermal field measured at rotor outlet measuring section. Firstly, the peak-to-peak temperature in different EWs injection cases is considered, then the reasoning focuses on differences between total temperature fields achieved in the studied plant operating conditions.

8.8.1 Peak-to-peak temperature

The EW remaining magnitude can be analyzed by looking at peak-to-peak temperature values, as already done at stator outlet section. The two injection positions and both EWG working frequencies are considered. Fig. 8.39 shows the $T_{peak-peak}$ fields in OP3 condition for different EWG setups. By comparing these $T_{peak-peak}$ values with ones in maps at stator outlet, it becomes clear that the EWs attenuation is further increased during convection through rotor row since temperature fluctuations have even lower amplitude. Values of $T_{peak-peak}$ are larger for the $10Hz$ injection than for $100Hz$ and they result to be very bounded in the latter case. In LE case, the maximum value assumed by peak-to-peak temperature is about 3.5% of the maximum one at stator inlet measuring section for $10Hz$ and 4.1% for $100Hz$, while it is about 3% of one at stator inlet measuring section in MP injection case for $10Hz$ and 3.6% for $100Hz$, see Fig. 6.7 for stator inlet values. So, considering the whole stage, it can be stated that in OP3 the EWs attenuation is stronger when injection takes place in correspondence of MP at stator inlet, mainly due the greater interaction with secondary flows.

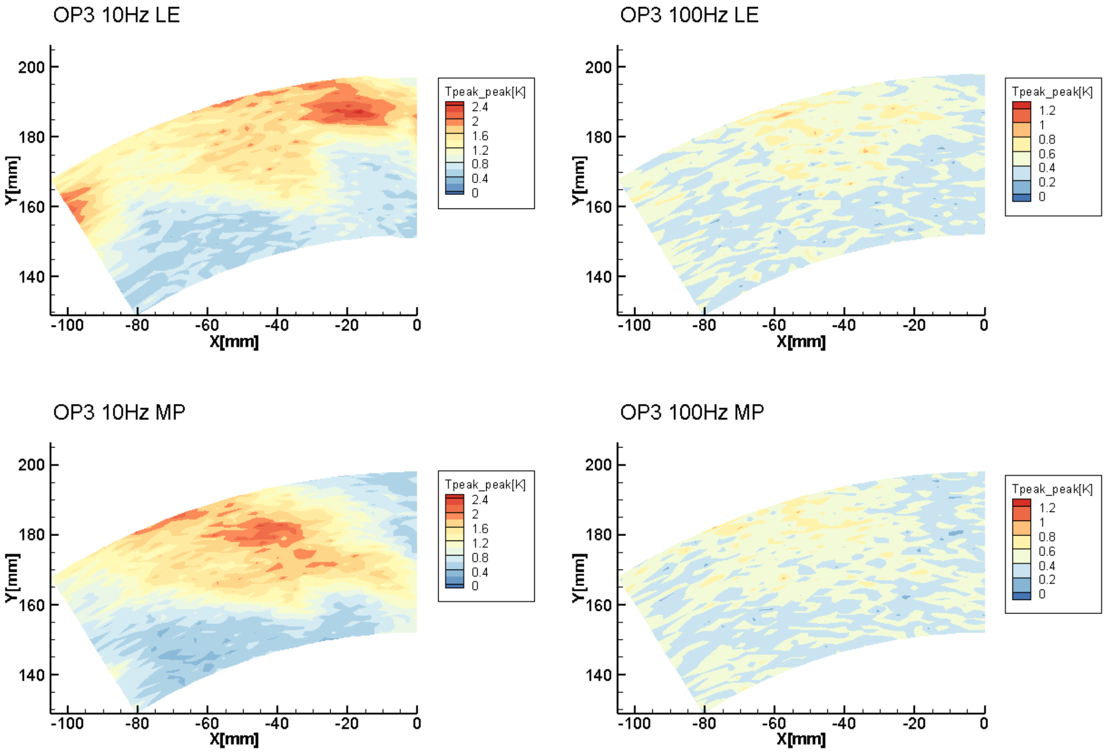

Figure 8.39: $T_{peak-peak}$ maps in OP3 for different EWG working conditions

The same maps can be realized for OP3U and OP3L, Fig. 8.40 and Fig. 8.41. Also in these two off-design working conditions, the temperature fluctuations associated to $100Hz$ injection show very low amplitude if compared to $10Hz$. However appreciable differences exist between OP3, OP3U and OP3L when injection frequency is set at $10Hz$. OP3L features the highest $T_{peak-peak}$ values, meaning that the injected

EWs are less attenuated and temperature field unsteadiness is more pronounced. Moreover, in Figs. 8.40 and 8.41 the highest $T_{peak-peak}$ regions are not located at the same spatial coordinates, so EWs migration is significantly affected by rotor regime and secondary flows that develop inside the rotor blades passages. A common aspect is that for LE case the EWs concentrate close to the tip region and extend circumferentially, even if the maximum $T_{peak-peak}$ regions are shifted in azimuthal direction depending on operative condition. This shift could be related to absolute flow angle α at rotor exit, which remarkably varies between OP3, OP3U and OP3L, see Fig. 8.6. Regarding the MP case, the EWs distribute well radially except in OP3L, in which EWs seem to remain more concentrated close to tip region. The lower EWs attenuation and diffusion in OP3L, for both injection positions, could be linked to the aerodynamic field characterizing this operating condition which does not promote work extraction in the tip region. In fact, flow separation due to high loading may be also strengthened by positive incidence given by upstream injected hotter flow, thus further reducing work exchange inside rotor row and leading to better EWs persistence at the outlet.

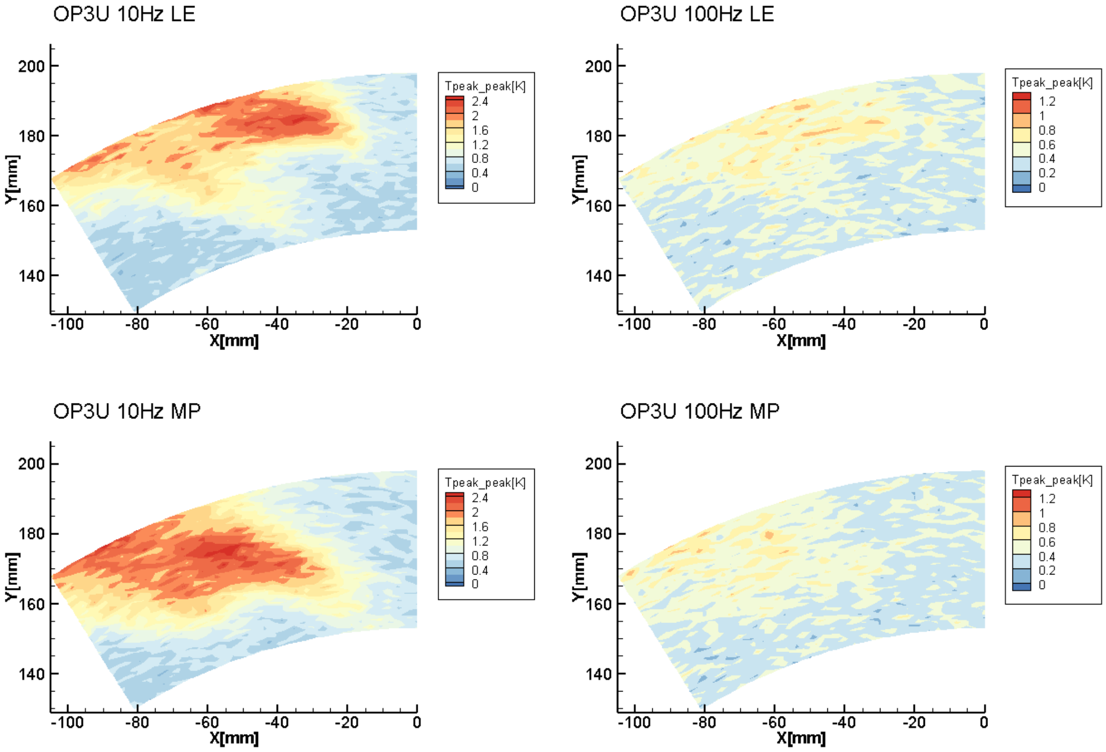

Figure 8.40: $T_{peak-peak}$ maps in OP3U for different EWG working conditions

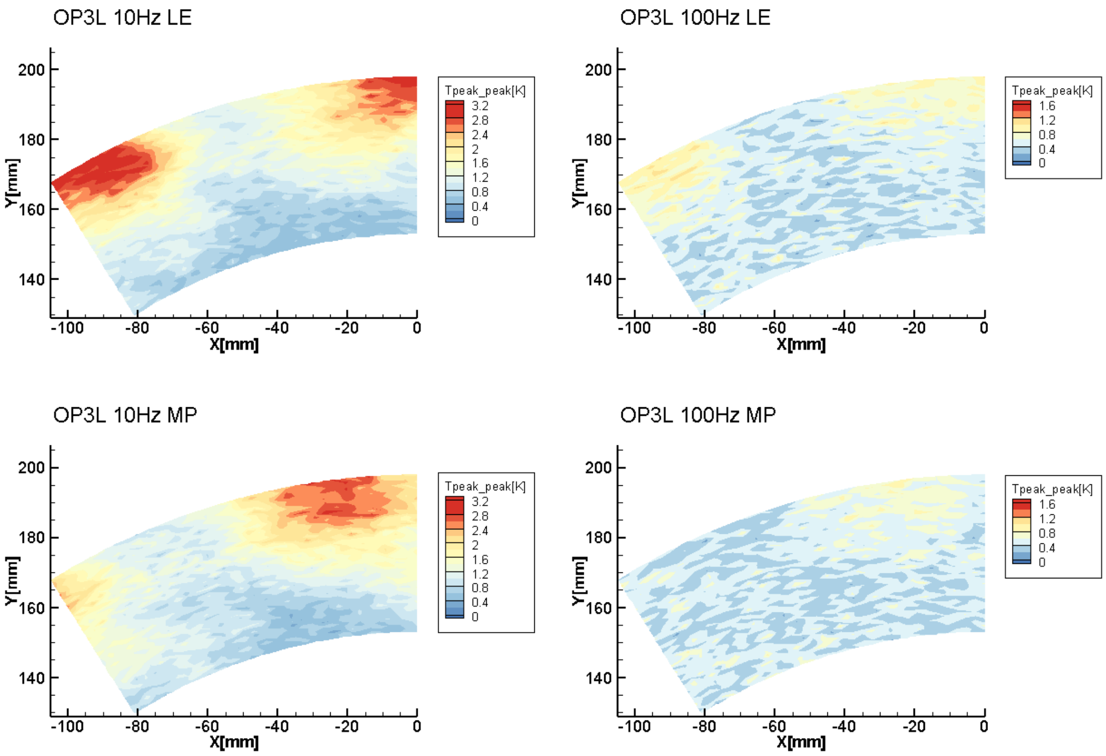

Figure 8.41: $T_{peak-peak}$ maps in OP3L for different EWG working conditions

In Table 8.1 and Table 8.2, the maximum peak-to-peak temperature values for OP3, OP3U and OP3L are collected to give an idea about maximum temperature fluctuation associated to EWs injection at $10Hz$ and $100Hz$ cases, respectively.

Table 8.1: Maximum peak-to-peak temperature $[K]$ values for OP3, OP3U and OP3L with injection frequency equal to $10Hz$

	OP3	**OP3U**	**OP3L**
LE	2.7	2.5	3.3
MP	2.3	2.8	3.1

Table 8.2: Maximum peak-to-peak temperature $[K]$ values for OP3, OP3U and OP3L with injection frequency equal to $100Hz$

	OP3	**OP3U**	**OP3L**
LE	1.0	1.1	1.2
MP	0.9	1.0	0.9

Thanks to circumferential mass average algorithm, it's possible to determine the evolution of mass averaged $T_{peak-peak}$ along the dimensionless span at rotor outlet measuring section and compare it with profiles already found upstream and downstream stator. This comparison allows to have a graphical representation of EWs attenuation during convection through the turbine stage in OP3, OP3L and OP3U. Figs. 8.42 and 8.43 show the profiles of peak-to-peak temperature coming from circumferential mass average in $10Hz$ injection frequency case for both LE and MP, that is the most representative. Regardless of the injection location, OP3L is the operating condition in which EWs survive better, as already seen in the previous maps.

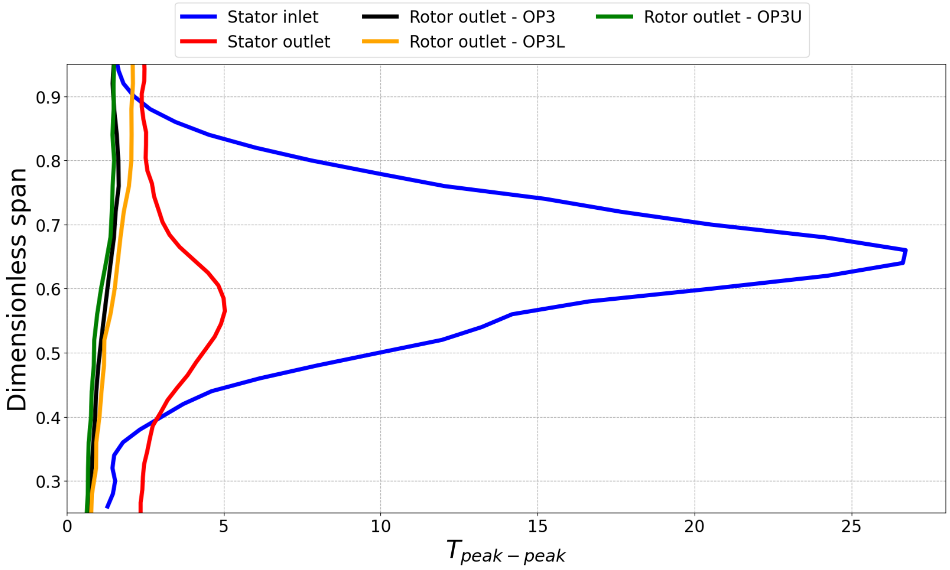

Figure 8.42: Circumferential mass averaged $T_{peak-peak}$ profiles in OP3, OP3U and OP3L for $10Hz$ LE injection

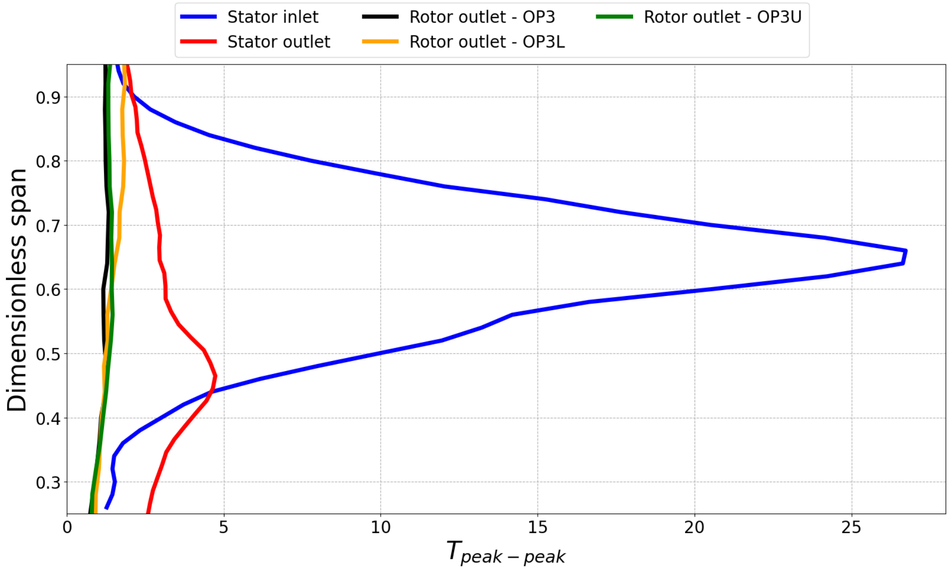

Figure 8.43: Circumferential mass averaged $T_{peak-peak}$ profiles in OP3, OP3U and OP3L for $10Hz$ MP injection

Fig. 8.44 shows the $T_{peak-peak}$ fields in OP2 condition for different EWG setups. In LE case, the maximum value assumed by peak-to-peak temperature is about 4.1% of the maximum one at stator inlet measuring section for $10Hz$ and 6.1% for $100Hz$, while it is about 4.4% of one at stator inlet measuring section in MP injection case for $10Hz$ and 6.3% for $100Hz$. So the EWs injected at $10Hz$ are more weakened than ones injected at $100Hz$ in terms of percentage of maximum $T_{peak-peak}$ measured at stator inlet. However fluctuation amplitudes in $100Hz$ case are very low, so EWs effect on temperature field are almost negligible. In OP2, the EWs seem to be concentrated above midspan both for LE case and MP case, but in LE one they are more spread circumferentially rather than in MP injection. The maximum values of peak-to-peak temperature reached in $10Hz$ injection are $2.5K$ for LE and $2.7K$ for MP, while in $100Hz$ are about $1K$ for both LE and MP cases. However, the profile of mass averaged $T_{peak-peak}$ along the span is necessary to get an idea about attenuation of injected EWs, once they have reached rotor outlet measuring section. Figs. 8.45 and 8.46 compare the $T_{peak-peak}$ profiles found at stator inlet and rotor outlet in $10Hz$ injection for LE and MP clocking position, respectively.

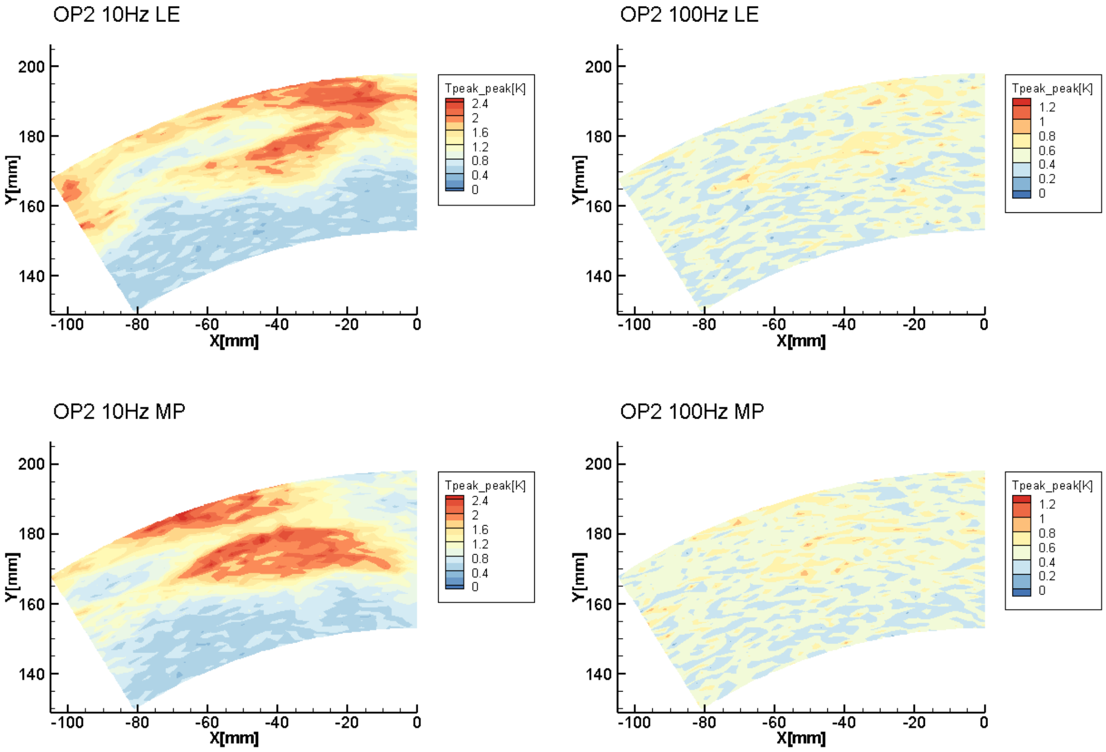

Figure 8.44: $T_{peak-peak}$ maps in OP2 for different EWG working conditions

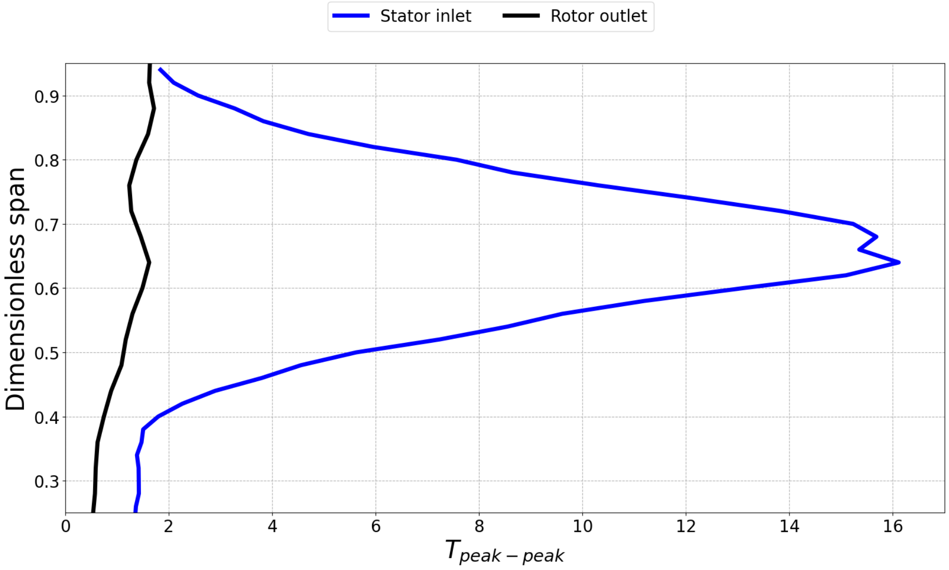

Figure 8.45: Circumferential mass averaged $T_{peak-peak}$ profiles in OP2 for $10Hz$ LE injection

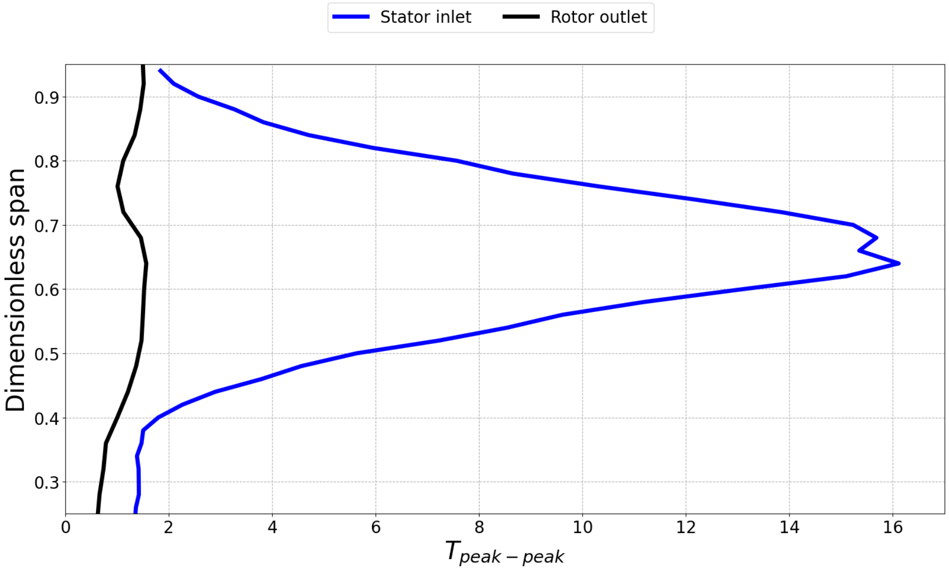

Figure 8.46: Circumferential mass averaged $T_{peak-peak}$ profiles in OP2 for $10Hz$ MP injection

In conclusion, Fig. 8.47 shows the peak-to-peak temperature profiles found at rotor outlet measuring section, in all plant operating conditions (OP3, OP3U, OP3L, OP2) for $10Hz$ injection in LE and MP clocking positions. In both LE and MP cases, among all operating conditions, the one characterized by highest $T_{peak-peak}$ is OP3L.

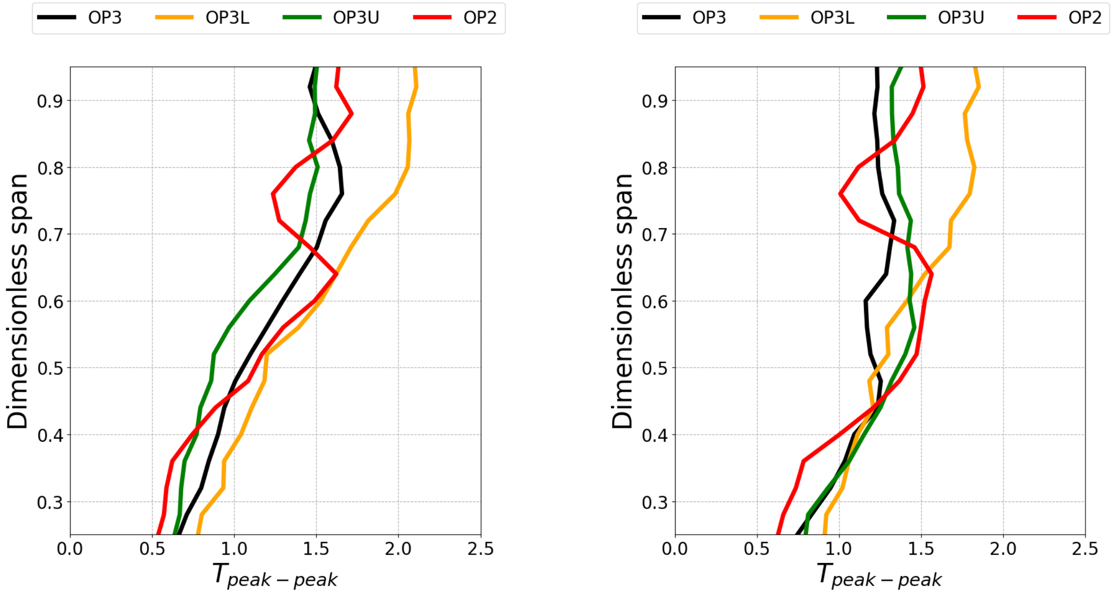

(a) (b)

Figure 8.47: Circumferential mass averaged $T_{peak-peak}$ profiles in OP3, OP3U, OP3L and OP2 for LE (a) and MP (b) injection positions with injection at $10Hz$

8.8.2 Total temperature difference maps

In this section total temperature fields obtained for different injector working conditions are compared. To perform this, the fields are subtracted among each other and ΔT_t maps are obtained. Given that Clean maps and ones obtained in LE and MP cover different ranges of angular position, a Python code developed by the Authors is used to make different maps comparable, as already discussed in Section 7.1.1. For sake of brevity, only some examples related to LE injection case in OP3, OP3L, OP3U and OP2 (Figs. 8.48–8.51) are reported because similar conclusions can be drawn in MP case despite the change in morphology of the fields. The zones where ΔT_t is greater than zero are directly consequence of the EWs injection and the ones where it assumes values lower than zero mean that work extraction has been modified. By looking at Fig. 8.48, it's clear that Noinj is characterized by higher temperature values with respect to Clean: the ΔT_t in $10Hz$-Noinj is lower than in $10Hz$-Clean. This means that in OP3 Noinj case, the introduction of swirl profile causes a decrease of extracted work.

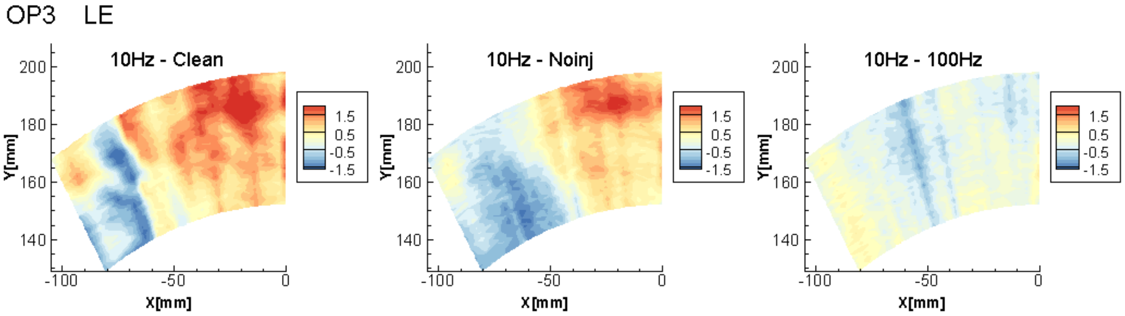

Figure 8.48: $\Delta T[K]$ in OP3

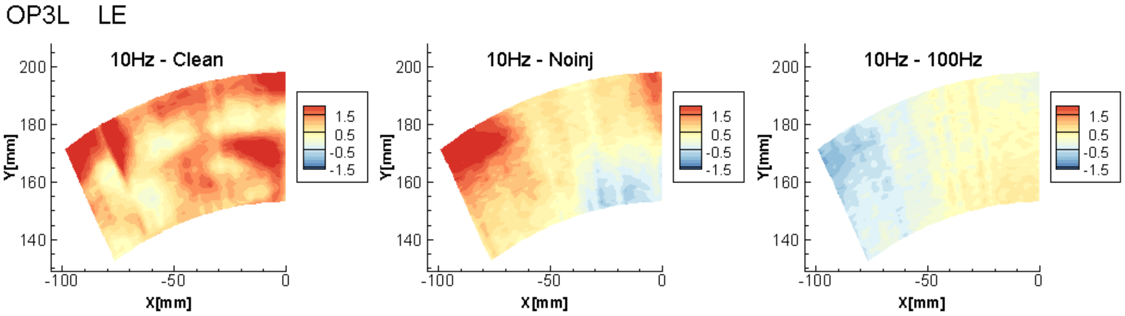

Figure 8.49: $\Delta T[K]$ in OP3L

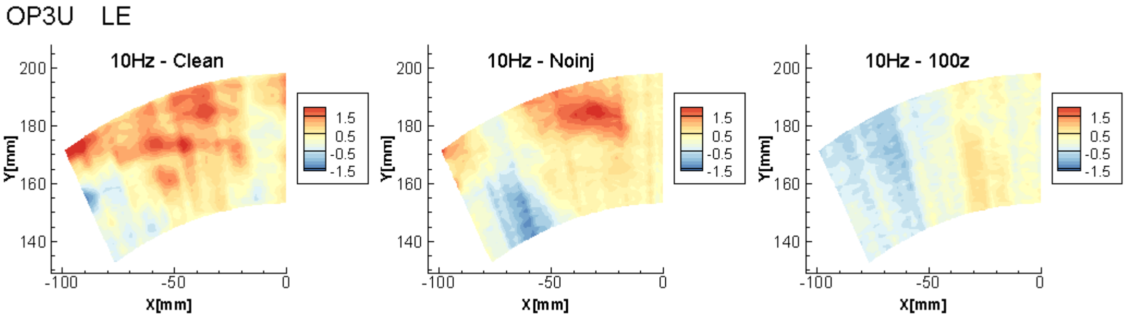

Figure 8.50: $\Delta T[K]$ in OP3U

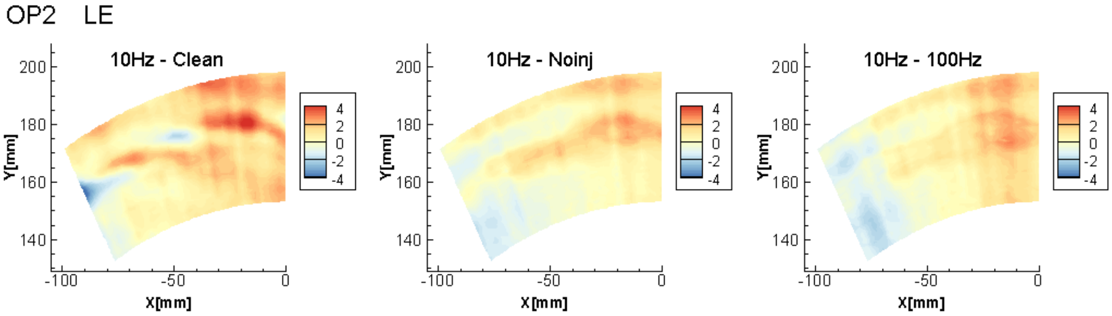

Figure 8.51: $\Delta T[K]$ in OP2

Chapter 9

Conclusions

The experimental campaign carried out during this work has considered both the injection of swirled entropy waves and different plant operating conditions. The purpose is to simulate what happens in modern combustors which are characterized by the generation of flow non-uniformities that are advected towards the turbine stage. Three measuring sections (upstream of the stator, downstream of the stator and downstream of the rotor) have been considered in order to get comprehension about non-uniformities effects on aero-thermodynamics during their convection through the stage. Moreover, the study has also taken into account off-design operating conditions to study the interaction between the rotor loading condition and the effects related to the injected perturbations.

Aerodynamic and thermal measurements performed by the Authors at stator inlet during the experimental campaign show clear agreement with the ones performed during previous studies. This similarity of imposed inlet boundary conditions guarantees the possibility to compare previously acquired data with the ones collected by the Authors for all the considered measuring sections.

At stator inlet some discrepancies among different operative conditions are already visible; those differences, in particular in terms of absolute flow angle, have for sure effects on the disturb convection throughout the whole stage.

At stator outlet measuring section, the EWs are found mainly at the center of blade passage and looking at $T_{peak-peak}$ maps it is possible to notice differences in EWs magnitude and migration depending on injection position. In particular, in LE case the maximum peak-to-peak values are greater and are located at a radial position higher than in MP case. The difference in magnitude can be related to the interaction between swirled EWs and secondary flows, which result to be stronger for MP injection case. However for both injection positions, the EWs are found at a radial coordinate which is lower than the one upstream of the stator but this is due to blade leaned geometry. This effect is much stronger in MP injection. Regarding aerodynamic considerations, it has been proved that injection frequency and temperature have almost negligible effects on losses and that the injected swirl profile represents the biggest contribution to the increase of losses. The maximum value in mass averaged loss profiles is obtained when injection takes place at LE. The α angle is strongly affected by the perturbation injection, especially between 40% and

80% of the span where α follows very different trend depending on EWG working condition and injection position. The changes in absolute flow angles directly affect the relative flow angle, whose values are also dependent on flow temperature. The effect of temperature is clearly visible, for example, in the incidence profile for OP3 MP injection cases: the EWs and HS injection leads to higher incidence values, thus affecting rotor aerodynamics.

For what concerns rotor outlet measurements, the whole set of acquired data has been analyzed and this highlighted strongly non linear effects on the rotor aerothermodynamics with the change of loading conditions. In fact thermal disturbs have different morphology between the operating conditions, however at rotor outlet temperature perturbations are found for each operative condition in the upper part of the channel, due to the rotor bowing. Instead the change of expansion ratio, carried out imposing cinematic similitude at rotor, seems to introduce minor changes in aerodynamic. On one hand the Authors suggest that the degradation of turbine inlet flow uniformity has similar detrimental effects on both the considered in-design conditions. On the other hand, this non uniformity, when off-design conditions are considered, shows unclear trends, introducing even beneficial effects in terms of entropy production while compared to the case with turbine uniform inlet flow. In both design and off-design conditions, a well defined trend highlights how the non-uniform turbine inlet flow leads to a more uniform turbine outlet flow. This is proved by looking at standard deviation fields. Those aerodynamic effects are not negligible and could imply tangible changes of turbine performances. In fact, from the magnitude of disturbances persistence at rotor outlet, it is clear that among the aerodynamic one and the thermal one, the former has greater effects and should be of major concern. However further investigations are suggested in order to well understand the role covered by the mass flow rate rearrangement on losses inside the rotor.

The study carried out during this thesis exposes some further critical aspects to be investigated. First of all it could be interesting to perform the missing thermal measurements at stator outlet in case of high expansion ratio, in order to fully characterize the operative condition. In addition future developments are suggested to focus on improving the injector swirling action, in order to get the same swirl profile in all the considered injection conditions.

Appendix A

Combustion noise

Given that combustion noise is considered to be one of major sources of noise in aeroengines and gas turbines, it's fundamental to investigate the mechanisms of its generation. Noise arises in combustion systems mainly for two reasons: burners operate with the working fluid in turbulent motion and heat is being released. This causes noise of its own accord, since an unsteady pressure field is generated [21].
Combustion noise consists of two components: direct and indirect combustion noise. The direct noise is generated in and radiated from the region undergoing turbulent combustion and it is caused by unsteady heat release rate in the reactive region [1, 21]. According to Bragg, who assumed turbulent flame as a collection of eddies, each eddy acts as a monopole source of sound which is statistically independent of the neighboring eddies (each eddy is characterized by own heat release rate) [1].
The indirect combustion noise is generated downstream of the combustor when a fluid with non-uniform entropy and vorticity distribution is accelerated [1,21], thus it originates from the entropy waves acceleration through the turbine stage (Fig. A.1). Direct noise and entropy waves are always generated in tandem. Indirect noise is also known as entropy noise [1], however it more precisely refers to the noise generated by the acceleration of both entropy and vorticity waves [22].

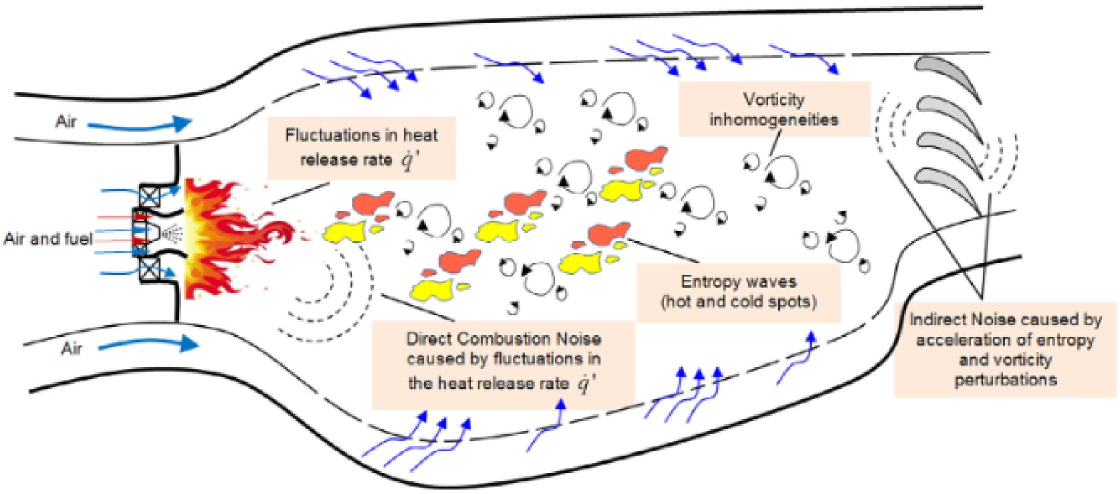

Figure A.1: Illustration of combustion noise sources in a gas turbine [1]

The lean premixed and stratified combustion that occurs in low-NOx combustors, leads to an unsteady heat release rate which produces significant velocity and temperature non-uniformities. So, some hot and cold spots (at higher and lower entropy respectively) in the flow originates and persist to the turbine. If inviscid momentum equation is taken into account:

$$\frac{Dv}{Dt} = -\frac{1}{\rho}\nabla p \tag{A.1}$$

it's clear that hot spots behave in different way: acceleration due to pressure gradient of fluid particles in those regions differs from the neighboring ones because of different densities [21, 22]. The coupling between hot spots generated by combustion and particle acceleration in the mean flow gives rise to pressure perturbations, to which ear is sensitive.

When an entropy wave undergoes acceleration, one component of the generated entropy noise propagates back upstream toward the combustor (Fig. A.2), while the other propagates downstream. The upstream propagating component can come back into the combustor, perturb the rate of combustion leading to possible thermoacoustic instability [1, 22].

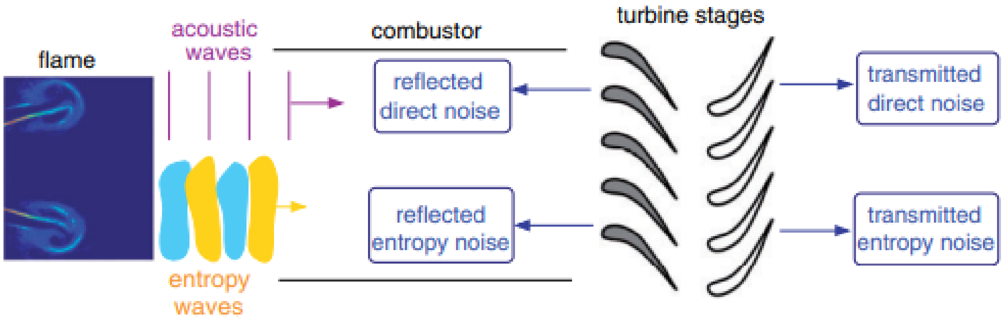

Figure A.2: Entropy wave reflection [22]

The turbulence in the flow can also diffuse the entropy disturbances and therefore reduce their potential for sound generation [22]. Because of the general complexity of transport and diffusion in turbulent flows, some important aspects about entropy waves are still unexplored and the aim of this work is to extend the comprehension of these phenomena.

In the last years, the reduction of noise has become more important and some projects with the objective of achieving low noise propulsion systems have been carried out. One of these is RECORD (Research on Core Noise Reduction), that was an European project joined also by Politecnico di Milano. RECORD focused on the analysis of the combustion noise and of its interaction with the turbine stage, with the purpose of understanding how to limit its amplification.

Appendix B

Turbine stator leaned geometry effects

The stator row considered in the present thesis has a particular geometry, which, as emphasized by several studies [23], has a strong effect on the flow trajectories and secondary flows upstream, downstream and throughout the stator vanes. The so called ”leaned” geometry, Fig. B.1, is built up by translation of the blade-to-blade profile section along a correspondent inclined blade axis; the following axis is inclined of a given angle, with respect to the radial direction, in a plane perpendicular to the one formed by the axial-radial directors.

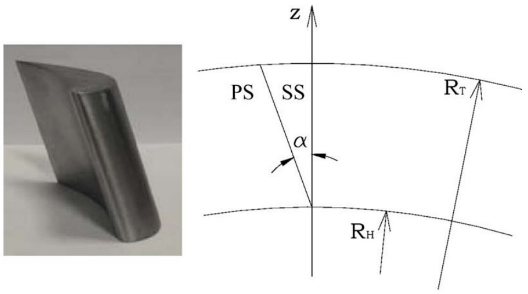

Figure B.1: Leaned geometry example

As a consequence, the blades differs from the so called ”Prismatic” ones, which present a stacking only in radial direction. In addition no sweep nor twist are present. The effect of the leaned geometry is here reported in a synthetic manner as its knowledge is necessary to understand the results obtained by measurements on the turbine facility used during this study. In general, at stator inlet, at stator outlet and through the vanes, the leaned geometry impacts strongly on the pressure contours. The pressure field modification impacts in turn on the flow by the imposition of thrusts and consequential trajectories modifications. The effects here reported refers to studies carried out in linear cascades [23], in order to exclude the effects on the flow given by the annular curvature.

Figures concerning pressure contours in this chapter refer to what an observer placed upstream of the measuring plane would see by facing the measuring plane itself.

B.1 Stator inlet effect

Upstream of a leaned stator row the pressure contours are modified in a manner presented in Fig. B.2. The values reported in the following figures do not refer to the turbine studied during this thesis work, however they are here reported in order to give a quantitative idea of the phenomenon magnitude example.

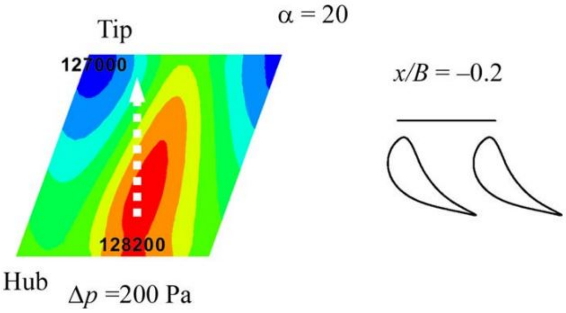

Figure B.2: Pressure contours upstream of a leaned stator row,

As it can be observed a core of high pressure is found in the hub region, while a core of low pressure is found at the case region. Those contours presents hence a pressure difference, in a direction normal to the end-walls, which causes a thrust on the flow from hub to case.

B.2 In-vane effect

The effect of the leaned blades on pressure contours inside the stator vane is presented in Fig. B.3.

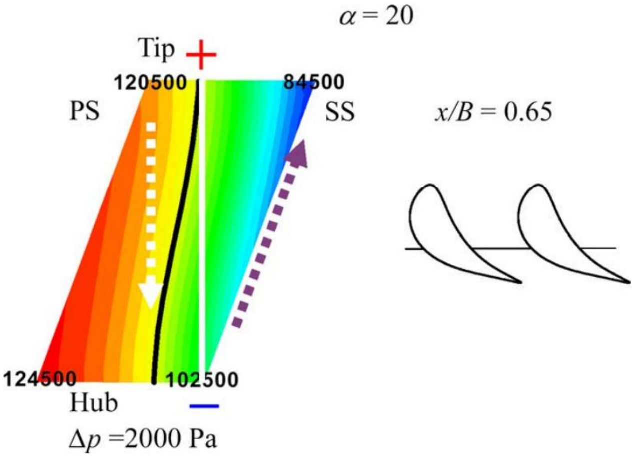

Figure B.3: Pressure contours inside a vane of a leaned stator row

As it can be observed a pressure inside the channel presents two trends in two different directions. Pressure increases moving from pressure side towards suction

side, as normally observed, but it also increases, on the blade surfaces, moving from tip to hub. This trend, coupled with the blade leaning, causes two opposite flow movements inside the vane channel. The flow near the blade surfaces is pushed from hub region to tip region, while, the flow in the mid-pitch of the channel is pushed from tip region to hub region.
Of the two blade side surfaces the one which is more affected by the pressure gradient is the suction one, as a consequence the horseshoe and passage vortexes, flowing close to the blade suction side, are thrust in the hub-to-tip direction [23].

B.3 Stator outlet effect

Downstream of a leaned stator row the pressure contours are modified in a manner presented in Fig. B.4.

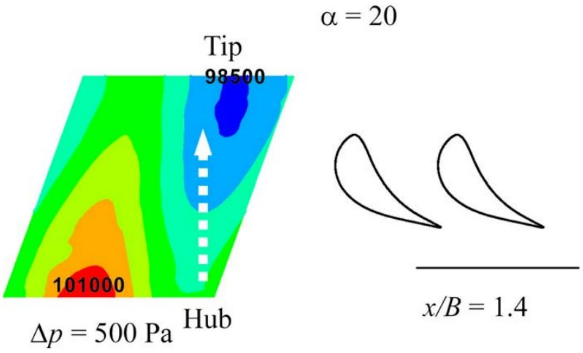

Figure B.4: Pressure contours downstream of a leaned stator row

At stator outlet the leaned geometry presents once again the effect of pushing the flow from hub region towards case region.

B.4 Conclusions on leaned geometry

The overall effect of leaned geometry can be fully appreciated thanks to experimental campaigns and accurate CFD models. In fact a general consideration on how the main flow features are deflected by the aforementioned pressure contours is reported thanks to an experimental campaign in [23].
through the whole stator expansion the fluid experiences a double inversion in thrust direction, in fact if upstream and downstream of the stator the pressure pushes from tip to hub, inside the vanes the effect results reversed. This thrust trend deeply affect the flow pathline, in Fig. B.5 it is in fact reported an example of mass-averaged velocity in z direction, $\bar{v}_z$ normalized by a 3D mass-averaged velocity on a plane at constant axial coordinate, $\bar{\bar{v}}$. It has to be kept in mind that the study has been carried out on a linear cascade and the z direction coincides with the one

perpendicular to the blade-to-blade plane (x = axial coordinate increasing moving from leading edge to trailing edge; B = axial cord of the blade profile).

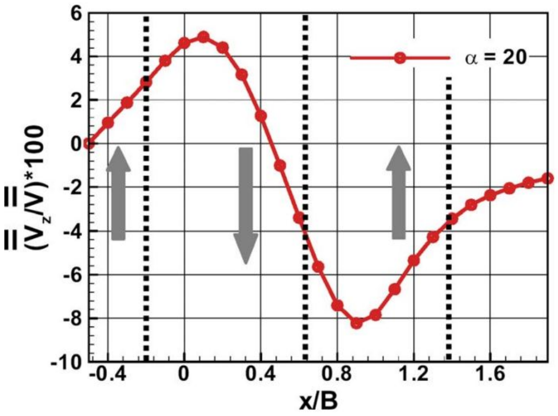

Figure B.5: Trend of normalized velocity in z direction plotted against the non-dimensional axial coordinate

Downstream of the passage, z velocity is negative negative pitch angle, even if the flow thrust already changed its sign. This result evidences strong action experienced by the fluid inside the passage [23].

B.4.1 Effects on secondary vorticity

Some suggestions can be made on the influence of leaned geometry on secondary vorticity and losses development through the passage. Those phenomena affect strongly the flow observed downstream of the cascade, which is of particular interest for the present thesis study.

Previous studies propose an approach based on the coupling of the flows imposed by the lean pressure contour and the natural secondary vorticity found even in prismatic stator rows. Fig. B.6 helps in understanding the nature of the coupling.

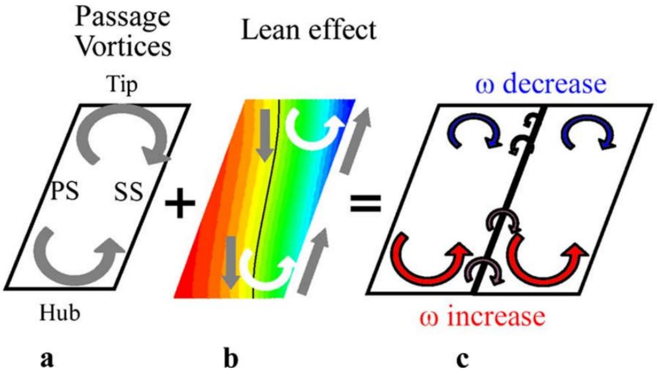

Figure B.6: Coupling effect of secondary vorticity and leaned effects; (a,b) refer to in vane conditions, (c) refers to downstream of the trailing edge

As it can be observed in the figure above, in the upper part of the channel natural secondary vorticity and lean induced flow impose rotations opposite in sign, while in the lower part they impose rotation with same sign. The consequential effect of the interaction of the two flow is hence a decrease of secondary vorticity on the upper part of the channel and an increase in the lower part, Fig. B.6 (c). This induces a different generation process even between hub and tip horseshoe vortex.

In addition, due to the pressure gradient on blade surface and due to secondary flows, a difference in terms of span-wise velocities is found at the trailing edge. This difference causes the wake vorticity to be reduced behind the upper trailing edge part, while it causes it to increase in the lower part.

Another interesting point comes from the observation of CFD and experimental results carried out in the lower half part of a leaned channel, and from the comparison of those with the results obtained for a prismatic channel, Fig. B.7 [23].

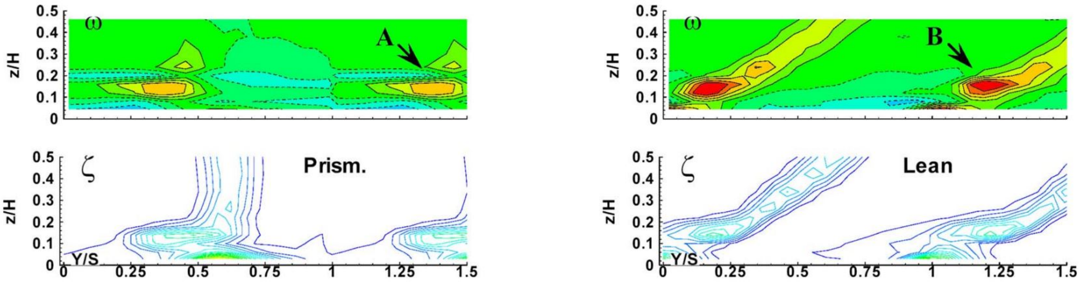

Figure B.7: Experimental loss, ζ, and vorticity, ω, fields in the lower part of the channel and downstream of the stator outlet

Usually, secondary vorticity is proportional to blade loading and flow deflection throughout the passage. On the contrary, blade lean produces a secondary vorticity growth where blade loading decreases [23].

However losses measured for the leaned passage are lower in terms of magnitude and extension with respect to the ones measured for the prismatic cascade. The reason can be found in the blade loading distribution along the span, lower at the hub than at the tip [23].

Appendix C

Expansion through a blade row

In this chapter it is analyzed the expansion process of the working fluid through a blade row, with focus on the statoric row. Basic thermodynamic and fluid dynamic concepts will be hence recalled. Starting from simple cases of flow expansions and adding complexity step by step it is possible to understand the gas behavior through a 3D stator vane.

It is important to highlight that, considering the gas flow as a system, through the stator vanes no work exchange takes place and it can be assumed as a first approximation that no heat exchange with ambient is involved.

C.1 Flow through a duct

The first case of interest is the one concerning 1D reversible flows. So considering the first law of thermodynamics for an open system, Fig. C.1.

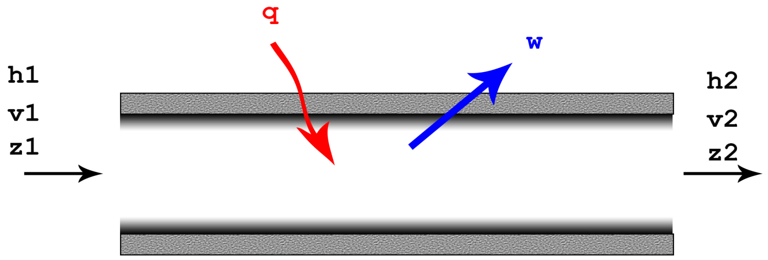

Figure C.1: 1D open system scheme

$$h_1 + \frac{1}{2}v_1^2 + gz_1 + q = h_2 + \frac{1}{2}v_2^2 + gz_2 + w \tag{C.1}$$

$$h_i = enthalpy = u + \frac{p}{\rho} \tag{C.2}$$

$$u = internal\ energy$$

$$p = pressure$$

$$\rho = density$$
$$v_i = flow\ velocity$$
$$z_i = elevation$$
$$q = heat\ exchanged$$
$$w = work\ exchanged$$

Heat is considered positive if it enters the system, while work is positive if it is done by the system itself. Neglecting the potential energy variation in gas flow, assuming the process as adiabatic and considering no work exchange, the first law obtained is:

$$h_1 + \frac{1}{2}v_1^2 = h_2 + \frac{1}{2}v_2^2 \tag{C.3}$$

Starting from stagnation enthalpy definition, it can be derived the so called "Stagnation temperature":

$$c_pT_0 = c_pT + \frac{1}{2}v^2 \tag{C.4}$$

$$T_0 = T + \frac{v^2}{2c_p} \tag{C.5}$$

The result of this procedure lead to the conclusion that the so called "Stagnation enthalpy" stays constant in absence of heat exchange and work exchange.
Stagnation enthalpy is the enthalpy obtained by a full deceleration of the flow to zero velocity.

$$h_0 = h + \frac{1}{2}v^2 \tag{C.6}$$

Equation (C.3) can be rewritten in the form:

$$h_{01} = h_{02} \tag{C.7}$$

Considering the deceleration process as isentropic even the "Stagnation pressure" can be defined, thanks to the usage of the second Gibbs equation.

$$Tds = dh - \frac{dp}{\rho} \implies dh = \frac{dp}{\rho} \qquad ds = 0 \tag{C.8}$$

by integrating Equation (C.8) along the isentropic deceleration and introducing the hypothesis of incompressible flow at constant density:

$$h_0 - h = \int_{p_0}^{p} \frac{dp}{\rho} = \frac{p_0}{\rho} - \frac{p}{\rho} \tag{C.9}$$

$$\implies$$

$$p_0 = p + \frac{1}{2}\rho v^2 = stagnation\ pressure \tag{C.10}$$

C.2 Area change along the flow

A further step necessary to understand what happens to the flow through a statoric row is the introduction of a possible area variation along a duct. Assuming 1D steady, reversible and adiabatic flow it can be easily studied the flow through a channel with varying cross sectional area.

$$\dot{m} = \rho v A = constant \tag{C.11}$$

Differentiating the conservation of mass:

$$\frac{d\rho}{\rho} + \frac{dA}{A} + \frac{dv}{v} = 0 \tag{C.12}$$

Differentiating the stagnation enthalpy conservation:

$$h_0 = constant \longrightarrow dh = -vdv \tag{C.13}$$

Elaborating RHS of Equation (C.8):

$$vdv = -\frac{1}{\rho}dp = -\frac{1}{\rho}\Big(\frac{\partial p}{\partial \rho}\Big)d\rho = -c^2\frac{d\rho}{\rho} \tag{C.14}$$

$$c = speed\ of\ sound$$

Merging Equation (C.12) and Equation (C.14) it is obtained:

$$(M^2 - 1)\frac{dv}{v} = \frac{dA}{A} \tag{C.15}$$

This notorious equation describe the behavior of gases velocity in dependence of area variation and Mach number. In particular a subsonic flow faces an increase in velocity passing from a larger cross sectional area to a smaller one. Instead a supersonic flow faces an increase in velocity when it passes from a smaller cross sectional area to a larger one.

For what concern this study the considered mach number have always been lower than unity.

A further step in the analysis of flows is the consideration of an irreversible, hence non isentropic, flow.

C.3 Analysis on nature of irreversibly

This further analysis can start from the energy balance through a duct for an irreversible 1D flow.

$$\dot{Q} + \dot{m}(u_1 + \frac{p_1}{\rho_1} + \frac{1}{2}v_1^2 + gz_1) = \dot{m}(u + \frac{p}{\rho} + \frac{1}{2}v^2 + gz) + \dot{W} \tag{C.16}$$

This energy balance is carried out between the entrance of a duct and a generic location along its length l.

Differentiating the balance with respect to l:

$$\dot{m}\frac{du}{dl} = \dot{Q}' - \dot{m}\Big[\frac{d(p/\rho)}{dl} + \frac{1}{2}\frac{dv^2}{dl} + g\frac{dz}{dl}\Big] - \dot{W}' \tag{C.17}$$

This procedure can be repeated for the Second Law formulation:

$$\dot{m}(s - s1) = \int_{l_1}^{l} \frac{\dot{Q}'}{T} dl + \int_{l_1}^{l} \dot{S_p}' dl \tag{C.18}$$

$$\Longrightarrow$$

$$\dot{m}\frac{ds}{dl} = \frac{\dot{Q}'}{T} + \dot{S_p}' \tag{C.19}$$

At first it has been analyzed the in-compressible flow case for which it holds the simplified first Gibbs equation $Tds = du$.

Substituting the first Gibbs equation in the second law differential and assuming, as done before no heat nor work exchange:

$$\dot{m}\frac{du}{dl} = T\dot{S_p}' \tag{C.20}$$

Now this last equation can be equated to the differential of the energy balance (first law differential), neglecting the potential energy term as done before.

$$\dot{m}\Big[\frac{d(p/\rho)}{dl} + \frac{1}{2}\frac{dv^2}{dl}\Big] = -T\dot{S_p}' \tag{C.21}$$

Dividing everything by the mass flow rate and integrating the equation along the considered length, from l_1 to l_2:

$$\frac{p_2}{\rho} + \frac{1}{2}v_2^2 = \frac{p_1}{\rho} + \frac{1}{2}v_1^2 - \int_{l_1}^{l} Ts_p' dl \tag{C.22}$$

Hence, as a result of an irreversible process, the so called "stagnation pressure" decreases.

$$p_{01} > p_{02}$$

This decrease can be considered as a loss in the mechanical energy stored by the flow.

However the energy conservation implies that this energy have to be still contained in the flow. In fact it can be observed, starting from the integral of Equation (C.20), that this loss in mechanical content can be traduced in a gain in internal energy.

$$u_2 - u_1 = \int_{l_1}^{l_2} Ts_p' dl \tag{C.23}$$

At this point a simple and similar analysis can be carried out for compressible flows. The reference Gibbs equation would be in this case the second, and it is considered in its differential form for stagnation quantities with respect to the duct length coordinate:

$$T_0\frac{ds}{dl} = \frac{dh_0}{dl} - \frac{1}{\rho_0}\frac{dp_0}{dl} \tag{C.24}$$

Equating the Gibbs equation differential and the differential form of the second law, holding all the previous hypothesis on work and heat exchange:

$$\dot{m}\Big[\frac{dh_0}{dl} - \frac{1}{\rho_0}\frac{dp_0}{dl}\Big] = T_0\dot{S_p}' \tag{C.25}$$

Since no work nor heat exchange is are present:

$$\frac{dh_0}{dl} = 0 \tag{C.26}$$

Hence:

$$\frac{\dot{m}}{\rho_0}\frac{dp_0}{dl} = -T_0\dot{S}_p{}' \tag{C.27}$$

Even in the compressible case the drop in stagnation pressure can be re conduced to the entropy formation rate.
In conclusion the flow in the statoric row would result to be accelerated by the converging shape imposed to the cross sectional area of the flow. Plus at the same time the flow would face the conservation of stagnation enthalpy, due to the absence of heat and work exchange, and the drop in stagnation pressure due to irreversible nature of the process.

C.4 Sources of entropy in stator expansion

Once it has been clarified the importance of entropy production from the energetic point of view it is useful to analyze which are the main mechanisms of entropy generation through the statoric vanes of an axial turbine.
The complex phenomena at the root of the entropy production used in the 1D model have been found to be strictly linked to the nature of turbomachines themselves. In fact the three-dimensional, viscous, highly unsteady, transitional, turbulent, and compressible flows found in a turbine stage, such as the one studied during this work, are deeply different from the flows in theoretical 1D or even 2D cases.
To briefly describe the loss mechanisms of interest it is useful however to take into account the ones used during mean-line 1D design for estimation of stage efficiency.

- Profile or primary loss
- Loss due to the trailing edge thickness
- Secondary flow loss
- Exit loss

Among those the mechanism of major interest for this thesis regard the losses due to secondary flows.

C.4.1 Secondary Flow vortices

To understand secondary flows and their effects, as it has been done during this study, it is necessary first to have a clear idea of which are the mechanisms at the basis of their formations.
In general a flow within a turbomachine can be subdivided in two different components: The flow in absence of viscous effects on hub and casing, in absence of

clearances and in absence of radius variation called "primary flow"; and the so called "secondary flow".
As a result the secondary flow represents the effect of boundary layers, clearances and radial variations within stator (and even rotor). All the flow patterns obtained by the end wall boundary layers and the flow core interaction have vortex characteristic.

C.4.1.1 Passage vortex and trailing vortex

The dominant vortex is the "passage vortex", Fig. C.2, which is formed as a result of the interaction between the low energetic end-wall boundary layer (at hub/casing) and the governing pressure difference within the blade channel. The fluid particles in the boundary layers tend to move from the pressure side to suction side and form, on blade hub and tip regions, counter-rotating vortices. A passage vortex could even interact with the neighboring channel passage vortex in the wake zone and trigger in this way a so called "trailing vortex", Fig. C.4.

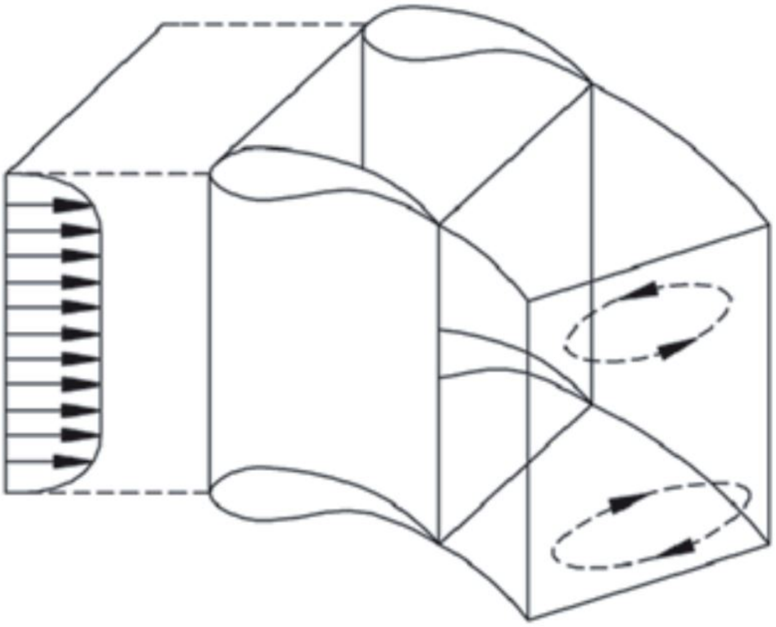

Figure C.2: Scheme of the passage vortex [24]

As a consequence of this passage vortex the flow turning increases at end walls boundary layers and decreases at some distance from the walls. This phenomenon is called "overturning" at the wall.

C.4.1.2 Corner vortices

For each blade passage the four corners between blades, hub and case are characterized by the possible formation of vortices driven by the passage vortex.

C.4.1.3 Horseshoe vortex

This kind of vortex is consequence of the difference in stagnation pressure between core flow and end wall flow at the blade leading edge. The stagnation pressure is higher within the the core and lower in the end wall boundary layer.
The consequential vortex, Fig. C.3, wraps around the leading edge and forms two different rotating structures [25]: the pressure side leg and the suction side leg, Fig. C.4.

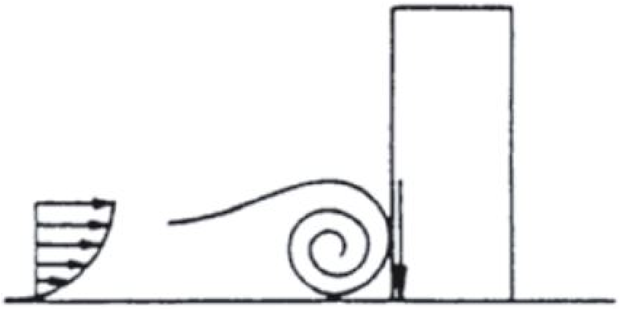

Figure C.3: Side view of horseshoe vortex formation mechanism on a cylinder, a similar behavior is observed on the blades leading edges [24]

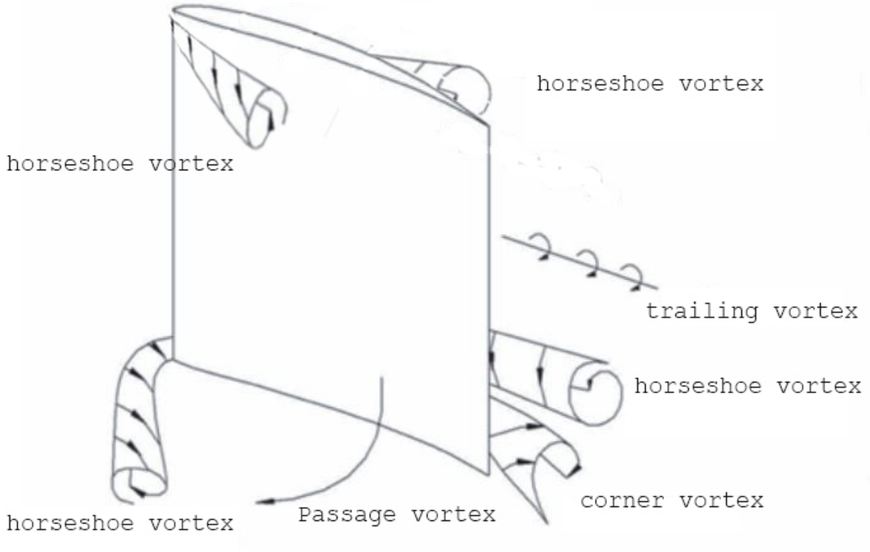

Figure C.4: Horseshoe vortex together with the other described structures [24]

As it can be observed from the previous figure the horseshoe vortex has a strong interaction with the passage vortex.
In fact the passage vortex on the left vane drives the passage vortex leg created on the pressure side towards the suction side of the blade. Those two different vortices has same rotation sense. The fact of having the same rotation sense promote the

merging of thwe two structures making the difference between them mostly invisible at outlet [25].

On the other hand the passage vortex on the rightward vane and the horseshoe vortex leg on the suction side have counter-rotating sense. Hence they do not coalesce but they reinforce each other.

The horseshoe suction side leg may occupy the angle of the vane or instead having a corner vortex underneath. This underneath vortex is formed in particular with separated flow at the corner between suction side and end walls. Typically no corner vortex forms in the pressure side corner where no stall occurs. It is important to keep in mind that through the stator, in absence of clearance spaces, both hub and casing end walls lead to the formation of horseshoe vortices.

C.4.1.4 Secondary flows typical of the rotoric row: Leakage vortex and Scraping vortex

Throughout the statoric row the secondary flows have two additional vortical structures due to the presence of a clearance at casing. The leakage vortex is the consequence of the pressure gradient among the clearance space imposed by the aerodynamic field of the blade. In fact part of the flow in one channel leak through the clearance space, due to the pressure side suction side pressure gradient on the blade itself, and as a result when it gets into the adjacent channel it forms a vortical structure.

The so called scraping vortex is instead caused by the relative motion of the blades with respect to the casing. Fig. C.5 shows the described vortical structures for the rotor channels.

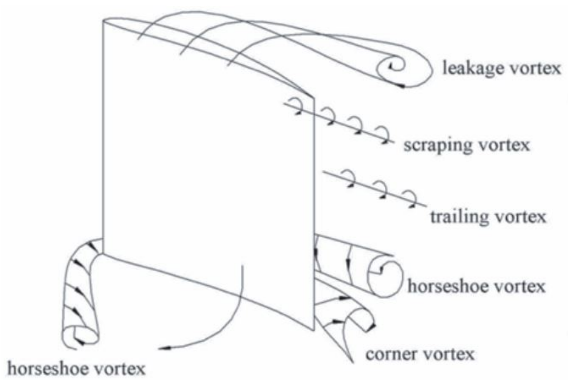

Figure C.5: Vortical structures for the rotor vane [24]

Bibliography

[1] Ann Dowling and Yasser Mahmoudi Larimi. "Combustion Noise". In: *Proceedings of the Combustion Institute* 35 (Nov. 2015). DOI: `10.1016/j.proci.2014.08.016`.

[2] Andrea Notaristefano and Paolo Gaetani. "Transport of Swirling Entropy Waves through an Axial Turbine Stator". In: *International Journal of Turbomachinery, Propulsion and Power* 6.4 (2021). ISSN: 2504-186X. DOI: `10.3390/ijtpp6040045`. URL: `https://www.mdpi.com/2504-186X/6/4/45`.

[3] Andrea Notaristefano and Paolo Gaetani. "Design and Commissioning of a Combustor Simulator Combining Swirl and Entropy Wave Generation". In: *International Journal of Turbomachinery, Propulsion and Power* 5.4 (2020). ISSN: 2504-186X. DOI: `10.3390/ijtpp5040027`. URL: `https://www.mdpi.com/2504-186X/5/4/27`.

[4] Paolo Gaetani and Giacomo Persico. "Transport of Entropy Waves Within a HP Turbine Stage". In: Turbo Expo: Power for Land, Sea, and Air Volume 2A: Turbomachinery (June 2018). V02AT45A022. DOI: `10.1115/GT2018-76459`. eprint: `https://asmedigitalcollection.asme.org/GT/proceedings-pdf/GT2018/50992/V02AT45A022/2788491/v02at45a022-gt2018-76459.pdf`. URL: `https://doi.org/10.1115/GT2018-76459`.

[5] Paolo Gaetani and Giacomo Persico. "Technology Development of Fast-Response Aerodynamic Pressure Probes". 2020. DOI: `10.3390/ijtpp5020006`. URL: `https://www.mdpi.com/2504-186X/5/2/6`.

[6] Giacomo Persico, Paolo Gaetani, and Berardo Paradiso. "Estimation of turbulence by single-sensor pressure probes". In: (Apr. 2008).

[7] S. Szepessy & P. W. Bearman. "Analysis of a pressure averaging device for measuring aerodynamic forces on a circular cylinder". In: *Experiments in Fluids* (1993). DOI: `https://doi.org/10.1007/BF00944913`.

[8] Andrew Chen and Chiachung Chen. "Evaluation of Piecewise Polynomial Equations for Two Types of Thermocouples". In: *Sensors* 13.12 (2013), pp. 17084–17097. ISSN: 1424-8220. DOI: `10.3390/s131217084`. URL: `https://www.mdpi.com/1424-8220/13/12/17084`.

[9] ASM Handbook Committee. *Properties and Selection: Nonferrous Alloys and Special-Purpose Materials*. ASM International, Jan. 1990. ISBN: 978-1-62708-162-7. DOI: `10.31399/asm.hb.v02.9781627081627`. URL: `https://doi.org/10.31399/asm.hb.v02.9781627081627`.

[10] Balázs Illés, Olivér Krammer, and Attila Géczy. “Chapter 2 - Infrared reflow soldering”. In: *Reflow Soldering*. Ed. by Balázs Illés, Olivér Krammer, and Attila Géczy. Elsevier, 2020, pp. 63–99. ISBN: 978-0-12-818505-6. DOI: `https://doi.org/10.1016/B978-0-12-818505-6.00002-9`. URL: `https://www.sciencedirect.com/science/article/pii/B9780128185056000029`.

[11] Emile Webster. “A critical review of the common thermocouple reference functions”. In: *Metrologia* 58.2 (Feb. 2021), p. 025004. DOI: `10.1088/1681-7575/abdd9a`. URL: `https://doi.org/10.1088/1681-7575/abdd9a`.

[12] *Thermoelectric Effect*. `https://www.efunda.com/designstandards/sensors/thermocouples/thmcple_theory.cfm?search_string=seebeck`.

[13] “First-Order System: Transient Response of a Thermocouple to a Step Temperature Change”. In: ().

[14] Sara Vassallo. “Compressibility effect on the unstedy blade row interaction in a HP turbine stage.” PhD thesis. 2017.

[15] Francesco Tredici Francesco Rapisarda. “Transport analysis of swirling entropy waves in a turbine stage”. PhD thesis. 2020.

[16] Giorgio Scherini Sofia Sagliocco. “Swirling entropy waves generation and transport across a HP turbine nozzle”. In: (2019).

[17] *Impact of Swirling Entropy Waves on a High Pressure Turbine*. Vol. Volume 2D: Turbomachinery — Multidisciplinary Design Approaches, Optimization, and Uncertainty Quantification; Radial Turbomachinery Aerodynamics; Unsteady Flows in Turbomachinery. Turbo Expo: Power for Land, Sea, and Air. V02DT39A009. June 2021. eprint: `https://asmedigitalcollection.asme.org/GT/proceedings-pdf/GT2021/84935/V02DT39A009/6757450/v02dt39a009-gt2021-59598.pdf`. URL: `https://doi.org/10.1115/GT2021-59598`.

[18] J. Anthoine and Von Karman Institute for Fluid Dynamics. *Measurement Techniques in Fluid Dynamics: An Introduction*. Von Karman Institute for Fluid Dynamics, 2009. URL: `https://books.google.it/books?id=QJwGngEACAAJ`.

[19] Mora Alessandro. “Analisi del flusso in palettature di turbina caratterizzate da geometria fortemente tridimensionale”. In: (2004).

[20] P. Gaetani et al. “Investigation of the Flow Field in a High-Pressure Turbine Stage for Two Stator-Rotor Axial Gaps—Part II: Unsteady Flow Field”. In: *Journal of Turbomachinery* 129.3 (July 2006), pp. 580–590. ISSN: 0889-504X. DOI: `10.1115/1.2472393`. eprint: `https://asmedigitalcollection.asme.org/turbomachinery/article-pdf/129/3/580/5729143/580\_1.pdf`. URL: `https://doi.org/10.1115/1.2472393`.

[21] Warren C. Strahle. “Combustion noise”. In: *Progress in Energy and Combustion Science* 4.3 (1978), pp. 157–176. ISSN: 0360-1285. DOI: `https://doi.org/10.1016/0360-1285(78)90002-3`. URL: `https://www.sciencedirect.com/science/article/pii/0360128578900023`.

[22] Ignacio Duran Aimee S Morgans. “Entropy noise: A review of theory, progress and challenges”. In: (2016). DOI: `10.1177/1756827716651791`.

[23] Dossena Vincenzo D’Ippolito Gabriele and Mora Alessandro. “The Influence of Blade Lean on Straight and Annular Turbine Cascade Flow Field”. In: *Journal of Turbomachinery* 133.1 (Sept. 2010). ISSN: 0889-504X. DOI: `10.1115/1.4000536`.

[24] Erik Dick. *Fundamentals of Turbomachines*. Springer, Dordrecht, 2015. ISBN: 978-94-017-9627-9. DOI: `https://doi.org/10.1007/978-94-017-9627-9`.

[25] Seppo A. Korpela. *Principles of Turbomachinery*. John Wiley & Sons Inc, 2019. ISBN: 9781119518082.